IRFU-SPP/Saclay09-2010

Institut de Recherche sur les lois Fondamentales de l'Univers (IRFU)

THÈSE

présentée à

l'Université Paris-Sud 11

pour obtenir le titre de

Docteur en Sciences,

Spécialité:

Physique des particules

par

Claudio Giganti

Particle Identification in the T2K TPCs and study of the electron neutrino component in the T2K neutrino beam

Soutenue le 23 septembre 2010

Devant un jury composé de :

Stephane	Lavignac	
Achille	Stocchi	*Président du Jury*
Johannes	Timmermans	*Rapporteur*
Francois	Vannucci	*Rapporteur*
Marco	Zito	*Directeur de thése*

Contents

1 The neutrino physics **4**

1.1 The discovery of the neutrinos 4

1.2 The neutrino in the Standard Model 6

1.2.1 The problem of the neutrino masses 7

1.3 The neutrino oscillation 10

1.3.1 The theory of the neutrinos oscillation 10

1.3.2 The matter effects 14

1.4 Neutrino oscillation experiments 16

1.4.1 The Solar Neutrinos 16

1.4.2 Reactor Antineutrinos 17

1.4.3 Atmospheric neutrino oscillations 19

1.4.4 Long-Baseline neutrino experiments 21

1.5 The present and the future in neutrino oscillation physics 22

1.5.1 Neutrino Factories 24

1.5.2 Beta Beams 25

1.6 The leptogenesis hypothesis 25

2 The T2K experiment **29**

2.1 Physics motivations 31

2.1.1 ν_e appearance 31

2.1.2 ν_μ disappearance . . . 34
2.2 The T2K oscillation analysis . . . 38
2.2.1 Physics requirements at ND280 . . . 38
2.2.2 Physics requirements for the ND280 tracker . . . 41
2.3 The beam line . . . 42
2.3.1 The off-axis neutrino beams . . . 43
2.3.2 The T2K neutrino beam . . . 46
2.3.3 Neutrino flux simulation . . . 52
2.4 The far detector: SuperKamiokande . . . 54
2.5 The near detector facility: ND280 . . . 57
2.5.1 The on-axis detector: INGRID . . . 59
2.5.2 The off-axis detectors . . . 60

3 The T2K TPCs **66**
3.1 Principles of gaseous detectors . . . 66
3.1.1 Primary Ionization . . . 66
3.1.2 Motion of charge carriers in the gas . . . 68
3.2 The Time Projection Chamber . . . 72
3.2.1 Measurement of the momentum . . . 73
3.3 The Micro Pattern Gas Detector . . . 75
3.3.1 The Micro Mesh Gaseous Detector . . . 75
3.4 The T2K TPCs . . . 77
3.4.1 The TPC physics goals . . . 77
3.4.2 The mechanical structure . . . 79
3.4.3 Gas System . . . 81
3.5 The gas amplification and readout: Bulk MicroMegas . . . 81
3.6 The Front-End electronic . . . 84

3.7 The TPCs calibration . . . 88
3.7.1 Laser Calibration system . . . 89
3.7.2 Gas monitoring chamber . . . 90
3.8 The offline TPC software . . . 91
3.8.1 The Monte Carlo simulation . . . 91
3.8.2 The Reconstruction packages . . . 92

4 The particle identification in the TPC 97
4.1 Introduction . . . 97
4.1.1 Ionizing collisions . . . 98
4.1.2 Energy required to produce ion pairs . . . 99
4.1.3 Range of primary electrons . . . 99
4.2 Calculation of energy loss . . . 100
4.2.1 Force on a charged particle travelling through a polarizable medium . 101
4.2.2 The Photo-Absorption Ionization model . . . 104
4.2.3 Integral functions of Collision Cross Section . . . 106
4.2.4 Straggling functions . . . 108
4.3 The energy loss simulation in GEANT4 . . . 111
4.3.1 The cross-section model . . . 111
4.3.2 The energy loss simulation chain . . . 111
4.4 The particle identification method . . . 112
4.4.1 Cluster energy . . . 112
4.4.2 Cluster selection . . . 114
4.4.3 The truncated mean method . . . 115
4.5 Implementation of the method . . . 116
4.5.1 The optimization of the truncation fraction . . . 116
4.5.2 Calibration of the number of samples . . . 118

4.5.3 Calibration of the sample length . . . 118
4.5.4 Parametrization of the energy loss in the TPC . . . 121
4.6 Particle identification validations . . . 124
4.6.1 Single monoenergetic particles . . . 124
4.6.2 Simulated neutrino interactions . . . 125
4.6.3 Particle identification performances . . . 126

5 MicroMegas and TPC tests 130
5.1 MicroMegas modules characterization . . . 130
5.1.1 Test Bench at CERN . . . 130
5.1.2 Cosmic test in the HARP field cage . . . 133
5.2 The TPC beam tests . . . 140
5.2.1 The M11 beamline . . . 140
5.2.2 The data taking: typical plots . . . 144
5.3 Energy resolution studies . . . 147
5.3.1 Deposited energy on the different MicroMegas modules . . . 147
5.3.2 Deposited energy resolution for different particle samples . . . 149
5.4 Stability of the deposited energy measurement . . . 149
5.4.1 The correction for the gas pressure . . . 150
5.4.2 Stability of the data taking . . . 150
5.4.3 Truncated mean dependence on the drift distance . . . 151
5.5 Calibration of the truncated mean . . . 153
5.5.1 Number of samples calibration . . . 153
5.5.2 Sample length calibration . . . 155
5.6 Dependence of the deposited energy on the particle momentum . . . 157
5.6.1 Resolution at different momenta . . . 157
5.6.2 Truncated mean versus momentum . . . 158

5.6.3 Separation between electrons and muons . . . 158
5.6.4 Studies of electrons efficiencies and muons contaminations . . . 160
5.7 Straggling functions . . . 164
5.8 Conclusions . . . 166

6 Installation and commissioning of the TPCs in the ND280 facility 167
6.1 Installation of the TPCs in the ND280 pit . . . 168
6.2 Online Monitoring . . . 170
6.3 TPC calibration chain . . . 171
6.3.1 MicroMegas calibration with cosmics . . . 174
6.3.2 MicroMegas calibration with through going muons . . . 175
6.4 Deposited energy measurements . . . 179
6.4.1 Energy deposited by cosmic tracks . . . 179
6.4.2 Systematic effects on the measurement of the deposited charge . . . 182
6.4.3 Muons and electrons samples: comparison of the data with the Monte Carlo . . . 184
6.4.4 Energy deposited by beam related events . . . 188
6.4.5 PID performances: pulls . . . 192

7 Analysis of the T2K beam electron component using the ND280 tracker 194
7.1 Introduction . . . 194
7.1.1 The ν_e sources in the T2K beam . . . 196
7.1.2 ν_e fluxes at ND280 and SuperKamiokande . . . 198
7.2 Measurement of the ν_e component: Monte Carlo analysis . . . 201
7.2.1 Monte Carlo sample . . . 201
7.2.2 Particle Identification methods . . . 203
7.2.3 Lepton track selection . . . 203
7.2.4 Electrons selection . . . 206

7.2.5 Background rejection in the electron sample 208
7.2.6 Properties of the selected sample 211
7.3 Additional background coming from full spill simulation 213
7.4 Measurement of the electromagnetic background 216
7.5 Conclusions 217

8 Selection of neutrinos interactions in the Tracker with the first T2K physics run 219

8.1 The first T2K physics run 220
8.1.1 The selection criteria 220
8.1.2 Analysis efficiencies 223
8.2 Muon neutrino sample in the tracker 226
8.3 Electron neutrino selection in the tracker 229
8.3.1 Muon misidentification probability 230
8.3.2 Selection of electron neutrino candidates 232
8.3.3 Cross-check of the ν_e selection: the positive analysis 235
8.4 Measurement of the ν_e component 236
8.5 Conclusion 239

9 Conclusions 240

Introduction

This thesis describes the work done on the TPCs of the Near Detector of the T2K experiment. T2K is an experiment installed in Japan and its main purpose is the measurement of the last angle of the neutrino mixing matrix, θ_{13}. The other two angles of the matrix have already been measured in the last years, through the phenomenon of the neutrino oscillations, showing that the neutrinos have masses different from zero.
The measurement of the missing angle θ_{13} is of fundamental importance for the neutrino physics as, if this angle is different from zero, CP violation in the lepton sector can occur.

Up to now only upper limits on the value of θ_{13} exist: the aim of T2K is to measure this angle or to put upper limits on it with a sensitivity 20 times better than the current limit. This measurement will be done measuring the appearance at the far detector, SuperKamiokande, of electron neutrinos in the muon neutrino beam produced at JPARC.

The main background to the measurement of θ_{13} is the electron neutrinos produced together with the muon neutrinos in the beam: this component, expected to be of the order of 1% of the total neutrino flux, has to be measured at the T2K Near Detector, before the oscillations. This can be done selecting neutrino interactions in the Near Detector tracker and using the TPC particle identification capabilities to distinguish electrons from muons. This allows to select a sample of electron neutrino interactions and to measure their spectrum at the Near Detector.

During this thesis I have developed the methods to perform the particle identification in the TPCs: the method is based on the measurement of the truncated mean of the energy deposited by the charged particles in the gas: at the typical energy of the T2K neutrinos the difference in the deposited energy between muons and electrons is of the order of 40% and for this reason a resolution better than 10% is needed to distinguish the two particles: as we will show in the thesis, with our method we measured a deposited energy resolution of 7.5% for Minimum Ionizing Particles.

I developed and tested the TPC PID methods using a Monte Carlo simulation based on the Near Detector official software. The energy loss curve was parameterized as a function of the $\beta\gamma$ of the particle and then we defined a pull variable to give the particle identification probability. These methods are described in the chapter 4 of this thesis.

We also validated the PID methods using the TPC beam test. I directly participated to these beam tests that were performed at TRIUMF for each of the TPCs in 2008 and 2009. The beam provided monoenergetic particles (pions, muons and electrons) with momenta up to 400 MeV/c. I analyzed the data of the beam tests for each of the TPC, checking the dependencies of the deposited energy on the momentum, the angle, the number of samples and the external conditions. This analysis allowed us to validate the PID methods and the TPC performances before the installation in Japan and the results are shown in chapter 5.

In the Autumn of 2009 the TPCs were installed and commissioned at JPARC, in the Near Detector hall. During the thesis I spent 4 months at JPARC working on the installation of the TPCs, on the electronics and the data acquisition commissioning and on the TPC online monitoring. I also analyzed the first cosmics and beam data taken in 2010 to check the Particle Identification measurements. The results are shown in chapter 6.

I also made a Monte Carlo based analysis to measure the electron neutrino component in the T2K beam: the analysis, described in chapter 7, mainly uses the TPC PID capabilities and shows the feasibility of this measurement, with a residual background mainly coming from electrons entering the TPCs and not generated by ν_e.

Finally in the chapter 8 I will show the analysis at the Near Detector of the first physics run of the T2K experiment. We performed a selection of the electron neutrinos interactions in the near detector tracker, together with a selection of the muon neutrinos interactions. With these data we were able to perform a first measurement of the ratio between ν_e and ν_μ at the Near Detector.

Chapter 1

The neutrino physics

The neutrino physics is one of the most important field of contemporary particle physics. In fact, recent neutrino experiments not only gave precise measurements of the Standard Model parameters but they also discovered something new, not expected in the Standard Model: as we will show in this chapter, the solar and atmospheric neutrino data directly show that neutrinos have masses and that the lepton flavor is not conserved.
The hypothesis of oscillation of massive neutrinos can fit the data provided that the mixing angles among the neutrinos are large, in contrast with what happens in the quark sector. Present data strongly disfavor alternative exotic explanation, like neutrino decay or oscillation into sterile neutrinos.
In the future new experiments should confirm and complete this picture. New oscillation effects, like the oscillation of muon neutrinos into electron neutrinos at the atmospheric oscillation length and the observation of CP violation may be established, while other experiments will be able to detect the absolute value of the neutrino masses and will test the nature of neutrinos. Moreover understanding neutrino propagation will open applications in the domains of astrophysics, cosmology and geology.

1.1 The discovery of the neutrinos

According to our current theoretical framework, the neutrino is an elementary particle, without internal structure nor electric charge and sensitive only to the weak and to the gravitational interactions.
Neutrinos are naturally produced by the nuclear fusion reactions in the stars, by the supernovae explosions, in the cosmic rays cascades in the Earth's atmosphere or by natural radioactive processes. Intense artificial sources of neutrinos are the nuclear reactors and the

neutrino beams, produced with particles accelerators.
The existence of the neutrino was first proposed by Pauli in 1930 to explain the continuous electron energy spectrum observed in nuclear β-decays. At the time, β-decay was understood to be the decay of a heavier nucleus A into a lighter nucleus B with the emission of an electron.
In such a two-body decay, if A decays at rest, then according to the conservation of energy, the energy of the outgoing electron should be

$$E_e = \frac{M_A^2 - M_B^2 + m_e^2}{2M_A} \tag{1.1}$$

where M is the mass, yielding a monochromatic energy spectrum. Instead, β-decay experiments observed a continuous electron energy spectrum, with a maximum value of the observed energy E_e^{max} extremely close to E_e. Pauli proposed that another particle that he called the neutron (now known as the neutrino, ν) was being emitted in the decay, $A \rightarrow Be^{-}\nu$ and inferred that this particle should be: electrically neutral (to conserve charge), with spin 1/2 (to conserve angular momentum) and weakly interacting. Finally the new particle should have a mass lighter than the electron mass, given the experimental observation that $E_{max} \sim E_e$.
After the discovery of the neutron done by Chadwick in 1932 [1], Fermi gave a first theoretical interpretation of the β-decay [2], in which he explained it as a neutron that decays into a proton, an electron and a neutrino. This is also the first time in which this new particle was named neutrino.
Now we know that the β-decay occurs with the exchange of the intermediate boson W, and the Fermi theory is the low energy limit of this process.

In 1956, Reines and Cowan [3] succeeded in detecting anti-neutrinos from the inverse β-decay

$$\overline{\nu}_e + p \rightarrow e^{+} + n \tag{1.2}$$

using a nuclear reactor, proving the existence of neutrinos for the first time.
In 1962, another type of neutrino was detected in an experiment at Brookhaven National Laboratory [4]. This was the first experiment using a neutrino beam coming from pion decays and the experimental result was that there is one type of neutrino associated with the electron and a second type of neutrino associated with the muon. The neutrino discovered by Reines and Cowan was an electron neutrino (ν_e) while the new neutrino was a muon neutrino (ν_μ). Electrons and muons and their associated neutrinos are called leptons.
In 1975, a third type of charged lepton, the tau (τ), was discovered. It was assumed then that a third type of neutrino, ν_τ , must exist. The tau neutrino was finally directly observed

in 2001 by the DONUT experiment at Fermilab [5].
The conservation of the lepton flavor implies that each neutrino is coupled with the corresponding charged lepton, forming with him a doublet. In case of charged-current interactions, the ν_x ($\overline{\nu}_x$) will be transformed in the lepton x^- (x^+), where x is one of the three charged lepton (e,μ,τ).

1.2 The neutrino in the Standard Model

The Standard Model [6] requires the presence of three neutrino families, ν_e, ν_μ, ν_τ that together with the corresponding charged leptons form the doublets of the weak interaction. Neutrinos are electrically neutral as they do not interact electromagnetically. They are also color-neutral (color is the charge associated with the strong interaction) as they do not interact strongly. Thus, neutrinos can only interact via the weak interaction. There are two types of weak interactions: charged-current (CC) and neutral-current (NC). CC interactions are mediated by charged W bosons and couple neutrinos to their charged lepton partners. NC interactions are mediated by the neutral Z boson and couple neutrinos to themselves.
In the definition of the Standard Model neutrinos are massless: for all the other fermions the so-called Dirac masses are provided by the Higgs mechanism that couples the right-handed singlets with the left-handed doublets via the Yukawa coupling constant, providing a mass of the form of

$$m_l \bar{l}_L l_R + m_q \overline{q}_L q_R \tag{1.3}$$

In this context the masses of the different fermions are given by m_i:

$$m_i = \frac{v}{\sqrt{2}} \Gamma_i \tag{1.4}$$

where v is the vacuum expectation value of the Higgs field and Γ_i is the Yukawa coupling constant, that assumes different values for the different fermions. To explain the observed masses Γ_i varies from ~ 1 for the heaviest fermion, the quark top, to $\sim 10^{-5}$ for the lighter charged fermion, the electron.
The neutrinos are instead massless in the Standard Model; the right-handed singlet is not present in the theory and the neutrinos are fully described by the Lagrangian term

$$\mathcal{L}_\nu = \overline{\nu} i \not{D} \nu \tag{1.5}$$

that includes a kinetic term plus the gauge interaction with the massive vector bosons, $\overline{\nu} Z \nu$ and $\overline{\nu} W l_L$.

Experiments that can measure the mass of neutrinos directly (such as β-decay experiments) so far have only been able to set upper limits.
The current upper limit obtained by tritium decay experiments is $m_\nu < 2\ eV/c^2$ [7]. A limit on neutrino mass can also be obtained from cosmological data. This limit is model dependent and according to the different models the upper limit on the sum of the neutrino masses Σm_i varies between 0.2 and 1 eV/c^2, being the most stringent limit on neutrino masses so far [8].
Other experiments are currently looking for the double β-decay without neutrinos that, if discovered, requires a neutrino mass different from zero.
Nevertheless, even if a direct measurement does not exist yet, there is an indirect proof of the existence of a neutrino mass different from zero: the observation, in different experiments, of the phenomenon of the neutrino oscillations.

1.2.1 The problem of the neutrino masses

After the discovery of the neutrino oscillations it became clear that the neutrinos had non-zero masses and it was necessary to consider their masses within the Standard Model. The most natural way to include these masses is to consider the neutrinos as all the other fermions, adding to the Standard Model definition, the right-handed singlets neutrinos. Adding these fields the neutrino masses are provided, as for all the others fermions, by the Higgs mechanism:

$$m_D^i \overline{\nu}_L^i \nu_R^i \tag{1.6}$$

where i is the neutrino family. This term conserves the lepton number; m_D is called a Dirac mass and has the same form of the fermion masses of equation 1.4

$$m_D^i = \frac{v}{\sqrt{2}} \Gamma_{\nu^i} \tag{1.7}$$

The problem of this model is that, to explain the actual limits on the neutrino masses, the Yukawa coupling constants Γ_{ν^i} have to be of the order of 10^{-11} and no explanations exist of the smallness of the neutrino masses.

An alternative way to include the neutrino masses is to add to the Standard Model Lagrangian a term of dimension 5 of the form

$$\mathcal{L} = \mathcal{L}_{SM} + \frac{k^{ij}}{M}(\nu_L^{iT}\epsilon\phi)C(\phi^T\epsilon\nu_L^j) \tag{1.8}$$

where k^{ij} is a coupling constant, C is the charge conjugation matrix that makes the mass term Lorentz invariant and M is a scale factor necessary to keep the Lagrangian of dimension 4. This term couples the left-handed fields ν_L with the Higgs field ϕ and when the Higgs field acquires its vacuum expectation value, the neutrino field acquires a mass of the form

$$m_M \nu_L^T C \nu_L \tag{1.9}$$

with m_M given by

$$m_M = \frac{v^2}{M}k^{ij} \tag{1.10}$$

In this way no unnatural coupling constants are necessary and the neutrinos masses are simply proportional to v^2/M and can be as little as we desire if $v << M$. The neutrino mass in this case is called a Majorana mass term and the lepton number is violated by 2 units. The lepton number violation has no consequences on the Standard Model, as its conservation is not required and was only an accident of the Standard Model.
The difference between the Dirac and the Majorana mass terms is that the first requires the presence of right-handed neutrinos while the latter does not need a right-handed neutrino and, as the lepton number is not conserved, in this term nothing distinguishes neutrinos from antineutrinos.
This has an important consequence: in nature we observe only two types of neutrinos, the neutrinos, ν_L, that have negative helicity (that means that the spin is opposite to the momentum) and their CPT conjugate, the antineutrinos $\overline{\nu}_R$, that have positive helicity. This is perfectly compatible with the picture of massless neutrinos, but, if now we assume that neutrinos are massive particles it is possible to consider a Lorentz transformation that reverses the sign of the momentum and therefore the helicity, introducing two new states, ν_R and $\overline{\nu}_L$.
In the Dirac case the neutrino is different from the antineutrino and all the four states exist. In the Majorana case instead, the neutrino being is own antiparticle, only two states are left, that are distinguished by the helicity.
So far we considered the Dirac and the Majorana case as two completely distinct cases, but the two can be mixed and we can extend the model, adding to the Standard Model a right-handed neutrino with a Majorana mass term. The mass term, as for the left-handed neutrinos is given by

$$M_R \nu_R^T C \nu_R \tag{1.11}$$

In this way the right-handed neutrino has both a Dirac mass term given by 1.6 and the Majorana mass term that again violates the Lepton number. As ν_R is a singlet we do not need to couple it to the Higgs field: no relation between M_R and the Higgs vacuum expectation value v exists and M_R can be as large as we want. The interesting thing is that we can relate M_R to the mass of the light neutrinos: let us consider the two processes of figure 1.1: the two processes are the same if the mass of the heavy right-handed neutrino propagator M_R is large. This provides the relation

$$\frac{\Gamma^2_{\nu^i}}{M_R} \sim \frac{k^{ij}}{M} \tag{1.12}$$

This is the see-saw mechanism[9]: there are two Majorana particles, the right-handed neutrino that is a heavy particle and the observed left-handed neutrino that is a light particle with a mass related to the right-handed neutrino $m_L \sim v^2/M_R$ (see 1.10). To explain the actual limits on the neutrino masses (according to oscillation experiments $5 \times 10^{-2}\ eV$ is the minimum mass of the heaviest neutrino), we need a mass M_R of the order of $10^{15}\ GeV$. This scale is close to the mass of grand unification suggested, for instance, by the Minimal Supersymmetric Standard Model (MSSM).

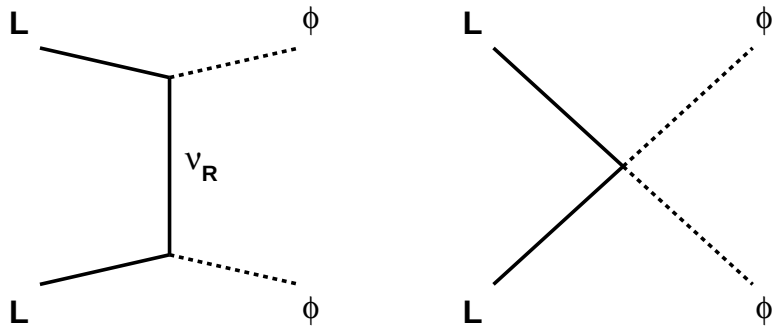

Figure 1.1: Feynman diagram for a lepton-Higgs coupling mediated by an heavy right-handed neutrino (left) and its low energy approximation (right).

The question whether the neutrinos are Dirac or Majorana particles is still an open question: experimentally it is possible to answer this question studying processes that violate the lepton number. If such a process will be observed the neutrinos have to be Majorana particles. An example is given by the neutrinoless double beta decay where the neutrino

emitted in the β-decay interacts as an antineutrino, producing an inverse β-decay. The final result of the process is to have a double β-decay with the emission of 2 electrons and without neutrinos, violating the lepton number by 2 units. Many experiments are now searching the double beta decay without neutrinos (for example CUORE[10], GERDA[11], EXO[12] or SUPER-NEMO[13]) but up to now this process has not been observed.

1.3 The neutrino oscillation

The phenomenon of the oscillation is of fundamental importance in the neutrino physics, because it is, so far, the only evidence that the neutrinos have a mass different from zero and that the lepton numbers are not conserved.
The first experimental evidence suggesting that neutrino oscillation might occur was brought in the 1968 by the Homestake experiment, but as we will see in this section, it remained controversial for several years and it has been commonly accepted only when Super-Kamiokande and SNO results were published in 1998 and 2002.
In this section we will show that, from a theoretical point of view, the neutrino oscillation is described by a neutrino mixing matrix with four free parameters: three mixing angles and and a CP violating phase, δ. The aim of the oscillation experiments is the measurement of these parameters.
The neutrino oscillation experiments are not sensitive to the nature of the neutrinos. If the neutrinos are Majorana particles to completely describe them we need two more phases, the Majorana phases, that do not affect the neutrino oscillations.

1.3.1 The theory of the neutrinos oscillation

In 1957, when the second neutrino family had not yet been discovered, Bruno Pontecorvo suggested the possibility of having neutrino oscillations of the type $\nu \leftrightarrow \overline{\nu}$ [14]. After the discovery of a second neutrino family, the ν_μ, different from the ν_e, Z. Maki, M. Nagakawa and S. Sakata considered the possibility of having an oscillation of neutrinos among the different families, introducing the concept of mixing [15].
The theory is based on quantum mechanical principles: if neutrinos have a nonzero mass and the mass eigenstates do not correspond to the flavor eigenstates, then neutrinos can mix. This is analogous to the mixing in the quark sector. The flavor states, $|\nu_\alpha\rangle$, are superpositions of the mass states, $|\nu_i\rangle$:

$$|\nu_\alpha\rangle = \sum_i U^*_{\alpha i} |\nu_i\rangle \tag{1.13}$$

where $\alpha = e, \mu, \tau$ and i = 1, 2, 3 while U is the unitary mixing matrix and $|\nu_i >$ are the mass eigenstates m_i.
The neutrinos are produced in a flavor eigenstate $|\nu_\alpha\rangle$ because this particle is produced via weak interaction where a $|\nu_\alpha\rangle$ of a well defined flavor is produced together with the corresponding lepton α.

Assuming that a neutrino ν_α is produced at time $t = 0$ by a weak interaction in a flavor eigenstate, we have

$$|\nu(t=0)\rangle = |\nu_\alpha\rangle = \Sigma_i U^*_{\alpha i} |\nu_i\rangle \tag{1.14}$$

To understand how the state evolves in time, we apply the time dependent Schrödinger equation to each ν_i component of ν_α in the reference system of that component. This gives

$$|\nu_i(\tau_i)\rangle = e^{-im_i\tau_i} |\nu_i\rangle \tag{1.15}$$

where m_i is the mass of ν_i and τ_i is the time in the ν_i rest frame. In this section, natural units ($\hbar = c = 1$) are used. The phase factor is Lorentz-invariant and thus may be written in terms of laboratory frame time t and position L,

$$|\nu_i(t)\rangle = e^{-i(E_i t - p_i L)} |\nu_i\rangle \tag{1.16}$$

where E_i and p_i are the energy and momentum of ν_i in the laboratory frame. The neutrino is highly relativistic, and thus we can make the approximation $t \sim L$ giving

$$|\nu_i(L)\rangle = e^{-i(E_i - p_i)L} |\nu_i\rangle \tag{1.17}$$

Assuming that ν_α is produced with momentum p, all the mass eigenstate components of ν_α have a common momentum, $p_i = p$. We can also assume that the neutrino masses m_i are sufficiently small compared with the momentum so that we can make the approximation $E_i = \sqrt{p^2 + m_i^2} \sim p + \frac{m_i^2}{2p}$, then the equation 1.17 becomes

$$|\nu_i(L)\rangle = e^{-i(m_i^2/2p)L}\,|\nu_i\rangle \tag{1.18}$$

Finally, let $E \sim p$ be the average energy of all the mass eigenstate components of the neutrino we can write

$$|\nu_i(L)\rangle = e^{-im_i^2 L/2E}\,|\nu_i\rangle \tag{1.19}$$

The initial state mass components, described by equation 1.14 evolve independently with the time, acquiring a phase $e^{-im_i^2 L/2E}$. Thus for a neutrino born as a ν_α that has propagated for a distance L, the state vector is:

$$|\nu(L)\rangle = \Sigma_i U_{\alpha i}^*\,|\nu_i(L)\rangle = \Sigma_i U_{\alpha i}^* e^{-im_i^2 L/2E}\,|\nu_i\rangle \tag{1.20}$$

The neutrino is thus produced at $t = 0$ in a pure flavor eigenstate $|\nu_\alpha\rangle$, which is a particular superposition of the mass eigenstates. After travelling a distance L, the neutrino state evolves into a different superposition of the mass eigenstates $|\nu(L)\rangle$.
Let us assume that at this point the neutrino is detected. The detection, as well as the production, occurs via a weak interaction, for example a charged current interaction in which a lepton is produced with a defined flavor corresponding to the one of the neutrino. The probability of observing a neutrino that was in flavor state α at time $t = 0$ in flavor eigenstate β at time $t = L$ is

$$P(\nu_\alpha \to \nu_\beta) = |\,\langle \nu_\beta\,|\,\nu_\alpha(L)\rangle\,|^2 = |\Sigma_i U_{\alpha i}^* e^{-im_i^2 L/2E} U_{\beta i}|^2 \tag{1.21}$$

The equation 1.21, using the properties of the complex exponential and the unitarity of the matrix U, can be rewritten, defining $W_{\alpha\beta}^{ij} = U_{\alpha i}^* U_{\beta i} U_{\alpha j} U_{\beta j}^*$ as

$$P(\nu_\alpha \to \nu_\beta) = \delta_{\alpha\beta} - 4\sum_{i>j} \Re(W_{\alpha\beta}^{ij}) sin^2(\frac{\Delta m_{ij}^2 L}{4E}) \pm 2\sum_{i>j} \Im(W_{\alpha\beta}^{ij}) sin(\frac{\Delta m_{ij}^2 L}{2E}) \tag{1.22}$$

where $\Delta m_{ij}^2 = m_i^2 - m_j^2$ is the difference of the square masses of the two eigenstates. The $\pm$ signs distinguish neutrinos from antineutrinos and the imaginary part correspond to the CP violation term. It is easy to demonstrate that if the imaginary part of the equation 1.22 is different from zero, then $P(\nu_\alpha \to \nu_\beta) \neq P(\overline{\nu}_\alpha \to \overline{\nu}_\beta)$.
As the equation 1.22 is complicated, it is useful to study the simplest case in which two neutrino families exist. In this case the matrix U can be written as a rotation

$$U = \begin{pmatrix} cos\theta & sin\theta \\ -sin\theta & cos\theta \end{pmatrix} \tag{1.23}$$

where the mixing angle θ is the only parameter needed to describe the mixing. In this case, the probability of flavor change becomes

$$P(\nu_\alpha \to \nu_\beta) = sin^2(2\theta) sin^2(\frac{1.27\Delta m^2 L}{E}) \tag{1.24}$$

while the survival probability is

$$P(\nu_\alpha \to \nu_\alpha) = 1 - sin^2(2\theta) sin^2(\frac{1.27\Delta m^2 L}{E}) \tag{1.25}$$

where Δm^2 is the difference between the squared masses of the two mass eigenstates and is measured in $(eV/c)^2$, L is measured in km, and E is measured in GeV. The factor 1.27 comes from including the relevant values of $\hbar$ and c.
This equation means that, including only the first two families ($\alpha = \mu$ and $\beta =$ e), if we produce a pure ν_μ beam, at the distance L it will be composed by a mixture of ν_μ and ν_e. The amount of the mixing, for fixed L and beam energy E, is given by two free parameters: the mass square difference Δm^2 and the mixing angle θ.
In the case of three neutrino families, the matrix U can be written as a 3×3 unitary matrix

$$U = \begin{pmatrix} c_{12}c_{13} & s_{12}c_{13} & s_{13}e^{-i\delta} \\ -s_{12}c_{23} - c_{12}s_{23}s_{13}e^{i\delta} & c_{12}c_{23} - s_{12}s_{23}s_{13}e^{i\delta} & s_{23}c_{13} \\ s_{12}s_{23} - c_{12}c_{23}s_{13}e^{i\delta} & -c_{12}s_{23} - s_{12}c_{23}s_{13}e^{i\delta} & c_{23}c_{13} \end{pmatrix} \tag{1.26}$$

where $c_{ij} = cos\theta_{ij}$ and $s_{ij} = sin\theta_{ij}$. In this case the parameters describing the mixing are four, three angles, θ_{12}, θ_{23} and θ_{13},and the CP violating phase δ.

The observation of the neutrino oscillations has two main consequences:

- The neutrinos have a mass different from zero
- The lepton flavor is not conserved if a neutrino can oscillate into another neutrino with a different flavor

In the more general case, there is not only the phase δ, called Dirac phase, but there are two additional phases, called Majorana phases, that do not have effects on the neutrino oscillation.

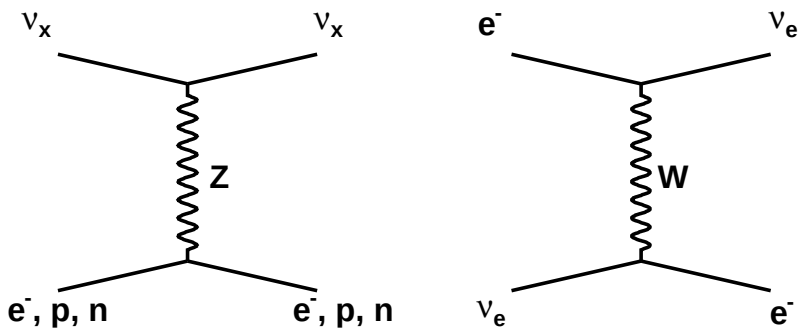

Figure 1.2: Feynman diagram for neutral (left) and charged (right) neutrino interactions with matter. In the neutral current case the neutrino x can be indifferently e, μ, τ.

1.3.2 The matter effects

Neutrinos that travel into matter (where matter can be the Earth, the Sun or a supernova) undergo forward scattering from particles they encounter along the way and this scattering modifies their propagation. This results in a different oscillation probability from the one in the vacuum and is known as the Mikheyev-Smirnov-Wolfenstein (MSW) effect[17], [18].
The interactions with the matter occur in two different ways (see figure 1.2): through neutral current, that affect equally all the neutrino flavors and through charge current on the electrons contained in the medium. This latter interaction affects only electron neutrinos. This means that the $\nu_e - \nu_e$ element of the Hamiltonian H will include the interaction energy

$$V = \sqrt{2} G_F N_e \tag{1.27}$$

where G_F is the Fermi constant and N_e is the number of electrons per unit volume. In the two flavors approximation we can then write the interaction potential as

$$H = \frac{\Delta m^2}{4E} \begin{pmatrix} -\cos\ 2\theta_V & \sin\ 2\theta_V \\ \sin\ 2\theta_V & \cos\ 2\theta_V \end{pmatrix} + \sqrt{2} G_F N_e \begin{pmatrix} 1 & 0 \\ 0 & 0 \end{pmatrix} \tag{1.28}$$

The matter effects can be seen in the solar neutrino oscillation. This oscillation occurs between two flavors: the produced ν_e oscillate into another state ν_x that is a linear combination of ν_μ and ν_τ. The Hamiltonian can be written, in the $\nu_e - \nu_x$ space, as the sum of two terms (as in the case of 1.28)

$$H = H_V + H_M(r) = \frac{\Delta m^2_\odot}{4E} \begin{pmatrix} -\cos\ 2\theta_\odot & \sin\ 2\theta_\odot \\ \sin\ 2\theta_\odot & \cos\ 2\theta_\odot \end{pmatrix} + \begin{pmatrix} V(r) & 0 \\ 0 & 0 \end{pmatrix} \tag{1.29}$$

H_V is the Hamiltonian in the vacuum and $H_M(r)$ contains the matter effects and it depends on the Sun radius r, as N_e depends on r.
From H_V we can see that the two-neutrino oscillation in vacuum cannot distinguish between a mixing angle $\theta_\odot$ and an angle $\theta'_\odot = \pi/2 - \theta_\odot$. But these two mixing angles represent two different physical situations: supposing $\theta_\odot < \pi/4$ if the mixing angle is $\theta_\odot$ the lighter mass eigenstate will be more ν_e than ν_x while if it is $\theta'_\odot$ we will have the opposite situation. These two possibilities are discriminated by the neutrino propagation through solar matter. In fact the neutrino interaction energy V has a definite, positive sign and the $\nu_e - \nu_e$ element of the solar H, defined by $-(\Delta m^2_\odot/4E)cos\ 2\theta_\odot + V(r)$ has a different value if the solution is given by $\theta_\odot$ (Small Mixing Angle) or $\theta'_\odot$ (Large Mixing Angle).
As we will see, solar and reactor neutrino data establish that the behavior of solar neutrinos is governed by a Large-Mixing-Angle (LMA) MSW effect. We can also estimate the probability $P(\nu_e \to \nu_e)$ that an electron neutrino produced in the Sun is observed as an electron neutrino on Earth. We can focus on neutrinos produced by ^8B decay that have an energy of $6{-}7\ MeV$. At $r \sim 0$, where neutrinos are created the interaction energy V is $0.75 \times 10^{-5}\ eV^2/MeV$ and for the observed value of $\Delta m^2_\odot$ of $8 \times 10^{-5}\ eV^2$, H_M dominates. This means that $H(r \sim 0)$ is, in first approximation diagonal and a ^8B neutrino, born as ν_e is not only in a flavor eigenstate but also in an eigenstate of the Hamiltonian H. This eigenstate will be the heavier, since $V > 0$. Assuming that the propagation is adiabatic (that means that the variation of the matter density has a typical scale longer than the neutrino oscillation length) it will remain in the heavier eigenstate of the potential H_V through its propagation inside the Sun. When the neutrinos leave the Sun, their eigenstate in vacuum can be written as

$$\nu_2 = \nu_e \sin\theta_\odot + \nu_x \cos\theta_\odot \tag{1.30}$$

This is an eigenstate of H_V so the neutrino will remain in this state while travelling to the Earth where the probability of observing a ν_e is

$$P(\nu_e \to \nu_e) = \sin^2\theta_\odot \tag{1.31}$$

For $\theta_\odot < \pi/4$ this probability is less than 1/2.
A confirmation of the fact that the matter effects are not negligible is that if they were negligible we would have to apply the equation 1.25 to measure the survival probability. Given the values of the solar parameters, the distance of the Earth from the Sun and the typical energy of solar neutrinos, what we would observe is the mean value of the survival

probability (obtained in averaging the oscillation probability of equation 1.25 over many periods) that cannot be less than 1/2 for any mixing angle. The observation of the ν_e survival probability smaller than 1/2 requires an oscillation influenced by the matter effects through the equation 1.30.

1.4 Neutrino oscillation experiments

In the last 50 years many experiments were done to discover and understand the neutrino oscillations. In particular four different sources of neutrino were studied: the Solar neutrinos, the anti-neutrinos produced by reactors, the Atmospheric neutrinos and the neutrinos produced by accelerators.

1.4.1 The Solar Neutrinos

The first experiment to measure the flux of the neutrino produced in the Sun was proposed and realized by R. Davis in the late 60's in the Homestake mine [16].

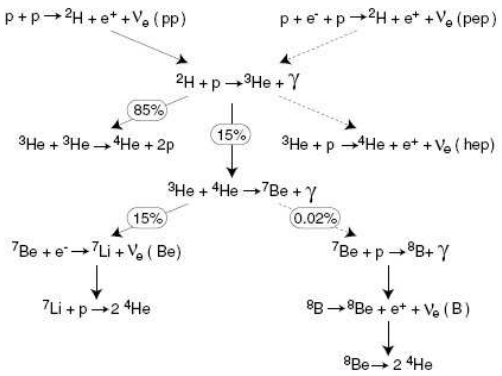

Figure 1.3: Different fusion reactions in the Sun producing neutrinos.

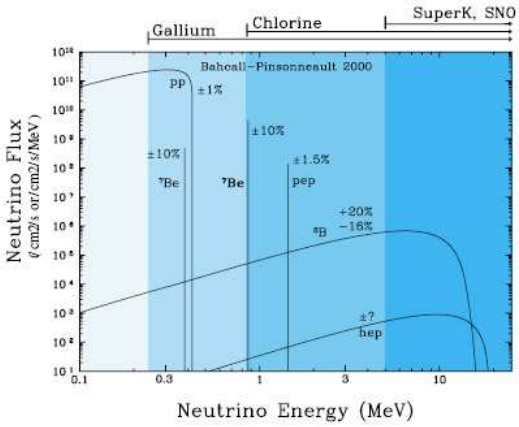

Figure 1.4: Flux of neutrinos coming from the Sun. According to their energy, neutrinos are accessible at the different experiments shown on the top of the plot.

The power of the sun is produced by different fusion reactions (see figure 1.3), which produce only ν_e with the energy spectrum shown in figure 1.4. The typical ν_e flux reaching the Earth is equal to 10^8 $\nu_e/s/m^2$. The experiment proposed, built and operated by Davis was

able to detect only ν_e by inverse beta decay reaction in a tank of 400 m^3 of C_2Cl_4. Then the counting of the number of radioactive Ar nuclei produced by the reaction $Cl + \nu_e \rightarrow Ar + e^-$ gives the electron neutrino flux.
The result of this counting was that the ν_e detected from the sun are only about one third of those expected by the theoretical prediction of the Standard Solar Model (SSM) [19].
The widely accepted explanations of this discovery at the time were that the SSM predictions were wrong or that the experimental result was wrong. Both these explanations are ruled out, the first one by the progress in our understanding of the Sun and the latter by the fact that, in the following years, several experiments have measured the deficit of neutrinos with different techniques: Homestake, Gallex[20], Sage[21] and GNO[22] using the inverse beta decay and Kamiokande[23] and SuperKamiokande[24] using water Cerenkov detectors.
The only solution left to explain the deficit of solar neutrinos is that ν_e transform into something else, which is not detectable by an inverse beta decay detector. Neutrino oscillation would do that, transforming a ν_e into a linear superposition of the three neutrino families, conserving the total neutrino flux. The proof of this would be an experiment able to prove that the total neutrino flux was conserved.
The solution was established in 2002 by the SNO experiment. SNO is a heavy water (D_2O or ^2H_2O) Cerenkov detector[25], whose great innovation is the sensitivity not only to the ν_e charged current interaction but also to the neutral current interactions of neutrinos of any flavor with the Deuterium nuclei. The free neutron is then detected and with this measurement it is possible to measure the total solar neutrino flux.
Comparing the measured flux from the charged and the neutral current interactions we have

$$\phi_{CC} = \phi_e = 1.70 \pm 0.07(stat)^{+0.09}_{-0.010}(syst) \cdot 10^6 \frac{\nu}{cm^2 s} \quad (1.32)$$

$$\phi_{NC} = \phi_e + \phi_\mu + \phi_\tau = 4.90 \pm 0.24(stat)^{+0.29}_{-0.027}(syst) \cdot 10^6 \frac{\nu}{cm^2 s} \quad (1.33)$$

The measurements of the fluxes demonstrate that solar neutrinos, born as ν_e, arrive on the earth as a mix of ν_e, ν_μ and ν_τ of which ν_e is only one third. This result is the final clarification of the solar neutrino puzzle.

1.4.2 Reactor Antineutrinos

Nuclear reactors are a powerful source of $\overline{\nu}_e$ coming from β^- decay of unstable isotopes produced by fission reactions. The neutrino flux and energy spectrum can be calculated with relatively high precision knowing the composition and the burn-up of the reactor fuel and the power of the reactor.

The antineutrino energy spectrum is in the same energy range (few MeV) of the solar neutrinos and a reactor experiment, located at a sufficiently long distance, has sensitivity to measure the solar oscillation parameters.
Until recently, reactor neutrino experiments were always located too close to the reactor source and gave negative results for the oscillations (see figure 1.5).

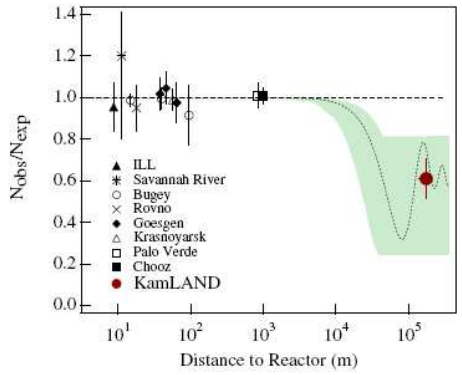

Figure 1.5: Ratio of measured neutrinos over expected neutrinos versus distance for different reactor antineutrino experiments. The read point shows the Kamland result, in agreement with the disappearance predicted by solar neutrino oscillations.

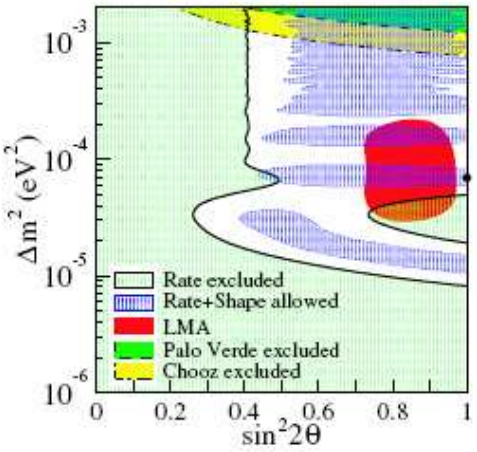

Figure 1.6: Allowed zone for the oscillation parameters $\sin^2\theta_{12}$ and Δm^2_{12} from the Kamland measurements. The red zone represents the preferred solution for the same parameters coming from solar neutrino experiments and Large Mixing Angle hypothesis.

In 2002 the first evidence of oscillation of reactor neutrinos was found by the KamLAND experiment[26].
KamLAND is located in Japan and detects ν_e produced by 16 reactors situated at an average distance of 160 km. The result of Kamland (figure 1.5) confirms the disappearance of ν_e according to solar neutrino prediction. Moreover the uncertainty on the solar oscillation parameter measurements is reduced once the results of KamLAND are combined with other experiments: in particular SNO results, as it is presented in figure 1.6, confirm the LMA (Large Mixing Angle) solution as the preferred one.
Another interesting result for the neutrino oscillation coming from reactor experiments is given by the CHOOZ experiment[27]. CHOOZ produced the most significant limit, up to now, on the angle θ_{13} of the neutrino mixing angle.
The detector was located in France, about 1 km away from two nuclear reactors which generate a total thermal power of $\sim$ 8.5 GW. The neutrinos generated from the fission decays

have an average energy of 3 MeV. The results of CHOOZ ruled out from the possible explanation of the atmospheric neutrino oscillation, described in the next section, the oscillation $\nu_e \rightarrow \nu_\mu$ and provided the limit $\theta_{13} < 10^\circ$ for $\Delta m^2_{13} = 3 \cdot 10^{-3}\ eV^2$.

1.4.3 Atmospheric neutrino oscillations

After the Sun, the other main natural source of neutrinos is the earth atmosphere. An intense flux of cosmic rays, primarily protons, arrives on the high atmosphere producing a huge number of secondaries, in particular pions. These particles then decay in flight via $\pi^\pm \rightarrow \mu^\pm + \nu_\mu(\overline{\nu}_\mu)$. The produced muons again decay according to $\mu^\pm \rightarrow e^\pm + \nu_e(\overline{\nu}_e) + \overline{\nu}_\mu(\nu_\mu)$. The typical energy spectrum of atmospheric neutrinos starts at about hundred MeV and extends up to several GeV.

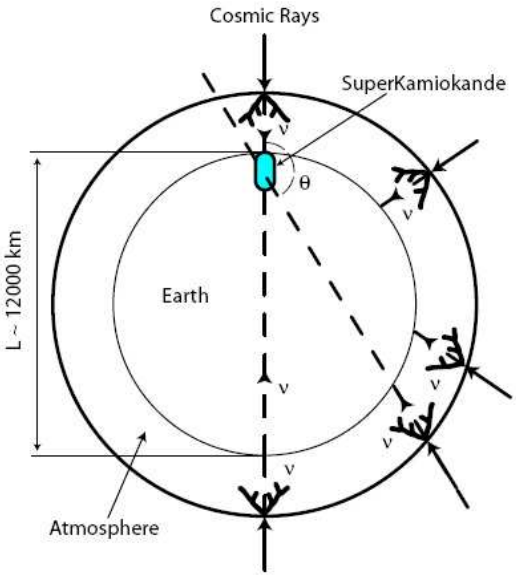

Figure 1.7: Different flight distances, between their production point and SuperKamiokande, for neutrinos produced in cosmic ray interactions with the Earth atmosphere.

The measurement of the atmospheric neutrino oscillation requires a different technique from that used for solar neutrinos, mainly because the atmosphere cannot be considered as a point-like source at fixed distance, like it was the case of the Sun. Neutrinos can be generated at any point of the atmosphere, thus neutrinos of the same energy born at the same time can travel very different distances before reaching the detector and this gives different oscillation probabilities (see figure 1.7). To study the oscillation probability it is

necessary to have detectors able to recognize the direction of the incident neutrino and the water-Cerenkov technique proved to be the most effective for this purpose.
A detailed description of the water Cerenkov technique will be given in the next chapter. In general when neutrinos interact with matter via the charged current they generate leptons. If they interact in water and if the lepton energy is above the water Cerenkov threshold, which is few MeV for electrons and few hundreds MeV for muons, light is emitted on a cone centered on the lepton trajectory.
The typical water Cerenkov detector is composed of a huge water tank equipped with an array of phototubes mounted on its wall used to record the Cerenkov light.
If the lepton stops inside the detector, the amount of Cerenkov light is used to determine the energy of the lepton, and hence of its neutrino parent. Moreover muons and electrons can be separated by the shape of their Cerenkov rings, giving in this way also the flavor of the primary neutrino.

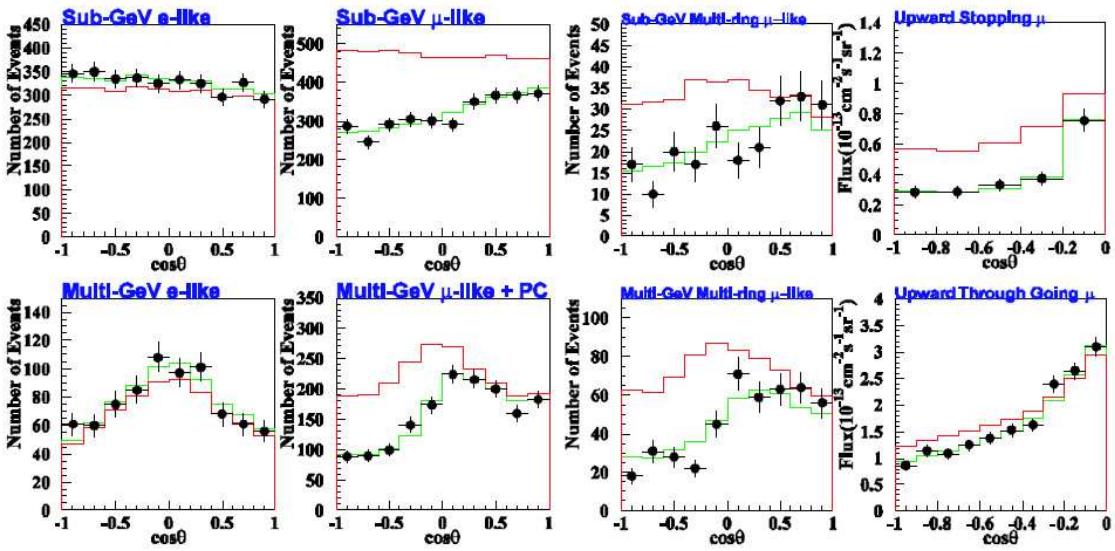

Figure 1.8: SuperKamiokande results[24]. The neutrino fluxes are measured in bins of the zenith angle θ and divided in two categories, muon events created by a ν_μ interaction, and electron events, created by a ν_e interaction. A further division is done according to the energy of the lepton.

The larger detector of this type is SuperKamiokande[24], a 50 kton water Cerenkov detector. In addition to the solar neutrinos SuperKamiokande observes atmospheric neutrinos, separating the neutrino flux for different directions (see figure 1.8). The experiment counts ν_e and ν_μ in bins of the zenith angle θ ($\cos\theta = 1$ for the neutrinos coming from the zenith and $\cos\theta = -1$ if they come from the nadir). The experimental result, first presented in

1998 is that ν_μ coming from the bottom, hence traversing the Earth, are half of those coming from the top. The easiest explanation could be: neutrinos have interacted with the Earth. But the asymmetry does not appear for ν_e (see figure 1.8), and we also know that the Earth is practically transparent for neutrinos with energy lower than few GeV. The only possible explanation is that atmospheric ν_μ transform into a linear superposition of neutrinos, which does not include ν_e, since there is no excess in the ν_e flux coming from the opposite side of the Earth.
The SuperKamiokande results provided a strong evidence of the existence of neutrino oscillations with a different Δm^2 from the solar neutrinos.

1.4.4 Long-Baseline neutrino experiments

A very interesting way to study the neutrino oscillations parameters, in particular the atmospheric ones (Δm_{23} and θ_{23}) and the undiscovered θ_{13} is given by long baseline neutrino experiments that use neutrinos produced by accelerators and detected in a near detector (before the oscillation) and in a far detector (after the oscillation).
The advantages of such experiments is that they can produce very intense neutrino beams, having enough statistics to measure the oscillation parameters and with a well defined L/E ratio. These experiments are particularly useful if we know the value of Δm^2_{23}. In fact knowing Δm^2 we can choose the L/E ratio that maximize the oscillation probability.
The details of the production of a neutrino beam will be given in the next chapter: a beam is produced by interactions of a proton beam with a target. These interactions produce hadrons (in particular pions) that are then focused into a decay tunnel of sufficient length to let them decay into muons and neutrinos. The surviving pions and the muons are then absorbed by a a beam dump, while neutrinos travels towards the detectors.

Experiments of this type took data in past years (K2K[28]) or are still running (Minos[29], Opera[30]) and improved the knowledge of the oscillation parameters measured by SuperKamiokande using atmospheric neutrinos. In particular the most precise measurement of Δm^2_{23} is actually provided by the Minos experiment (see figure 1.9).
The subject of this thesis, T2K, is the most recent example of long-baseline experiment and the key concepts of this experiment will be fully explained in the next chapters.

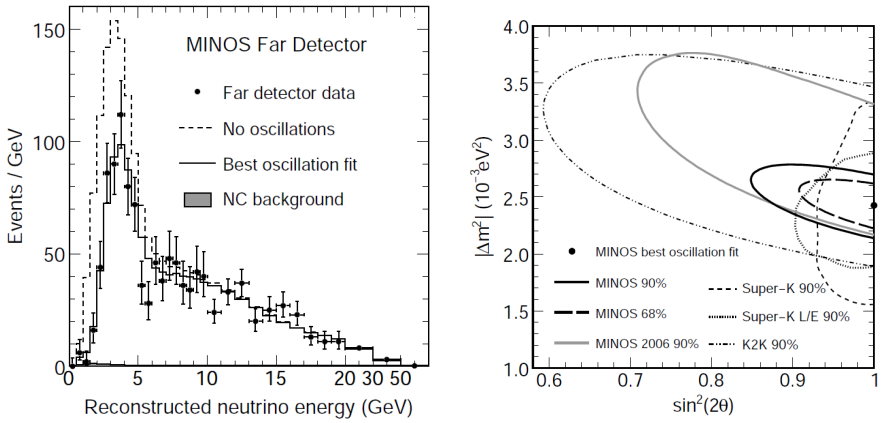

Figure 1.9: Results of the Minos experiment: on the left plot the reconstructed neutrino energy spectrum compared with the expected spectrum in the hypothesis of no oscillation and the best oscillation fit. On the right plot the contour lines of the parameters $\sin^2(2\theta_2 3)$ and Δm^2_{23} that best fit the data, including systematic errors

1.5 The present and the future in neutrino oscillation physics

The picture of the neutrino oscillation experiments has undergone many improvements in the last years. The actual state of the art can be summarized in the following points (see figure 1.10):

- the atmospheric neutrino parameters have been measured by SuperKamiokande and long baseline experiments. ν_μ oscillate into a linear superposition of states mainly composed by ν_μ and ν_τ. The actual most stringent limits on the oscillation parameters, provided by Minos experiment is $\sin^2 2\theta_{23} > 0.90$ (90% C.L.) and $\Delta m^2_{23} = (2.43 \pm 0.13) \times 10^{-3}\ eV^2$;
- the solar neutrino puzzle has been solved by SNO and KamLAND. ν_e oscillate into a linear superposition of the three neutrino families (e, μ and τ); the angle θ_{12} is $\sim 32°$ (Large Mixing Angle with matter effects is the preferred scenario) and $\Delta m^2_{12} = 8.0^{+0.6}_{-0.4} \times 10^{-5} eV^2$;
- the angle θ_{13} is not larger then 10° according to the CHOOZ limit.

In the next future, reactor experiments (Double CHOOZ and Daya Bay) and long baseline neutrino experiments (T2K and Nova) will continue the search for θ_{13}, increasing the sensitivity of at least one order of magnitude with respect to the CHOOZ limit.

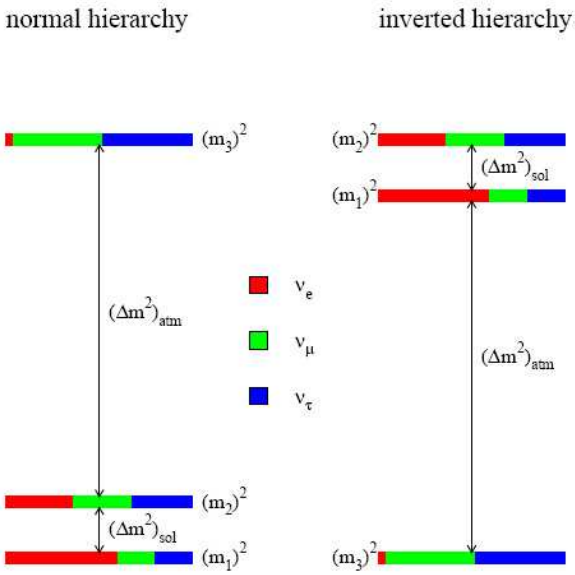

Figure 1.10: Normal and inverted neutrino mass orderings. The different colors show from left to right the relative weights of the different flavor eigenstates (ν_e, ν_μ and ν_τ) in a given mass eigenstate.

If a non zero θ_{13} will be discovered many new measurements in the neutrino physics will be possible:

- the CP violating phase δ can be measured in long-baseline experiments, studying differences in the oscillation probability for neutrinos and antineutrinos, $P(\nu_\mu \to \nu_e) \neq P(\overline{\nu}_\mu \to \overline{\nu}_e)$
- with long baselines it will be possible to use the oscillations in the matter to discriminate the sign of Δm^2_{23}. The sign of Δm^2_{23} establishes the mass hierarchy of the neutrinos. A positive Δm^2_{23} means that the neutrinos separated by the atmospheric mass splitting are heavier than those separated by the solar mass splitting (normal hierarchy) while a negative Δm^2_{23} indicates the opposite situation (inverted hierarchy). In the case of normal hierarchy, $\Delta m^2_{23} > 0$, the matter effects enhance $\nu_\mu \leftrightarrow \nu_e$ oscillations, suppressing $\overline{\nu}_\mu \leftrightarrow \overline{\nu}_e$ while in the case $\Delta m^2_{23} < 0$ the opposite will happen;

- the sign of $\theta_{23} - 45°$, which tells whether the neutrino state with mass m_3 contains more ν_τ or ν_μ can be measured from a combination of reactor $\overline{\nu}_e$ disappearance and accelerator ν_μ disappearance and ν_e appearance.
  This measurement is not possible in ν_μ disappearance experiments that are not able to distinguish between θ_{23} and $\theta'_{23} = \pi/2 - \theta_{23}$. The actual band on $sin^2\theta_{23}$ allows for θ_{23} the wide range between 1/3 and 2/3;

It is important to notice that the first two points both result in a different oscillation probability between neutrinos and antineutrinos and it will be necessary to be able to distinguish the real CP violation due to the δ phase from the fake effect produced by the matter effects.
As we will see in the next chapters with the T2K experiment we will be able to search for θ_{13} with a sensitivity of an order of magnitude better than the CHOOZ limit. However it will not be able, at least in its first phase, to determine the mass hierarchy and to discover CP violation. To reach these goals it will be necessary to produce both, ν_μ and $\overline{\nu}_\mu$ beams, using more powerful beams and larger detectors.
One possibility is to modify the T2K experiment, building a more powerful beam and using two far detectors at different distances to study the matter effects on the neutrino oscillations, improving in this way the sensitivity to the mass hierarchy.
Other hypotheses that are being studied are to build neutrino beams using new technologies. The main ideas in this field concern the Neutrino Factories[31] and the Beta Beams[32].

1.5.1 Neutrino Factories

The idea of the neutrino factories is to produce beams using neutrinos coming from the decay of the muons. In current neutrino beam experiments, the muons are produced together with the neutrinos from the pion decays. These muons can be accumulated in storage rings and accelerated. Then they decay into $\nu_\mu + \overline{\nu}_e$ (if μ^- were accumulated) or into $\nu_e + \overline{\nu}_\mu$ (if μ^+ were accumulated). The neutrino factories are optimized to search for $\nu_\mu \leftrightarrow \nu_e$ or $\overline{\nu}_\mu \leftrightarrow \overline{\nu}_e$ oscillations by looking at the *wrong sign* $\mu^\pm$ appearance.
For example using μ^+ decays, they will produce $\overline{\nu}_\mu$ (detected as μ^+) and ν_e (detected as e^-). If ν_e oscillate into ν_μ they will be detected as μ^-. The use of a magnetized far detector will provide the possibility to distinguish the charge of the muons, measuring in this way the oscillation parameters.
Moreover the possibility to use beams coming from μ^+ or μ^- decays will give the possibility to study possible differences in the $\nu_\mu \leftrightarrow \nu_e$ and $\overline{\nu}_\mu \leftrightarrow \overline{\nu}_e$ oscillations measuring the phase δ and if $\delta \neq 0$ the CP violation in the lepton sector.
The energy of the baseline and the distance and the nature of the detectors are under investigations and many hypotheses are being studied to build a neutrino factory with the maximum possible sensitivity.

1.5.2 Beta Beams

The Beta Beams follow the same concept of the neutrino factories but they use, to produce a neutrino beam, β-decaying ionized nuclei. In this way it is possible to produce intense and perfectly pure ν_e or $\overline{\nu}_e$ beams and search for $\nu_e \rightarrow \nu_\mu$ or $\overline{\nu}_e \rightarrow \overline{\nu}_\mu$ oscillations without the need of a magnetized detector.
The concrete possibilities to produce a Beta Beams are:

- A $\overline{\nu}_e$ beam obtained collecting $^6He^{++}$ nuclei: their decays $^6He^{++} \rightarrow {}^6Li^{+++}\ e^-\ \overline{\nu}_e$ generate a $\overline{\nu}_e$ beam.
- A ν_e beam obtained collecting ^{18}Ne nuclei: their decays $^{18}Ne \rightarrow {}^{18}F\ e^+\ \nu_e$ generate a ν_e beam.

The energy of the neutrino beam obtained with these methods depends on the energy at which it is possible to accelerate the ions and it can vary between 0.5 and 1 GeV/c. The main technological problem to produce a Beta Beam comes from the difficulties in producing and storing a large number of ions, necessary to have enough intense neutrino beams and also for this technology many possibilities are under investigation to establish the best configuration for the beamline and the detectors.

1.6 The leptogenesis hypothesis

Today one of the main reasons of interest in studying neutrinos is the possibility to explain the observed excess of matter over anti-matter in our universe via the leptogenesis mechanism[33].
Our matter dominated universe can be explained only with an extremely tiny excess of matter, in the primordial universe. The excess is described by the parameter η:

$$\eta = \frac{n_B - n_{\overline{B}}}{n_\gamma} = (6.21 \pm 0.16) \times 10^{-10} \tag{1.34}$$

and it is inferred mainly from two observables:

- the Big Bang nucleosynthesis [34], that predicts the abundances of the light elements, D, ^3He, ^4He and ^7Li that depend essentially only on the parameter η;
- the anisotropies in the Cosmic Microwave Background [35], seen in the temperature fluctuations of the CMB.

These two independent observables are in agreement and provide the measurement of the baryon density in the Universe and so the value of η.
The explanation of the baryon asymmetry as coming from initial conditions, that means a Big Bang asymmetric between baryon and antibaryon is unlikely. To explain the observed value of η a very strong fine tuning is necessary, with an initial asymmetry of the order of 10^{-7}.
Moreover if we accept the inflation theory to explain the observed Universe, it predicts that, at the inflation time, all the asymmetry eventually present in the Universe would have been erased.

An alternative idea to explain the asymmetry is to assume that the hot big-bang started with zero asymmetry and explain the excess of the baryon as the result of a dynamical evolution. This is the basic idea of the baryogenesis.
The baryogenesis is possible if three conditions (the Sakharov conditions [36]) are fulfilled:

1. the baryon number B is violated
2. C and CP are violated (otherwise baryons and antibaryons are generated at the same rate)
3. departure from the thermal equilibrium along the history of the Universe:in conditions of thermal equilibrium, if CPT is conserved, $n = \overline{n}$ because $n = e^{-\frac{m}{kT}}$ and $\overline{n} = e^{-\frac{\overline{m}}{kT}}$ (with $m = \overline{m}$ imposed by CPT invariance).

These conditions are qualitatively fulfilled in the Standard Model and are realized in nature:

1. The baryon number is violated by the sphaleron, a Standard Model process that involve nine left-handed quarks and three left-handed leptons and violates the lepton and the baryon number by 3 units. What is conserved in the Standard Model is only $B-L$. The sphalerons are not observed because their amplitude is small at the actual temperatures but, in the history of the Universe, when the temperatures were higher, they were not suppressed.
2. The weak interactions maximally violate C and violate CP via the Kobayashi-Maskawa mechanism.
3. Within the Standard Model departure from the thermal equilibrium occurs at the electroweak phase transition

Even if qualitatively present, these mechanisms are not able to quantitatively explain the observed baryon asymmetry and new mechanisms are needed: in particular the CP violation in the quark sector brings an asymmetry of 10^{-20} that is not enough to explain the observed value of η. Also the departure from the thermal equilibrium at the electroweak phase transition is not strong enough and the asymmetries eventually created are mainly erased. The only condition satisfactory fulfilled is the baryon number violation introduced by the sphalerons.
A way to overcome these problems is to generate the observed asymmetry in the lepton sector and then propagate it to the baryons via the sphaleron processes. This model is called leptogenesis and is based on the fact that, as we showed in section 1.2.1, if the neutrinos are Majorana particles we can introduce a heavy singlet fermion N_i that modifies the Standard Model Lagrangian

$$\mathcal{L} = \mathcal{L}_{SM} - \Gamma^*_{\alpha j}(\overline{L}_\alpha \phi^*) N_j - \frac{1}{2} M_j N_j N_j^C \tag{1.35}$$

where $\alpha, \beta = e, \mu, \tau$ and j is the number of singlet fermions. When adding the singlet N_i all the Sakharov conditions are fulfilled:

1. The lepton number is violated by the Lagrangian: if N_i has lepton number 1, M_i violates it by 2 units and if N_i has lepton number 0, $\lambda_{\alpha i}$ violates it by one unit.

2. New sources of CP violation are possible since there are some irreducible phases in the complex matrix $\lambda_{\alpha k}$.

3. Also the departure from the thermal equilibrium is possible: N_i does not have any gauge interaction but only Yukawa interactions and if λ is small enough these interactions can be slower than the expansion rate of the Universe.

It can also be shown that the leptogenesis not only explains the observed asymmetry in a qualitatively way, but also the quantitative constraints are plausibly satisfied and the baryon asymmetry can be dynamically created by the decays of the lightest singlet fermion N_1, without any fine tuning.
Moreover in this model it is possible to explain two apparently uncorrelated phenomena, the baryon asymmetry and the lepton masses, within the same framework, adding to the Standard Model a heavy singlet fermion.
Unfortunately it is very difficult to directly test the leptogenesis. A direct proof would be to produce the heavy neutrino N_1 and measure CP violation in its decays, but these neutrinos are too heavy to be produced. Also indirect tests coming from the observation of asymmetries in the neutrino cosmic background are far to be reached.
However it is possible to search for circumstantial evidences supporting the leptogenesis:

the observation of the neutrinoless double beta decay would provide the evidence that the neutrinos are Majorana particles and that the first Sakharov condition is fulfilled, while the observation, in the next generation of neutrino long baseline experiments, of the CP violation in the lepton sector would support the possibility to fulfill the second Sakharov condition.

Chapter 2

The T2K experiment

T2K is a long baseline neutrino experiment that started its first physics run in March 2010[37]. It uses a ν_μ neutrino beam produced in the accelerator complex of JPARC, in Japan. Neutrinos are detected in a near detector (ND280) at 280 m from the production point and in a far detector, SuperKamiokande, already used by the K2K experiment.

Figure 2.1: Map of the Japan, showing the T2K ν beam from J-PARC to SuperKamiokande.

The main physics goals of the T2K experiment are:

- Measurement of θ_{13} (or improvement in sensitivity of a factor of 20 on the present CHOOZ limit) by measuring ν_e appearance in the ν_μ beam.
- Precise measurement of Δm^2_{23} and θ_{23} in the ν_μ disappearance channel.

- Search for sterile components in ν_μ disappearance channel, by detecting neutral-current (π^0) events in SuperKamiokande

The length of the baseline is 295 km and given a value of $\Delta m^2_{23} = 2.5 \times 10^{-3}\ eV^2$, the maximum of the oscillation probability will be at a neutrino energy of 700 MeV/c. The T2K experiment uses an off-axis neutrino beam with an energy spectrum peaking in this range (see figure 2.2).
The neutrinos come from the interactions on a graphite target of the 30 GeV proton beam produced in a synchrotron accelerator in the JPARC facility. The expected neutrino fluxes at SuperKamiokande for ν_μ and ν_e are shown in figure 2.2. The nominal power of the proton beam is 0.75 MW in the Phase-I of the experiment. The accelerator based neutrino experiments are characterized and approved to have a certain number of protons that hit the target (Protons On Target, POT). T2K requires 10^{21} POT per year. At the nominal power of 0.75 MW, $\sim$ 3000 hours of operations per year will be necessary to reach this value. The T2K Phase-I has been approved for 5 years and a total of 5×10^{21} POT will be collected at the end of the experiment.

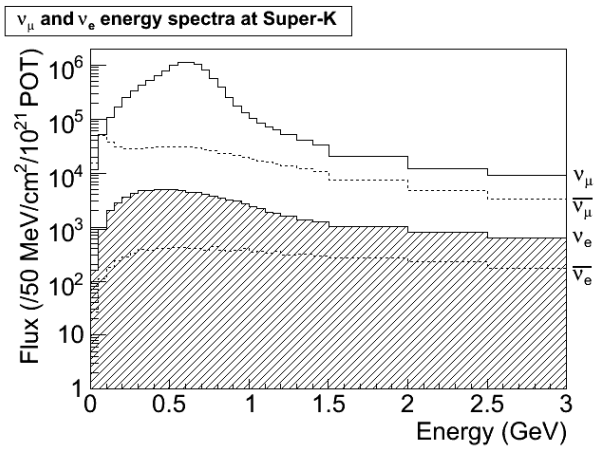

Figure 2.2: Expected composition of the T2K flux at SuperKamiokande: ν_μ (black), $\overline{\nu}_\mu$ (red), ν_e (green) and $\overline{\nu}_e$ (blue).

In this chapter we will introduce the main physics measurements that we will perform in the T2K experiment and then we will describe the three main parts of the experiment: the beamline, the far detector and the near detector complex.

2.1 Physics motivations

As it was explained in chapter 1 the neutrino oscillations can be parameterized using 5 parameters (3 angles and 2 mass differences) and the δ phase. The measurement of three of these parameters, θ_{13}, θ_{23} and Δm_{23} are accessible to the T2K experiment and in a second phase it will be also possible to search for the δ phase if the angle θ_{13} will be measured.

2.1.1 ν_e appearance

The most important physics goal of the T2K experiment is the measurement of θ_{13}. This parameter has been extensively studied looking for $\overline{\nu}_e$ disappearance in reactor experiments. These experiments, in particular CHOOZ[27], did not observe any evidence of $\overline{\nu}_e$ disappearance at the atmospheric oscillation length, providing an upper limit on the magnitude of θ_{13}. In the T2K experiment, θ_{13} can be measured by searching for the appearance of ν_e in the ν_μ beam. We already observed in SuperKamiokande and MINOS the disappearance of ν_μ but no significant evidence of ν_e appearance has been observed so far. Nevertheless the oscillation $\nu_\mu \rightarrow \nu_e$ is a sub-leading oscillation involving Δm^2_{31}.
The general expression for $P(\nu_\mu \rightarrow \nu_e)$ is a complicated formula that is derived taking into account the oscillation among 3 families given by 1.26. An approximate expression of this probability, that takes into account the measured values and limits on the oscillation parameters, is given by

$$\begin{aligned} P(\nu_\mu \rightarrow \nu_e) &= \sin^2 2\theta_{13} \sin^2 2\theta_{23} \sin^2 \Delta \\ &\pm \alpha \sin 2\theta_{13} \sin\delta \cos\theta_{13} \sin^2\theta_{12} \sin 2\theta_{23} \sin^3 \Delta \\ &- \alpha \sin 2\theta_{13} \cos\delta \cos\theta_{13} \sin^2\theta_{12} \sin 2\theta_{23} \cos\Delta \sin 2\Delta \\ &+ \alpha^2 \cos^2\theta_{23} \sin^2 2\theta_{12} \sin^2\Delta + \bigcirc\alpha^3 \end{aligned} \tag{2.1}$$

where $\alpha = \Delta m^2_{21}/\Delta m^2_{31}$ and $\Delta = \Delta m^2_{31} L/4E$. The existing limits from solar and atmospheric data show that $\alpha \sim 3 \times 10^{-2}$, the limits from CHOOZ shows that $\sin^2 2\theta_{13} <\sim 0.2$ and the value of δ is completely unknown.
The last term of equation 2.1 does not depend on θ_{13} but it depends on α^2 and it is negligible for the T2K experiment. For values of $\sin^2\theta_{13}$ within an order of magnitude of its current upper limit the first term of the equation dominates and it describes the relatively simple appearance of ν_e in the ν_μ beam:

$$P(\nu_\mu \to \nu_e) \sim \sin^2 2\theta_{13} \sin^2 2\theta_{23} \sin^2(1.27\Delta m^2_{13}[eV^2]L[km]/E_\nu[GeV]) \tag{2.2}$$

where $|\Delta m^2_{13}| \sim |\Delta m^2_{23}|$ (as $|\Delta m^2_{12}|$ is small compared to $|\Delta m^2_{23}|$), L is the flight distance of 295 km and E_ν is the neutrino energy. Equation 2.2 shows that the oscillation ν_μ to ν_e is expected to be observed around the maximum of the ν_μ disappearance.
If we want to measure the appearance of ν_e we need also to take into account the matter effects described in 1.3.2. The matter effects modify the propagation of the ν_e and so the observed oscillation parameters, Δm^2_{13} and θ_{13}. This modification can be parameterized defining an adimensional ratio

$$r = \frac{2\sqrt{2}G_F N_e E_\nu}{\Delta m^2_{13}} = \frac{N_e}{1.3 N_A/cm^3} \frac{E_\nu}{10GeV} \frac{2 \times 10^{-3} eV^2}{\Delta m^2_{13}} \tag{2.3}$$

that modifies the oscillation parameters:

$$\Delta m^2_M = \Delta m^2_{13} \sqrt{\sin^2 2\theta_{13} + (\cos 2\theta_{13} - r)^2} \tag{2.4}$$

and

$$\sin^2 2\theta_M = \frac{\sin^2 2\theta_{13}}{\sin^2 2\theta_{13} + (\cos 2\theta_{13} - r)^2} \tag{2.5}$$

at the T2K neutrino energy r is of the order of 10% and, given the expected number of ν_e events observed in SuperKamiokande (see 2.4), the matter effects are negligible.

In order to search for the ν_e appearance signal in SuperKamiokande, charged current quasi-elastic (CCQE) interactions are used. This is the dominant neutrino interaction at the T2K region (see figure 2.3) and is a two body interaction. This means that, assuming the target nucleon is at rest, it is possible to reconstruct the energy of the incoming neutrino by measuring only the momentum and the angle of the lepton produced in the CCQE interaction. The neutrino energy is given by:

$$E_\nu = \frac{2(m_N - E_B)E_l - (E_B^2 - 2m_N E_B + m_l^2 + \Delta M)}{2[(m_N - E_B) - E_l + p_l \cos\theta_l]} \tag{2.6}$$

where m_N is the mass of the neutron, E_B the binding energy, ΔM the mass difference between the neutron and the proton and m_l, E_l, p_l and θ_l are the mass, the energy, the

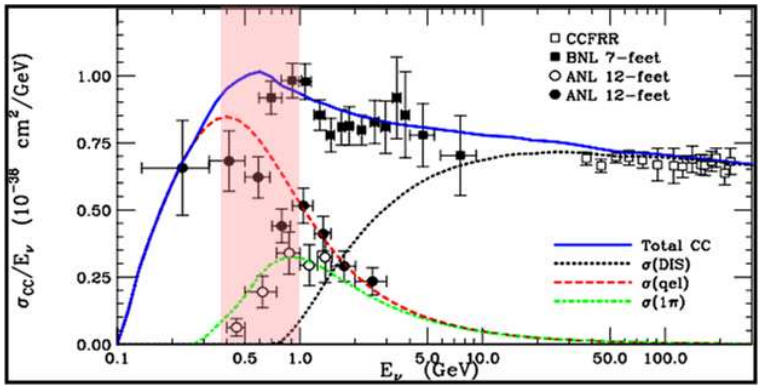

Figure 2.3: Neutrino cross-sections in the GeV region. The pink region corresponds to the energy of the T2K beam.

Selection	$CC\nu_\mu$ BG	$NC\nu_\mu$ BG	beam ν_e BG	CC ν_e signal
Fully contained, $E_{vis} > 100\ MeV$	2215	847	184	243
1 ring e-like, no decay electrons	12	156	71	187
$0.35 \leq E_\nu^{rec} \leq 0.85\ GeV$	1.8	47	21	146
e/π^0 separation	0.7	9	13	103

Table 2.1: Number of events selected in the ν_e appearance analysis as predicted by NEUT Monte Carlo for $5 \times 10^{21}\ POT$ exposure. For the calculation, $\Delta m^2 = 2.5 \times 10^{-3}\ eV^2$ and $\sin^2 2\theta_{13} = 0.1$ are assumed.

momentum and the angle of the lepton coming from the neutrino interaction ($l = e\ or\ \mu$). As it will be explained in section 2.4, in SuperKamiokande it is possible to distinguish ν_e from ν_μ interaction by observing the features of the Cherenkov ring. The selection of ν_e interactions, fully explained in [24], requires fully contained events in the 22.5 kt fiducial volume, with visible energy larger than 100 MeV, e-like ring and no decay electrons. A fully contained event is an event in which the lepton does not exit from the inner volume of the detector. This produces a ring in the detector, easily distinguishable from the full circles produced by the partially contained events, in which the particle is not contained in the detector. Moreover partially contained events will also give a signal in the SuperKamiokande Outer Detector.
Then interactions in which the reconstructed neutrino energy is larger than 350 MeV and smaller than 850 MeV are required to select events in the maximum oscillation energy region.

At this stage of the selection, as it is shown in table 2.1 the main background comes

from ν_μ neutral current (NC) interactions that produce a π^0, while the majority of the ν_μ producing a muons are rejected by the e-like ring request. The π^0 instead immediately decays in two γ and each of the γ will produce an electromagnetic shower that can be identified: in this case two e-like rings in SuperKamiokande are observed. The background arises from the fact that sometimes the two rings are overlapping or the energy of one of the γ is too low to produce an observable ring and the event is recognized as a ν_e event. Specific e/π^0 separation cuts have been developed:

- Very forward events ($\cos\theta_{\nu e} > 0.9$), likely generated by coherent π^0 production, are rejected. The angle $\cos\theta_{\nu e}$ is the angle between the direction of the neutrino and the one of the observed electron ring.
- The event is fitted in the hypotheses of 1 ring and of 2 rings. In the case of 2 rings we also reconstruct the invariant mass and if the invariant mass is larger than 100 MeV/c^2 or the two rings hypothesis has a better likelihood, the event is rejected.

After these rejections, the two backgrounds, the one coming from intrinsic ν_e contamination and the one coming from $NC\pi^0$ events have comparable size. In figure 2.4 the reconstructed ν_e energy spectrum after 5 years of running, assuming $\Delta m^2_{13} = 2.5 \times 10^{-3}\ eV^2$ and $\sin^2 2\theta_{13} = 0.1$ is shown. In table 2.1 are reported the numbers of expected events in SuperKamiokande for the same values of Δm_{13}, $\sin^2 2\theta_{13}$ and POT. In this hypothesis the background is expected to be of the order of 20%.
In figure 2.5 the sensitivity of the T2K experiment to $\sin^2 2\theta_{13}$ and Δm^2_{13} for different values of the δ phase is shown. The T2K sensitivity will be a factor of 20 better than the current experimental limit.

2.1.2 ν_μ disappearance

The other important purpose of the T2K experiment is the precise measurement of the *atmospheric* parameters θ_{23} and Δm^2_{23}. The current best measurements of these parameters are provided by the MINOS experiment[29] and favor $\sin 2\theta^2_{23}$ to be 1 but still with an uncertainty of $\sim 10\%$.
The atmospheric oscillation parameters will be measured in the ν_μ disappearance channel. The survival probability is given by

$$P(\nu_\mu \to \nu_\mu) = 1 - \sin^2 2\theta_{23} \cos^4\theta_{13} \sin^2(1.27\Delta m^2_{23}[eV^2]L[km]/E_\nu[GeV]) - P(\nu_\mu \to \nu_e) \quad (2.7)$$

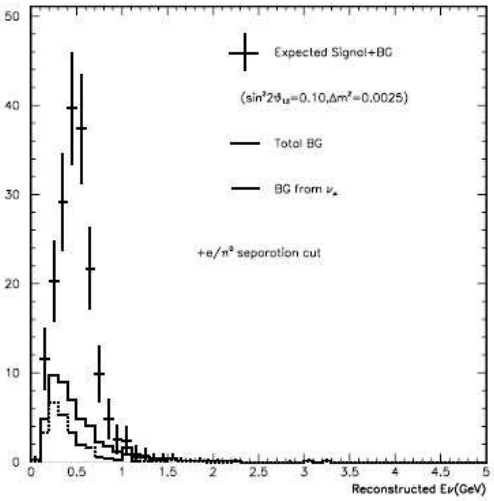

Figure 2.4: Reconstructed electron neutrino energy distributions in SuperKamiokande. The points with error bars show the expected signal+background, the solid histogram shows the total background and dashed histogram shows the background from ν_μ interactions for an off-axis angle of 2.5° and an exposure of 5×10^{21} POT.

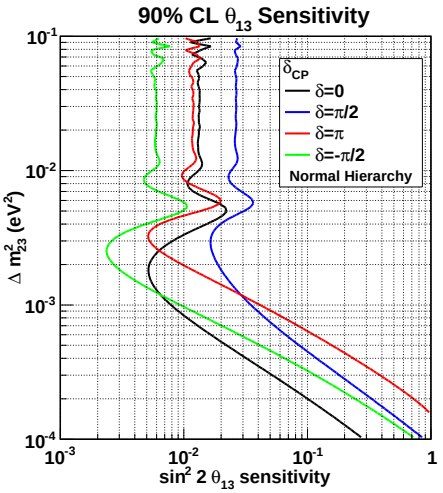

Figure 2.5: T2K sensitivity to θ_{13} at the 90% confidence level as a function of Δm^2_{23}. Beam is assumed to be running at 750kW for 5 years, using the 22.5 kton fiducial volume SK detector. Sensitivity for different values of δ_{CP} are plotted on different contours. The systematic error fraction assumed for this calculation is 10%. The following oscillation parameters are assumed: $\sin^2 2\theta_{12} = 0.8704$, $\sin^2 2\theta_{23} = 1.0$, $\delta m^2_{12} = 7.6 \times 10^{-5}\mathrm{eV}^2$, normal hierarchy.

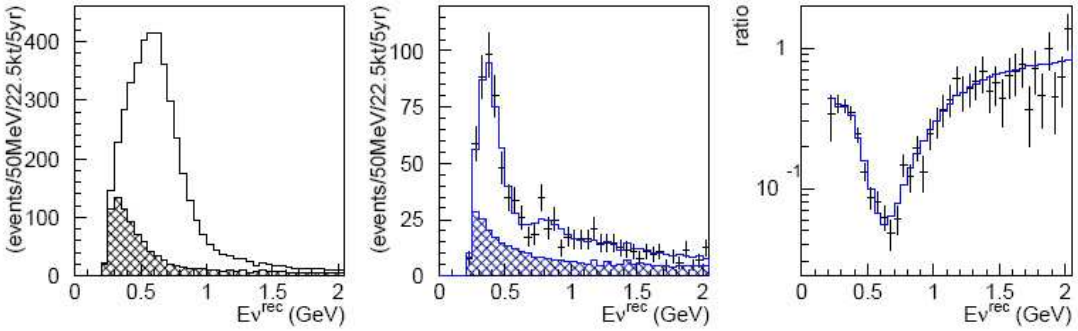

Figure 2.6: Reconstructed energy spectrum of neutrinos at SK. On the left plot the solid histogram shows the expected energy spectrum without oscillation, on the central plot the expected energy spectrum of 1 ring $\mu-like$ events with oscillation for ($\sin^2 2\theta_{23}$, Δm^2_{23})=(1.0, $2.7 \times 10^{-3}\ eV^2$) is shown. The error bars show the statistical error. In both figures, the hatched histogram shows the non-CCQE events. On the right plot the ratio of the measured spectrum with neutrino oscillation to the expected one without neutrino oscillation is shown. The solid histogram shows the fit result of the oscillation.

this equation expresses the fact that, measuring the neutrino energy spectrum at SuperKamiokande, a clear dip will be observed around 600 MeV according to the actual knowledge of Δm^2_{23}(see figure 2.6). The position of the dip corresponds to Δm^2_{23} and the depth corresponds to θ_{23}.

As described in 2.1.1 the dominant interaction mode in the T2K energy region is the CCQE. To select ν_μ events in the far detector the same selection criteria already used for the SuperKamiokande atmospheric neutrino analysis will be used: no activity in the outer detector, one $\mu - like$ ring, reconstructed energy larger than 30 MeV and vertex in the SuperKamiokande 22.5 kt fiducial volume.

In figure 2.6 the expected reconstructed neutrino energy at SuperKamiokande, without and with the oscillation are shown. The spectrum with the oscillation is obtained using $(sin^2 2\theta, \Delta m^2) = (1.0, 2.7 \times 10^{-3}\ eV^2)$. In table 2.2 the expected number of events selected in SuperKamiokande in the hypothesis of no oscillation are shown. In table 2.3 the number of events selected for different values of the Δm^2_{23} is shown.
In figure 2.7 the sensitivity of the T2K experiment to Δm^2_{23} and θ_{23} as a function of Δm^2 is shown. The best sensitivity will be obtained for a value of $\Delta m^2 \sim 2.5 \times 10^{-3} eV^2$.

Selection	CCQE	CC-nonQE	NC	Total ν_μ
Generated in FV	4114	3737	3149	11000
Fully Contained	3885	3011	1369	8265
$E_{vis} \geq 30MeV$	3788	2820	945	7553
Single ring $\mu - like$	3620	1089	96	4805

Table 2.2: Expected number of events selected in SuperKamiokande as predicted by NEUT Monte Carlo for 5×10^{21} POT exposure without oscillation.

$\Delta m^2(eV^2)$	CCQE	CC-nonQE	NC	Total ν_μ
No oscillation	3620	1089	96	4805
2.0×10^{-3}	933	607	96	1636
2.3×10^{-3}	723	525	96	1344
2.7×10^{-3}	681	446	96	1223
3.0×10^{-3}	800	414	96	1310

Table 2.3: Expected number of events selected in SuperKamiokande as predicted by NEUT Monte Carlo for 5×10^{21} POT exposure for different values of Δm^2_{23} with $\sin^2 2\theta_{23} = 1.0$ and $\sin^2 2\theta_{13} = 0.0$.

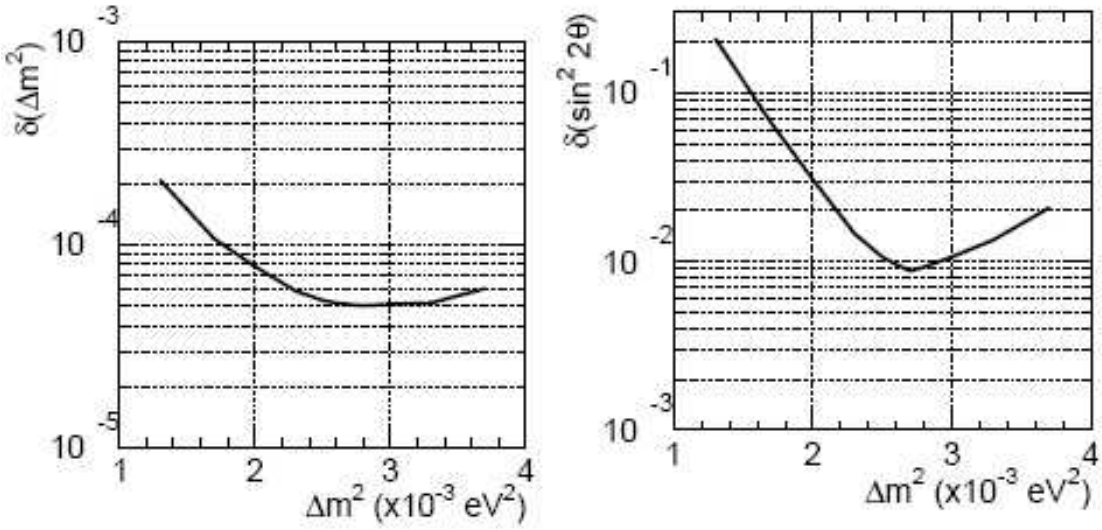

Figure 2.7: The expected 90% C.L. sensitivity on the neutrino oscillation parameters Δm^2_{23} (left) and $\sin^2 2\theta_{23}$ (right) for the offaxis angle of 2.5°

2.2 The T2K oscillation analysis

The ν_μ disappearance and the ν_e appearance analysis will be performed in the T2K experiment combining the measurements at the near and at the far detector. This strategy is common to the majority of the long baseline experiments that measure the neutrino flux in the far detector and compare it with the expected flux unmodified by the oscillation. This latter flux is measured in a near detector that intercepts the flux when the oscillation is still negligible.
In an ideal case, if both detectors are far enough from the neutrino source they will accept the same solid angle and if the detector efficiencies and systematics are the same it is sufficient to measure the neutrino beam at the near detector in order to predict it at the far detector. In practice the near detector is different from the far in terms of acceptance, materials and responses and what is measured (see figure 2.8) is the product of the detector efficiencies (ϵ), the neutrino cross-section (σ) and the neutrino flux (ϕ):

$$N(E_\nu) = \int \epsilon(E_\nu)\phi(E_\nu)\sigma(E_\nu) \tag{2.8}$$

To extrapolate the flux at the far detector it is necessary to understand the beam and the detector responses and correct for the differences. This is done using a beam Monte Carlo, that, on the basis of the observed flux at the near detector, predicts what will be the unmodified flux at the far detector. The simulation depends on the geometry of the focusing system and of the decay tunnel and on the hadron production: a dedicated hadroproduction experiment, NA61, has been taking data at CERN to study the hadron production with a T2K replica target. Data from this experiment will be very important to have a better knowledge of the T2K flux.

2.2.1 Physics requirements at ND280

The strategy that will be used to measure neutrino oscillation parameters in T2K can be summarized in 3 steps:

1. measure the T2K neutrino spectrum at the near detector;
2. extrapolate it to the far detector to know the expected neutrino spectrum at the far detector in no oscillation hypothesis
3. compare the observed spectrum at the far detector with the expected one without oscillation

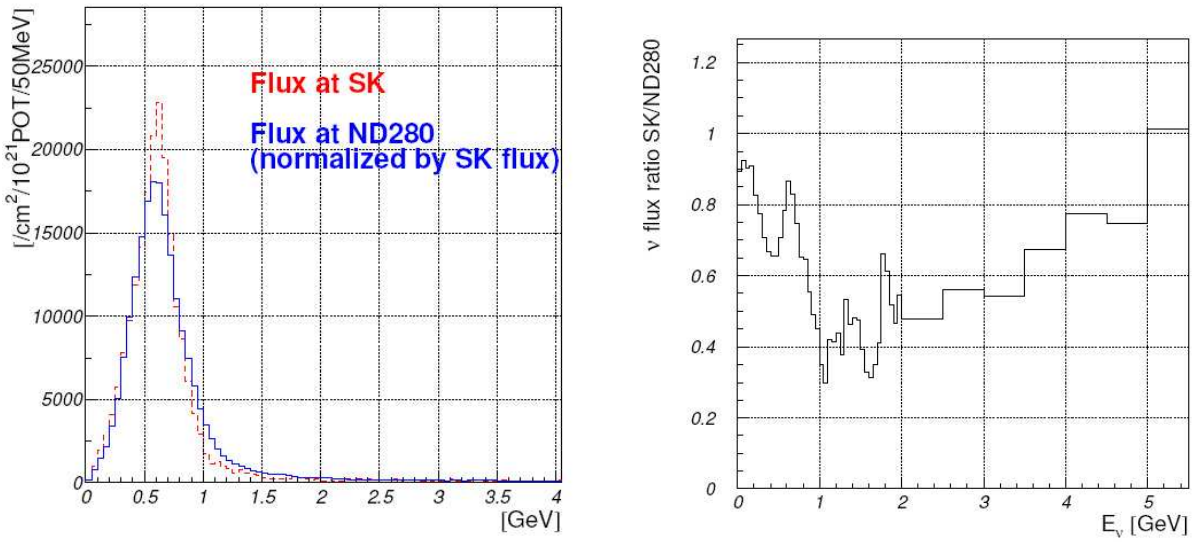

Figure 2.8: Expected neutrino fluxes as a function of neutrino energy for T2K at the Near Detector and at SuperKamiokande (left) predicted by the Monte Carlo simulation. On the right plot the far-to-near flux ratio.

From the comparison between the expected and the observed spectrum the oscillation parameters will be measured. In ND280 the different detectors have different purposes. In particular the tracking section, composed by 2 Fine Grained Detectors (FGD) and 3 TPCs is mainly devoted to measure the ν_μ and ν_e fluxes and charged current cross sections while ECAL and P0D mainly measure π^0 production cross-sections that are one of the main background to the ν_e appearance signal.

Fluxes and cross-sections When we measure a neutrino spectrum we always measure a combination of neutrino cross-sections and fluxes. To overcome this problem, in the long baseline neutrino experiments, the CCQE cross-section is used as the reference one and measurements of flux multiplied by CCQE cross-section ($\Phi_\nu \times \sigma_{CCQE}$) are done. For specific neutrino interaction the ratios of the cross-section to the CCQE (σ/σ_{CCQE}) are also determined. The reason for using CCQE as the reference cross-section is that it is theoretically well understood, pure samples can be obtained with good efficiency and also the neutrino energy can be reconstructed.
Neutrino oscillations make the spectra at the far detector significantly different from the spectra at the near detector, so it is not sufficient to compute $\Phi_\nu \times \sigma$ at the near detector

but we need to measure the different reactions as a function of the neutrino energy, normalized to the CCQE cross-section.

Far/Near extrapolation The neutrino spectrum at the far detector is estimated by correcting the neutrino spectrum measured at the near detector by an extrapolation function obtained by the beam Monte Carlo simulation (the so called far/near ratio). This extrapolation is one of the main problem in the determination of the oscillation parameters because the two spectra are different and do not simply scale with the $1/r^2$ law. This is partially related to the off-axis configuration chosen for the T2K neutrino beam and partially related to the different distances at which the far and the near detectors are installed.
As we will show in section 2.3 the off-axis spectrum implies the presence of a maximum for the neutrino energy. This maximum is degraded and enlarged by the following effects:

- The divergence of the pion beam, due to the fact that the pions produced by the interactions between the proton beam and the target have a non negligible transverse momentum;
- The size of the neutrino production source: the decay tunnel has a length of 100 meters and is not seen as a point-like source by the detectors;
- The angular size of the detectors with respect to the neutrino.

At SuperKamiokande the two last effects can be neglected as the source can be considered point-like and the angular dimensions of the detector are negligible due to the long distance between the neutrino production point and SuperKamiokande (295 km). At ND280 instead all these three effects are important: the size of the decay tunnel is $\sim$ 30 $mrad$ and the size of the detector is $\sim$ 14 $mrad$.
This, together with the different efficiencies of the Near and Far detectors, results in the difference between the spectra at the near and the far detector shown in figure 2.8 and to extrapolate the measured spectrum at the near detector to the expected one at the far detector without oscillation it is necessary to use the beam Monte Carlo simulation to measure the $Far/Near\ Ratio$. This ratio is defined as

$$R^{F/N} = \frac{\phi^{SK}(E_\nu)}{\phi^{ND}(E_\nu)} \tag{2.9}$$

$\phi^{SK}(E_\nu)$ and $\phi^{ND}(E_\nu)$ are the neutrino fluxes respectively at the far and at the near detectors. These fluxes can be predicted by the Monte Carlo simulation once the geometry of the decay volume and the momenta and directions of the pion parents of neutrinos are

provided. The main uncertainty of the Monte Carlo simulation is the pion production model at the proton target and simulations showed that the result is robust at the 5% level changing the pion production model.
The pion production model can also be checked at the Near Detector. Moreover it will be possible to use the radial dependency of the energy spectrum to reduce the systematic error of the far/near extrapolation.
In fact, the off-axis near detector covers an area of 14 mrad. This large angular coverage, on one side complicates the prediction of the flux at the far detector, which covers a solid angle of the order of 0.1 mrad. On the other hand, the near detector has sufficient width to observe the running of the neutrino energy as a function of the off-axis angle checking in this way the Monte Carlo prediction for the variation of the beam profile with energy, which is the main input to calculate the far/near ratio.
Once $R^{F/N}$ is determined, the expected number of events at SuperKamiokande will be simply given by

$$N^{SK}_{i,exp} = N^{ND}_{i,obs} R^{F/N} \tag{2.10}$$

where i is the energy bin.

2.2.2 Physics requirements for the ND280 tracker

As we showed in section 2.2.1 the role of the tracker is to measure ν_μ and ν_e fluxes and spectra and neutrino charged current cross-sections. For the flux determination, the CCQE cross-section is used as the reference one ($\Phi_\nu \times \sigma_{CCQE}$).
The first role for the tracker is to isolate a clean sample of CCQE events, coming from the interaction:

$$\nu_\mu + n \rightarrow \mu^- + p \tag{2.11}$$

in the tracker both the tracks, the muons and the protons, are reconstructed. The reconstruction of the proton, often done only in the FGD because the proton has low momentum and not always enters in the TPC, allows to select a high purity CCQE sample. Moreover in the TPC also the pions produced in non quasi elastic interactions are reconstructed, providing the possibility to study others neutrino interactions.

Neutrino spectrum The neutrino spectrum will be measured using the reconstructed muon momentum and direction in CCQE events (equation 2.6). The muon momentum

needs to be known with a moderate resolution because the neutrino energy reconstruction is affected by the smearing due to the Fermi motion in the nucleon target, that is of the order of 10% for neutrinos with typical energies of the T2K beam. However, in the determination of the ν_μ disappearance parameters, the muon momentum scale plays a crucial role being one of the main systematic to the measurement. The muon momentum scale is required to be understood at the 2% level.

Beam composition One of the major background to the ν_e appearance measurement in SuperKamiokande is due to the ν_e component in the beam (see section 2.1.1) and it is necessary to measure this component in the ND280 detector.
This can be done by reconstructing a sample of CCQE events where the lepton is identified as an electron. This identification can be done using the TPC ionization measurement, together with ECAL and SMRD informations. The main difficulty will be to identify electrons in a sample dominated by muons: the ν_e contamination is expected to be 0.5% of the ν_μ in the $0.4 - 0.8\ GeV$ energy range.
Another important analysis is the study of the high energy neutrino spectrum (above 1 GeV). These neutrinos, mainly due to kaon decays, are responsible for a large fraction of the ν_e component in the beam, through the K_{e3} decays ($K^+ \to \pi^0 + e^+ + \nu_e$). Therefore the measurement of high momentum muons could help understanding the hadron production models and help in this way the prediction of the ν_e flux.

Estimating backgrounds for SuperKamiokande Many of the background contributions in SuperKamiokande to the ν_μ disappearance measurement comes from neutrino interactions with the production of 1 or more π in the final state: in particular charged current interactions with the production of one π ($CC1\pi$) with the pions that is below the Cherenkov threshold in SuperKamiokande. Also neutral current events ($NC1\pi$ or $NC - multi\pi$) will contribute to this background. Understanding pion production and absorption mechanisms via nuclear re-interactions is fundamental to understanding these backgrounds and the goal is to measure differential cross-section for neutrino interactions with pions in the final state, in particular $CC1\pi$.

2.3 The beam line

The T2K experiment uses an off-axis neutrino beam. As for all the other long baseline experiments, the beam is mainly composed of muon neutrinos coming from the pion two body decays.
As we will show in this section, the pions are produced by interaction of a proton beam with

a target. After the production they are focused by 3 magnetic horns and then enter in a decay tunnel where they can decay into μ^+ and ν_μ.
The beam is then sent to the near detector and to the far detector that are misaligned with respect to the beam of an angle of 2.5°. The off-axis configuration allows the production of an almost monochromatic neutrino beam with a mean energy centered on the maximum of the oscillation signal.

2.3.1 The off-axis neutrino beams

T2K is the first example of an off-axis neutrino beam (originally introduced in [38]). The idea is to build a neutrino beam from the two body decay of charged pions that is not directly directed to the detectors but is slightly misaligned (by few degrees) with respect to them.
The advantages of an off-axis neutrino beam, with respect to the conventional neutrino beams, is to have a more intense and narrower beam, centered at the interesting energy region to observe the oscillation signal.
This can be easily seen, as showed in [39], with some calculation on the 2-body decays kinematics. Let us consider a pure π^+ beam, produced by interactions of a proton beam with a source, entering in a decay tunnel. The pions will decay according to $\pi^+ \rightarrow \mu^+\nu_\mu$. In the pion rest frame the neutrino has a maximal energy given by

$$E_\nu^* = \frac{m_\pi^2 - m_\mu^2}{2m_\pi} = 29.8MeV, \tag{2.12}$$

where * indicates quantities in the pion rest frame.
The neutrino 4-vector, for $|\vec{P}_\nu| \gg m_\nu$ will be in the pion rest frame:

$$P_\nu = (E_\nu, E_\nu \sin\theta, 0, E_\nu \cos\theta) \tag{2.13}$$

If we boost to the laboratory frame, using the Lorentz boost $\gamma_\pi = E_\pi/m_\pi$, the neutrino 4-vector is then:

$$P_\nu = (\gamma_\pi E_\nu^*(1 + \beta_\pi \cos\theta^*), E_\nu^* \sin\theta^*, 0, \gamma_\pi E_\nu^*(\beta_\pi + \cos\theta^*)) \tag{2.14}$$

The pion has spin zero, so the decay is isotropic in pion rest frame and a relation for the angle θ between the neutrino and the parent pion can be obtained from the 1 and 3 components of 2.13 and 2.14,

$$\tan\theta \sim \frac{E_\nu^* \sin\theta^*}{\gamma_\pi E_\nu^*(1+\cos\theta^*)} \sim \frac{E_\nu^* \sin\theta^*}{E_\nu} \tag{2.15}$$

Since $\sin\theta^*$ cannot exceed unity, in the laboratory frame there is a maximum angle at which the neutrino of energy E_ν can be emitted. Using the result of 2.12, the maximum angle is

$$\theta_{max} \sim \frac{E_\nu^*}{E_\nu} \sim \frac{30MeV}{E_\nu}. \tag{2.16}$$

Equation 2.15 can also be rewritten as a function of the θ angle, in the form

$$E_\nu \sim \frac{E_\nu^* \sin\theta^*}{\tan\theta} \leq \frac{E_\nu^*}{\tan\theta} \tag{2.17}$$

that means that for a given angle $\theta \neq 0$ there is a maximum energy at which neutrinos can be emitted, while for $\theta = 0$ the energy of the neutrino is proportional to the energy of the parent pion.

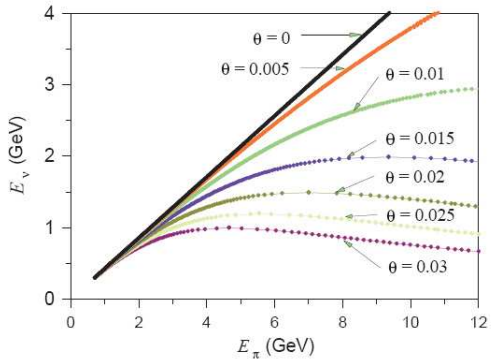

Figure 2.9: Expected neutrino energy as a function of the parent pions energy for different values of the off-axis angle. In this simulation the energy of the proton beam was 12 GeV.

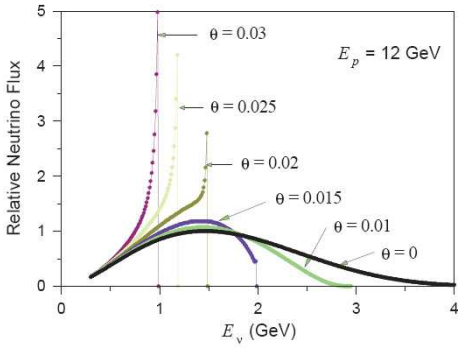

Figure 2.10: Expected neutrino energy spectrum for different value of the off-axis angle.

In figure 2.9 the neutrino energy as a function of the parent pions energy for different off-axis angle is shown. As it was expected from equation 2.17, for $\theta \neq 0$ there is a maximum possible neutrino energy and a large range of pions energy contributes to a small range of neutrino energy resulting in an enhancement of the neutrino spectrum. The existence of the neutrino maximum energy $E_{\nu,max} = (29.8\ MeV)/\theta$ allows to choose the off-axis angle in

such a way to enhance the neutrino spectrum at the desired energy. The neutrino spectrum for different off-axis angles is shown in figure 2.10.
The presence of a transverse momentum of the pions focalized by the horn, results in real spectra without the hard edge shown in figure 2.10. In figure 2.11 a more realistic simulation of the T2K neutrino spectra for different values of the off-axis angle is shown. The off-axis angle chosen for the experiment is 2.5° that according to equation 2.17 corresponds to an energy peak of

$$E_\nu = \frac{29.8\ MeV}{\theta} = 683 MeV \tag{2.18}$$

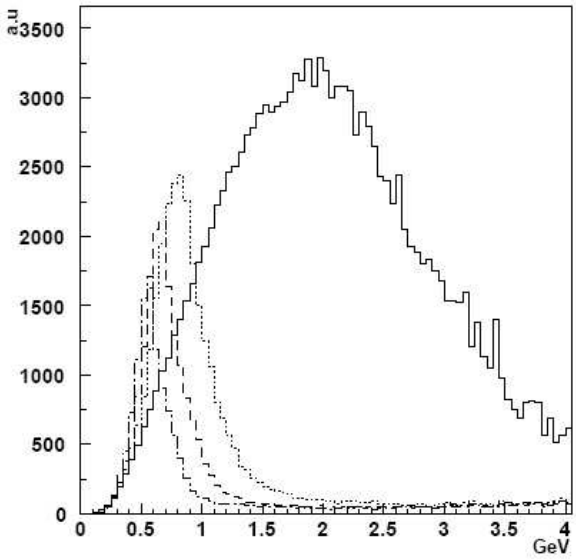

Figure 2.11: Expected energy spectrum of neutrinos in the T2K experiment for various off-axis angle. The solid line shows the on-axis configuration, the dotted, dashed, and dash-dotted lines show the off-axis angles of 2.0°, 2.5° and 3.0°, respectively.

Another advantage of the off-axis beam is that it reduces the ν_e contamination in the beam. As it was shown in section 2.1 this contamination, is one of the main background to the ν_e appearance signal. It comes from decays of muons and kaons (the so-called k_{e3} decay, that has a branching ratio of 5%) in the decay tunnel according to relations:

$$\mu^\pm \rightarrow e^\pm + \overset{(-)}{\nu}_\mu + \overset{(-)}{\nu}_e \tag{2.19}$$

and

$$K^+ \rightarrow \pi^0 + e^+ + \nu_e. \tag{2.20}$$

These are both 3 body decays, while the off-axis strategy enhances the number of neutrinos coming from a 2 body decay. This means that using an off-axis beam, at the peak energy, the neutrino spectrum will be less affected by the ν_e contamination.

2.3.2 The T2K neutrino beam

The T2K neutrino beam is produced at the J-PARC (Japan Proton Accelerator Research Center) complex, in the city of Tokai.
To produce a neutrino beam, 4 main components are necessary:

- A proton beam that interacts with a target, producing hadrons;
- A system of magnetic horns to focus, according to their charge, desired hadrons and reject the others;
- A decay tunnel where the hadrons decay into neutrinos;
- A beam dump to stop all the particles that are not neutrinos.

The primary beamline The complex is formed by a *LINAC* accelerator of 181 MeV, followed by a *Rapid Cycling Synchrotron* (RCS) of 3 GeV and as Main Ring (MR) a proton synchrotron that accelerates protons up to 30 GeV. In figure 2.12 a picture of the JPARC complex and a schematic view of the neutrino beamline are shown.

The proton design intensity is 3.3×10^{14} proton per pulse, at a repetition rate of 0.31 Hz. Therefore the maximum power of the beam is 0.75 MW. The beam is extracted in spills of 5.6 μs. In each spill there are 8 bunches (limited at 6 for the 2010 run) each of a length of 58 ns.
The protons are extracted toward the inside of the MR (see figure 2.12) and enter in a transport line where they are bent by almost 90° to SuperKamiokande direction. The transport beamline can be divided into three parts:

- the preparation section, a series of conducting magnet and collimators that are used to adjust the beam for the transportation;

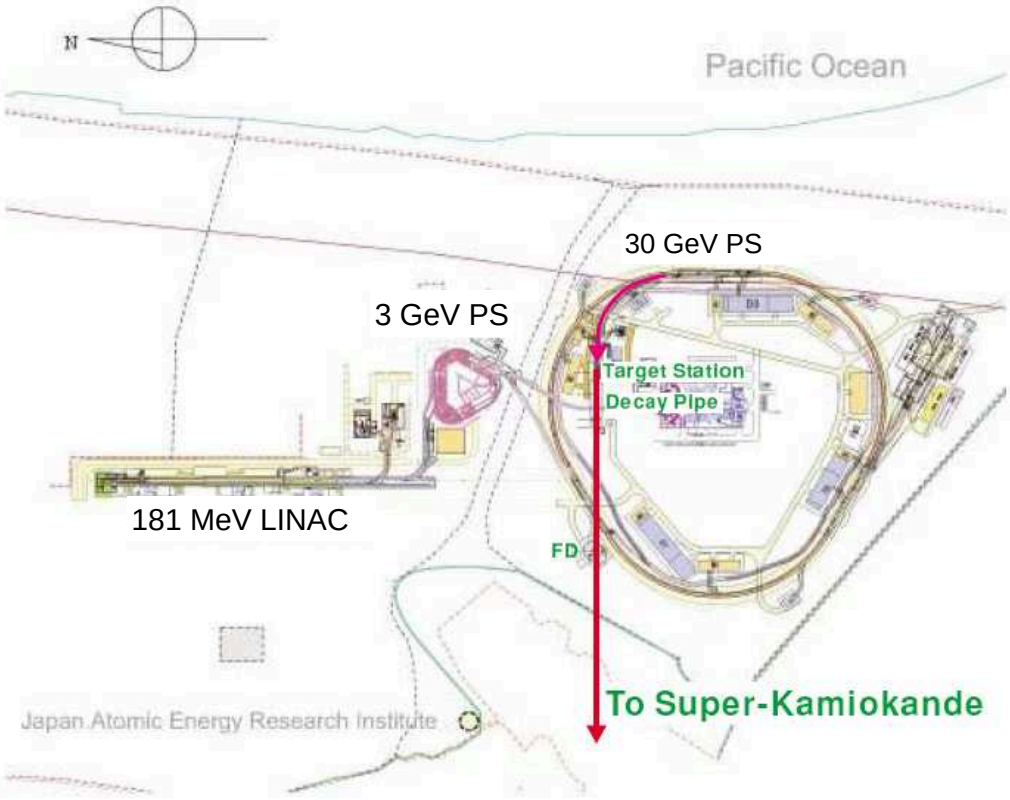

Figure 2.12: Accelerator complex of JPARC.

- the arc section, consisting of 28 combined function super-conducting magnets. These magnets have both a dipole (2.6 T) and a quadrupole component (18.6 T/m). This technology allows to reduce the number of magnets and to have larger acceptance of the primary beam. In the arc section protons are curved by $\sim 80°$;
- the final focusing section, where separated dipoles and quadrupoles make the beam parallel and adjust its direction to properly hit the target.

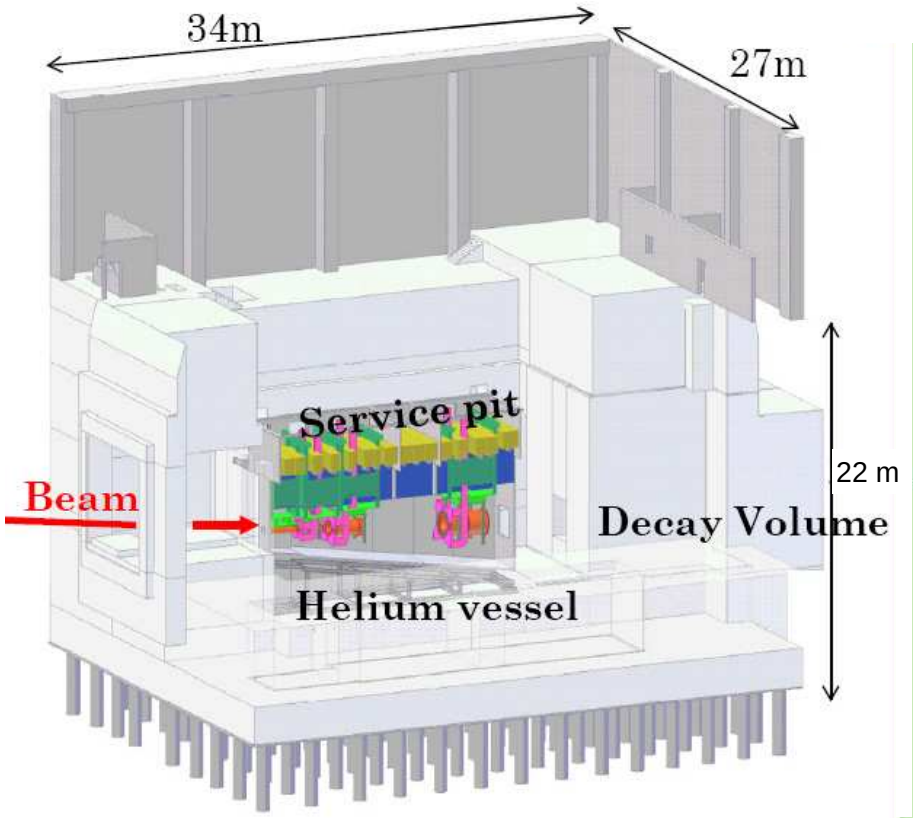

Figure 2.13: Design of the T2K target station. The target station is installed between the final focusing region and the decay volume. The positions of the target and of the three horns are also shown.

The target station After the final focusing section the protons enter in the target station, where the T2K target and the horn system are installed.
The target station, shown in figure 2.13, is installed 12 meters underground and it has been designed to contain the radiation and to assure the cooling of the target and of the magnetic horns with water.

The target and the horns are contained in an aluminium volume filled with helium to avoid the air activation. Iron blocks are placed around the target station to assure the shielding of the region.

T2K target The target is typically one of the limiting factor in building intense neutrino beams. In fact the target undergoes very strong mechanical stresses and radiation damages. This arise from the fact that the neutrinos cross-sections are so small that to have a high enough amount of interactions in the detectors it is necessary to use proton beams, from which neutrinos are produced, as intense as possible.

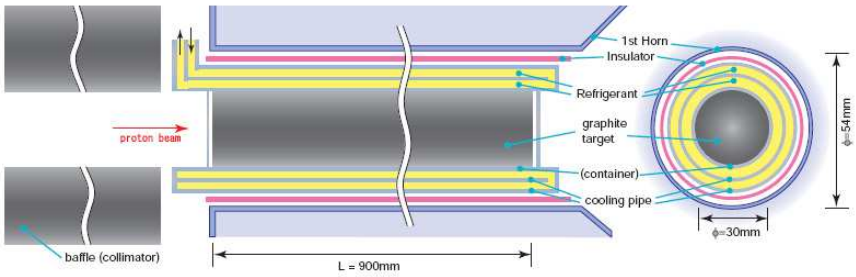

Figure 2.14: Conceptual design of the T2K target: the 90 cm graphite target is placed inside the first of the three horns.

The T2K target, shown in figure 2.14, is installed in the inner conductor of the first horn and is made by a graphite bar, 90 cm long (that corresponds to two interaction lengths for a density $\rho = 1.8\ g/cm^3$) and with a diameter of 3 cm. In the target about 80% of protons interact generating pions and kaons that will decay into neutrinos.
The graphite was chosen because the intensity of the beam is so high that the target temperature immediately rises due to the energy deposited by the protons and materials with higher Z would be strongly damaged. Between the low-Z materials graphite was chosen because the melting point is high and it has good thermal stress resistance. Moreover it is stable and easy to handle.
The cooling system consists of a co-axial double layer cooling pipe that maintains the target independent from the horn. It uses the flow of gaseous helium to cool the target and keep its temperature between 400 and 800 $^\circ C$ where the radiation damage for the graphite is minimum.

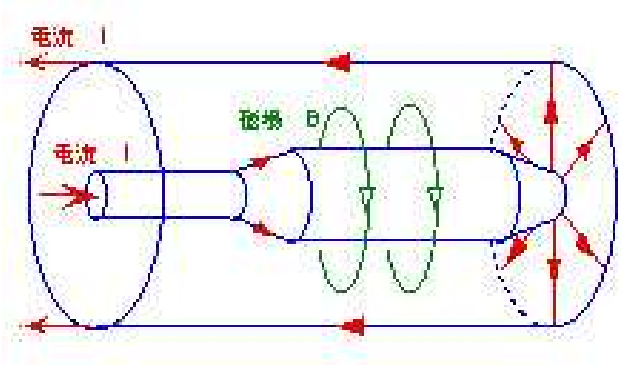

Figure 2.15: Principle of a magnetic horn.

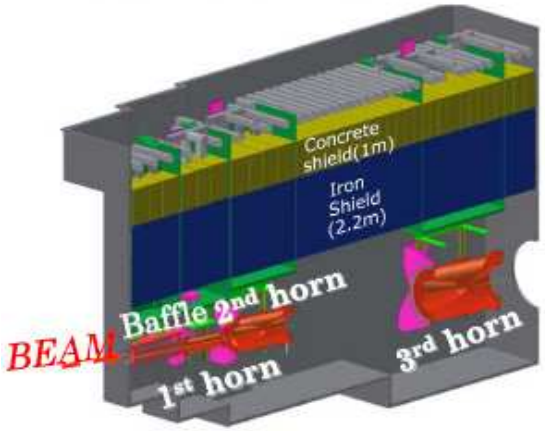

Figure 2.16: Disposition of the 3 horns in the T2K target station.

The magnetic horns The magnetic horns are used, in all the neutrino beams, to focus hadrons with a given charge (positive if we want to produce a neutrino beam, negative if we want an anti-neutrino beam) and reject the others. In figure 2.15 the working principle of the horn is shown. Very intense pulsed currents (hundreds of kA) circulate into the horns when the protons arrive, producing intense magnetic fields (of the order of few Tesla) that are able to deviate the hadrons produced in the interaction between the protons and the target. The horn surfaces are optimized to have mesons exiting the target parallel to the direction of the primary beam.
For the T2K experiment, 3 horns are used (see figure 2.16). In each horn a current of $300 \sim 320\ kA$ circulates. The first horn is the shortest one, with an outer diameter of 36 cm and a length of 140 cm. The second horn has a length of 200 cm and a diameter of 80 cm and the third one has a length of 250 cm and a diameter of 140 cm. The target is placed in the inner conductor of the first horn. The optimization of the system is described in [40].

The decay tunnel and the beam dump The focused hadrons enter in a decay tunnel where they can decay according to

$$\pi^+ \rightarrow \mu^+ + \nu_\mu \tag{2.21}$$

The length of the decay tunnels depends on the energy of the pions. It is a compromise between two needs: we want a tunnel long enough to let as many pions as possible decay, increasing the intensity of the neutrino beam but we also do not want that the muons coming from pions decays produce ν_e and $\overline{\nu}_\mu$ according to

$$\mu^+ \rightarrow e^+ + \nu_e + \overline{\nu}_\mu. \tag{2.22}$$

The length of the T2K tunnel is 110 meters and it has a rectangular shape. The height of the tunnel gradually increase to accept off-axis beam between 2 and 3 degrees. This has been done to keep the freedom to tune the off-axis angle to the most recent measurement of Δm^2_{23}. In fact an angle of 2° corresponds to $\Delta m^2_{23} = 3.28 \times 10^{-3}\ eV^2$ while a 3° angle corresponds to $\Delta m^2_{23} = 2.18 \times 10^{-3}\ eV^2$.
The decay tunnel is filled with Helium to reduce the absorption of pions and the walls are made of iron plates equipped with a water cooling circuit to remove the heat load by secondary particles. The entire tunnel is surrounded by 6 meters of concrete to shield the radiation.
At the end of the tunnel there is a beam dump to stop surviving hadrons and muons. The beam dump is formed by 230 cm of graphite, 135 cm of copper and an iron shielding. Both graphite and copper are cooled by water and air to remove the heat load from the particles which hit the dump.
Immediately after the beam dump there is a system to detect muons that are not stopped by the beam dump. These muons have an energy larger than 5 GeV (because they have penetrated the beam dump) and the expected flux of muons in the muon pit is $\sim 10^8/cm^2/spill$. This system of detectors, called Muon Monitor (MUMON), is used to monitor spill by spill the beam intensity and profile (or direction) to check the position of the proton beam and the efficiency of the horn focusing system. This is possible because the muons are produced by the same hadrons that produce neutrinos (see 2.21) and their properties are strongly correlated.
The beam position needs to be controlled with an accuracy of 1 mm to assure that the beam arrives to SuperKamiokande.
The MUMON detector is formed by two independent systems: an array of ionization chambers and an array of semiconductor detectors.
The ionization chamber is a simple device to monitor the beam for a long run period and it is also suitable to cover the large area of the beam profile. The weak points of this system are the slow response and the weak signal over the unknown background coming from the beam dump.
To overcome these weak points also a semiconductor detector is used. Such a detector has a fast response and is less sensitive to background because of the large and fast signal. Problems for the semiconductor may arise from the long term stability due to radiation damages.

2.3.3 Neutrino flux simulation

The T2K beamline is simulated using a program, called $JNUBEAM$ that uses $GEANT3$ simulation[44] and has been developed by T2K collaborators.
The simulation starts with the interactions between the protons and the target. The production of the secondary hadrons is described using the $GCALOR$ program[45] interfaced with GEANT3. Then the hadrons are propagated through the geometry and the magnetic field of the beamline, including target, cooling envelope, magnetic horns, decay pipe and beam dump. If the particles decay into the tunnel before encountering one of the tunnel wall, a neutrino is generated and $JNUBEAM$ proceeds in the following way:

- SuperKamiokande is far enough to be considered point-like and for a two body decay ($\pi \to \mu\nu$ or $K \to \mu\nu$) the neutrino energy is completely determined. For a three body decay ($K \to \pi^0 e\nu_e$ or $\mu \to e\nu_\mu\nu_e$) instead the neutrino energy is randomly extracted from the appropriate distribution probability. Then the probability that the parent particle produces a neutrino of this energy in the direction of SuperKamiokande is computed.
- For the Near Detector instead it is necessary to consider the size of the detector and the neutrino source cannot be considered point-like. In this case, in order to boost the statistics, decays leading to a neutrino are generated 1000 times each and the neutrino 4-vector is stored if its direction intersects the Near Detector.

The characteristics of the neutrino beam depend on the geometry of the target, the magnetic horns and the decay tunnel, on the characteristics of the parent hadrons beam and on the hadroproduction cross-sections.
JNUBEAM has been developed and used to optimize the conception of the T2K target, horns and decay tunnel and the larger uncertainties came from the knowledge of the hadron beam produced by the interaction between the proton beam and the target. The hadron cross-section in fact are known with an error of the order of 30%.

The study of hadroproduction: the NA61 experiment

In all the accelerator based neutrino oscillation experiments a large uncertainty in the beam Monte Carlo simulation, necessary to propagate the observed spectra at the Near Detector to the expected one at the Far Detector, comes from the knowledge of the parent hadrons spectra.
The T2K experiment will use the results of the NA61 experiment [46] to constrain the hadrons production models. This experiment is an upgrade of the NA49 experiment, that was a large

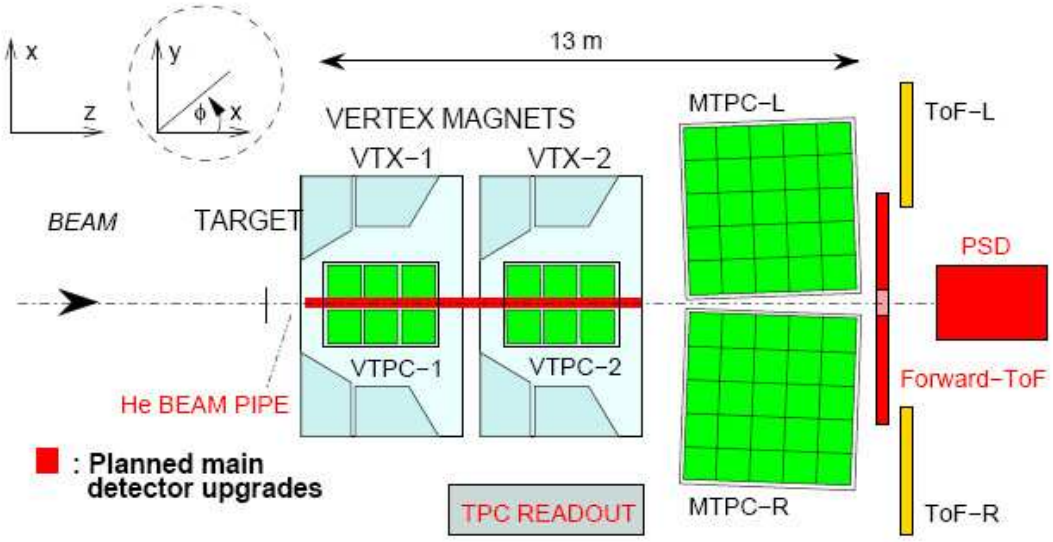

Figure 2.17: Setup of the NA61 experiment.

acceptance hadron spectrometer operating with a beam extracted from the CERN SPS. The experimental apparatus, shown in figure 2.17 is composed of four large TPCs, two of them operating in the magnetic field generated by two super-conducting magnets (1.5 and 1.1 T) and two located downstream the magnets, symmetrically with respect to the beam direction. Also two Time Of Flight detector arrays and a set of calorimeters are installed.
The purpose of the experiment is to study the hadronic final states produced by collisions of various beam particles on a fixed target. In particular for the T2K experiment the hadrons produced in the collisions between a 30 GeV proton beam and a target identical to the one used in T2K will be observed.
For the purposes of the T2K experiment the far-to-near ratio has to be known at the level of 2%. This requires a measurement of the differential cross-section for pion and kaon production to a 2-3% level in the phase space and conditions of the T2K beam. This requires the reconstruction, in the NA61 experiment, of 5×10^5 pions and 10^5 kaons.
NA61 data with thin target from the 2007 run have already been analyzed: pion spectra measurements with 20% systematic errors have been performed, while 2007 data with T2K replica target and 2009 data, with larger statistics, are currently being analyzed.

2.4 The far detector: SuperKamiokande

The SuperKamiokande detector[24] is a cylindrical 50 kton water Cherenkov detector located at Kamioka Observatory in Gifu Prefecture, 295 km away from JPARC. It is located in an underground mine under the Ikenoyama mountain, at a mean depth of 1000 meters. This depth is equivalent to 2700 meters of water, and the flux of cosmic rays is reduced by five orders of magnitudes compared to the one on the surface of the earth.

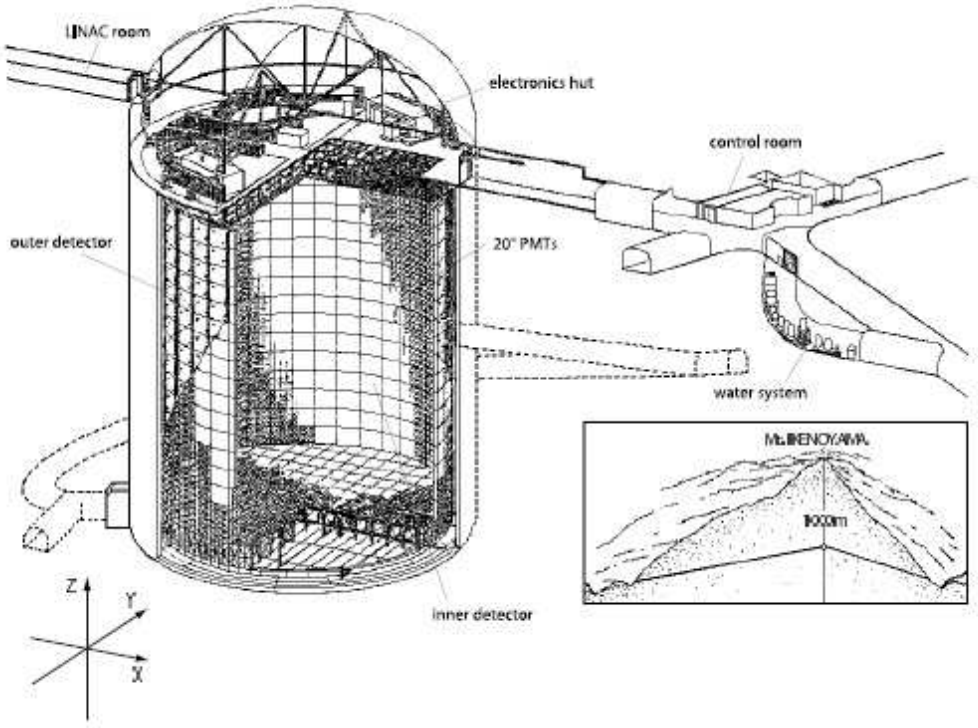

Figure 2.18: A view of the SuperKamiokande detector.

The SuperKamiokande detector started taking data in April 1996, aiming for nucleon decay searches and the study of atmospheric and solar neutrinos. The running period of the first five years is called SK-I. After being suspended for maintenance, an accident occurred in November 2001. In the accident 60% of the PMTs were lost. The detector was rebuilt with half of the PMTs in December 2002 and the running period after the accident is called SK-II. Between the fall 2005 and the spring 2006 the detector has been instrumented again with all the PMTs (SK-III).
A schematic view of the detector is shown in figure 2.18. The size of the water tank is

41.4 m in height and 39.3 m in diameter and it contains a total of 50 ktons of pure water. SuperKamiokande consists of two concentric, optically separated water Cherenkov detectors. The inner detector (ID), contains 32 ktons of water and 11146 20-inch PMTs are attached inward, on the support structure, at intervals of 70 cm in the SK-I period. In SK-II, the number of PMTs was 5182, while in the SK-III all the PMTs were replaced and the total number of PMTs is 11146. A schematic view of a 20-inch PMT is shown in figure 2.19 and a complete description can be found in [41]. In SK-II and SK-III, the PMT photocathode is covered with an acrylic cover while a fiber reinforced plastic (FRP) case cover the whole phototube. This prevents damages coming from a chain reaction caused by the wave propagation that follows the implosion of one PMT. This chain reaction caused the accident of 2001. The transparency of the acrylic cover in water is 98% for wavelengths longer than 400 nm and 95% for a 350 nm wavelength.

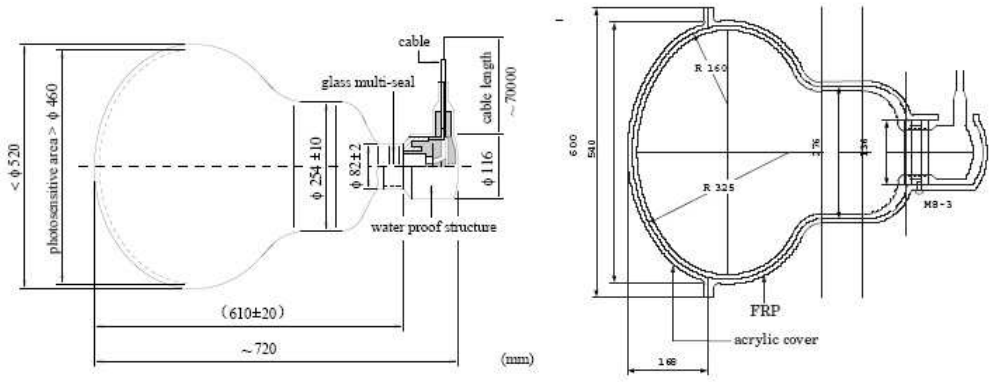

Figure 2.19: The 20-inch photomultiplier used in the SuperKamiokande detector.

The 50 cm PMTs were specially designed to have good single photoelectron (p.e.) response. The quantum efficiency, maximal at 400 nm, is 20%.
The ID is surrounded by the outer detector (OD), a cylindrical shell of water 2.6 to 2.75 m thick.. The OD is optically isolated from the ID, and is instrumented with 1885 outward-facing Hamamatsu R1408 20 cm PMTs, providing an active veto that covers all the SuperKamiokande surface and a thick passive radioactivity shield.
A complete description of the SuperKamiokande detector can be found in [42].

Principles of the water Cherenkov detectors The SuperKamiokande PMTs detect photons emitted via Cherenkov effect by charged particles that cross the water.
The Cherenkov effect was first observed by Cherenkov in 1937 and then explained by Frank

and Tamm.
The Cherenkov effect occurs because the light group velocity in a medium is different from the one in the vacuum and it depends on the refraction index (n) of the crossed medium. In particular for water $n = 1.33$ and $v_l = c/n \sim 0.75\ c$.
When a relativistic charged particle crosses the medium with a velocity $v > v_l$, its electric field polarizes the atoms of the nonconducting material and the atoms respond by emitting light in a cone at an angle determined by the refraction index of the material. The process can be compared to that of a shock wave of sound generated when an airplane exceeds the speed of sound in air.
The opening angle θ of the cone is

$$\cos\theta = \frac{1}{\beta n} \tag{2.23}$$

the light emitted by the particle will propagate on the surface of this cone and the trajectory of the particle corresponds to the cone axis (figure 2.20).

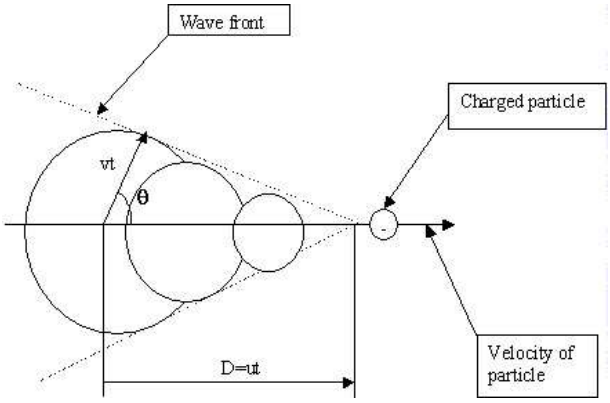

Figure 2.20: Principle of the Cherenkov effect. The particle propagating at the velocity u in a medium where the light propagates at the velocity v, emits photons in a cone with an angle $\cos\theta = v/u = 1/\beta n$.

From equation 2.23 we can derive that:

- for an ultrarelativistic particle ($\beta = 1$) the opening angle is maximal and has a value of $\arccos(1/n) = 41.9°$ in the water;
- if $n\beta < 1$ there is no Cherenkov emission. This means that the Cherenkov effect has a threshold that depends on the velocity of the charged particle in the water.

The thresholds depend on the mass of the particle: in fact given the threshold on β, $\beta = 1/n = 0.752$, this results in a threshold for the energy of the particles given by

$$E_k = \gamma m_k c^2 = \frac{1}{\sqrt{1-\beta^2}} m_k c^2 = 1.52 m_k \tag{2.24}$$

where m_k is the mass of the particle k and E_k its energy threshold. The threshold is equal to 775 keV for electrons, 160 MeV for muons and 1.4 GeV for protons. Given these thresholds and the energy of the T2K beam, the protons produced in neutrino interactions are usually below the Cherenkov threshold and are not detectable in SuperKamiokande. Instead the electrons, above an energy of a few MeV are always ultrarelativistic particles and their opening angle is maximal. This helps in distinguishing muons from electrons tracks in the detector.
Once emitted the light propagates towards the cylinder surface and each PMT register the integrated charge and the time. The reconstructed charge on all the PMTs on the SuperKamiokande surface forms a ring, if the particle stops, and a full disc if the particle escapes the detector. The shape of the ring is different between electrons and muons given the different propagation mechanisms of the two particles. The muons propagate in water without emitting other particles and the shape of the resulting Cherenkov cone has sharp edges (see figure 2.21), while the electrons emit, during their propagation, a large number of photons via bremsstrahlung. The photons convert in water producing electromagnetic showers at an angle slightly different from the angle of the original electron and the resulting Cherenkov cone detected on the SuperKamiokande surface has fuzzier edges with respect to the ones produced by muons (see figure 2.21).

The events like the one on the left of figure 2.21 are called $\mu - like$ ring, while the events on the right of figure 2.21 are $e - like$ rings. This effect, together with the electron maximum opening angle, allows to clearly distinguish electrons from muons in SuperKamiokande.

2.5 The near detector facility: ND280

For the physics goals of the long baseline experiments it is necessary to have a far detector to measure the neutrino flux after the oscillation and a near detector to precisely measure characteristics of the neutrino beam, in particular flux and spectra before the oscillation and to measure neutrino cross sections.
In the case of the T2K experiment the near detector facility has been installed at 280 meters from the target and it is composed of an on-axis detector (INGRID) used to measure the beam direction and an off-axis complex of detectors (ND280).

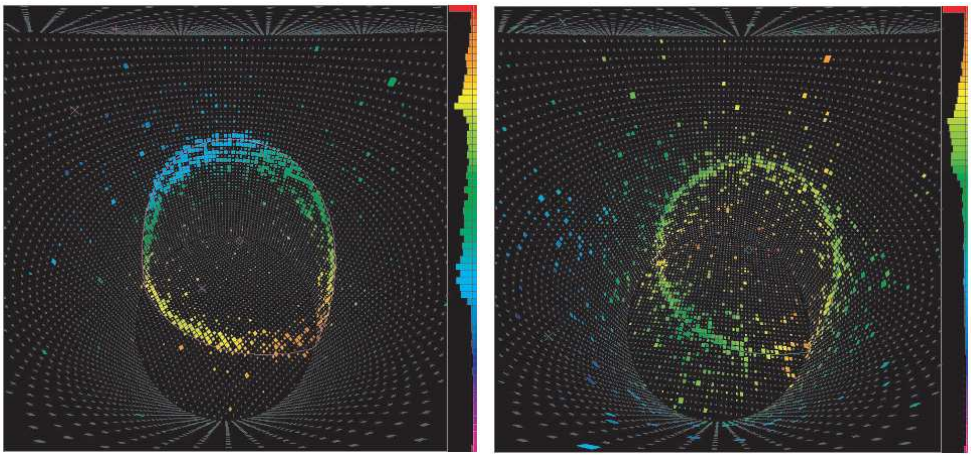

Figure 2.21: Left plot: muon signal coming from a typical ν_μ interaction in SuperKamiokande. Right plot: electron signal coming from a typical ν_e interaction in SuperKamiokande. Notice that in these events the light shape is much less regular than in the one that we observe in the $\mu - like$ events.

The measurements required at ND280 are related to the physics analysis described in section 2.1. In particular for the ν_μ disappearance studies it is important to measure the flux of the ν_μ and their spectrum. Also neutrino cross-sections need to be measured for neutrino interactions that the far detector will not recognize assigning them the wrong neutrino energy.
For the ν_e appearance study, the flux and the spectrum of electron neutrinos must be known, together with the cross-sections for interactions that the far detector will misinterpret as coming from ν_e.

In SuperKamiokande, as well as in ND280, the neutrino energy is reconstructed according to the formula 2.6. This formula works in the case of charged current quasi elastic interaction (CCQE) in which $\nu_l + n \rightarrow l^- + p$. The other possible interactions (see figure 2.3) are three or more bodies interactions for which the formula 2.6 does not properly reconstruct the neutrino energy and are a background to the measurement of E_ν. In particular inelastic reactions producing a π^0 in the final state are one of the main background to the ν_e appearance signal.
In this section we will describe the detectors installed in the ND280 facility and in the next chapter we will fully describe the TPCs of the T2K experiment.

2.5.1 The on-axis detector: INGRID

The on-axis neutrino detector is used to monitor the neutrino beam observing particles produced by neutrino beam interactions. While MUMON is sensitive only to high energy muons because of the high muon momentum threshold, INGRID is sensitive to a large portion of the neutrino spectrum and it is used to monitor the beam properties day by day.

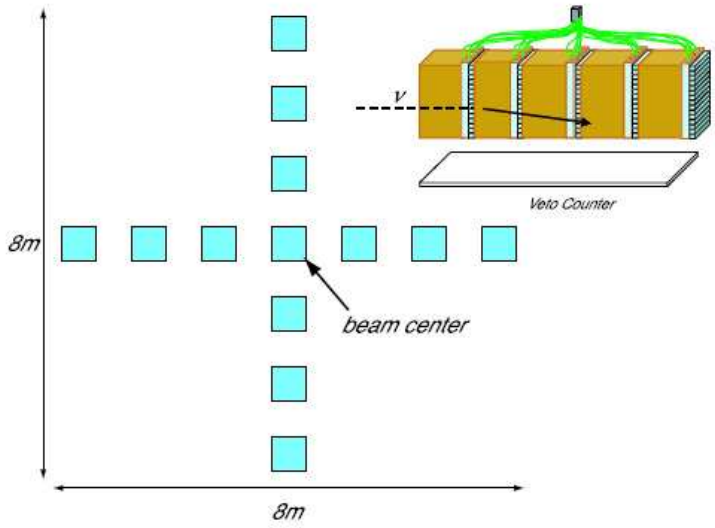

Figure 2.22: Schematic view of the INGRID detector.

INGRID consists of 7 + 7 identical units, arranged to form a grid which samples the beam on a 8 × 8 m^2 area as shown in figure 2.22. The target of neutrino interaction is iron and extruded scintillators, read by Wave-Length-Shifting (WLS) fibers, are used to detect muons coming from the neutrino interactions. The events are selected requiring a number of hits in successive tracker counters greater than two and no hits in the veto counters. The mass of each INGRID module is 10 t and it will observe, at the nominal T2K power, $\sim$ 10000 events per day. INGRID will cover a beam area of 5 m^2 and the expected performance, according to simulations, is to measure the beam direction with a precision of 0.1 $mrad$, well in agreement with the experimental request to monitor the beam direction within 1 $mrad$.

2.5.2 The off-axis detectors

The off-axis near detector complex is designed to measure the neutrino beam energy spectrum, the flavor content before the neutrino oscillation and the interaction cross-sections. The detectors are off-axis with respect to the neutrino beam, along a line that connects the average pion decay point to SuperKamiokande.
The ND280 detector is illustrated in figure 2.23 and consists of different elements, described in the following paragraphs.
The expected number of events in the ND280 detectors for the different neutrino interaction channels is shown in table 2.4.

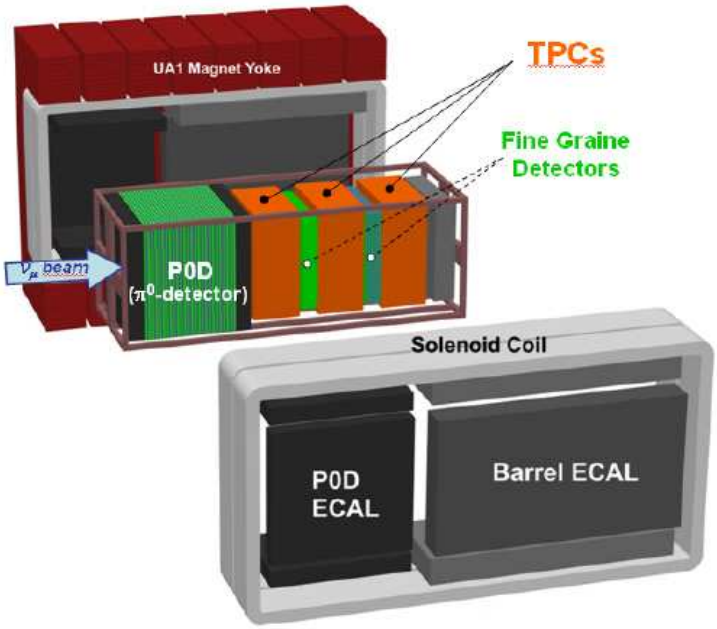

Figure 2.23: Schematic view of the ND280 offaxis detector.

The key idea of the off-axis detector is the use of a magnet in which the detectors are contained. The presence of the magnet makes possible to measure the charge and the momentum of the particle produced by the neutrino interactions according to their curvature, using a tracker system.
In this way it is possible to distinguish between neutrino and antineutrino interactions and, for a neutrino interaction, identify the lepton track as the negative one and measure the spectrum of the neutrino interacting in ND280 by measuring the lepton spectrum in the case of CCQE interactions.

Interaction mode	Fraction	Events/10^{21} POT/ton
$CC - QE$	38%	65038
$CC - p\pi^+$	11%	17846
$CC - p\pi^0$	3%	4887
$CC - n\pi^+$	3%	5107
$CC - Coherent\ \pi^+$	1%	2189
$CC - multi\ \pi$	7%	11943
$CC - DIS$	8%	13057
$NC - Elastic\ n$	9%	15671
$NC - Elastic\ p$	8%	13581
$NC - n\ \pi^0$	2%	2837
$NC - p\ \pi^0$	2%	3519
$NC - p\ \pi^-$	1%	1931
$NC - n\ \pi^+$	1%	2300
$NC - Coherent\ \pi^0$	1%	1099
$NC - multi\ \pi$	2%	3639
$NC - DIS$	2%	4022

Table 2.4: Total number of events predicted by the NEUT Monte Carlo for the Near Detector, per ton and per 10^{21} POT (one year of data taking at the nominal power). The fractions of different interaction modes are also shown.

The Magnet ND280 uses the ex-UA1 magnet operated with a horizontal uniform magnetic field of 0.2 T, perpendicular to the neutrino beam direction. The curvature induced by the magnet will be used to measure the momenta of charged particles produced by neutrino interactions in the near detector. The inner dimensions of the magnet are $3.5 \times 3.6 \times 7.0$ m^3. The magnet consists of two symmetric halves and each half consists of 8 C-shaped flux return yokes made of low-carbon steel plates. The total weight of the yoke is 850 t. The magnetic field is produced by aluminum coils that operate at a current of 3 kA.
According to simulations the field is quite uniform in intensity and direction, with transverse components exceeding 1% only in regions close to the coils.

The Tracker system The tracker is installed downstream the P0D detector and it is optimized to measure the momenta of charged particles, particularly muons and pions produced by charged current interactions and to measure the ν_e contamination in the beam. The tracker is composed of three TPCs and two FGDs (Fine Grained Detectors).

- The three **TPCs** measure the 3-momenta of charged particles produced by neutrino interactions and will provide the most accurate measurement of the neutrino energy spectrum. Moreover the measurement of the ionization rate will determine the particle identity, in particular distinguishing muons from electrons. A complete description of the TPCs is given in chapter 3.

- The 2 **FGDs** are installed downstream the first and the second TPC and consist of layers of finely segmented scintillating tracker bars. The FGDs provide the target mass for neutrino interactions that will be measured by the TPCs and can also measure the direction and ranges of recoil protons produced by charged current interactions, distinguishing charged current quasi elastic reactions (CCQE) and non quasi elastic (CC-nonQE).
  Each FGD has dimension of 200 cm $\times$ 200 cm $\times$ 30 cm for a total mass of 1.2 tons and consists of $x-y$ layers of plastic scintillator bars readout with Wave-Length-Shifting (WLS) fibers. The second FGD is a water enriched detector, alternating each $x-y$ scintillator layer with 3 cm thick layers of passive water. The comparison between the neutrino interaction rates in the first and in the second FGD allow to unfold the yields from carbon and oxygen separately through a statistical subtraction. This knowledge is useful to decrease the systematic errors in the extrapolation of the neutrino fluxes measured in the near and in the far detector as also the neutrino interactions in SuperKamiokande occur on oxygen nuclei.
  The detector is similar to the K2K SciBar detector [43], that has already shown the capability and the importance of detecting both, the muon and the proton tracks produced in a CCQE interaction. The size on each FGD scintillator bar is $1.0 \times 1.0 \times 200$ cm^3 and this high segmentation allows to precisely measure the momentum of the

stopping particles. To collect and propagate the light along the scintillator, Kuraray Y11 wave-length shifting fibers with a diameter of 1.5 mm are used. The typical attenuation length for a fiber is 350 cm and a readout on both the ends of the fibers is used in order to reduce non-uniformities in the response across the detector and to allow low threshold settings on individual channels through the use of a coincidence between the two ends of each fiber.
The fibers are read by Multi-Pixel Photon Counters (MPPCs). This technology is common to all the ND280 Detectors (with the exception of the TPCs) and will be briefly described in the following.

The π^0 Detector (P0D) The P0D detector sits at the upstream end of ND280, and is optimized to measure the rate of neutral current and charged current π^0 production. The P0D consists of tracking planes composed of plastic scintillating bars alternating with lead foils. Inactive layers of passive water in sections of the P0D provide a water target for measuring neutrino interactions on oxygen useful to extrapolate systematics on SuperKamiokande.
The P0D is approximately cubical, and in the final ND280 configuration will be covered on all 6 sides by the electromagnetic calorimeter. The P0D is composed of 76 tracking planes perpendicular to the beam direction. The tracking planes are constructed of polystyrene triangular scintillating bars fabricated by co-extrusion with a reflective layer TiO_2 and a central hole for a WLS fiber. Each bar has a 3 cm base, a 1.5 cm height and a length of 180 cm. The light collected is transported to the photo-sensors using clear optical fibers.
The total mass of the P0D is 17.6 tons and it is expected to collect approximately 60000 neutral current single-π^0 events for an exposure of 10^{21} POT (1 year of data taking at the T2K nominal intensity).
The expected energy resolution for a fully contained event is

$$E_{res}^{P0D} = 10\% + \frac{3.5\%}{\sqrt{E(GeV)}} \tag{2.25}$$

and the efficiency to reconstruct a π^0 with a momentum larger than 200 MeV is 33%.

The Electromagnetic calorimeter (ECAL) The purpose of the Electromagnetic Calorimeter is to detect and characterize electromagnetic energy produced by neutrino interactions in the inner detectors (P0D, FGD, TPC), in particular photons produced by the decay of π^0 and electrons produced by ν_e interactions.
There are two different types of calorimeters modules in the T2K Near Detector: both are sampling calorimeters using layers of 1 cm thick, 4 cm wide plastic scintillator bars. The difference between the two modules is the number of active layers and their sampling fractions.

The main module, installed downstream the tracker system, consists of 34 active layers separated by 1.75 mm of lead sheet for a total effective thickness of 11 radiation lengths. The active area of the module transverse to the beam direction is $204 \times 204 \times 50$ cm^3 and the total weight is 7.0 t.
The second module has a coarser design, with only 6 active layers of scintillator separated by 4 cm thick lead sheets. The total thickness of this module is 4.5 X_0, the weight is 4.0 t and the active area is $280 \times 280 \times 50$ cm^3.
In the final T2K configuration modules of the Electromagnetic Calorimeter will be installed also on the sides of the Tracker and of the P0D in order to completely surround the others ND280 detectors and intercept particles produced at all the solid angle.

The side muon range detector (SMRD) The side muon range detector is placed in the iron yokes of the magnet. Each C-shape element consists of 5 cm iron plates with 1.7 cm of air gaps between the plates. The SMRD detector instruments these regions with 1 cm thick plastic scintillator with Wave-Length-Shifting fibers embedded into the scintillator, read by photo-sensors.
The SMRD is used to detect the momentum of the muons produced in neutrino interactions in the inner ND280 detectors, emitted at large angles. The momentum of these muons is not measured in the TPC but can be measured from their range in the magnet yoke. According to the Monte Carlo simulations a muon energy resolution less than 10% can be achieved.

The MPPCs All the ND280 detectors with the exception of the TPCs use Multi-Pixel Photon Counters (MPPCs) to read the WLS fibers. These detectors are a multi-pixel semiconductor photodiode consisting of pixels on a common substrate and have the advantage of being able to operate in a magnetic field. Each MPPC has an area of 1.3×1.3 mm^2 (optimized to read the 1 mm diameter fibers) and is composed of 667 pixels. The area of each pixel is 50×50 μm^2.
The operating voltage is 70 V and at this value each pixel operates as an independent Geiger micro-counter with the Geiger discharge initiated by a photoelectron and a gain determined by the charge accumulated in the pixel capacitance. Each pixel operates as a binary device but the MPPC on the whole is an analogue detector with the dynamic range limited by the finite number of pixels.
The sensitivity of the MPPCs have been tested using a blue LED and the results are shown in figure 2.24. The resolution is determined by the electronic noise and the intrinsic stability of the gain allows to see the ADC signal with separated peaks that correspond to different numbers of pixels.
The typical gain of MPPC at the working conditions is measured to be about 5×10^5 and the RMS of the distribution is 4.5%. Using a threshold of 0.5 photoelectrons the measured dark noise rate at the room temperature is of the order of 1 MHz/mm^2.

The total number of MPPCs used in the ND280 detectors is 60000.

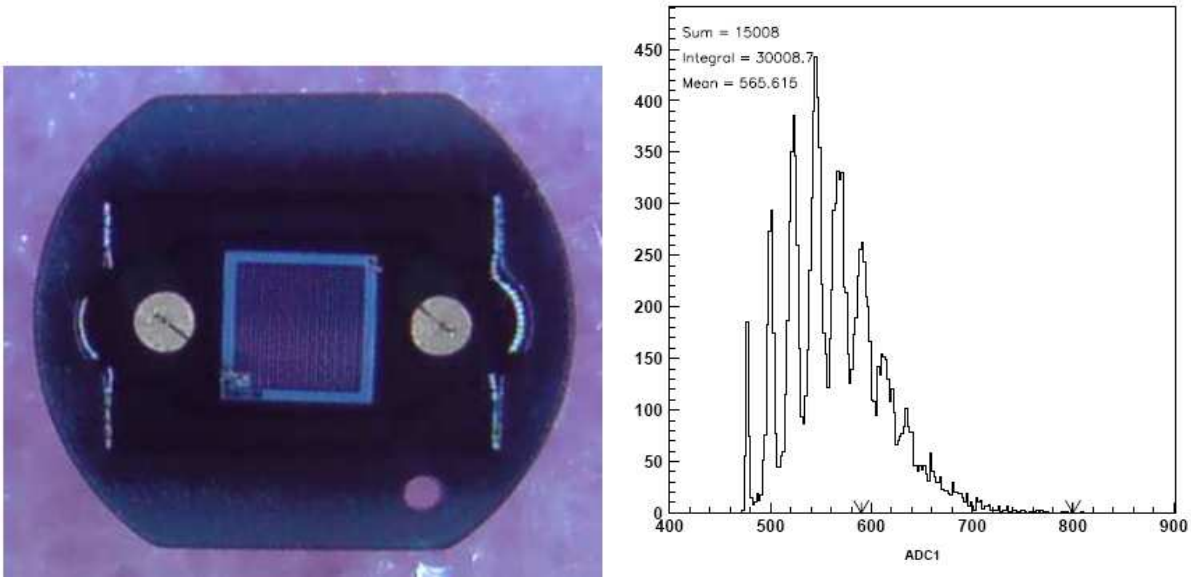

Figure 2.24: MPPC photosensor (left) and spectrum of LED flash of low amplitude (right).

Chapter 3

The T2K TPCs

In this chapter we will describe the TPCs of the T2K experiment.
We start describing the fundamental processes and working principles of gaseous tracking systems and their readout. Then we will describe in details the TPCs and the Bulk MicroMegas used in T2K. We will also show the validation chain of the MicroMegas modules and some results obtained during tests of a MicroMegas prototype. More beam test results, with the complete system will be shown in the chapter 5.

3.1 Principles of gaseous detectors

A TPC is a gaseous detector used to detect charged particles thanks to the ionization produced in the gas. The basic working principles of a TPC are common to all the gaseous detector and are based on the primary ionization of the gas molecules, the drift, the multiplication of the primary electrons and the detection of the amplified signals. In this section we will describe these processes.

3.1.1 Primary Ionization

When a relativistic charged particle crosses a gaseous detector it loses energy exchanging numerous low energy-virtual photons with the electrons in the gas molecules. If the energy of these photons is above the ionization potential they will ionize the molecule, with the emission of an electron. Instead, if the energy is below the ionization potential, the photon will simply excite the molecule.
This electron can then ionize or excite other molecules producing secondary electrons, usually

created close the primary interaction point. There is also some probability that the secondary electron has a kinetic energy large enough to travel away from the interaction point, creating a separated track. In this case the electrons are called δ-ray and whether an electron can be classified as a δ-ray depends on the sensitivity of the specific detector.
At the end of these processes a certain number of electrons has been produced along the trajectory of the track. The mean energy loss is given by the Bethe-Bloch equation [47]

$$-\frac{dE}{dx} = 4\pi N_A r_e^2 m_e c^2 z^2 \frac{Z}{A}\frac{1}{\beta^2}\Big[\frac{1}{2}\ln\frac{2m_e c^2\beta^2\gamma^2 T_{max}}{I^2} - \beta^2 - \frac{\delta}{2}\Big] \tag{3.1}$$

where z is the charge (in unit of e) of the incident particle, Z is the atomic number of the absorber particle, A is the atomic mass number, N_A the Avogadro number, r_e the classical electron radius, β and γ are the usual kinematic variables, $m_e c^2$ is the electron mass, I is the mean excitation energy of the atom, T_{max} is the maximum possible kinetic energy that can be imparted to a free electron and δ is a parameter that takes into account corrections due to density effects. The value of the dE/dx is given in $MeVg^{-1}cm^2$.
In the region between $\beta\gamma = 0.1$ and $\beta\gamma = 100$, the density effects are negligible. The measurement of the dE/dx in the gas along the track together with the measurement of the momentum, allows the identification of the particle (see figure 3.1).

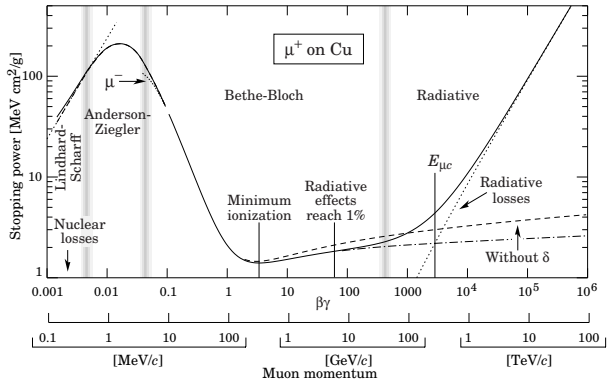

Figure 3.1: Average energy loss given by the Bethe-Bloch formula as a function of $\beta\gamma$ for μ^+ in copper

3.1.2 Motion of charge carriers in the gas

Drift

The electrons and ions created during the ionization process drift through the gas volume, due to the influence of electric and magnetic fields. The behavior of electrons and ions during the drift is different: the electrons scatter with the gas molecules and after the collision the electron direction is not related to its direction before the collision. The average motion depends on the orientation of the electric and magnetic fields while the drift speed only depends on the magnitude of the electric field. When colliding with atoms an energy loss occurs while between the collisions, the charged particles acquire energy due to the acceleration from the electric field and in the case of electrons an equilibrium between these two processes is reached:

$$\frac{x}{v_d \tau} \lambda E_G = eEx \tag{3.2}$$

where τ is the mean time between two collisions, λ is the mean energy loss, E_G is the equilibrium energy, e the electron charge, x the traveled distance and E the electric field.
The drift velocity v_d is the extra-velocity that the electron picks up when it moves into an electric field and it is equal to its acceleration along the field multiplied by the average time τ between two collisions:

$$v_d = \frac{eE}{m} \tau \tag{3.3}$$

This velocity reaches a local maximum if the atoms become invisible to the electrons and this occurs when the quantum mechanical wavelength of the particle is equal to the width of the potential in which it travels (the Ramsauer effect [48]). In general drift chambers are operated at the electric field where the maximum is reached to minimize the sensitivity of the drift velocity to field inhomogeneities.
In the case of the ions instead, they, being much heavier than electrons, lose most of their energy in collisions. In contrast to the randomly distributed direction of electrons after a collision, ions keep a large fraction of their initial momentum leading to smaller changes in their direction.

Diffusion

A charge cloud of electrons or ions travelling through a gas volume will be subject to scattering processes with the gas molecules. Assuming that the change in the direction of

motion is equally distributed over all the angles, the diffusion is described by a Gaussian law and at a distance r from the cloud center, the density $n(r)$ is given by

$$n(r) = (\frac{1}{\sqrt{4\pi Dt}})^3 \exp \frac{-r^2}{4Dt} \tag{3.4}$$

with a mean squared deviation $\sigma_D^2 = 2Dt$. Assuming exponentially distributed distances between collisions and isotropic scattering σ_D can be computed. Using the mobility of the drifting particles:

$$\mu = \frac{v_d}{E} = \frac{e}{m}\tau, \tag{3.5}$$

obtained using equation 3.3 and their average energy $\epsilon = (1/2)\mu^2$ it can be shown that

$$D = \frac{2\epsilon}{3m}\tau \tag{3.6}$$

and from this

$$\sigma_D^2 = 2Dt = \frac{2DL}{\mu E} = \frac{4\epsilon L}{3eE} \tag{3.7}$$

From this equation it is clear that the diffusion is proportional to the square root of the travelled distance L and this sets a limit to the accuracy of the track measurement. It is desirable to have σ_D as low as possible that means low electron energies at high drift fields. In the thermal limit the energy is proportional to the temperature, $\epsilon = (3/2)k_BT$ and the diffusion is a decreasing function of the field, independent from the gas:

$$D = \sqrt{\frac{2k_BT}{eE}} \tag{3.8}$$

A more accurate picture of the diffusion mechanism emerged in 1967 when Wagner and collaborators [50] showed that the diffusion of a cloud of electrons along the field is different from the one in the direction normal to the field and we distinguish between longitudinal (D_l) and transverse diffusion (D_t):

$$\sigma_l = D_l\sqrt{L} \tag{3.9}$$

$$\sigma_t = D_t\sqrt{L} \tag{3.10}$$

Influence of magnetic fields

The presence of a magnetic field alters the drift velocity as well as the diffusion.
In general the velocity vector of a particle of mass m and charge e moving in an electric field $\overrightarrow{E}$ and in a magnetic field $\overrightarrow{B}$ obeys the equation of the motion:

$$m\frac{d\overrightarrow{v}}{dt} = e(\overrightarrow{E} + \overrightarrow{v} \times \overrightarrow{B}) \tag{3.11}$$

To take into account the slowing down of the drifting particles by the gas molecules, following the approach introduced by Langevin [51], we can introduce a friction force $\overrightarrow{f} = -K\overrightarrow{v}$ and the equation 3.11 becomes

$$m\frac{d\overrightarrow{v}}{dt} = e(\overrightarrow{E} + \overrightarrow{v} \times \overrightarrow{B}) - K\overrightarrow{v} \tag{3.12}$$

Defining $\tau = m/K$ the characteristic time between two collisions, the velocity vector is constant if $t \gg \tau$ and is equal to the drift velocity vector $\overrightarrow{v}_d$ which obeys

$$\frac{\overrightarrow{v}_d}{\tau} - \frac{e}{m}\overrightarrow{v}_d \times \overrightarrow{B} = \frac{e}{m}\overrightarrow{E} \tag{3.13}$$

In terms of the cyclotron frequency $\omega = (e/m)B$ the solution of 3.13 can be written as

$$\overrightarrow{v}_d = \frac{e}{m}\tau E\frac{1}{1+\omega^2\tau^2}(\overrightarrow{u}_E + \omega\tau(\overrightarrow{u}_E \times \overrightarrow{u}_B) + \omega^2\tau^2(\overrightarrow{u}_E \cdot \overrightarrow{u}_B)\overrightarrow{u}_B) \tag{3.14}$$

where $\overrightarrow{u}_E$ and $\overrightarrow{u}_B$ are the unit vectors in the direction of the fields. The equation 3.14 is the Langevin formula and shows that for arbitrary oriented electric and magnetic fields, the drift velocity vector has components along the directions of $\overrightarrow{E}$, $\overrightarrow{B}$ and $\overrightarrow{E} \times \overrightarrow{B}$ with the magnitude depending on the dimensionless parameter $\omega\tau$.
If no magnetic field is applied, $\omega\tau = 0$ and the drift velocity points the direction of the electric field, $\overrightarrow{v}_d = \mu\overrightarrow{E}$ while in presence of a magnetic field, the magnitude of $\overrightarrow{v}_d$ is reduced by a factor

$$\frac{|\overrightarrow{v}_d(\omega)|}{|\overrightarrow{v}_d(0)|} = (\frac{1+\omega^2\tau^2\cos\phi}{1+\omega^2\tau^2})^{1/2} \tag{3.15}$$

where ϕ is the angle between $\overrightarrow{E}$ and $\overrightarrow{B}$. This latter equation shows that the drift velocity is unaffected by the magnetic field if it is oriented parallel to the electric field.

Moreover, due to the different mass of electrons and ions, the effect of the magnetic field on the electrons drift is several orders of magnitude larger than in the case of the ions.

Attachment

Electrons created in the amplification process can be captured by the gas molecules. These electrons will not contribute to the signal measured on the anode and the probability of this process is given by the electron affinity of the gas. For noble gases this effect is small and can be neglected.
Some problems can arise if gas impurities are present in the gas. For example, oxygen has a high electron affinity and can significantly reduce the signal of a gaseous detector. The loss of primary electrons will degrade the performance of the detector and should be avoided. For this reason in a gaseous detector it is important to continuously monitor the presence of oxygen in the gas mixture and keep it at the level of few particles per million (ppm).
As it will be shown later we have done measurements of the attachment in the T2K TPC. The attachment results to be negligible and no dependence of the gain on the drift distance has been observed.

Amplification

An electron accelerated by an electric field of a few 10^4 V/cm can reach sufficient energy between collisions to ionize the gas, thus starting an avalanche. Inside this avalanche various physical processes can occur: single and multiple ionization, optical and metastable excitations, recombination as well as energy transfer by collisions between atoms. The amplification factor, also referred to as gain, is described by the first Townsend coefficient α. It specifies the number of electrons N created on a path length dx

$$dN = N\alpha dx \tag{3.16}$$

α is a function of the electric field and of the gas type and because of the various complex processes involved in the amplification, there is no analytical expressions for it. The gain also depends on the gas density ρ, because when ρ increases the mean free path of an electron decreases, reducing in this way the gain.
Gaseous detectors are usually operated in the proportional mode. This means that the signal produced is proportional to the number of primary electrons. During the avalanche process photons are created with enough energy to ionize further atoms. These photons can travel farther than the extent of the original avalanche and initiate other avalanches. This can cause too much charge for the counter and results in the loss of the proportionality. These photons are the reason why a quenching gas (typically CO_2 or complex molecules like

methane and isobutane) is usually mixed into the noble gas. These molecules have a high cross section for photons of various energies due to their many degrees of freedom and are able to absorb the photons produced in the avalanche.

3.2 The Time Projection Chamber

The concept of the Time Projection Chamber (TPC) was invented in the late 1970's by David Nygren and is the basis for the tracking of the charged particles in a large number of particle and nuclear physics experiments. The TPC is based on the principle of determining the three dimensional track positions, by measuring the time of drift of the primary electrons along the field directions (see figure 3.2). The sensitive volume of a TPC is generally made up of a cylindrical or box-like parallelepipedic gas volume, with an homogeneous electric drift field applied between the endplates. A charged particle creates primary ionization along its trajectory when passing through the active volume. Then the produced ions drift to the cathode and the electrons drift to the anode. Before reaching the anode the electrons have to be amplified to produce a detectable signal: this is obtained using wires (MWPC) or micro-pattern gaseous detector (MPGD) to detect the drift electrons providing a two dimensional projection of the track on the readout plane. Thanks to the uniform field in the drift region the drift velocity is constant and the third coordinate of the hits is determined from the arrival time of the signals on the readout plane.
A TPC is intended to measure the momentum of charged particles from the curvature of the tracks in a uniform magnetic field and for this purpose it is placed inside a magnetic field. Usually the magnetic field is oriented along the direction of the electric field, reducing in this way the electron transverse diffusion coefficient by large factors.
In TPCs operated so far the amplification was usually done with MPWC, thin wires that produce a high radial electric field close to their surface, enabling electrons to multiply. In such detectors the ions produced together with the electrons near the wire drift back towards the cathode, distorting the electric field.

A solution to avoid this problem is to use Micro Pattern Gas Detector, MPGDs (see section 3.3). These readout system do not use wires and consist in a device where the two electrodes are separated by a width of the order of 100 μm: in this region a high electric field is applied, producing the multiplication of the electrons.
The TPCs play a key role in the tracking system of several modern particle physics experiments because they cover large volumes thus providing a large number of measurements along the track. Due to the low density of the gas the TPCs introduce little material along the particle trajectories keeping the multiple scattering to a minimum and giving the possibility to measure other characteristics of the tracks in outer detectors.

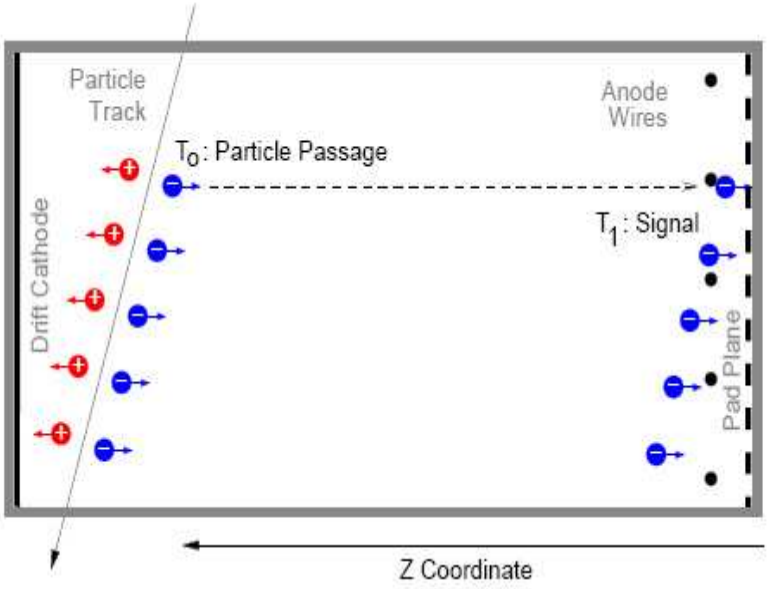

Figure 3.2: Working principles of a TPC. The charge detected on the segmented anode gives a 2D projection of the particle track. Combined with a measurement of the drift time, the track can be reconstructed in all three dimensions.

The measurement of track points on the pad plane is realized by weighting the charge detected on the pads and a careful choice of the pad pitch allows a precise measurement of the avalanche average position. The resolution in the drift direction primarily depends on the longitudinal diffusion in the gas.

3.2.1 Measurement of the momentum

A charged particle of charge e and momentum (p_x, p_y, p_z) traversing the volume of a TPC is curved by the axial uniform magnetic field $(0, 0, B_z)$ and its trajectory is an helix. In the plane perpendicular to the magnetic field the projected trajectory is a circle arc of radius

$$R = \frac{p_t}{eB} \tag{3.17}$$

where $p_t = (p_x^2 + p_y^2)^{1/2}$ is the particle transverse momentum. Expressing the momentum

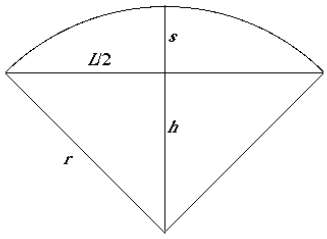

Figure 3.3: Measurement of the sagitta of one curved track.

in units of GeV/c, the radius in meters, the field in Tesla, the transverse momentum can be written as

$$p_t \sim 0.3Br \tag{3.18}$$

The radius r can be expressed in terms of the sagitta s of the projected track (see figure 3.3) and, for high momentum tracks, for which $s \ll l$ (where l is the length of the track),

$$p_t = \frac{eBl^2}{8s} \tag{3.19}$$

The resolution of the momentum measurement depends on the number of points measured along the track. For N_p equidistant points and neglecting multiple scattering, the momentum and sagitta relative resolution are given by the Gluckstern formula [52]

$$\frac{\sigma_{p_t}}{p_t} = \frac{\sigma_s}{s} = \sigma_{xy}\frac{p_t}{eBl^2}\sqrt{\frac{720}{N_p+4}} \tag{3.20}$$

Where σ_{xy} is the point resolution on the transverse plane. The total particle momentum is then determined measuring the polar angle Θ between the track and the direction of $\overrightarrow{B}$

$$p = \frac{p_t}{\sin\Theta} \tag{3.21}$$

where the precision on Θ depends on the resolution in the drift direction z, on N_p and on the track length L:

$$\frac{\sigma_\Theta}{\Theta} = \frac{\sigma_z}{L}\sqrt{\frac{12(N_p-1)}{N_p(N_p+1)}} \tag{3.22}$$

3.3 The Micro Pattern Gas Detector

In recent years there has been a lot of *R and D* efforts towards replacing the wire chambers with the Micro Pattern Gas Detectors in high energy physics experiments.
These detectors use inter-electrode distances of the order of 100 μm and are fabricated by means of printed-circuit-boards (PCB) techniques such as photolithography, etching and plating. Such a technique offers design flexibility and a large variety of MPGDs have been developed. The first example of these detectors has been the Micro Strip Gas Counters[53], first introduced in 1988. In the recent years, two other MPGDs have been largely used: the Gas Electron Multiplier (GEM)[54] and the Micro Mesh Gaseous Detector (MicroMegas). The latter is the detector used for the T2K TPCs and will be described here.

3.3.1 The Micro Mesh Gaseous Detector

The MicroMegas Detector was invented by I. Giomataris, G. Charpak, and collaborators in 1995[55]. The MicroMegas principle is shown in figure 3.4: the gas volume is separated by a thin micromesh in two regions, one where the conversion and electron drift occur and one, with a thickness of the order of 100 microns, where the amplification takes place. In the amplification region, a very high field (40 to 70 kV/cm) is created by applying voltages of few hundred volts between the mesh and the anode plane, which collects the charge of the avalanche. The anode can be segmented into strips or pads. The grid has a hole pitch of $20 - 50$ μm and is maintained above the anode plane by means of insulating pillars.

The advantages of MicroMegas are due to the smallness of the amplification gap and the configuration of the electric field on the two sides of the mesh. The gap being very small, the size of the avalanche and hence the signal rise time are very small, and in absence of longitudinal diffusion this would lead to an electron signal of a few nanoseconds and an ion signal usually less than 50-100 ns. Starting from the avalanche concentrated in the last few microns of the gap, the ions flow back to the mesh in the almost uniform amplification field. The fast signal and ion collection allows high rates to be sustained.

The electron collection efficiency is almost 100% if the field ratio between the drift and

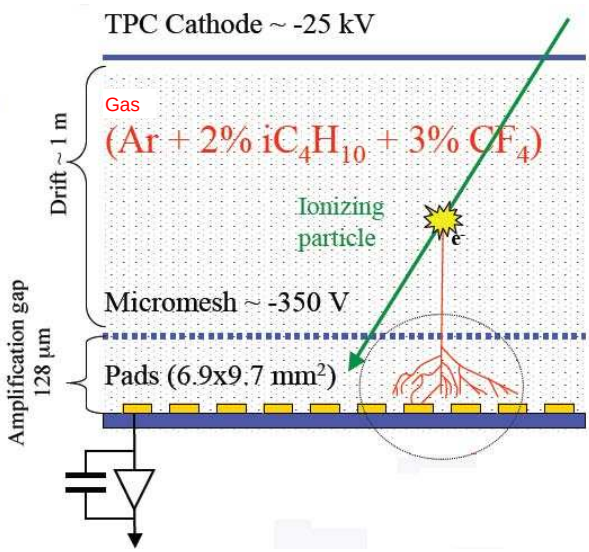

Figure 3.4: Schematic view of the Micromegas detector used in T2K. The ionization electrons drift towards the micromesh that is placed 50-100 micron above the anode. The micromesh is supported by short cylindrical pillars. Between the mesh and the anode, segmented to form pads, an avalanche is produced.

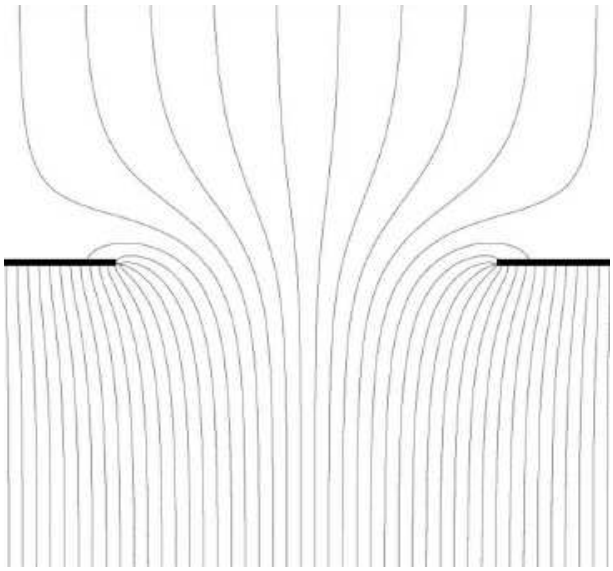

Figure 3.5: Field line configuration for a MicroMegas detector

the amplification regions is large enough and the mesh thin enough. In addition, it can be shown that for a given voltage applied to the grid, the gas gain exhibits a flat maximum as a function of the gap, reached for a value of a few tens to hundreds microns, depending of the gas mixture. These two properties provide an excellent energy resolution.
If the mesh pitch is less than $20 - 50\ \mu m$ and the ratio between the electric field in the amplification region and in the drift region is large enough (typically of the order of 100) the extension of the avalanche is as large as the inter-hole space, forcing most of the ions to drift back to the mesh instead of going back to the drift volume, avoiding in this way distortions due to the ion space charge in the TPC. A last advantage of the MicroMegas technology is the compactness of the volume used for the gas amplification.
The MicroMegas technology has been chosen for the TPCs of the T2K experiment and is also used for several physics experiments, like for instance as a kaon beam spectrometer in KABES [56], as an X-ray detector for axions search in CAST[57]. Also in the COMPASS experiment[58] 12 large MicroMegas chambers are part of the tracking system.

3.4 The T2K TPCs

In the ND280 facility 3 identical TPCs are installed (see figure 2.23), the first downstream the P0D, the second downstream the first FGD and the third one downstream the second FGD. In figure 3.6 a view of the main components of the TPC is shown, while in [59] can be found a complete description of the detector.

The outer dimensions of each module are $2.5\ m\ \times\ 2.5\ m$ in the plane perpendicular to the neutrino beam and $0.9\ m$ along the beam direction. The TPC is composed of an inner box that forms the field cage and the drift volume and an outer box, that surrounds the inner box and forms a CO_2 volume that provides electrical insulation. The TPC works at atmospheric pressure.
In table 3.1 a summary of the TPC characteristics is shown. The meaning of the different parameters will be made clear in the following of this chapter.

3.4.1 The TPC physics goals

From the previous considerations, we can state that the key measurements that the TPC system needs to provide are:

- momentum resolution better than 10% around 1 GeV/c. Given the low operating magnetic field (0.18 T) this will require good space point resolution, that is obtained

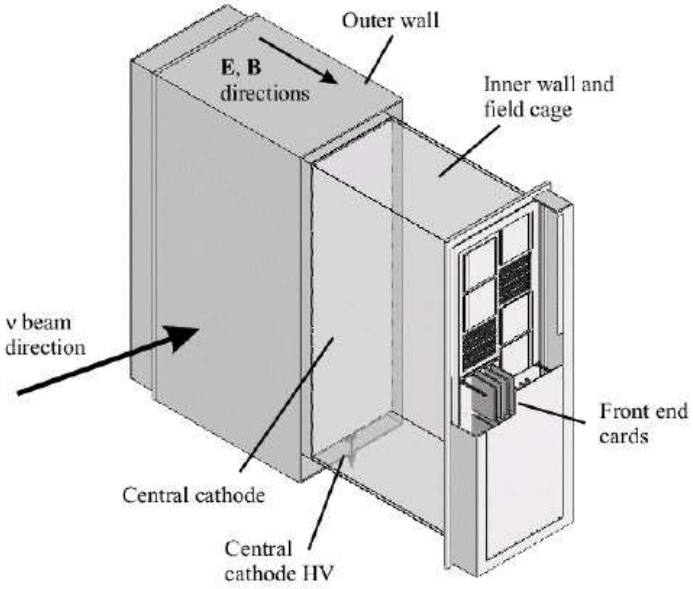

Figure 3.6: Schematic view of the T2K TPC detector.

using a segmented readout plane (see section 3.5);

- understand energy scale at the level of 2%. This goal can be met using a combination of magnetic field measurements and mapping, controlling the electric field distortions and using an absolute momentum calibration physical signal (for example the invariant mass of the K^0 produced by neutrino interactions);

- perform the particle identification through the measurement of the ionization energy loss, with the purpose to identify electrons from muons in the $0.5 - 1.0\ GeV/c$ region. To achieve a 3 σ separation, a resolution on the dE/dx measurement below 10% is needed.

The last point is the main subject of this thesis. As it will be shown in the next chapters, methods to perform the particle identification using the truncated mean have been developed and tested with beam test data. Moreover we performed an analysis of the ν_e component in the beam based on the Monte Carlo simulation that we will show in the chapter 7.

Outer dimensions	$2.5 \times 2.5 \times 1\ m^3$
Maximum drift distance	90 cm
Gas mixture	$Ar : CF_4 : iC_4H_{10}$ (95 : 3 : 2)
Cathode High Voltage	$25\ kV \rightarrow E = 280\ V/cm$
Drift speed	$7.9\ cm/\mu s$
Transverse diffusion coefficient	$237\ \mu m/\sqrt{cm}$
Total number of readout channels	124272
Pad dimensions	$6.9 \times 9.7\ mm^2$
MicroMegas High Voltage	$-350\ V \rightarrow \sim -27\ kV/cm$
MicroMegas Gain	~ 1500 (at $-350\ V$)
ASIC sampling time	40 ns
ASIC peaking time	200 ns

Table 3.1: TPC parameters in the default running conditions (magnetic field of 0.2 T)

3.4.2 The mechanical structure

The inner box includes the box walls, a central cathode that divides in two parts the drift region and two endplates, where the readout modules are installed. The box walls, as well as the central cathode, are constructed from 1/32 inch copper-clad G10, laminated onto both surfaces and 11.6 mm thick rohacell, giving a total thickness of 13.2 mm.
The endplate is machined from a solid plate of G10 and on the external surface the MicroMegas modules are installed.
The outer box consists of four walls and two endplates. The four walls are constructed from an aluminum-framed, aluminum-clad, rohacell laminate and the total thickness is 15.2 mm. To provide the electric field, strips are installed on the inside and the outside of the side walls of the inner box. The strip width is 10 mm with a 1.5 mm gap between the strips. The strips are connected to a resistor chain ($R = 20\ M\Omega$) electrically connected to the central cathode to provide the uniform electric field inside the inner volume. According to simulations the electric field is uniform to better than 10^{-4} for distances larger than 20 mm from the inner side wall.
In figure 3.7 some pictures of the first T2K TPC, taken at the time of the construction, are shown. In these pictures it is possible to see the different parts of the TPC.

Figure 3.7: Assembly of the TPC module 0. On the upper left the inner box is shown with its field cage strips used to provide the electric field(upper right). On the bottom left plots there is a view of the cathode seen by the endplate and on the bottom right the MicroMegas modules installed on the endplate.

3.4.3 Gas System

The gas system is chosen to obtain the best possible determination of the momentum of charged particles and of their energy loss in the TPC. For these purposes important parameters are the transverse diffusion coefficient (which affects the momentum resolution) and the achievable gain. Other conditions are set by cost and safety issues and by the requirement of a mixture as stable as possible against contaminations, mixing inaccuracies and density changes.
The mixture chosen for the TPC inner box is a mixture of Argon, CF_4 and iC_4H_{10} (95:3:2). At a magnetic field of 0.2 T, this gas has a small expected transverse diffusion coefficient, 280 $\mu m/\sqrt{cm}$ at the electric field corresponding to the peak of the drift velocity (290 V/cm) and for a magnetic field of 0.2 T, small e^- attachment, high gain and good point resolution. In figure 3.8 the expected transverse diffusion coefficient and drift velocity for the $Ar : CF_4 : iC_4H_{10}$ mixture, as a function of the electric field are shown. These plots are obtained using the Magboltz program for the simulation[60].
The Argon molecules are the main target for the ionization, the CF_4 is important to increase the drift velocity in the drift region and the iC_4H_{10} is used as a quencher to absorb the photons, mainly emitted in the amplification region, that, if not absorbed, can start other avalanches, bringing the MicroMegas out of the proportional region.
An important task for the gas system is to maintain the oxygen contamination in the inner volume at the level of 10 ppm. In fact a larger contamination would cause the phenomenon of the attachment in the TPC gas and consequently a dependence of the signal on the drift distance.
To keep under control the oxygen contamination one gas volume is changed every 6 hours. The region between the inner and the outer box is filled with CO_2: this gas has been chosen for its good dielectric rigidity necessary because the inner box in the center of the TPC is at a potential of 25 kV while the outer box is at ground.

3.5 The gas amplification and readout: Bulk MicroMegas

In the T2K TPCs the MicroMegas technology (see section 3.3.1) is used to detect the drift electrons. To produce the modules, a new production method, called Bulk MicroMegas, developed by a CERN-Saclay collaboration[61], is used.
The Bulk technique allows to produce detectors in a single process and it consists in laminating a woven mesh on a PCB (print circuit board) covered by a photo-imageable polyimide film. The Bulk MicroMegas modules have the advantage of being robust, allowing the production of large areas made in one piece, minimizing the dead zones between the modules.
Each TPC is read by 24 Bulk MicroMegas modules, 12 on each readout plane, disposed in

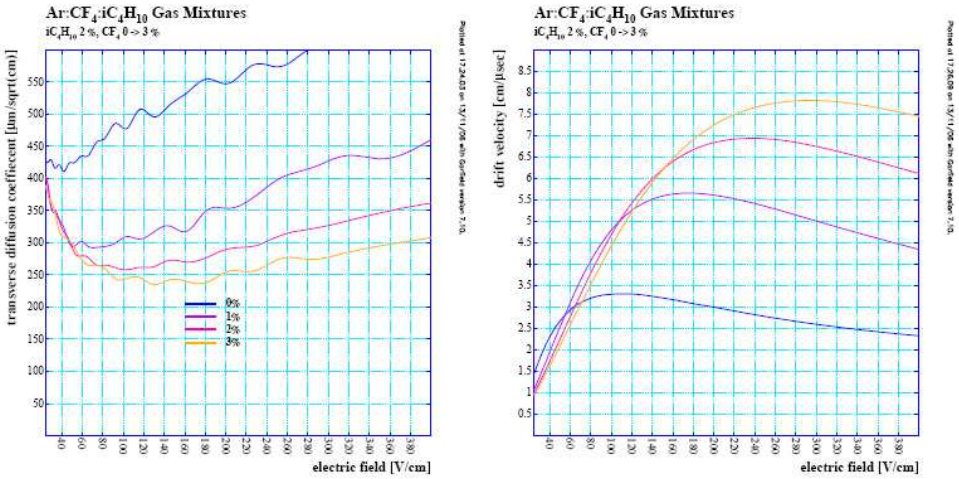

Figure 3.8: Expected transverse diffusion coefficient (left) and drift velocity as function of the applied drift field for fractions of CF_4 between 0% (blue) and 3% (yellow) according to the Magboltz simulation. The iC_4H_{10} is kept constant at 2%.

two columns of six modules each. The dead zone between the two columns is 21 mm, while the dead zone between two modules of the same column is 7.7 mm. To prevent as much as possible horizontal tracks to entirely cross the dead zone between two modules, the two columns are misaligned one with respect to the other by 5 cm.
Each module has a dimension of 34×36 cm^2 and is segmented in 1728 pads (1726 active), for a total active area of ~ 3 m^2 for each TPC. The total number of channels of the TPCs is of the order of 124000.
The Micromegas modules are installed on the TPC readout plane with an accuracy of $\pm$ 0.2 mm in Y and Z and the micromeshes of the 12 modules, forming an array, have to be coplanar within 0.1 mm in Z. One advantage of the T2K MicroMegas modules is that they are completely independent and they can be mounted and dismounted from the outside of the TPC field cage, without any internal connections between a module and the readout plane. In case of failure, this makes the detector replacement easier, and prevent as much as possible dust from entering the field cage.

The T2K Bulk-MicroMegas modules consist of a segmented PCB used as anode covered by a sandwich of 2 layers of 64 μm Pyralux PC1025 photoimageable coverlay by DuPont, used to define the 128 μm amplification gap and a 430 LPI (lines per inch) woven micromesh, 30 μm thick. These components are laminated together and undergo UV exposure with an appropriate mask. After a chemical development, the 20736 pillars with 400 μm diameter

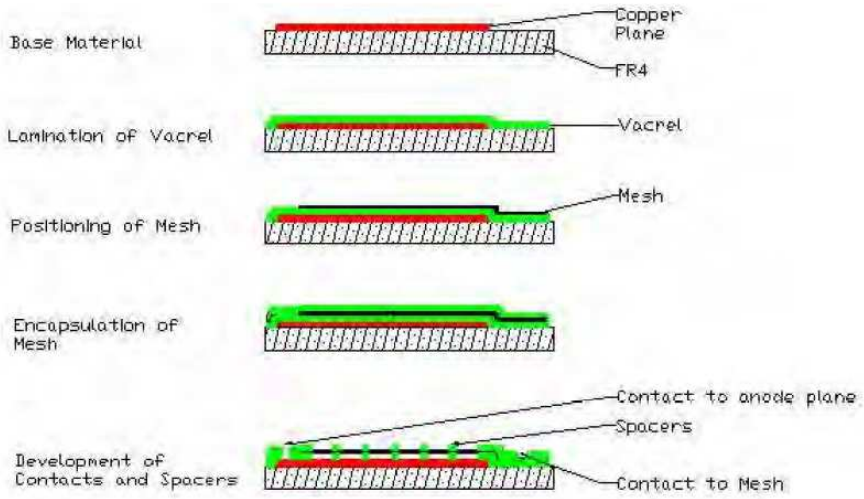

Figure 3.9: Production sequence of a Bulk MicroMegas module.

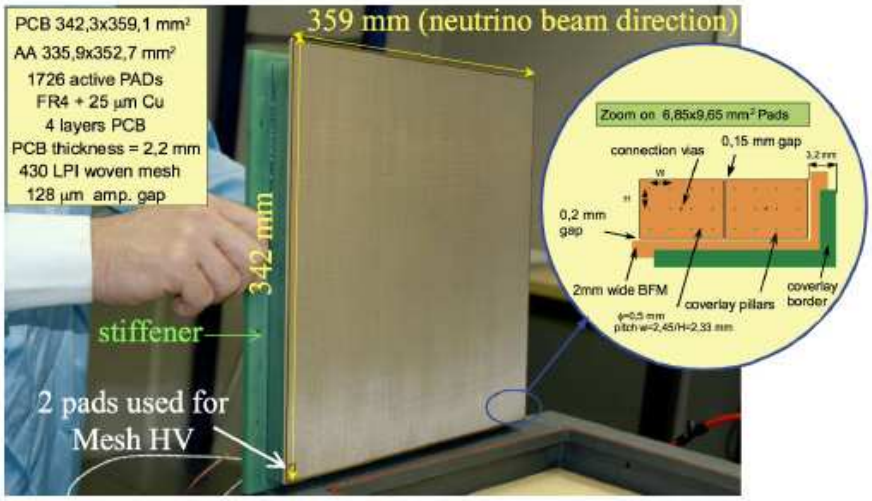

Figure 3.10: A 34×36 cm^2 T2K Bulk MicroMegas module glued on the stiffener. In the zoom we can see two pads on the corner of the detector with the relative structures.

define the 128 μm amplification gap thickness. A 3.2 mm wide border at the edge made of a copper strip called BFM (border frame mesh) and a polyamide coverlay are also produced during the process. It allows to hold the stretched mesh without using an external additional frame (see figure 3.9). In this way, large surfaces can be instrumented with a compact, thin and robust low mass detector. A photo of the detector is shown in figure 3.10.
The detector is then glued on a FR5 mechanical frame with a 100 μm mechanical tolerance to stiffen the detection surface and to ensure good positioning, thereby ensuring a uniform drift electric field near the detection plane.
The total thickness of the Bulk MicroMegas is 19.5 mm. The 1728 pads have dimensions of 6.9×9.7 mm^2 and are arranged in 48 rows and 36 columns. Two pads located in one corner are used for the mesh high voltage connection from the backside of the PCB. The high segmentation of the detector and the high gain ($10^3 - 10^4$) allow to reach the required performances in terms of momentum and energy resolution.
The T2K operative MicroMegas high voltage is 350 V: at this voltage an average gain of 1600 is reached and the measured number of sparks is 0.1 sparks per module per hour.
A full explanation of the manufacturing process of the T2K Bulk MicroMegas can be found in [62].

3.6 The Front-End electronic

The requirement for the TPC electronic system is to be able to record all the beam events. The nominal T2K event rate is 0.3 Hz (corresponding to the frequency of extraction of the protons from the JPARC Main Ring) and the electronics is designed to read at a rate up to 20 Hz, providing a comfortable bandwidth to record cosmic rays triggers, pedestals and laser calibration events.
The readout consists of two main parts: on-detector electronics, directly mounted on the MicroMegas module and off-detector electronics, housed in a standard rack.

Each of the 72 Micromegas modules is readout by six Front-End Cards (FECs) and one Front-End Mezzanine (FEM) card as shown in figure 3.11. Each FEC reads out an area of 48×6 pads (288 channels). On each FEC four custom-made front-end ASICs AFTER (Asic For Tpc Electronic Readout) chips[63] are mounted. Each AFTER chip reads out an area of 12×6 pads (72 channels).
The FEM communicates via a full-duplex gigabit class optical link with the off-detector Data Concentrator Card (DCCs). Each DCC communicates with four MicroMegas modules (three DCCs to readout one endplate) and a total of 18 DCCs are used in the T2K TPCs.

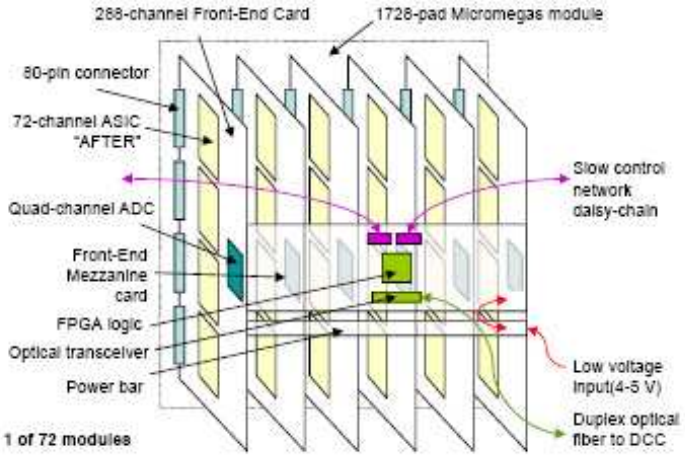

Figure 3.11: Scheme of the readout architecture of a detector module.

AFTER ASIC chips The purpose of this device is to shape and sample the signals coming from the MicroMegas pads. The large drift length of the TPC requires an accurate method to obtain the coordinate informations by continuously sampling pad signals in analog memory arrays.
The AFTER chip samples detector pad signals in a 511-bin Switch Capacitor Array (SCA) at a user defined frequency (up to 50 MHz). The sampling window can be adequately set through the sampling time (time difference between two consecutive samples). In the case of the T2K TPCs the maximum drift distance is 90 cm. Given the electrons drift velocity in the $ArCF_4iC_4H_{10}$ gas mixture (7.8 $cm/\mu s$) this distance is covered in approximately $12\mu s$. If we add the width of the T2K neutrino beam ($3\mu s$) we obtain an acquisition window of approximately $15\mu s$. To cover this window with enough safety we decided to set the sampling time to 40 ns that corresponds to an acquisition window of $20\mu s$.
Other important parameters of the AFTER chips are the charge range and the shaping time. The charge range establishes how many electrons correspond to one ADC count. We decided to set this parameter to 120 fC that corresponds to 183 electrons per ADC count. This value has to be chosen according to a compromise between the need of having a good resolution (smaller gain) and to avoid the saturation of the 12 bit chip (4095 ADC counts). As we will show in the following of this thesis first studies on the beam events show that with this choice of the gain approximately 2% of the hits saturate.
The last parameter, the shaping time, describes which is the time that the electronics will wait to collect the incoming electrons and produce the signals. This parameter is set to

200 ns and this means that all the electrons that arrive in the 200 ns time window will be properly collected and contribute to the electric signal.
In the running conditions, all these global parameters are managed by slow control.
Each AFTER chip contains 72 channels, each one reading one pad. In each channel there is an analog part dedicated to the conversion and the shaping of the input signal, and a switch capacitor array to store the analog signal until the reception of an external trigger signal. The analog multiplexed output of the chip is then converted by an external ADC. In figure 3.12 the typical signal registered in a MicroMegas row by the AFTER ASIC chip at the arrival of the primary electrons produced by a cosmic muon crossing the TPC is shown.

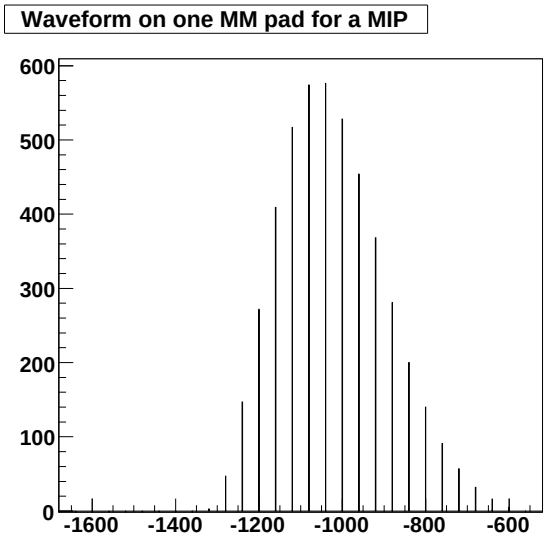

Figure 3.12: Observed signal on a MicroMegas row for a cosmic crossing the TPC during the tests in the ex-HARP TPC field cage.

As we can see from the figure a MIP produces a signal of approximately 1000 ADC at the peak. The typical pedestal RMS is of the order of 4.2 ADC counts, giving an excellent signal over noise ratio. During the TPCs operations, to limit the data size, we set a threshold of 4.5 times the pedestal RMS.
Finally the conversion factor k_C between ADC and fC is given by the formula:

$$k_C = \frac{1}{k_{ele}} \frac{fC_{in} fU_{dac}}{f_{BIT} Q} = \frac{1}{k_{ele}} \frac{4.7 \times 10^{-12}(F) \cdot 0.6(V)}{2^{14} \cdot 1.610^{-19}(C)} \tag{3.23}$$

where k_{ele} is a constant of the electronics measured for each pad (its mean value is 6.75).

Front-End Cards The Front-End Card performs three main functions: the digital conversion of 288 analog signals coming from a Micromegas detector, the calibration of the conversion function, and the monitoring of the board, checking the board power supply and the temperature.
The calibration is performed generating a signal through a capacitance in series to simulate an analog signal of a precisely known amplitude. The digital conversion of the 288 analog signal is performed in several stages that can be summarized as follows:

- amplification and shaping, analog storage and signal multiplexing: these tasks are performed by the AFTER chips, that store the information in the Switch Capacitor Array;
- conversion of the analog signals to digital values performed by a commercial device, the AD9229 from Analog Devices.

Another important taks of the FECs is to protect circuits from accidental over voltage due to spark in the detector: this is done using, for each pad, protection diodes connected to ground.

Front-End Mezzanine The Front-End Mezzanine is connected to 6 FECs and its main tasks are: to receive clock, trigger and synchronization information from its DCC; to duplicate the signals to the six FECs; to receive event data digitized by the ADCs of the FECs and to deliver event fragments to its DCC. The required input bandwidth is one of the challenging aspects of the FEM: given a 20 MHz conversion rate for the quad-channel 12-bit ADC of each FEC, the FEM has to receive and store an aggregate data flow of 5.76 Gbit/s. Transmission to and reception from the DCC occurs at $\sim 2\ Gbit/s$ each way. The core of the FEM is a large FPGA device that has to provide a few million gates, a couple of hundred I/O pins with an aggregate bandwidth of $\sim 20\ Gbit/s$.

Data Concentrator Cards The signals coming from the FEMs are collected by the Data Concentrator Cards (DCC)[64]. Each of these cards is connected to four FEMs, so 18 DCCs are needed to readout the three TPCs.
The DCCs are designed to distribute a reference clock to the front-end electronics and aggregate events from the 72 2 *Gbps* optical links: the events are then sent via a standard PC to the global data acquisition system of the experiment.
Each DCC is based on a commercial Field Programmable Gate Array (FPGA): the Xilinx ML405 development board[65]. An optical extension card has been designed and added to the ML405 to be able to connect four FEMs to each DCC.
At the inter DCC level a Slave Clock Module (SCM) is used to fanout the global clock and

the trigger information to the DCCs: each DCC is connected to the SCM by a standard RJ45 cable.
The central software element of the DCC is a command server program which receives orders from the TPC data acquisition PC over an Ethernet connection, decodes, translates and posts the corresponding commands to the front-end electronics over its optical communication links, receives the responses from the front-end, encapsulates them in Ethernet frames, and returns this information to the client PC. The requested acquisition rate is 20 Hz.

3.7 The TPCs calibration

One important task during the TPC operations is to assure that the data are taken in stable conditions for what concerns the gas properties, the electric and magnetic fields, the MicroMegas gain and the Front-End Electronics.
To monitor the TPCs during the runs two different systems are used: a laser calibration system and a gas monitor chamber.

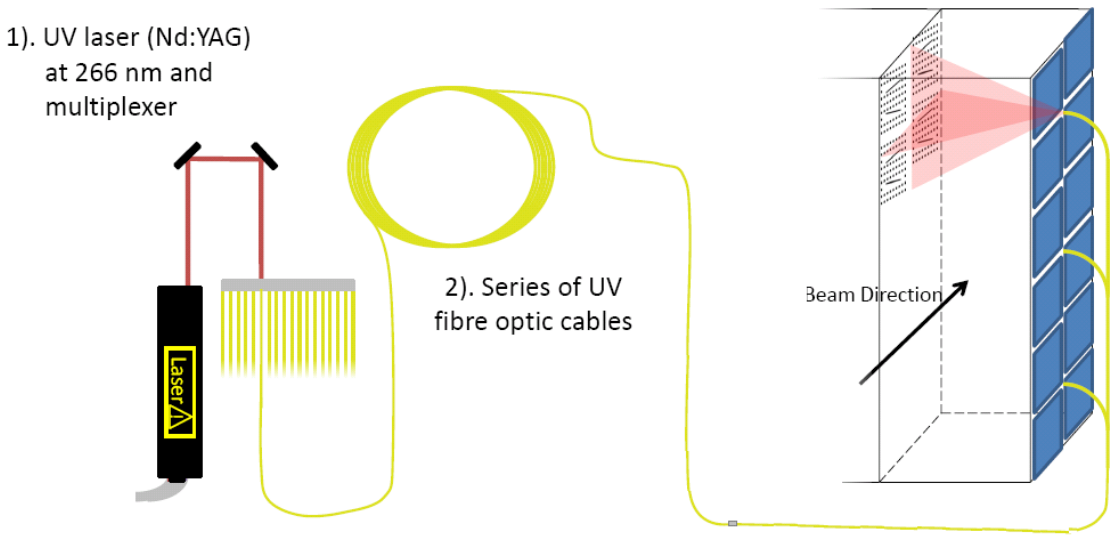

Figure 3.13: The laser system of the TPCs.

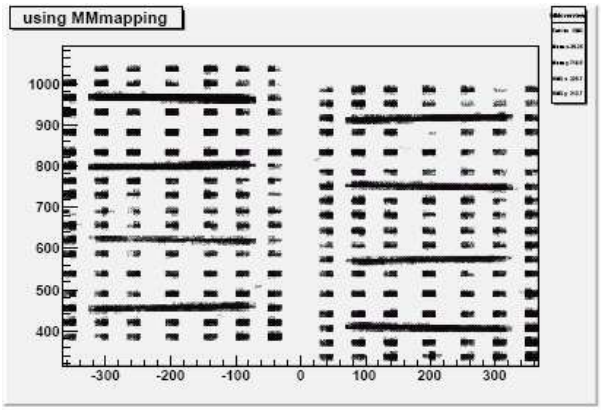

Figure 3.14: Laser events taken during the test with the module 0 of the TPC in the M11 beam test area at TRIUMF. During the tests 4 MicroMegas modules were read and we can see the signal coming from the Aluminium strips and the dots.

3.7.1 Laser Calibration system

To calibrate the TPCs, a UV-laser based calibration system is used. In this way, during the data taking, it is possible to provide a real time calibration of each TPC. This system is used to continuously measure:

- Absolute electric field distortions
- Absolute magnetic field distortions
- Relative gain of the system (to correct for the temperature and pressure effects)
- Drift velocity

A diagram of the laser setup is shown in figure 3.13: the laser used is a Nd:Yag UV laser that emits light at a wavelength of 266 nm. The light is then transported to the TPC readout plane with an optical fiber and is injected, from three different location per endplate, into the TPC drift region arriving on the central cathode where a pattern of aluminum strips and dots is mounted. When they are illuminated by the UV laser flash the strips and the dots release electrons via the photoelectric effect. These electrons drift towards the pad plane where they are amplified and detected by the MicroMegas modules producing an image of the strips and of the dots (see figure 3.14).

3.7.2 Gas monitoring chamber

The gas monitoring chambers work using the same principle as the TPC in terms of gas ionization, electron drift under a static electrical field and electron gas amplification. Their main task is to monitor the properties of the gas that is circulated in the large volume TPC. There are two monitoring chambers composed of a simple field cage (see figure 3.15) with a small sample gas volume where the same gas line that feeds the three TPCs is flowing and a MicroMegas readout module smaller than the ones used for the TPCs. One of the two chambers receives the gas at the beginning of the gas circuit, before entering the TPCs, while the second one receive the gas that is exiting from the TPCs.
On the cathode side an ^{55}Fe source and two ^{90}So sources are installed (see figure 3.16) that emit respectively 5.9 keV γ rays and $\beta - decay$ electrons. The signals produced by these events are then amplified and detected on the anode by the MicroMegas module and the analysis of their analysis allows the extraction of two important gas parameters: the drift velocity and the gain of the gas amplification. As the gas used in the monitor chambers and in the TPCs comes from the same gas line, the drift velocity and the gain are the same in both detectors.

Figure 3.15: Picture of one of the monitor chambers.

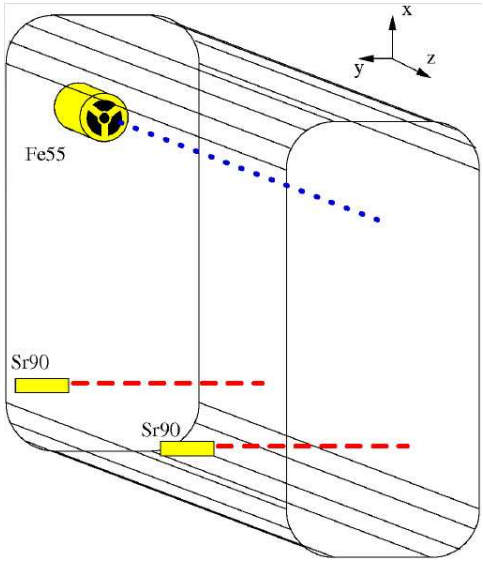

Figure 3.16: Layout of the monitor chamber.

3.8 The offline TPC software

The offline software for the TPC is embedded inside the official ND280 software. The framework is based on GEANT4 for the detector simulation and on ROOT for the data storage, handling and analysis.

3.8.1 The Monte Carlo simulation

The TPC geometry is implemented in GEANT4. All the material definition, size and position of the different parts of the TPC are simulated. During the simulation the tracking information is saved in special Monte Carlo hits to be further treated to produce the simulated electronic signals. The hits are created when the particle goes through a sensitive detector. For each hit the energy released by the particle is saved and to avoid large fluctuations in the energy loss in a given width of gas, the length of each hit is fixed to be not greater than 1 mm.
Once the hit is produced, the physics information is available through the time, the position and the energy loss associated to each hit. These informations are used to create ionization electrons along the track, with a number of electrons given by the energy lost divided by the ionization potential, $n_e = \Delta E/W_I$, with $W_I = 26\ eV$. Then these electrons are drifted from their creation point to the detection point. The drift velocity is constant so the drift time of an electron is proportional to its distance X from the readout plane, $T_{drift} = X/v_{drift}$. The drift velocity, as well as the transverse and the longitudinal diffusions are parameters that can be fixed by the user. The default values for the drift speed ($v_d = 7.8\ cm/\mu s$) and the diffusion ($\sigma_T = 237\ \mu m/\sqrt{cm}$ and $\sigma_L = 290\ \mu m/\sqrt{cm}$) are calculated from the Magboltz software for a drift field $E = 200\ V$ and a mixture $Ar : CF_4 : iC_4H_{10}$ $(95 : 3 : 2)$ in normal conditions. These values have been checked during the cosmic test in the ex-HARP field cage (see section 5.1.2).
Once the charge arrives to the readout plane the MicroMegas gain has to be simulated. The gain is simulated individually for all the primary electrons arriving to the mesh. To take into account the event by event gain fluctuations a Polya distribution is used

$$P_\theta(G) = \frac{\theta(\theta G/G_0)^{\theta-1}}{\Gamma(\theta)} \times \exp -\frac{\theta G}{G_0} \tag{3.24}$$

Simulations showed that to well simulate the signal, it is sufficient to use the value $\theta = 1$ that corresponds to an exponential distribution. This distribution is simulated by $G = -G_0 \times \log(1 - u_G)$ where u_G is extracted from a uniform distribution between 0 and 1.
The value of the gain, extracted from the comparison between data and Monte Carlo, has been set to 1950.

The last step of the simulation is the simulation of the electronic signal. The response function of the ASIC AFTER chips depends on the electronics parameters, in particular on the shaping time and on the sampling time. For the default condition, with a sampling time of 40 ns and a shaping time of 400 ns, the response function can be parameterized as

$$H(t) = A_0 \cdot (t/\tau)^3 \cdot \sin(t/(3.5/\tau)) \cdot \exp(-t/\tau) \tag{3.25}$$

where the parameters are: $A_0 = 0.91629$ and $\tau = (3.55 \times 20)\ ns$. Similar expressions has been obtained for the different possible electronic configurations.

3.8.2 The Reconstruction packages

The basic information in the TPC is contained in the sequence of digitized samples that for each trigger contains a vector of discrete values in time that represent the charge collected by a pad from the ionization track after diffusion. Each series corresponds to a complete readout sequence after any trigger and it can contain several neutrino interactions. Once the pad by pad electronics informations are collected, the first step is the application of the gain calibration constants and the removal of dead and noisy channels. The output of this process is a waveform that represents the charge acquired by a single pad along the readout time. The following step consist in searching for clusters of waveform in the same rows.
The clusters are then joined into tracks following a pattern recognition algorithm applied independently to each TPC. Before reconstructing the track the drift distance has to be determined to be able to predict the size of the electron cloud. This is done by determining the time at which the track was created (T_0) by matching it with signals in the fast detectors (FGD and ECAL).
Once the track is reconstructed the particle identification method is applied. This method has been developed during this thesis and will be fully explained in the next chapters.
Finally the reconstructed track is matched to tracks in other TPC and refitted to improve the accuracy in the determination of the track parameters.

Clustering

The clustering of the waveforms is done following a simple criterion of connectivity: waveforms have to overlap in time and have to be consecutive in space. As the direction of particles coming out from neutrino interactions is mainly horizontal, the clustering is done

within TPC vertical rows.
For tracks closer to the vertical direction, the clustering can be done in horizontal rows, in order to maximize the number of clusters to better reconstruct the track parameters.
The number of pads contained in a cluster depends on the drift distance that increases the diffusion. The number of pads is usually two for tracks that cross the center of the drift region but it can be one for tracks entering the TPC near the readout plane or three for tracks entering the TPC near the cathode, having in this way the maximum possible diffusion.

Track pattern recognition

Tracks are characterized as a series of clusters. The pattern recognition connects clusters and forms a track segment, that are connected together if they fulfill overlapping criteria. Once the segments are connected the reconstruction selects the combination that provides the longest reconstructed track segment. In this way it is possible to identify branches corresponding to hard δ ray emission or vertices inside the TPC volume. This is done identifying branches that leave the main track and have a minimum number of independent segments.

T_0 determination

In a TPC the drift coordinate is computed determining the drift time, but to do this we need to determine at which time the track is created. This cannot be done in the TPC as the drift time of primary electrons is much larger than the beam spill window (3 μs). To determine the T_0 informations coming from the fast detectors are used. For example in the case of particles that cross the TPC and the FGD, the TPC tracks are matched to the FGD signals which provide a time measurement with a resolution of few nanoseconds. The algorithm developed is based on matching detector signals at the entrance and exit of the track to provide the reference signal. It is also possible to use more than one detector or more than one plane for each detector to overconstrain the T_0 and reduce the amount of false matches.

Track reconstruction

The point and track reconstruction in one TPC is done with two different methods: in the first one, called point reconstruction method, the points are reconstructed independently and then are fitted using an helix model; in the second one, called likelihood method, the points are not reconstructed but the charge deposition distribution is used to fit the track model.

Both methods are implemented in the TPC reconstruction package of the nd280 software and can be used by the user.

Point reconstruction method The charge cloud space is represented by a gaussian

$$Q(x) = \frac{Q_0}{\sqrt{2\pi}\sigma} \exp \frac{-x^2}{2\sigma^2} \tag{3.26}$$

where σ is the charge width at the pad plane and is a function of the drift distance z through the transverse diffusion coefficient D_T (equation 3.10)

$$\sigma^2(z) = \sigma_0^2 + D^2 z \tag{3.27}$$

where σ_0 is the charge cloud smearing at the amplification level and is small in the case of MicroMegas.
When the track is perpendicular to the pad row the charge deposited on each pad of the row (Q_i) is computed as

$$Q_i = \int_{x^i_{min}}^{x^i_{max}} Q(x - x_p)dx = Q_0(erf(\frac{x^i_{max} - x_p}{\sqrt{2}\sigma}) - erf(\frac{x^i_{min} - x_p}{\sqrt{2}\sigma})) \tag{3.28}$$

where Q(x) is given by equation 3.26, x_p is the true point of the track in the pad row, (x^i_{min}, x^i_{max}) are the edge coordinates of the pad i and erf is the error function defined as

$$erf(z) = \frac{2}{\sqrt{\pi}} \int_0^z e^{-t^2} dt \tag{3.29}$$

In our case the different Q_i are known and it is possible to numerically invert the equation 3.28 and for a given σ reconstruct the position of the track x_p.
This method assumes that the track is perpendicular to the rows, keeping constant the distance to the lateral pads and the charge sharing due to the transverse diffusion. If the track is inclined the charge sharing depends on the distance of the track in the pad and on the longitudinal deposition along the track that is not uniform. This problem can be partially solved by recomputing the centroid once the track angle is estimated so that the distance to the adjacent pad can be computed more precisely.

Likelihood method The likelihood method is based on the same assumptions on charge sharing as the single point reconstruction. The main difference between the two methods is that here the points are not reconstructed but instead the observed charge is compared to a prediction assuming the track angle and position.
Also in this method the assumption is that the charge deposition is constant within a row. The likelihood method is based on a simple model of the charge deposition and electron drifting[67]. The number of primary electrons released in a row is of the order of 100. These electrons are amplified by the MicroMegas amplification system and the charge distribution is approximately multi-nomial. The number of electrons collected by a pad i with a gain g (ADC value per electron) is

$$n_i = ADC_i/g_i \tag{3.30}$$

where ADC_i is the charge collected in ADC units. Then we define a likelihood function

$$logL_{row} = \sum_i n_i logp_i + const \tag{3.31}$$

where p_i is the probability of a primary electron to be associated to the pad i

$$p_i = Q_i(\overrightarrow{x}, \overrightarrow{p}, \sigma)/\sum_j Q_j(\overrightarrow{x}, \overrightarrow{p}, \sigma) \tag{3.32}$$

where $Q_i(\overrightarrow{x}, \overrightarrow{p}, \sigma)$ is the predicted charge deposited in the pad i by a track with coordinate $\overrightarrow{x}$, momentum $\overrightarrow{p}$ and charge cloud width σ, while j runs over all the pads of the cluster containing the pad i.
The likelihood is maximized to obtain the track coordinates and the covariance matrix.
Once the track is reconstructed, independently from the method used for the reconstruction, the particle identification method is applied. This method, that will be explained in the next chapters, provides a particle identification (electron, muon, proton, pion or kaon) based on the measurement of the truncated mean of the track and of its momentum.

Long track reconstruction

The track reconstruction is done independently in the three TPCs. After the individual track segments have been found a matching is done between the segments in the TPCs and the reconstructed track in the others detectors, in particular the FGD and ECAL.
To match the tracks a Kalman filter algorithm[66] is used. This algorithm takes into account

the material distribution and the reconstructed track momentum to predict the track coordinates, angle and momentum at the matching plane. In the case of a track that cross two TPCs and the FGD between them, the matching plane is defined as the center of the FGD. The matching follows a standard quality criterion that computes the χ^2 of the matching. If several tracks fulfill the requirement the one with the best quality is selected.
The tracks are then refitted to improve the momentum resolution.

Chapter 4

The particle identification in the TPC

The Particle Identification (PID) in a gaseous detector is based on the fact that the ionization is a characteristic function of the particle speed β (see section 3.1.1). This means that measuring the momentum $p = Mc^2\beta\gamma$ and the ionization of a particle we can know its mass and identify it.
During this thesis we developed a method to perform the particle identification in the TPC: the method is based on the measurement, track by track, of the truncated mean of the energy deposited by the charged particles that cross the detector.
To be able to perform the particle identification it is necessary to have a good resolution on the energy loss. The design goal of the T2K TPCs is to have an energy resolution better than 10% for Minimum Ionizing Particles (MIP). This is needed to distinguish muons from electrons, allowing the measurement of the ν_e component in the T2K beam that is one of the main backgrounds to the ν_e appearance signal in SuperKamiokande.
In this chapter we will give an introduction explaining how the particles lose energy in the gas and then we will describe the truncated mean method developed to perform the particle identification in the TPC. In the next chapter we will show results regarding the studies on the TPC energy resolution (that is the basis of the particle identification) with the data taken in a beam test.

4.1 Introduction

In section 3.1.1 we briefly described the energy loss mechanisms in the gas, introducing the Bethe-Bloch equation 3.1 that describes the mean energy lost by a particle crossing a gaseous detector. In this section we will describe in more details the physics behind this process. A complete treatment of these processes can be found in [49].

4.1.1 Ionizing collisions

A charged particle that crosses a gaseous detector leaves a track of ionization along its trajectory. The ionization is left by random individual collisions with the electrons of the gas atoms (or molecules) in each of which the particle loses a random amount of energy E. The encounters are characterized by a mean free flight path λ between ionizing collisions. λ depends on the ionization cross-section per electron σ_I and on the density of the electrons in the gas N:

$$\lambda = \frac{1}{N\sigma_i}. \tag{4.1}$$

The number of encounters along a length L is on average L/λ while the probability of having k collisions follows a Poisson distribution

$$P(L/\lambda, k) = \frac{(L/\lambda)^k}{k!} \exp(-L/\lambda) \tag{4.2}$$

This equation provides a way to measure λ, measuring the probability of having zero encounters in a segment of length L. This probability is equal to $\exp(-L/\lambda)$.
The ionization is usually distinguished in primary and secondary ionization. In primary ionization a number of electrons are ejected from the atoms A encountered by the fast particle, for example a muon:

$$\mu A \rightarrow \mu A^+ e^- \tag{4.3}$$

but most of the charge along the track comes from the secondary ionization where electrons are ejected from atoms interacting with free electrons emitted in primary or others secondary interactions. This happens either in collisions of ionization electrons with atoms:

$$e^- A \rightarrow e^- A^+ e^- \tag{4.4}$$

or through intermediate excited states A^* according to

$$e^- A \rightarrow e^- A^*, \quad A^* B \rightarrow A B^+ e^-. \tag{4.5}$$

This latter mechanism occurs only if the excitation energy of A^* is larger than the ionization potential of B. In a gaseous detector A^* is usually the metastable state of a noble gas and B is one of the quencher added to the gas mixture to ensure the stability of the proportional operation.
The different contributions of these processes are in most cases unknown and only the total ionization is known.

4.1.2 Energy required to produce ion pairs

Due to the complexity of the microscopic processes involved, the mean energy required to produce a ion pair is not simply the ionization potential I of the gas. This happens because a certain amount of energy is lost in excitation of the gas molecules.
The total amount of ionization from all the described processes is characterized by the energy W spent, on average, in the creation of one free electron. This can be written as

$$W\overline{N}_i = \int_0^L \frac{dE}{dx} dx \simeq L < dE/dx > \tag{4.6}$$

where $\overline{N}_i$ is the averaged number of ionization electrons created along a trajectory of length L and $< dE/dx >$ is the average total energy loss per unit path length. The mean energy required for the ion pairs production W has to be experimentally measured for the different gas mixtures. Many measurements of W have been done and can be found in the literature ([68], [69]). An interesting example for our purposes is the case of the Argon. For this noble gas, the ionization potential is 15.8 eV while the energy W has been measured to be 26 eV.

4.1.3 Range of primary electrons

The primary electrons are emitted almost perpendicular to the track and they lose their kinetic energy E in collisions with the gas molecules, randomly scattering until they have lost their kinetic energy.
An important parameter is the range covered by the electrons before loosing all their kinetic energy. In a small fraction of ionizing collisions energetic electrons can be emitted from the gas molecules (so-called δ-rays). These electrons are stopped over a distance of several millimeters to a few centimeters and can produce large ionization clusters far from the particle trajectories, eventually causing an error when reconstructing the particle tracks.

The average range R_p depends on the electron energy E (in MeV/c). A parameterization, valid up to energies of few hundred keV is given by ([70]):

$$R_p(E) = AE(1 - \frac{B}{1+CE}) \tag{4.7}$$

with $A = 5.37 \times 10^{-4}\ g\ cm^{-2}\ keV^{-1}$, $B = 0.9815$ and $C = 3.12 \times 10^{-3}\ keV^{-1}$. Typical values of range for argon are about 30 μm for an electron of 1 keV and about 1.5 mm for an electron of 10 keV.

4.2 Calculation of energy loss

The energy lost by a charged particle crossing a medium is mainly due to the exchange of soft virtual photons between the charged particle and the atoms. The virtual photons cover a large energy band, from the soft ultraviolet to the X-ray region and this large bandwidth leads to the large fluctuations in the signal observed in thin absorbers (see figure 4.1). The straggling function $f(\Delta)$ describes the probability of an energy loss Δ when the particle crosses the medium.

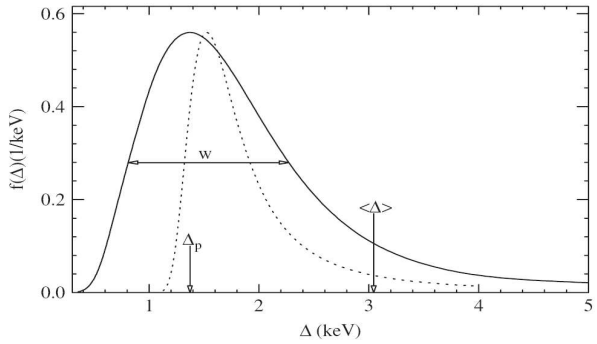

Figure 4.1: The straggling function $f(\Delta)$ (distribution of energy deposit) for particles with $\beta\gamma = 3.6$ traversing 1.2 cm of Ar gas is given by the solid line. The original Landau function is given by the dotted line. $\Delta_p(x, \beta\gamma)$ is the most probable energy loss while $\langle\Delta\rangle$ represents the mean energy loss [71]. The differences between the two curves will be made clear in the following of this chapter.

What we can measure is the number of ionization electrons and not the energy loss itself: the collisions include the excitation of bounded and unbounded atomic states and

hard scatters between the charged particle and quasi-free atomic electrons. The energy loss in a single collision extends from few eV up to the kinematic limit $E_{max} = 2m\beta^2c^2\gamma^2$ reached in a collision between a heavy charged particle and a free electron of mass m. The cross-section for these collisions is described by the Rutherford formula, $d\sigma/dE \propto 1/(\beta^2 E^2)$ and they contribute to the tail extending to high energies of figure 4.1.
If we restrict to the peak region of the distribution this is largely the result of soft collisions in which the atom absorbs a virtual photon, producing ionization. The energies involved in these collisions are characterized by the atomic structure of the material.
For the particle identification what we want to do is to determine, for primary ionization with what probability it will result in a total ionization of n electrons: then the total ionization over a length of track can be determined by summing over all the primary encounters in that length: using the concept, introduced in equation 4.6, of the average energy W required to produce one ion pair, the problem is then reduced in finding the energy spectrum $F(E)dE$ of the primary electrons, or, equivalently, the corresponding differential cross-section $d\sigma/dE$. Once this is known, we obtain λ (see equation 4.1):

$$\lambda = \frac{1}{\int N \frac{d\sigma}{dE} dE} \tag{4.8}$$

In the following of this section we will show how $d\sigma/dE$ can be calculated: to do this we will follow the procedure introduced by Allison and Cobb in [72]: we will start by computing the average total energy loss per unit distance, $< dE/dx >$, of a moving charged particle in a polarizable medium in a classical computation in which the medium is treated as a continuum characterized by a complex dielectric constant $\epsilon = \epsilon_1 + i\epsilon_2$. Then we will interpret the resulting integral over the lost energy in a quantum mechanical sense and from there we will define the concept of the differential cross-section $d\sigma/dE$.

4.2.1 Force on a charged particle travelling through a polarizable medium

In collisions in which the energy lost is small with respect to the energy of the incident charged particle, the electromagnetic field can be treated semiclassically. We can then derive the electric field $\mathbf{E}$ at the position of the particle $\mathbf{r} = \boldsymbol{\beta} ct$ and describe the mean energy loss per unit time as the effect of the electric field doing work on the particle:

$$< dE/dx >= \frac{e\mathbf{E}(\beta ct, t) \cdot \boldsymbol{\beta}}{\beta} \tag{4.9}$$

where e is the charge of the moving particle. To determine $\mathbf{E}$ we can use the Maxwell

equation in a nonmagnetic dielectric medium:

$$\nabla \cdot \mathbf{H} = 0; \qquad \nabla \times \mathbf{E} = -\frac{1}{c}\frac{\partial \mathbf{H}}{\partial t} \tag{4.10}$$

$$\nabla \cdot (\epsilon \mathbf{E}) = 4\pi\rho; \qquad \nabla \times \mathbf{H} = \frac{1}{c}\frac{\partial(\epsilon \mathbf{E})}{\partial t} + \frac{4\pi}{c}\mathbf{j} \tag{4.11}$$

The charge density and the flux are given by the particle moving with velocity $\boldsymbol{\beta} c$:

$$\rho = e\delta^3(\mathbf{r} - \boldsymbol{\beta} ct); \qquad \mathbf{j} = \boldsymbol{\beta} c\rho \tag{4.12}$$

If we introduce the potentials ϕ and $\mathbf{A}$:

$$\mathbf{H} = \nabla \times \mathbf{A}; \qquad E = -\frac{1}{c}\frac{\partial \mathbf{A}}{\partial t} - \nabla\phi \tag{4.13}$$

the equations 4.10 are satisfied identically and equations 4.11 become:

$$\nabla \cdot (\epsilon \nabla\phi) + \nabla \cdot (\frac{1}{c}\epsilon\frac{\partial \mathbf{A}}{\partial t}) = -4\pi e\delta^3(\mathbf{r} - \boldsymbol{\beta} ct) \tag{4.14}$$

and

$$\nabla(\nabla \cdot \mathbf{A}) - \nabla^2\mathbf{A} = -\frac{1}{c^2}\frac{\partial}{\partial t}(\epsilon\frac{\partial \mathbf{A}}{\partial t}) - \frac{1}{c}\frac{\partial}{\partial t}(\epsilon\nabla\phi) + 4\pi e\boldsymbol{\beta}\delta^3(\mathbf{r} - \boldsymbol{\beta} ct). \tag{4.15}$$

At this point we still have the freedom of operating a gauge transform. If we choose the Coulomb gauge, we can impose:

$$\nabla \cdot \mathbf{A} = 0 \tag{4.16}$$

In this case the equations 4.14 and 4.15 become:

$$\nabla \cdot (\epsilon \nabla\phi) = -4\pi e\delta^3(\mathbf{r} - \boldsymbol{\beta} ct) \tag{4.17}$$

and

$$-\nabla^2\mathbf{A} = -\frac{1}{c^2}\frac{\partial}{\partial t}(\epsilon\frac{\partial \mathbf{A}}{\partial t}) - \frac{1}{c}\frac{\partial}{\partial t}(\epsilon\nabla\phi) + 4\pi e\boldsymbol{\beta}\delta^3(\mathbf{r} - \boldsymbol{\beta} ct). \tag{4.18}$$

The solutions to equations 4.17 and 4.18 can be found by expressing all the fields in terms of their Fourier transforms:

$$F(\mathbf{r},t) = \frac{1}{2\pi^2}\int d^3k d\omega F(\mathbf{k},\omega)\exp i(\mathbf{k}\cdot\mathbf{r}-\omega t) \tag{4.19}$$

and are:

$$\phi(\mathbf{k},\omega) = \frac{2e\delta(\omega-\mathbf{k}\cdot\boldsymbol{\beta}c)}{k^2\epsilon} \tag{4.20}$$

and

$$\mathbf{A}(\mathbf{k},\omega) = 2e\frac{(\omega\mathbf{k}/k^2c-\boldsymbol{\beta})}{(-k^2+\epsilon\omega^2/c^2)}\delta(\omega-\mathbf{k}\cdot\boldsymbol{\beta}c) \tag{4.21}$$

Then the electric field in space and time, using the second of equation 4.13, can be expressed as

$$\mathbf{E}(\mathbf{r},t) = \frac{1}{(2\pi)^2}\int\int\frac{i\omega}{c}[\mathbf{A}(\mathbf{k},\omega)-i\mathbf{k}\phi(\mathbf{k},\omega)\exp i(\mathbf{k}\cdot\mathbf{r}-\omega t)]d^3k d\omega \tag{4.22}$$

and the mean energy loss per unit length, introduced in equation 4.9, at the point $\boldsymbol{r}=\boldsymbol{\beta}ct$ is

$$\begin{aligned} < dE/dx > = \frac{e\mathbf{E}(\beta ct,t)\cdot\boldsymbol{\beta}}{\beta} = \frac{e^2 i}{\beta 2\pi^2}\int\int\left[\frac{\omega}{c}\left(\frac{\frac{\omega\mathbf{k}\cdot\boldsymbol{\beta}}{k^2c}-\beta^2}{(k^2+\epsilon\omega^2/c^2)}-\frac{\mathbf{k}\cdot\boldsymbol{\beta}}{k^2\epsilon}\right]\right. \\ \left.\times\,\delta(\omega-\mathbf{k}\cdot\boldsymbol{\beta}c)\exp\left[i(\mathbf{k}\cdot\boldsymbol{\beta}c-\omega)t\right]d^3k d\omega\right. \end{aligned} \tag{4.23}$$

If we rewrite the d^3k integration as $2\pi k^2 dk d\cos\psi$ and we integrate over $\cos\psi$ we obtain

$$< dE/dx > = \frac{e^2 i}{\beta\pi}\int dk\int d\omega\frac{k}{\beta}\left[\frac{\omega\left(\frac{\omega^2}{k^2c^2}-\beta^2\right)}{(-k^2c^2+\epsilon\omega^2)}-\frac{\omega}{k^2\epsilon c^2}\right] \tag{4.24}$$

The integral over $d\omega$ is done for both, positive and negative frequencies. Since $\epsilon(-\omega)=\epsilon^*(\omega)$ we can combine positive and negative frequencies, obtaining:

$$< dE/dx >= \frac{2e^2}{\beta^2\pi}\int_0^{\inf} d\omega \int dk \left[\omega k(\beta^2 - \omega^2/k^2c^2))Im\left(\frac{1}{-k^2c^2+\epsilon\omega^2}\right] - \frac{\omega}{kc^2}Im\left(\frac{1}{\epsilon}\right)\right] \tag{4.25}$$

The only unknown quantity in equation 4.25 is the complex dielectric constant. ϵ depends on the wave number k and on the frequency ω. Once $\epsilon(k,\omega)$ is known, $< dE/dx >$ can be calculated for every β. $\epsilon(k,\omega)$ is in principle given by the structure of the atoms of the medium, but a simplified model, the Photo-Absorption Ionization model developed by Allison and Cobb in [72] is sufficient for our purposes.

4.2.2 The Photo-Absorption Ionization model

The Photo-Absorption Ionization (PAI) Model allows to relate the only unknown of our problem, $\epsilon(k,\omega)$ to the measured photo-absorption cross-section $\sigma_\gamma(\omega)$ and from this to introduce the differential cross-section $d\sigma/dE$.
Other models exists in the literature to compute the differential cross-section: in particular the Rutherford cross-section, that has been the first model developed and used by Landau to compute the transport equation in the gas[73]. This model represents the cross-section for the collision of two free charged particles, without considering the internal structure of the atom.
A more sophisticated approach is given by the Bethe Fano method[74] that considers the entire structure of the atom. This method is at our knowledge the best approximation of the reality but it is difficult to implement and no calculations for gases are available.
In the following of this section we will describe the PAI model that is a simplified model with respect to the Bethe-Fano model but has the advantage of being easier to compute in the case of gases.
Let consider the case of a a plane light-wave travelling along x in a medium. It will be attenuated by the medium if the imaginary part of the dielectric constant is larger than zero. The wave number k is related to the frequency ω by

$$k = \sqrt{\epsilon}\omega/c \tag{4.26}$$

In the case of free photons traversing a medium with an electron density N and atomic charge Z, the attenuation is given by the photo-absorption cross-section $\sigma_\gamma(\omega)$:

$$\sigma_\gamma(\omega) = \frac{Z\omega}{Nc}\frac{\epsilon_2(\omega)}{\sqrt{\epsilon_1(\omega)}} \sim \frac{Z\omega}{Nc}\epsilon_2(\omega). \tag{4.27}$$

The second form is valid for low density media in which $\epsilon_1 \sim 1$. $\sigma_\gamma(\omega)$ can be measured for many gases using the synchrotron radiation and in this way we know $\epsilon_2(\omega)$ (see for example [77], [78]). Then using the dispersion relation we can derive also the real part $\epsilon_1(\omega)$:

$$\epsilon_1(\omega) - 1 = \frac{2}{\pi} P \int \frac{x\epsilon_2(x)}{x^2 - \omega^2} dx \tag{4.28}$$

where P is the principal value.
In the quantum picture the (ω, k) plane appears as the kinematic domain of energy $E = \hbar\omega$ and momentum $p = \hbar k$ exchanged between the moving particle and the atoms and electrons of the medium. The exchanged photons in the real case are not free and the relation between energy and momentum transfer is different from the one of equation 4.26. Their relationship can be understood in terms of the kinematic constraints: the photons exchanged with free electrons at rest have $E = p^2/2m$ while the photons exchanged with bounded electrons, with binding energy E_1 and internal momentum $\mathbf{q}$, have $E \sim E_1 + (\mathbf{p} + \mathbf{q})^2/2m$.
The minimum momentum transfer at each energy E depends on the velocity β of the particle and is equal to $p_{min} = E/\beta c$. These quantities delimit a kinematic domain and the solution of the integral 4.25 requires the knowledge of $\epsilon(\omega, k)$ over the domain.
The PAI model proposed by Allison and Cobb consists in the extension of the knowledge of ϵ into the kinematic domain. A detailed discussion of this model can be found in [72], here we only want to stress the fact that according to this model it is possible to find an expression for $\epsilon_1(\omega, k)$ and $\epsilon_2(\omega, k)$ dependent only on $\sigma_\gamma(\omega)$ and then it is possible to integrate over k the integral 4.25 obtaining:

$$\begin{aligned} < dE/dx > = \int d\omega \frac{e^2}{\beta^2 c^2 \pi} [& \frac{Nc}{Z} \sigma_\gamma(\omega) ln \frac{2mc^2\beta^2}{\hbar\omega[(1 - \beta^2\epsilon_1)^2 + \beta^4\epsilon_2^2]^{1/2}} \\ & + \omega \left(\beta^2 - \frac{\epsilon_1}{|\epsilon|^2} \right) \Theta + \frac{1}{Z\omega} \int \sigma_\gamma(\omega') d\omega'] \end{aligned} \tag{4.29}$$

where $\Theta = (1 - \epsilon_1\beta^2 + i\epsilon_2\beta^2)$. This equation can be then reinterpreted, leaving the classical theory and recognizing the energy loss as being caused by a number of discrete collisions per unit length, each with an energy transfer $E = \hbar\omega$. If N is the number of electrons per unit volume and $d\sigma/dE$ the differential cross-section per electron per unit energy loss, the average energy loss is given by

$$< dE/dx > = - \int NE \frac{d\sigma}{dE} \hbar d\omega \tag{4.30}$$

obtaining an expression for the differential cross-section

$$\frac{d\sigma}{dE} = \frac{\alpha}{\beta^2\pi}\frac{\sigma_\gamma(E)}{EZ}\ln(\sqrt{[(1-\beta^2\epsilon_1)^2+\beta^4\epsilon_2^2]}) + \frac{\alpha}{\beta^2\pi}\frac{1}{N\hbar c}\left(\beta^2 - \frac{\epsilon_1}{|\epsilon|^2}\right)\Theta + \\ + \frac{\alpha}{\beta^2\pi}\frac{\sigma_\gamma(E)}{EZ}\ln\left(\frac{2mc^2\beta^2}{E}\right) + \frac{\alpha}{\beta^2\pi^2}\frac{1}{E^2}\int_0^E \frac{\sigma_\gamma(E')}{Z}dE' \tag{4.31}$$

In this equation the first two terms are referred as the transverse cross-section and are related to the magnetic vector potential term for which the electric field is transverse to the direction of the 3-momentum transfer, $\hbar\mathbf{k}$. In the first term we recognize the logarithmic term, responsible for the relativistic rise in the energy loss curve.
The last two terms are known as the longitudinal cross-section and they come from the electrostatic term in the Coulomb gauge, which has the electric field parallel to the momentum transfer. In particular the last term corresponds to the Rutherford cross-section, that historically has been the first derivation of the collision cross-sections and makes the approximation of considering the electrons bounded in the atoms as free particles, neglecting in this way the internal structure of the atoms.
Examples of cross-sections calculated with the PAI and the Rutherford models are shown in figure 4.2 and 4.3. As we can see from the figures the internal structure of the atoms has an important effect and peaks in the cross-section are observed corresponding to the different internal orbitals. These effects are not considered in the Rutherford cross-section that considers the electron bounded in the atom as free particle.

4.2.3 Integral functions of Collision Cross Section

Once the differential cross section is determined, to perform a Monte Carlo calculation of the straggling function it is necessary to know the macroscopic cross section.
This cross section is defined as the number of collisions per cm:

$$\Sigma_t(\beta\gamma) = N\int \frac{d\sigma(E;\beta\gamma)}{dE}dE \tag{4.32}$$

where N is the number of atoms per cm^3. The cross section determines the average number of collisions in a segment of length x, $N_c = x\Sigma_t$. Other important functions used to describe the stochastic energy loss in a gas are the cumulative probability density function

$$\Phi(E;\beta\gamma) = \frac{\int^E \frac{d\sigma(E;\beta\gamma)}{dE}dE'}{\int^{\inf} \frac{d\sigma(E;\beta\gamma)}{dE}dE'} \tag{4.33}$$

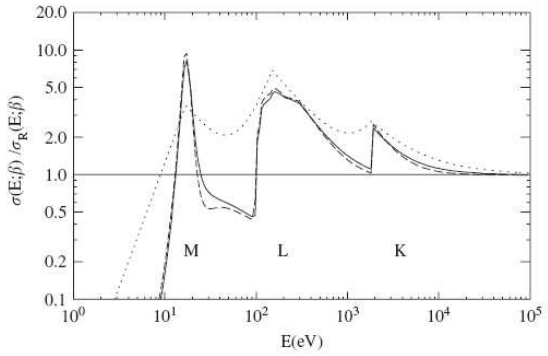

Figure 4.2: Inelastic collision cross-sections for single collisions in silicon by particles with $\beta\gamma = 4$, calculated with different theories. On the y-axis is represented the cross section divided by the Rutherford cross section. The collision cross sections are calculated using the Bethe Fano model (solid line) and the PAI model (dotted line).

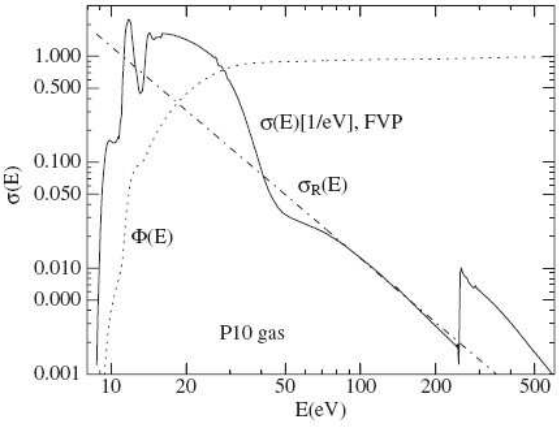

Figure 4.3: Inelastic collision cross-section for single collisions in P10 gas by ionizing particles with $\beta\gamma = 3.6$, calculated with PAI model theory (solid line) and Rutherford cross-section (dash-dotted line). The dotted line represents the cumulative probability density function [71].

and its complementary function $\Upsilon(E;\beta\gamma) = 1 - \Phi(E;\beta\gamma)$ that describe the probability of collision with energies larger than E. Examples of Υ computed using the PAI model for a P10 gas are given in figure 4.4. The dependence of Φ and Υ on $\beta\gamma$ is small and can be neglected.

A last useful set of definitions are the moments of $\sigma(E)$:

$$M_\nu(\beta) = N \int E^\nu \frac{d\sigma(E;\beta\gamma)}{dE} dE \tag{4.34}$$

With this definition the moment M_0 corresponds to the total Collision Cross Section (CCS) Σ_t, while the moment M_1 is usually called the stopping power $-dT/dx$, where T is the kinetic energy of the particles.

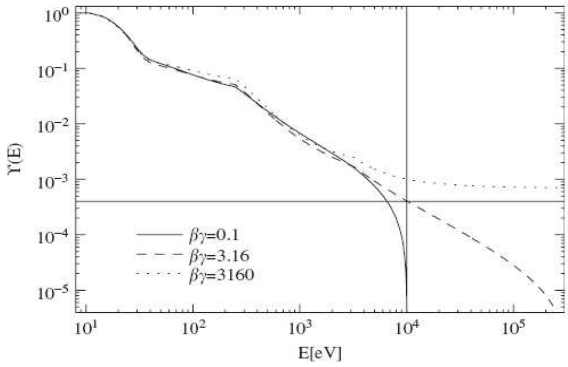

Figure 4.4: Probabilities $\Upsilon(E)$ for single collisions in P10 gas in which the energy loss exceeds a value E for different $\beta\gamma$ in P10 gas[71].

4.2.4 Straggling functions

The straggling functions $f(\Delta; x, \beta\gamma)$ represent the energy loss distribution functions and define the probability that a particle with an initial momentum $\beta\gamma$ loses a quantity of energy Δ crossing a thick of gas x.
These functions were firstly derived by Landau [73]. In his computation he used the Laplace transforms to solve the transport equation for the Rutherford cross-section. As we already discussed the Rutherford cross-section does not properly describe the cross-section in the gas.
When using different cross-section models the Landau method, even if formally correct, is not useful if we want to compute the straggling function. Starting from the the PAI cross-section, a better method to compute the straggling functions is to consider separately the distributions of the number of collisions in a segment x and the energy loss spectra for multiple collisions.
The number of collisions in a segment will follow a Poisson distribution

$$P(n) = \frac{N_c^n}{n!} e^{-N_c} \tag{4.35}$$

where $P(n)$ gives the fraction of particles suffering n collisions and $N_c = x\Sigma_t$ is the average number of collisions for all particles. The mean value of $P(n)$ is N_c and the width of the distribution is $1/\sqrt{N_c}$.
The spectra for multiple collisions can be calculated by convolution. Starting from the single

collision spectrum $\sigma(E)$, the n-fold convolution is obtained by iteration

$$\sigma(\Delta)^{*n} = \int_0^{\Delta} \sigma(E)\sigma^{*(n-1)}(\Delta - E)dE \tag{4.36}$$

with $\sigma(\Delta)^{*0} = \delta(\Delta)$ and $\sigma(\Delta)^{*1} = \sigma(E)$.
Then the straggling function will be obtained by the convolution

$$f(\Delta; x, v) = \sum_{n=0}^{\inf} \frac{N_c^n}{n!} e^{-N_c} \sigma(\Delta; v)^{*n} \tag{4.37}$$

These straggling functions can be computed analytically for any width of gas and any particle velocity, using the PAI cross-sections[71] and an example is shown in figure 4.1.
As we can see from the figure 4.1 the distribution is much broader than the one expected using the Landau calculation. This happens because in the Landau computation[73], the Rutherford cross-section was used. The Rutherford cross-section is:

$$\sigma_R(E) = \frac{2\pi Z^2 e^4}{mv^2} \frac{1}{E^2} = \frac{k_R}{\beta^2} \frac{1}{E^2}. \tag{4.38}$$

where k_R is given by

$$k_R = \frac{2\pi e^4}{mc^2} Z^2 \tag{4.39}$$

In these formulas m is the mass of the electron, Z is the atomic charge of the gas molecules and A the atomic mass of the absorber expressed in g/mol.
Using this formula the stopping power M_1 using the Rutherford cross-section is given by

$$M_1 = \frac{k}{\beta^2} \rho \frac{Z}{A} \ln \frac{E_{max}}{E_{min}} = \frac{k}{\beta^2} \rho \frac{Z}{A} 2 \ln \frac{2mv^2}{I} \tag{4.40}$$

where $E_{min} = I/2mv^2$ and $E_{max} = 2mv^2$.
The number of collisions is instead given by M_0:

$$M_0 = \frac{k}{\beta^2} \rho \frac{Z}{A} (\frac{1}{E_{min}} - \frac{1}{E_{max}}) \sim \frac{k}{\beta^2} \rho \frac{Z}{A} \frac{2mc^2\beta^2}{I^2} = k\rho \frac{Z}{A} \frac{2mc^2}{I^2} \tag{4.41}$$

Thus according to this model, 3600 collisions/cm are expected in argon, while using the more appropriate PAI cross section we have, for a minimum ionizing particles, $\sim$ 200 collisions/cm. As the width of the straggling function is given by $1/\sqrt{N_c}$ using the Rutherford

cross-section the distribution is much narrower than the one that we obtain using the PAI model.
This large difference is due to the fact that the Landau method has two limits of validity: the first is that the number of collisions in which the particle loses an amount of energy close to the maximum value of the transferable energy has to be small compared to the total number of collisions and the second is that the number of collisions in which the particle loses a small amount of energy has to be large in the path length under consideration.
This second condition is violated in thin absorbers such as gaseous detectors: in Landau's theory the energy lost in a given path length is the result of a large number of collisions; in gaseous detector, due to the low density of the material, if the path length is short enough, only few collisions with small energy loss take place and we need to take into account the energy fluctuations in each collision. At this small energy moreover we cannot neglect the atomic structure of the material.

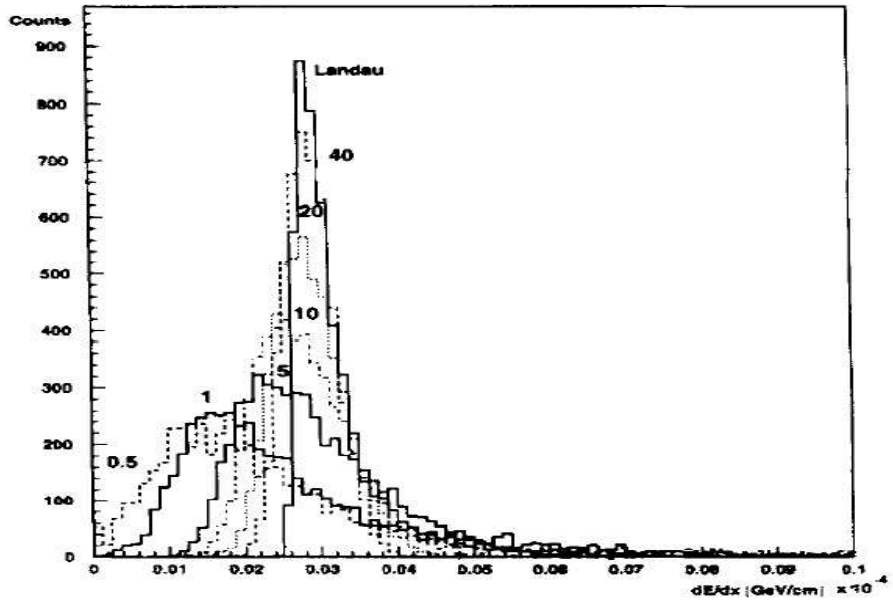

Figure 4.5: Energy loss distribution for a 3 GeV electron in argon as given by standard GEANT compared with the Landau. The width of the layers is given in centimeters.

This can be clearly seen in figure 4.5 where the energy loss for different widths of Argon is shown. From the figure we can see that with larger widths of gas, when the number of collisions becomes large enough, the distribution is more and more similar to the one expected by the Landau computation, using the Rutherford cross-section.

4.3 The energy loss simulation in GEANT4

4.3.1 The cross-section model

We showed that to describe the energy loss in thin material, such as a TPC, it is necessary to consider in the computation of the cross-sections between the fast particle and the matter, the internal structure of the atoms.
The most accurate model that takes into account the internal structure is the PAI model, that has the advantage of considering all the possible energy transfers with production of secondary electrons and photons. The problem of this model for the purpose of the simulation is that it makes the simulation chain very slow.
In GEANT4 as a default another model is instead used, the Urban model[79] that is based on a simpler model for the particle atom interaction that makes the simulation easier.
In this simplified model the atom is assumed to have only two energy levels, with binding energies E_1 and E_2. The interaction will then result either in an excitation with energy losses E_1 or E_2 or in an ionization with an energy loss distributed according to the function $g(E) \sim 1/E^2$.
A comparison between this model and the PAI model can be found in [79] and shows a good agreement between the two. In the following of this thesis this simplified model is used for the simulation and comparison between straggling function obtained using beam test data and the Monte Carlo simulation can be found in section 5.7.

4.3.2 The energy loss simulation chain

In the ND280 software, the simulation program, starting from the energy loss of a charged particle in the gas, up to the digitized signal in the front end electronics, proceeds in the following steps:

1. the energy released in each step along the particle trajectory is computed by GEANT4. The typical step length is of the order of few millimeters.

2. The energy lost E is transformed in a number of electrons n_e according to the formula $n_e = E/W$ where W is the mean energy necessary to create ion pairs introduced in section 4.1.2. For the TPCs gas mixture the value $W = 26.8\ eV$ has been used.

3. During the drift, attachment may take place. The attenuation length in the TPC was measured to be several meters, so the attachment is a minor effect and it does not occur in the simulation

4. Then the electronics response function is simulated. It depends on several parameters related to the ASIC AFTER electronics settings:

   (a) The conversion factor from electrons to number of ADC

   (b) The sampling frequency (40 ns in the default TPC configuration)

   (c) The shape of the electronic response, that is the typical time distance between the start of the signal and the peak (200 ns in the default configuration)

The last parameter that needs to be set is the gain of the MicroMegas modules. This parameter has been measured for each MicroMegas module at the test bench using a ^{55}Fe source. Results of the gain as a function of the MicroMegas voltage for different modules are shown in the next chapter (see figure 5.4).
To set this parameter in the Monte Carlo results from the TPCs beam tests have been used. We found that the value of the gain that maximizes the agreement between data and Monte Carlo is 1950 for a MicroMegas high voltage of 350 V.

4.4 The particle identification method

The TPC particle identification methods that we developed is based on the measurement of the truncated mean of the charge deposited in each track sample. The method is applied on all the reconstructed tracks and in this section we will describe it.
From this point we will use the ND280 reference system in which z is the beam direction, y is the vertical direction and x is the drift direction.

4.4.1 Cluster energy

The TPC raw data are processed with the ND280 reconstruction routines (see section 3.8.2). After the track finding, the first step is to produce clusters out of the signal on each pad of the readout planes. In the typical case of almost horizontal tracks, each cluster is composed of hits close together in space, in time and on the same Micromegas column. The total energy of the cluster (C_C) is computed from the sum of the charge of all the hits composing it. This measurement is the elementary building block of particle identification in the TPC. The corresponding gas layer crossed by a track is very thin and therefore the cluster charge presents the wide distribution discussed in the section 4.2.

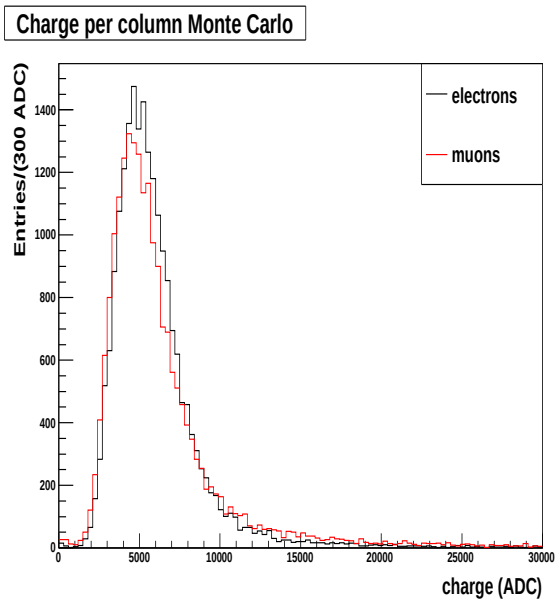

Figure 4.6: Cluster charge distribution in Monte Carlo for horizontal and monoenergetic electrons and muons with a momentum of $115 MeV/c$.

For a horizontal track crossing the TPC, 72 clusters are associated to it. However, in a typical neutrino interaction, particles can be emitted with large angles with respect to the beam direction. Some of the tracks will therefore have less than 72 measurements of the deposited energy and our algorithm takes this effect into account (the number of reconstructed points for tracks selected as muons coming from neutrino interactions will be shown in figure 8.9.
In this method we define the sample length (d) as the path length traversed by the track passing from one pad column to the next. For a track parallel to the readout plane, d is just the pitch of the readout columns, $d_0 = 9.7$ mm. The sample length depends on the local direction of the track and therefore may vary along the particle trajectory.
As the deposited energy and the shape of the distribution of the deposited energy depend on d, specific calibrations need to be applied to the cluster energy as discussed later. Notice that with real data also calibration factors depending on the external conditions (temperature, pressure, Micromegas HV etc) are applied. This simulation has been done with the gas temperature of 293 K, and pressure of 1 atm.
Studies of the dependence of the MicroMegas gain on the external pressure will be shown in chapter 5.

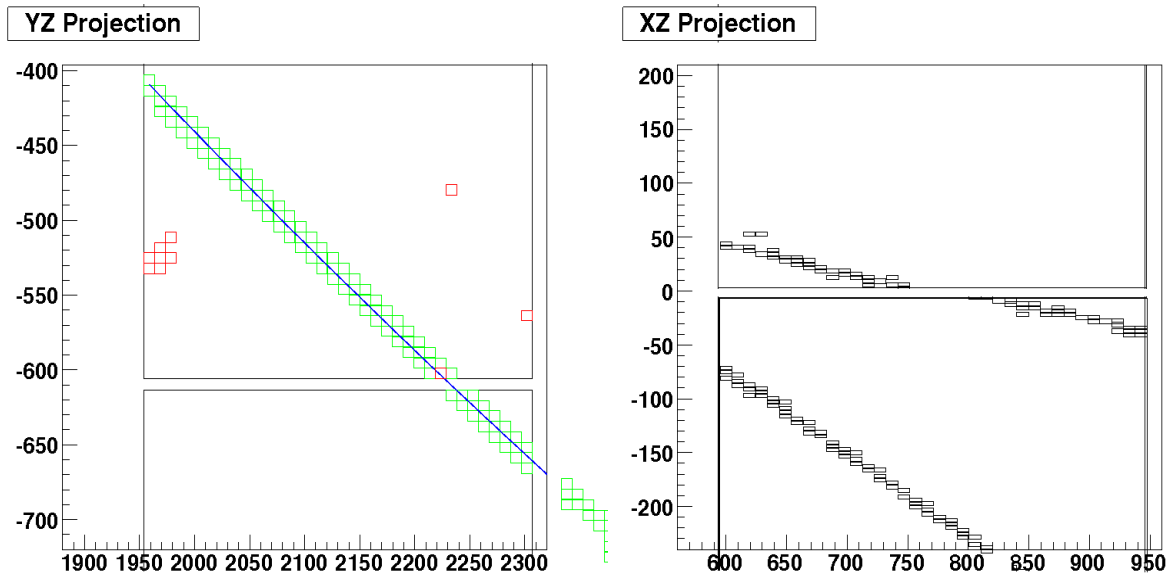

Figure 4.7: Event display showing a track crossing the dead zone between two MicroMegas modules (left) and with a track crossing the cathode (right).

4.4.2 Cluster selection

As it will be shown in 4.4.3, to perform the particle identification, we compute the truncated mean over a fraction of the clusters. Before computing the truncated mean a cluster selection is necessary, because some of the clusters will have less charge due to geometrical reason and they must be excluded from the truncated mean computation. In particular there are two effects that we must take into account and that are shown in figure 4.7.
The first one occurs when the primary electrons, produced by the crossing particle, arrive on the active region of the TPC in the gap between two MicroMegas modules (left event display of figure 4.7): between two modules there is a distance of 1.2 cm and electrons that drift towards this area will not give rise to an avalanche and the total detected charge in the cluster will be lower. In the case of a horizontal track reconstruction, by our definition of cluster (all the charge contained in one column), this effect takes place only at the horizontal edge of the MicroMegas modules (i.e. between two Micromegas modules in the same column) and not at the vertical one. The opposite happens in the case of a vertical reconstruction. To take into account this effect all the clusters that have the maximum amount of charge in one pad at the horizontal edge of one module are excluded from the computation of the truncated mean.

The second effect, shown on the right display of figure 4.7, occurs when a particle crosses the TPC cathode, moving from one drift region to the other. The cathode has a width of 13.4 mm and primary ionization occurring in this volume will not exit the cathode. For this reason the measured charge in the clusters will be lower. To take into account this effect we look at the X coordinate of the MicroMegas module with the maximum of the charge and if this coordinate changes from a column to the following one, we exclude the last cluster with the old coordinate and the first with the new one from the clusters used in the truncated mean computation.

4.4.3 The truncated mean method

The strategy that we adopt to perform the PID in the TPCs is the truncated mean method. The truncated mean energy deposit C_T per horizontal segment is:

$$C_T = \frac{1}{\alpha N} \sum_{i}^{\alpha N} C_C(i) \tag{4.42}$$

where $C_C(i)$ is the energy in cluster i, ordered according to increasing energy, N is the number of cluster energy measurements in the TPC and α is the truncation fraction.
The truncation is useful to cut the long tails of the charge distribution (visible on figure 4.6), resulting in a better resolution on the ionization and in our case also in Gaussian distribution of C_T. Discarding the measurements with the largest energy deposition corresponds to measuring a quantity closely related to the peak of the cluster energy distribution discussed in section 4.2. However, as we will show in the next sections, the limitation of C_T defined in equation 4.42 is that this quantity depends on the sample length, therefore on the track directions with respect to the pad plane and also on the number of samples used in the truncated mean. Our goal is to construct an estimator of the ionization with an expectation value that is independent of the sample length and the number of clusters. Therefore we define a calibrated truncated mean $\overline{C}_T$ in the following way

$$\overline{C}_T = \frac{1}{\alpha N f(N)} \sum_{i}^{\alpha N} g(d_i) C_C(i) \tag{4.43}$$

where $f(N)$ and $g(d_i)$ are calibration factors that depend on the number of clusters and on the sample length, respectively. By construction these factors are equal to unity for a horizontal track, defined as the reference track, parallel to the pad plane, whose projection in the pad plane is parallel to the longer pad side, and traversing the whole TPC. In other words, the measured energy loss of each track is re-calibrated to the corresponding quantity

for a track with 72 samples and angles equal to the reference track.
The assumption in this equation is that $f(N)$ and $g(d_i)$ can be factorized, as we will show in the next section. Non factorizable effects are expected to be small and will contribute to the systematic error of this measurement.
The task of the TPC PID is threefold as we need to:

1. compute the calibration factors $f(N)$ and $g(d_i)$;
2. compute the expected energy deposit C_E as a function of $\beta\gamma$;
3. compute the standard deviation σ_T of the distribution of $\overline{C}_T$ whose mean value is C_E.

Indeed with the knowledge of these quantities we can conduct any particle selection we wish, for instance by considering the probability that a particle of mass m and with the measured momentum gives the observed value of $\overline{C}_T$.

Analogously to the equation 4.43, we compute σ_T as

$$\sigma_T = \sigma_0 \xi(N) \zeta(d) \sqrt{\frac{C_E}{C_E(MIP)}} \tag{4.44}$$

where σ_0 is the Gaussian width for the MIP reference track with expected energy deposit $C_E(MIP)$, C_E is the expected energy deposit for a specific particle hypothesis, $\xi(N)$ and $\zeta(d)$ are calibration factors depending on the number of clusters and on the sample length, respectively. Notice that σ_T depends on $\beta\gamma$ through C_E and therefore for a given track for which the momentum has been measured, it depends on the particle type hypothesis that we have assumed.

4.5 Implementation of the method

4.5.1 The optimization of the truncation fraction

The truncation fraction α appearing in equation 4.43 has to be defined to optimize the resolution of the truncated mean measurement. Using a simulated sample of horizontal muons of 500 MeV/c, parallel to the readout plane, we found that the best energy resolution was obtained for a truncation fraction of 70% (figure 4.8). We find an energy resolution of 6.3% for these minimum ionizing particles (figure 4.9). This is in line with the truncation fraction used by previous experiments, typically in the range 70 to 80 % [49].

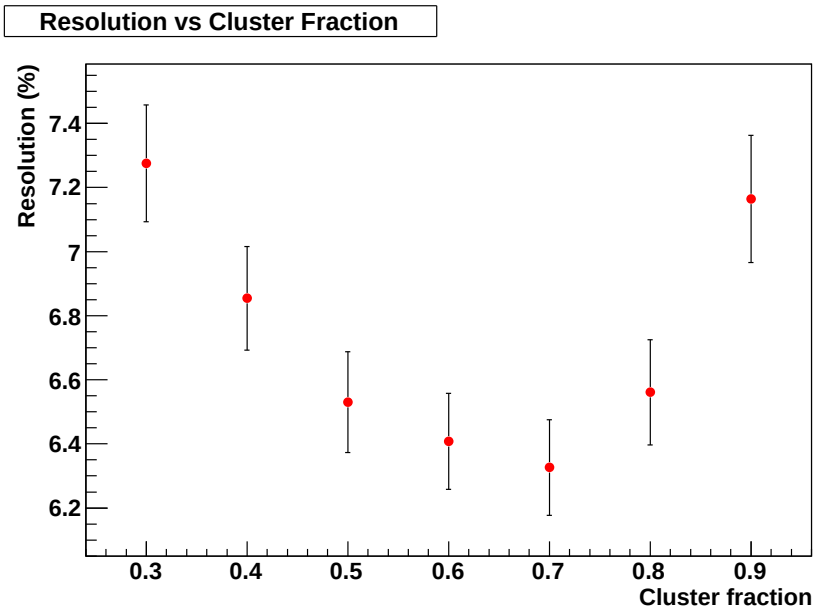

Figure 4.8: Energy resolution as a function of the truncation fraction for horizontal muons of 500 MeV

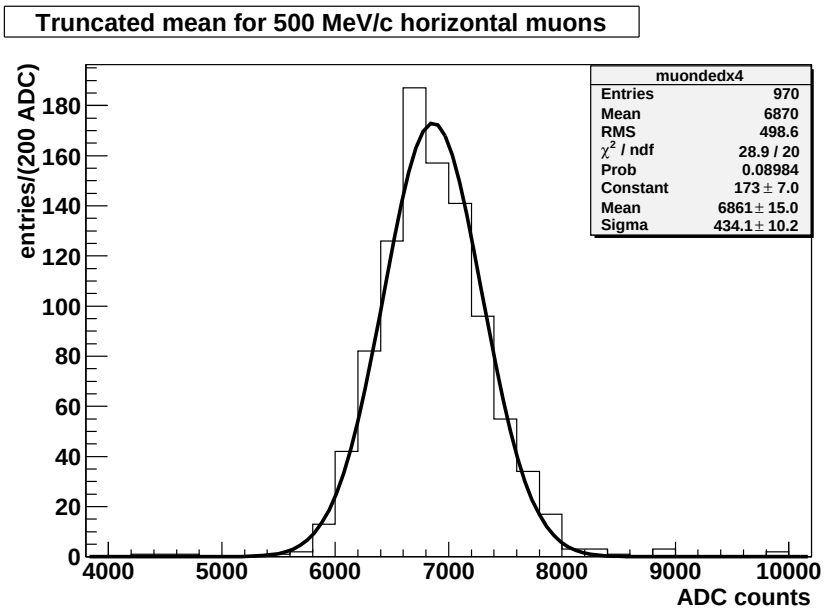

Figure 4.9: Calibrated truncated mean C_T for horizontal muons (momentum 500 MeV/c).

f_0	$(1.1 \pm 0.2) \cdot 10^{-4}$
f_1	$(2.3 \pm 0.5) \cdot 10^{-5}$
A_0	(-0.57 ± 0.02)

Table 4.1: Fit parameters for the number of samples calibration

4.5.2 Calibration of the number of samples

In the case of the T2K TPC the number of measurements for a track that crosses all the TPC is 72. Obviously there will be many particles produced in neutrino interactions that will exit from one side of the TPC, without crossing all the detector. In these cases the number of measurements will be less than 72 and the resolution on the deposited energy will be worse.
To study this effect samples of horizontal mono-energetic muons were used, computing the truncated mean using only a fraction of the total clusters. The number of samples used has been varied in the range between 24 and 72. In figure 4.10 the dependence of the truncated mean and of the Gaussian width of the distribution on this number is shown. A degradation of the energy resolution from 6% (using 72 measurements) to 11% (using 24 measurements) has been observed.
The relevant calibration factors for the truncated mean and the sigma, $f(N)$ and $\xi(N)$, have been parameterized according to the formulae

$$f(N) = 1 + f_0 \cdot (72 - N) + f_1 \cdot (72 - N)^2 \tag{4.45}$$

$$\xi(N) = (\frac{N}{72})^{-A_0} \tag{4.46}$$

and the resulting parameters are reported in table 4.1.

4.5.3 Calibration of the sample length

The calibration factor for the sample length $g(d)$ has been parameterized as

$$g(d_i) = \frac{1}{\sqrt{1 + (\tan\theta^i_{xz})^2 + (\tan\theta^i_{yz})^2}} \frac{1}{h(d_i)} \tag{4.47}$$

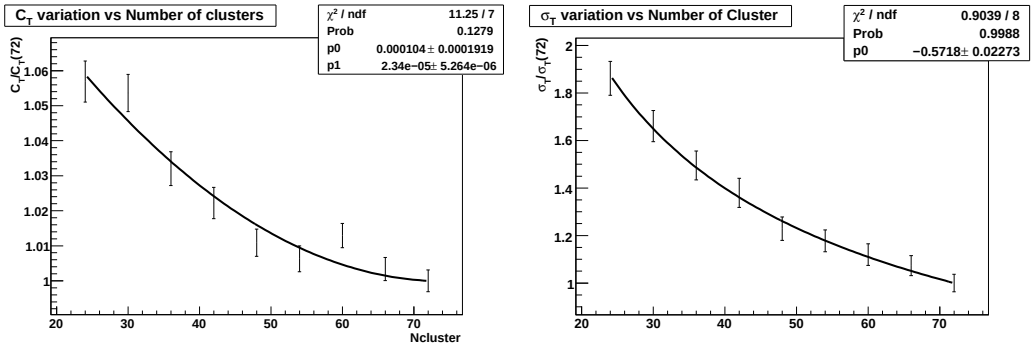

Figure 4.10: Relative variation of the truncated mean (left) and of the sigma (right) versus the number of samples

The first factor is inversely proportional to the sample length. There is an additional factor described by $h(d)$ taking into account that, with the truncated mean method, we are not measuring the average energy deposited per unit length given by the Bethe-Bloch formula but rather the peak of the distribution of the deposited energy. As it can be seen in figure 4.11, the peak over the sample length increases as a function of the width of gas crossed. This effect is related to what we previously discussed concerning the cross-section models: for a large width of gas the number of collisions per path length increases and so the fluctuation on the deposited energy becomes less important and the Landau computation is a better and better approximation of the reality. In the limit of infinite width of gas crossed what we should observe is a Landau distribution centered at the mean value of the distributions of figure 4.11.

This effect has been observed also in the Monte Carlo producing bent particles crossing the TPC (figure 4.12) and has been parameterized according to the formula

$$h(d) = 1 + h_0 \cdot (d - d_0) + h_1 \cdot (d - d_0)^2 \tag{4.48}$$

while for the Gaussian width the calibration factor is

$$\zeta(d) = \zeta_0 + \zeta_1 \cdot d \tag{4.49}$$

The parameters are reported in table 4.2.

We also observed in the Monte Carlo simulation (figure 4.13) that for electrons the shape of $h(d)$ is different from what is obtained for the other charged particles. This effect

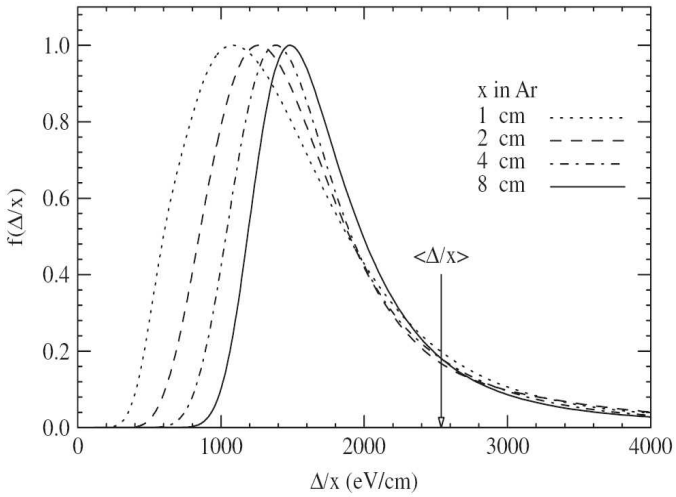

Figure 4.11: Straggling functions for different thickness of Argon. Notice that the abscissa is normalized to the gas thickness.

h_0	$(0.18 \pm 0.01)\ cm^{-1}$
h_1	$(-0.09 \pm 0.02)\ cm^{-2}$
ζ_0	(1.17 ± 0.07)
ζ_1	(-0.15 ± 0.05)

Table 4.2: Fit parameters for the sample length calibration

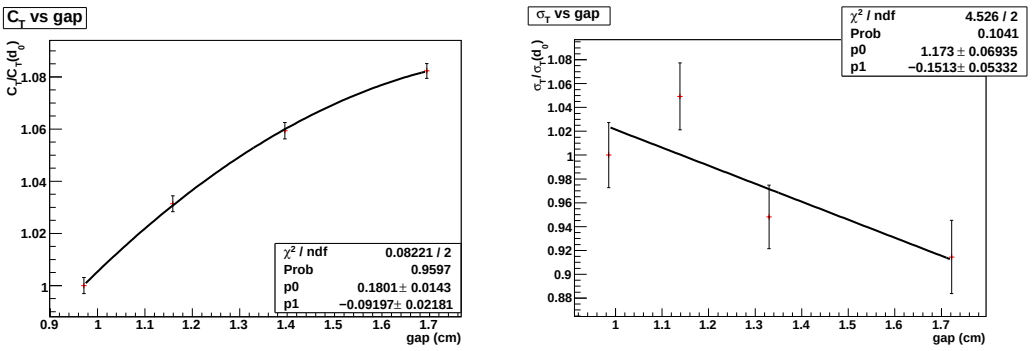

Figure 4.12: Relative variation of the truncated mean (left) and of the sigma (right) versus the sample length.

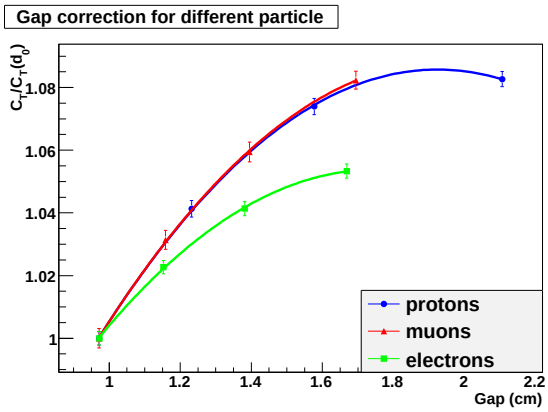

Figure 4.13: Relative variation of the truncated mean versus the sample length for electrons, muons and protons

is related to the differences in the ionization mechanisms between electrons and the others particles that cause different straggling functions for electrons. A more detailed study, using data and Monte Carlo, will be shown at the end of the next chapter.

4.5.4 Parametrization of the energy loss in the TPC

To perform the particle identification for a track it is necessary to compare the measured energy loss with the expected one for the different particle hypothesis. As it has been shown in the previous sections the expected energy loss, once calibrated for the sample length and the number of samples, is a function of only $\beta\gamma$.
This means that once the track momentum has been measured, knowing the mass of the particle, the expected energy loss is known if a parametrization of the energy loss curve has been performed. Notice that, also in this case, the curve is not simply the Bethe-Bloch curve, because we do not measure the average energy loss but rather the most probable energy loss.
To compute this parametrization, samples of different reference mono-energetic particles (electrons, muons and protons) with different momenta have been produced with the ND280 simulation program and for each sample the energy loss with the truncated mean method described above has been measured. For these tracks the calibration factors for the path and for the number of samples are equal to unity by definition.
The result is shown in figure 4.14, where the points with low $\beta\gamma$ (less than 1) correspond to protons, the points with intermediate $\beta\gamma$ (between 1 and 20) correspond to muons and those with higher beta gamma (larger than 500) correspond to electrons.

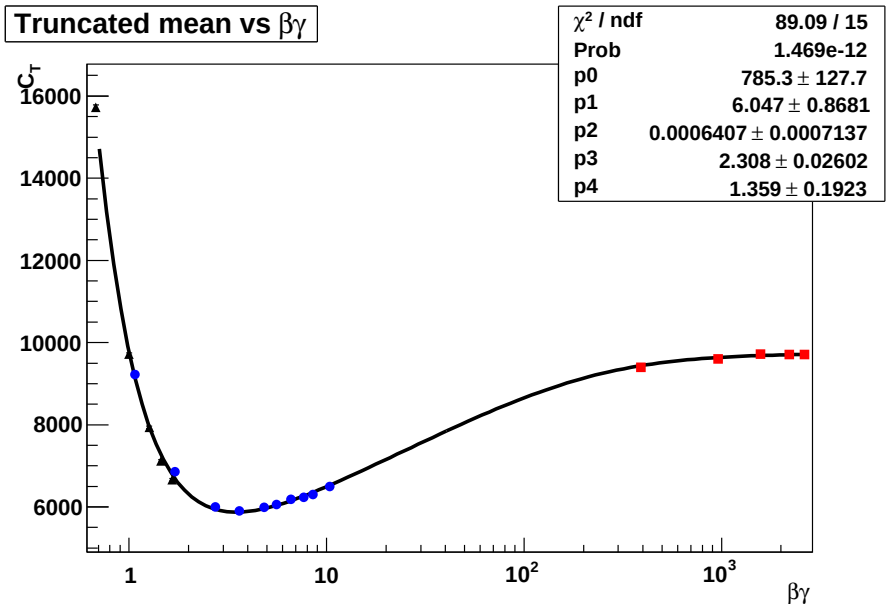

Figure 4.14: Deposited energy as a function of $\beta\gamma$: black points correspond to simulated protons, blue points to muons and red points to electrons

The curve has been parameterized according to the formula

$$C_E = \frac{e_0}{\beta^{e_3}} \cdot \{e_1 - \beta^{e_3} - log[e_2 + \frac{1}{(\beta\gamma)^{e_4}}]\} \tag{4.50}$$

and the fit parameters, e_0, e_1, e_2, e_3 and e_4 are reported in Table 4.3, while in figure 4.15 is shown the curve of C_E as a function of the momentum for the different particles.

Using this parametrization it is possible for each track, once the momentum has been measured, to compute the expected energy loss in the different particles hypothesis. For each reconstructed track in the TPC we compute the expected energy release for the 5 different particle hypotheses (electrons, muons, pions, kaons and protons) and then we define a pull δ_E to describe the distance between the expected and the measured value in the different cases. The pull variable is defined as

$$\delta_E(i) = \frac{\overline{C}_T - C_E(i)}{\sigma_o(i)} \tag{4.51}$$

e_0	(785 ± 128) ADC
e_1	(6.0 ± 0.9)
e_2	(0.0006 ± 0.0007)
e_3	(2.3 ± 0.2)
e_4	$1.4 \pm 0.2)$

Table 4.3: Fit parameters for the energy loss curve

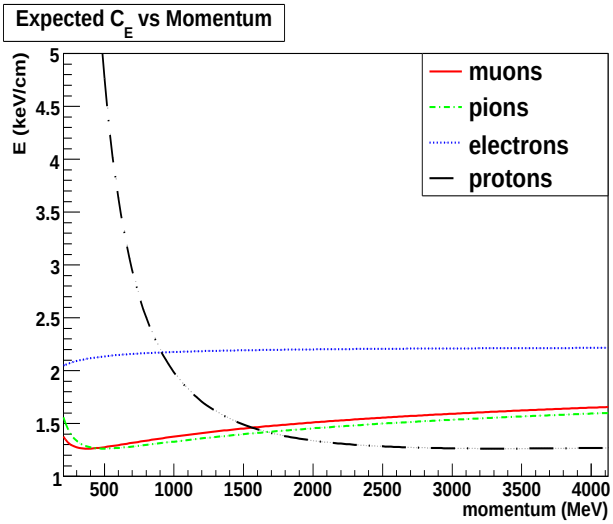

Figure 4.15: Expected energy loss (C_E) for different particles in the T2K TPC.

where i is the i-th particle hypothesis and $\sigma_o(i)$

$$\sigma_o(i) = \sigma_T(i) \oplus (dC_E/dp)\sigma_p \tag{4.52}$$

is the total width depending both on the variance of C_T, σ_T, and on the uncertainty in the momentum measurement σ_p. This second term is particularly important for particle with energy loss in the $1/\beta^2$ region where even a little shift in the particle momentum can bring a large difference in the expected energy loss. The width depends on the particle hypothesis i, because it is a function of the absolute value of the energy release according to the formula 4.44.

4.6 Particle identification validations

To validate the particle identification methods we simulated different particles in the TPC: we started using monoenergetic particles produced with different angles and momenta, then we also simulated neutrino interactions in the FGD and we analyzed the truncated mean for the tracks that entered the TPC.
Finally we also made a study of the resolution and the electron/muon separation.

4.6.1 Single monoenergetic particles

The first cross-check of the particle identification routine was done using samples of isotropic mono-energetic muons with a momentum between 300 and 1300 MeV/c. These particles were produced at the entrance of the TPC and for each reconstructed track the energy loss, calibrated for the path and for the number of samples was computed. To study the effect of the calibration, the pull has also been computed setting all the calibration factors to unity. As we can see from figure 4.16, once the calibration factors are considered, the pull distribution has a mean value compatible with 0 and a width compatible with 1.

Similar tests have been performed using samples of protons and electrons. In the case of electrons (figure 4.17), the sample length calibration seems to be overestimated. This is probably due to the presence of different ionization mechanism for the electrons that implies little differences in the dependence of the truncated mean on the sample length. This effect has been qualitatively observed also using the beam test data (see section 5.5).
In the case of the protons (Fig. 4.18), instead, the pull variance is larger than expected. As the proton curve in the T2K energy range is widely different from the curve of the other particles, this effect is not a serious problem for the identification of protons.

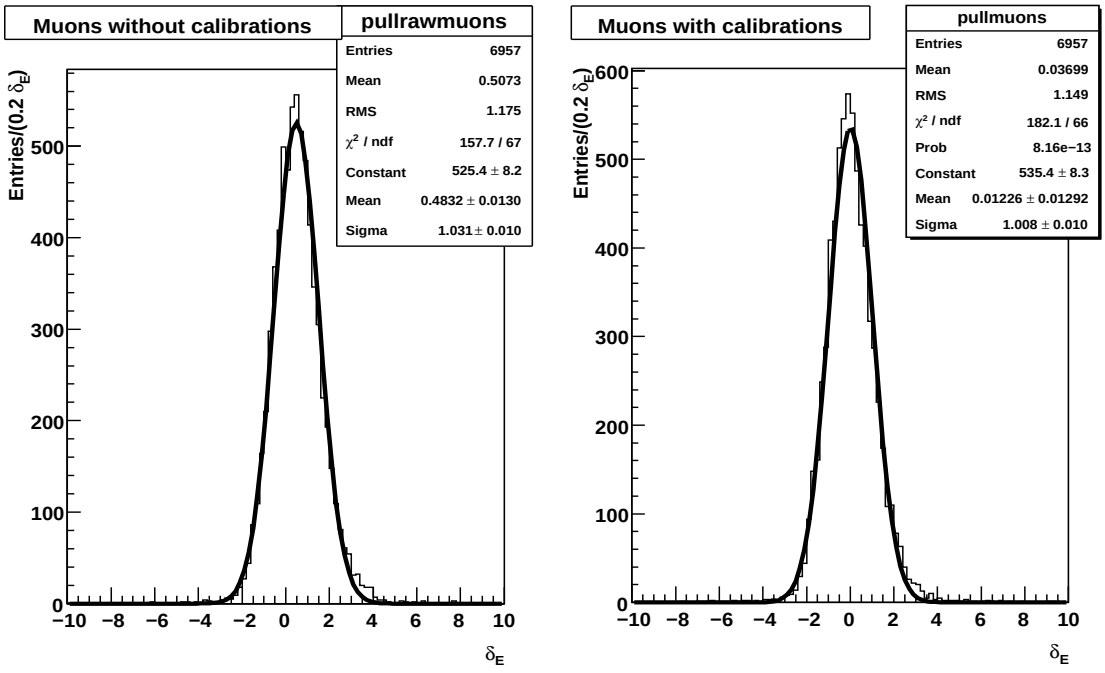

Figure 4.16: Pull plots for isotropic muons without (left) and with (right) the calibrations

4.6.2 Simulated neutrino interactions

To test the particle identification methods we also used simulated neutrino interactions in the FGD, measuring the calibrated truncated mean for each reconstructed track: the truncated mean versus the momentum (figure 4.19) and the pull distribution for the electron and muon hypotheses (figure 4.20) versus the momentum are shown.

As we can see with the particle identification method we can distinguish protons from muons and pions at momenta lower than 800 MeV/c and we can also distinguish the electrons from the muons and pions (the difference in the energy loss is of the order of 40% above 200 MeV/c). The pulls for the different particles are well centered in zero and the width are compatible with 1, with the exception of the electrons distribution that has a width of 1.5.

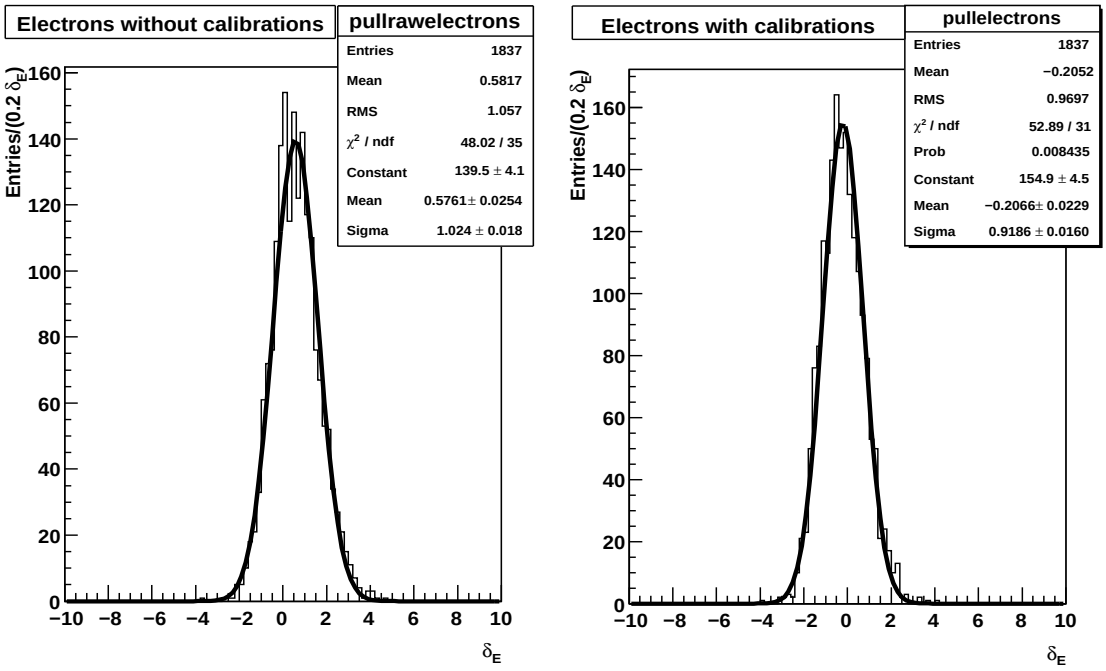

Figure 4.17: Pull plots for isotropic electrons without (left) and with (right) the calibrations

4.6.3 Particle identification performances

Finally we studied the performances of the particle identification routine in terms of resolution in the measurement of the deposited energy and electron/muon separation capability, that is the main reason of developing particle identification methods in the TPC. These studies were done using monoenergetic horizontal particles, electrons and muons, with momenta between 100 and 300 MeV/c. These momenta were chosen because it corresponds to the energy range of the particles during the M11 beam tests described in the next chapter.
For each sample we obtained the distribution of the truncated mean. In figure 4.21 it is shown the resolution on the deposited energy for the muons as a function of the momentum. The value of the resolution is below 7% in all the momentum range.

To study the separation between electrons and muons we defined the quantity N_σ as

$$N_\sigma = |\frac{C_E^\mu - C_E^e}{\sigma_T^\mu}| \tag{4.53}$$

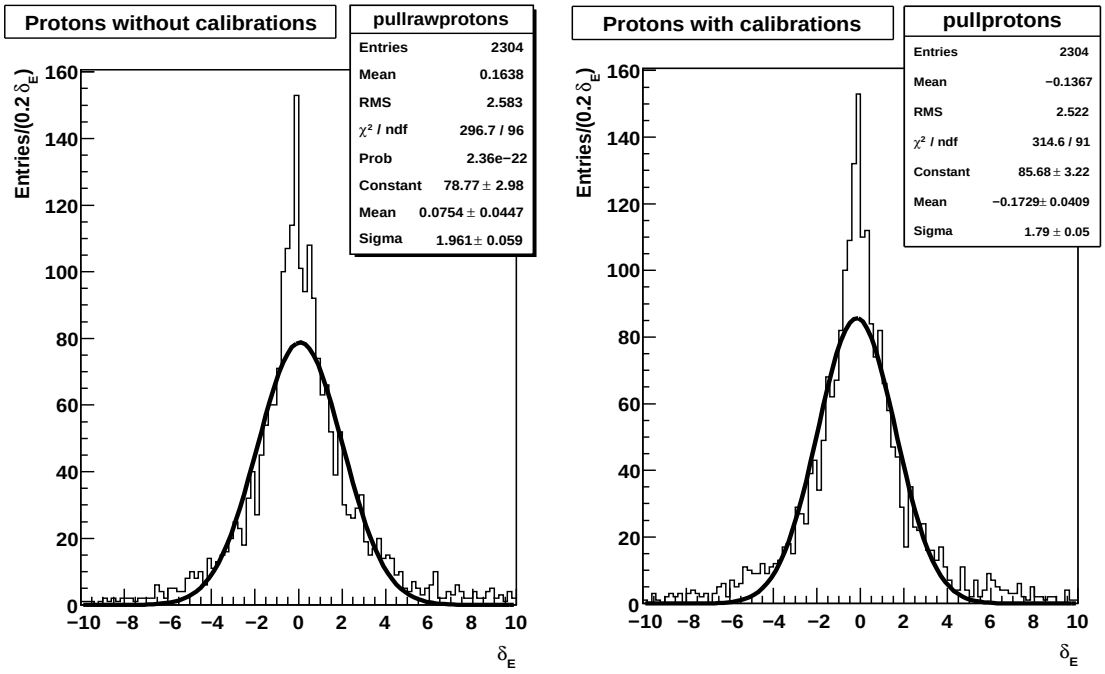

Figure 4.18: Pull plots for isotropic protons without (left) and with (right) the calibrations

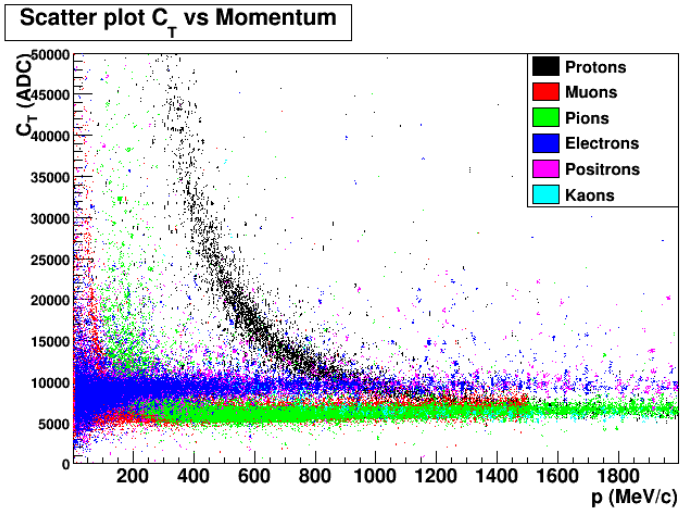

Figure 4.19: Truncated mean distribution C_T versus the reconstructed momentum for all the particles produced by neutrino interactions in the FGD and reconstructed in the TPC: on the left for particles with momenta between 0 and 5 GeV/c, on the right for momenta between 0 and 2 GeV/c

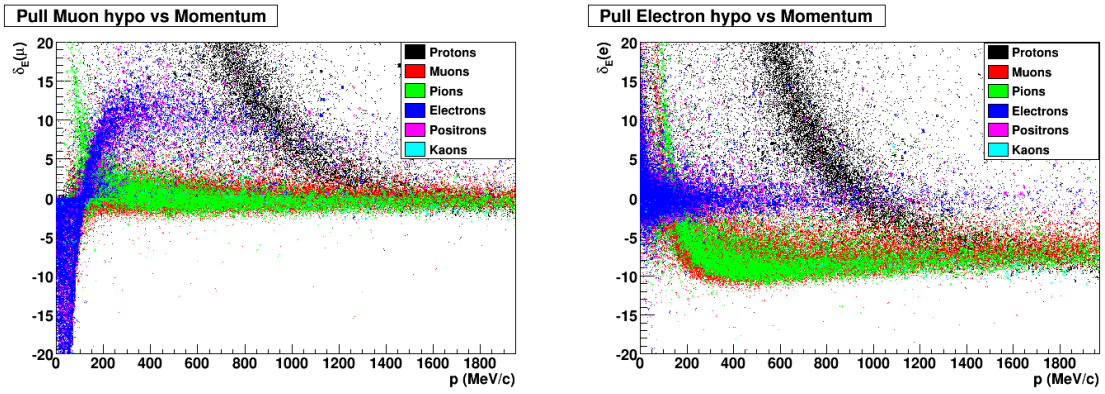

Figure 4.20: Truncated mean pull distribution in the muon and in the electron hypothesis as a function of the reconstructed momentum for all the particles produced by neutrino interactions in the FGD and reconstructed in the TPC

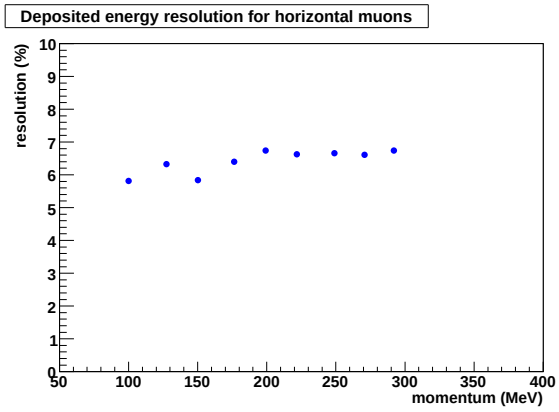

Figure 4.21: Resolution of the deposited energy measurement as a function of the momentum for monoenergetic horizontal muons

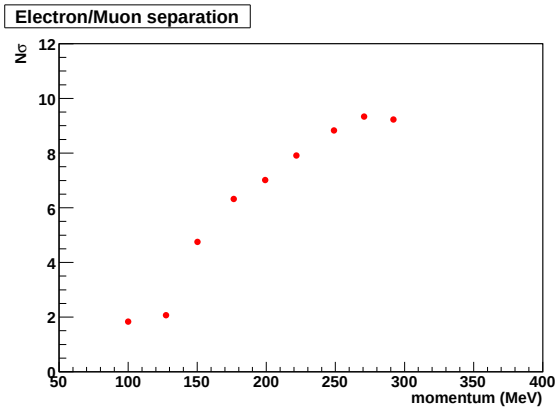

Figure 4.22: Electron/Muon separation as a function of the momentum for samples of monoenergetic horizontal particles

In figure 4.22 N_σ as a function of the momentum is shown. The separation between electrons and muons in the Monte Carlo simulation is larger than 5σ if the momentum is larger than 150 MeV and larger than 9σ at 300 MeV/c where the muons are near the minimum of the ionization.

Chapter 5

MicroMegas and TPC tests

During the preparation of this thesis and before the TPCs installation at Tokai, several tests have been performed to characterize and validate the MicroMegas and the TPCs.
In this chapter we will describe the observed performance; in the first part of the chapter we will describe the tests performed on the MicroMegas detectors and in the second part we will show the results of the tests done on the whole TPC, describing in particular its performance for the energy loss measurement necessary to perform the particle identification shown in chapter 4.

5.1 MicroMegas modules characterization

The MicroMegas modules used for the T2K experiment have been fully tested before being installed on the TPCs. All the 80 modules (72 installed in the TPCs and 8 spares) were characterized at CERN using a test bench.
Moreover to understand the performances of the MicroMegas detectors, in September 2007 one MicroMegas prototype has been installed in the field cage of the ex-HARP TPC experiment[81], and, using cosmic rays, it has been possible to study its spatial and energy resolution.

5.1.1 Test Bench at CERN

Immediately after the production the MicroMegas modules were characterized in a dedicated test bench at CERN (figure 5.1). During these tests the modules were mounted on a gas box made of $G10-FR4$ containing an aluminized mylar sheet as drift electrode and one

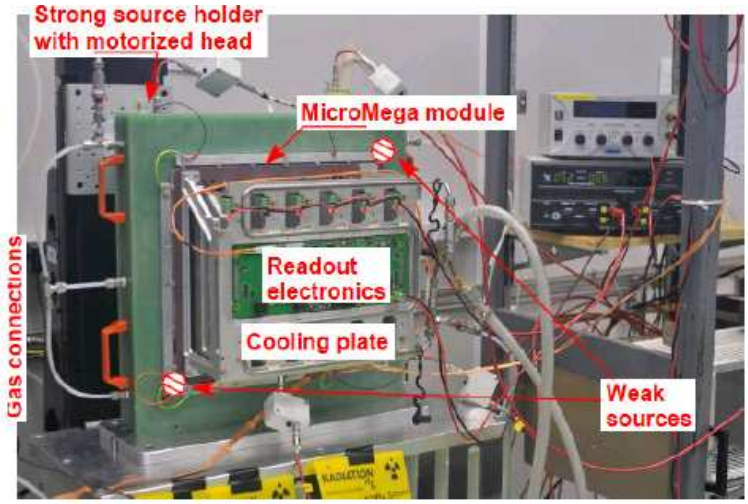

Figure 5.1: Setup of the Test Bench installed at CERN for the MicroMegas modules validation.

field strip to ensure uniform electric field for the 4 cm drift space. A 370 MBq ^{55}Fe source is placed on a (X,Y) motorized holder for pad-per-pad scanning over the whole active surface of the module. The iron source emits 5.9 keV photons that are absorbed by the Argon atoms. The electrons produced by these photons, under the influence of the electric field, cross the drift region and arrive on the MicroMegas surface producing avalanches. These signals allow to reconstruct pad per pad the energy resolution of the source. In figure 5.2 an example of the reconstructed spectrum is shown.

The purposes of the test bench were:

- Find faulty pads
- Measure the energy resolution using the 5.9 keV source
- Measure the pad per pad gain uniformity
- Determine the curve of the gain as a function of the voltage

For what concerns the faulty pads, only 12 faulty pads over 124272 channels were found, while the energy resolution for the iron source was of the order of 9% for all the modules with a good uniformity over the whole MicroMegas surface (the resolutions for a typical module are shown in figure 5.3). Also the gain was uniform over the MicroMegas surface, with a

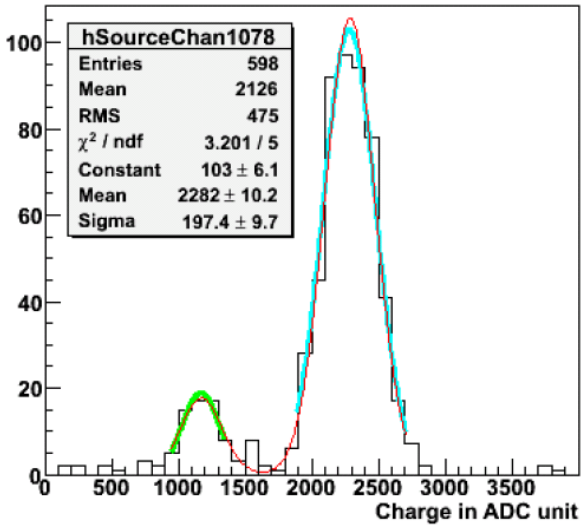

Figure 5.2: Spectrum of the ^{55}Fe source measured in one pad at the test bench.

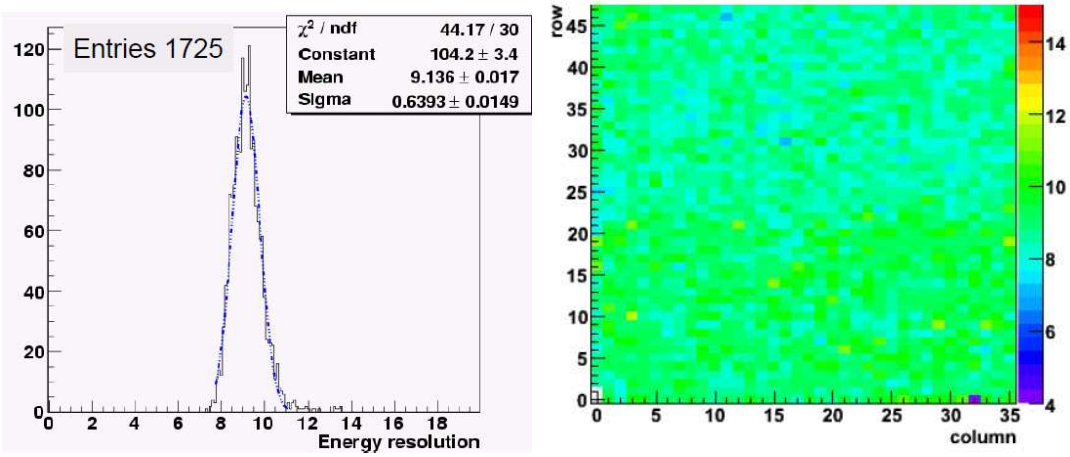

Figure 5.3: Left plot: energy resolution for the 5.9 keV photons for the 1726 active pads of one MicroMegas module. Right plot: two dimensional energy resolution map of one MicroMegas module.

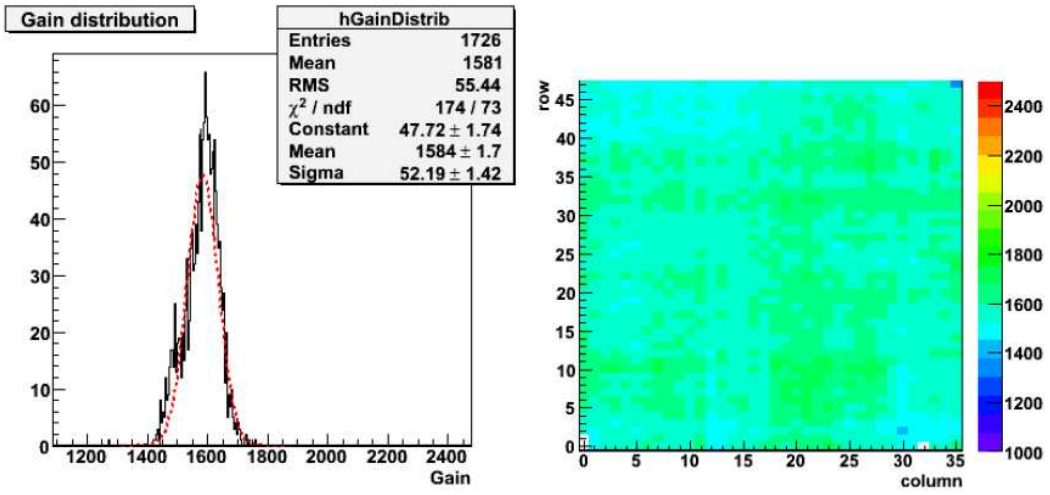

Figure 5.4: Left plot: typical gain dispersion for the 1726 active pads of one MicroMegas module. Right plot: two dimensional gain map of one MicroMegas module.

typical pad per pad spread of the order of 3% (figure 5.4).

Finally in figure 5.5 the curve of the gain as a function of the voltage is shown. At the working voltage of T2K (-350 V) a gain of 1650 is reached. The spark rate was measured to be of the order of 0.1 per hour and per module at the voltage of -350 V.

5.1.2 Cosmic test in the HARP field cage

In September 2007, a prototype of the MicroMegas detector was mounted in the ex-HARP field cage and cosmic rays data were taken. These tests were used to characterize and validate the performances of the MicroMegas module for the purposes of the T2K experiment and I performed the analysis of these data at the beginning of this thesis. The results of this tests can be found in [80].
During the tests the experimental setup consisted of the ex-HARP TPC field cage that is installed inside a solenoidal magnet. A description of the field cage can be found in [81]. Its dimensions are 80 cm of inner diameter and 154.1 cm in drift length, with the cathode set at a potential corresponding to an electric field of 160 V/cm. The field cage is mounted inside a solenoidal magnet, 90 cm in inner diameter with a length of 225 cm. A system of seven scintillators above and below the magnet provided the cosmic trigger signal.

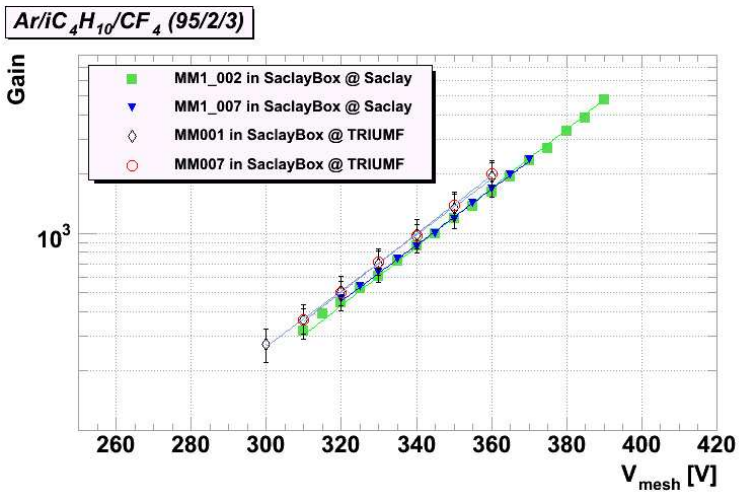

Figure 5.5: Curve of the gain versus the high voltage for different MicroMegas modules tested at the test bench.

The MicroMegas module was mounted on an aluminum endplate (see figure 5.6), covered on its inner surface by a large PCB and the module was read by the T2K Front-End-Electronic described in 3.6.

The tests lasted almost one month and have been performed with an $Ar : CF_4 : iC_4H_{10}$ (95:3:2) mixture, varying the MicroMegas voltages in the range $340-370\ V$ and the magnetic field in the range $0-0.4\ T$. Cosmic rays tracks are reconstructed and fitted, using the point reconstruction method (see section 3.8.2), separately in the two projections (one being the readout plane, the other the plane described by the vertical axis and the drift direction). A typical cosmic track as it is seen on the readout plane is shown in figure 5.7. Each cluster was defined considering all the charge contained in one MicroMegas row.
Also a ^{55}Fe source was installed on the cathode of the field cage. The energy resolution of the spectrum of the 5.9 keV photons emitted by source was of the order of 9%, in agreement with what has been measured at the test bench. A spectrum of the ^{55}Fe source is shown in figure 5.8 with superimposed the expected spectrum according to the Monte Carlo simulation.

On the left plot of figure 5.11 the distribution of the charge measured in a row is shown. As it is clear from the figure the distribution is not Gaussian. This is due to the mechanisms related to the energy release by a charged particle in the gas explained in chapter 4. This behavior, typical of all the gaseous detector, deteriorates the resolution of a single measurement and for this reason to perform the particle identification it is necessary to have

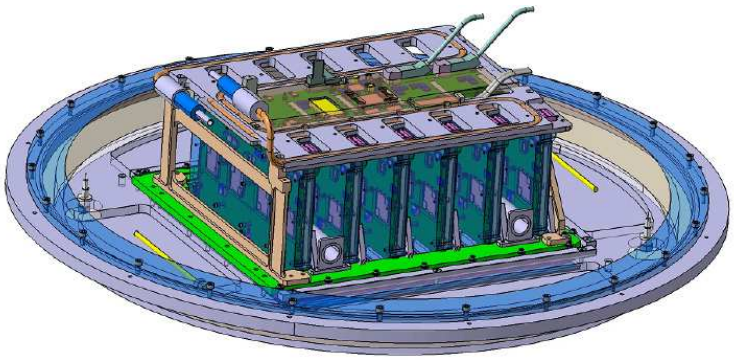

Figure 5.6: Experimental setup during the cosmic test in the HARP field cage: MicroMegas module with the 6 FECs, the FEM and the cooling system mounted on the endplate.

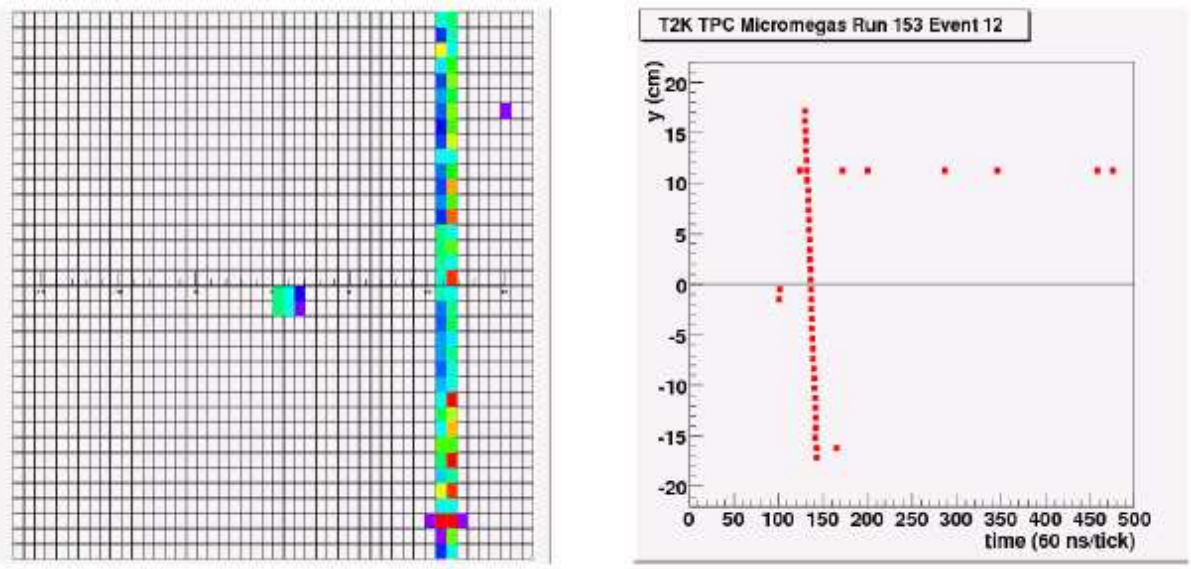

Figure 5.7: Event display of one event: on the left the event is reconstructed on the MicroMegas plane while on the right plot the vertical axis versus the time coordinate are shown. Each square corresponds to one MicroMegas pad and the long track is a cosmic ray while the hits in the center of the module correspond to one ^{55}Fe source event.

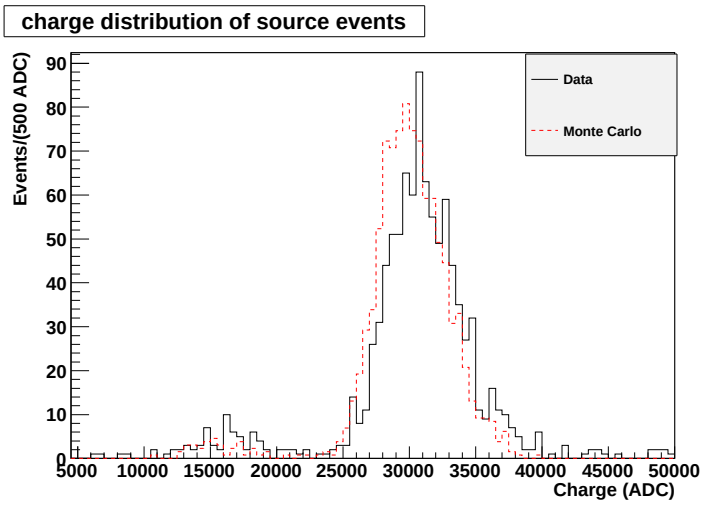

Figure 5.8: Reconstructed spectrum of the ^{55}Fe source for a magnetic field of 0.2 T and the electric field $E_d = 160\ V/cm$. The data are shown with a continued black line while the Monte Carlo simulation is represented by the red dashed line.

several charge measurements (72 in the case of the MicroMegas TPC) and then measure the truncated mean of the charge following the method described in chapter 4.
We measured the space point resolution considering the residual between the position of the cluster and the extrapolated track position without using this cluster. The cosmics were divided in bins according to their drift distance and the result, for the magnetic field of 0.2 T, is shown in figure 5.9. As expected, the resolution is better for clusters with more than one pad and decreases if the drift distance increases. We use as the reference value, the spatial resolution at a drift distance of 1 meter. The spatial resolution measured during these tests is 600 μm for 1 meter of drift. Using this value, the momentum resolution of the T2K TPCs can be extrapolated by the Gluckstern formula [52]:

$$\frac{\Delta_P}{P} = \frac{P(GeV/c)}{0.3} \frac{\sigma}{B(T)L^2(m)} \sqrt{\frac{720}{(N+4)}} \tag{5.1}$$

where σ is the point resolution, B the magnetic field, L is the length of the track and N is the number of measurements. In the T2K configuration, for an horizontal track, L is $\sim$ 70 cm, B is 0.2 T and N is the number of MicroMegas columns on one endplate, that corresponds to 72.
Using these values the expected momentum resolution results to be below 7% at 1 GeV,

better than the required performance of 10%.
The data have also been compared to a Monte Carlo simulation, where the entire experimental setup used during the test was simulated. As figure 5.9 shows, the data and the Monte Carlo simulation are in good agreement.
We also studied the gas properties using tracks that cross the field cage cathode or the endplate. Measuring the time difference between tracks that exit the cathode and tracks that hit the MicroMegas, gives a precise measurement of the drift velocity that resulted to be $v_d = (6.26 \pm 0.13)\ cm/\mu s$ for the electric drift $E_d = 160\ V/cm$, in agreement with the Magboltz prediction[60] ($v_d = 6.50\ cm/\mu s$).

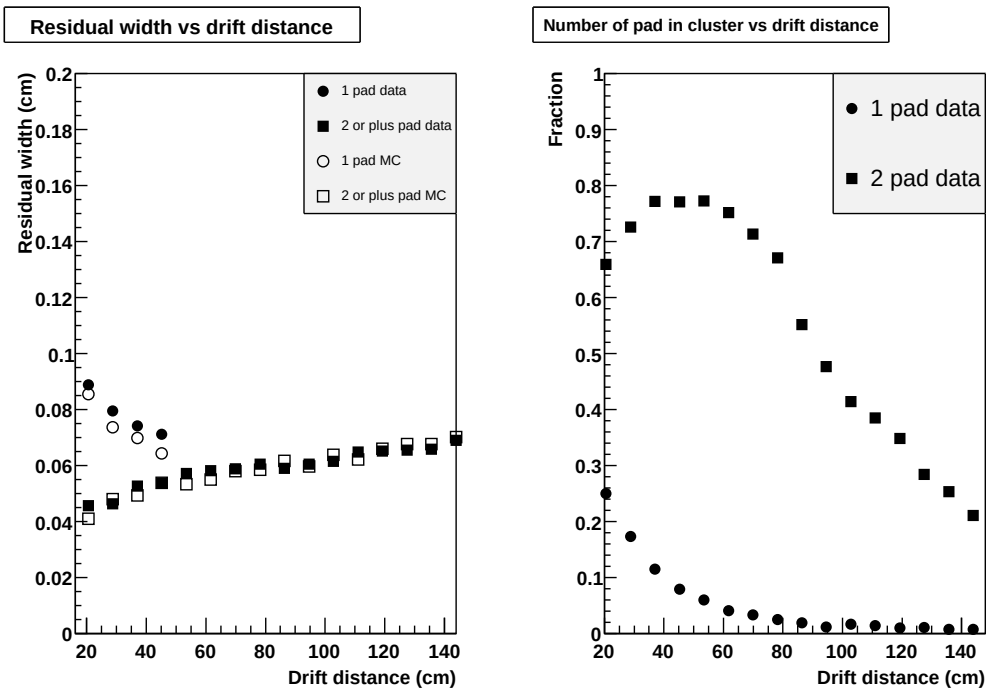

Figure 5.9: Left plot: gaussian width of the residuals for the clusters with one pad and two or more pads as a function of the drift distance for B=0.2 T. The open symbols show the width estimated using the Geant4 MC simulation. Right plot: the fraction of clusters with one pad (circles) and two pads (squares).

Then we measured the transverse diffusion coefficient, by measuring the width of the electron clouds as a function of the drift distance. The result for a magnetic field of 0.2 T is shown in figure 5.10. The points are fitted with the function

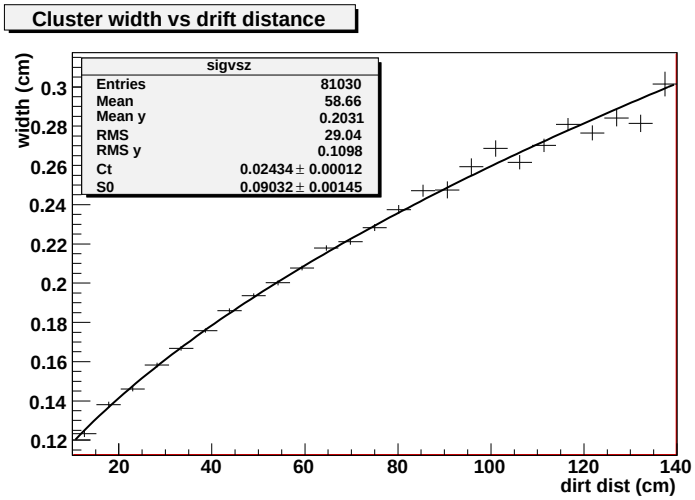

Figure 5.10: Width of the clusters as a function of the drift distance. The fit gives the value of the diffusion coefficient D_t

$$\sigma = \sqrt{D_t^2 z^2 + \sigma_0^2} \tag{5.2}$$

where D_t is the transverse diffusion coefficient, z is the drift distance and σ_0 is the value of σ for $z = 0$. The value obtained for a magnetic field of 0.2 T and an electric field of 160 V/cm is $D_t = (243 \pm 1)\ \mu m/\sqrt{cm}$, is in fair agreement with the value expected from the Magboltz prediction ($C_t = 237\ \mu m/\sqrt{cm}$).

Finally we performed a study of the energy deposited per unit length. We used a method similar to the one explained in the previous chapter, except that given the vertical cosmic direction, we considered for each track the charge detected in each MicroMegas row and we computed the truncated mean retaining the 80% of the samples with lower charge. During these cosmic tests, using track lengths of $\sim 36\ cm$ and 36 samples, we observed an energy resolution of $12.2 \pm 1.0\%$ for momenta between 700 MeV/c and 1 GeV/c (results are shown in figure 5.11).

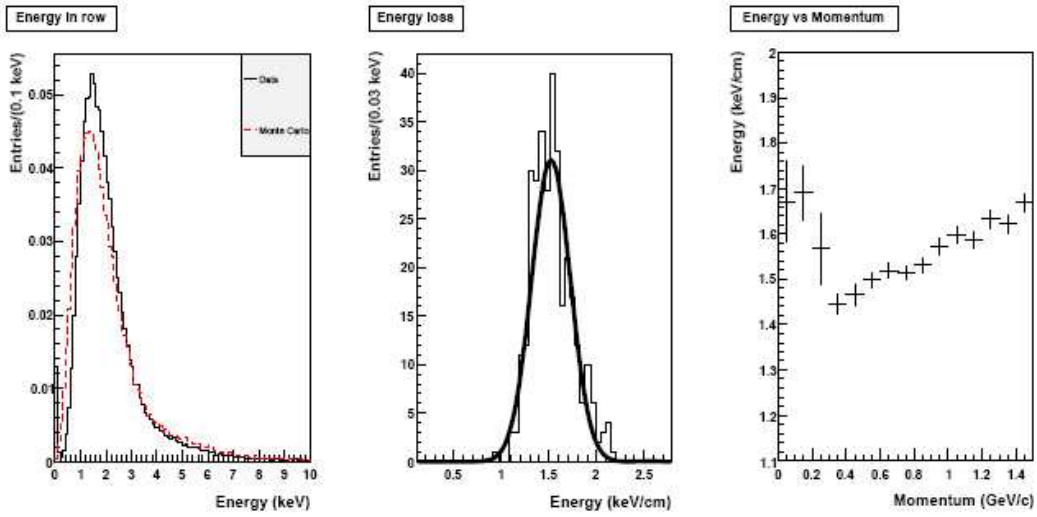

Figure 5.11: Left plot: the deposited energy per pad row for the data (continuous line) and the Monte Carlo simulation (dashed line). Middle plot: the 80% truncated mean for the tracks in the 0.7 to 1 GeV/c momentum interval. Right plot: measured energy deposit versus track momentum.

5.2 The TPC beam tests

After the TPC construction and the installation of the electronic, all the three TPCs modules underwent cosmic and beam test in the M11 area at TRIUMF, before being shipped to Tokai. The first TPC had two beam tests period, one in November 2008, with only four modules equipped with readout electronics, and one in April 2009 with all the electronics installed. The second TPC underwent beam test, with all the electronics installed, in July 2009 and the third one in November 2009. In this chapter we will show results obtained with the first TPC. The other two TPCs showed similar performances.
The M11 tests were used to check and debug the data acquisition chain and to perform quality checks on each TPC. In particular we used the beam test to study the capabilities of the particle identification methods described in the chapter 4 to identify the different particles. In figure 5.12 and 5.13 some pictures of the TPC in the M11 area are shown. During part of the test period also one FGD module was installed in the same beamline immediately downstream the TPC.

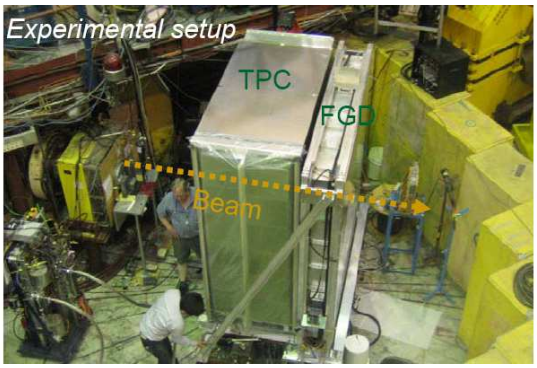

Figure 5.12: The experimental setup during the M11 test. The beam crosses before the TPC and then the FGD.

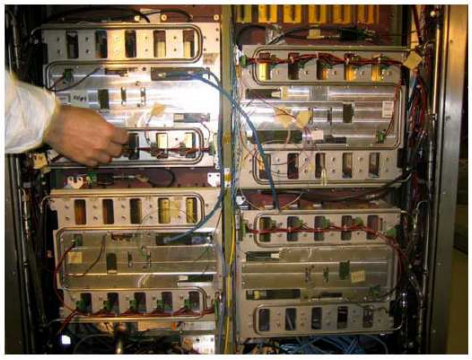

Figure 5.13: Four MicroMegas modules with their electronics installed on the TPC.

5.2.1 The M11 beamline

The M11 beamline is a secondary beamline of the TRIUMF facility. The main accelerator installed at TRIUMF is a cyclotron that produces 500 MeV protons, resulting from the injection of h^- ions. The cyclotron consists of a large magnet and two D shaped electrodes, separated by a small gap. The ions are bent by the magnetic field perpendicular to their velocity and are accelerated by the electrodes.
In this way their orbit increases until they reach the outer edge of the cyclotron. On the

edge stripping foils are installed and when the ions have the desired energy, they strike the foils and the electrons are separated by the ions, creating free protons that, moving in an opposite direction with respect to the negative ions, are extracted from the cyclotron.
Once extracted they travel to different experimental areas via different beam lines. Before entering the experimental areas, dipoles and quadrupoles magnets bend and focus the proton beam. In the case of the M11 beam line, at the entrance of the beam line, the protons hit a graphite target, producing a large number of mesons, in particular charged pions, that travel along the M11 beamline together with the protons. Then electrons and muons are produced into the beamline by the pion decays. During the beam tests the TPCs were installed at the end of the beamline. According to the processes described, a mixture of electrons, muons, pions and protons exit from the beamline. In their travel the particles encounter several magnets: the first selects the particle charge and in this way it was possible to have positive or negative particles. Obviously in this second case there were no protons in the beam.
Then the particles encounter a set of six quadrupoles. With appropriate settings it is possible to set the particles momentum, using the different curvature induced by the magnetic field to particles with different momenta. Using the quadrupoles it is possible to obtain a monochromatic beam with momenta up to 400 MeV/c.
Moreover a Time Of Flight system (TOF), composed of 3 scintillators, one inside the beamline (hodoscope scintillator), one upstream the TPC (front scintillator) and one downstream the TPC (back scintillator) allowed to select samples of different particles thanks to their different time of flight. In this way we could distinguish electrons, muons and pions for the majority of the momenta, obtaining a particle identification independent from the TPC output. The distance between the hodoscope and the front scintillators was 6.7 meters, while the back scintillator was installed $\sim$ 2.5 meters after the front scintillator. The time resolution of the TDC of the scintillators was 1 ns. A schematic view of the M11 beamline is shown in figure 5.14.

Two trigger combinations have been used during the tests: the first one is the coincidence between the hodoscope and the front trigger, while the second one is the coincidence between the front and the back scintillator. Due to the presence of the FGD that stopped low momentum particles, this second configuration was used only at high momenta. The TOF distributions in the two trigger configurations are shown in figure 5.15 and 5.16.
The particle composition in the beam is dependent on the momentum. In figure 5.17 the particle fractions observed as a function of the momentum are shown. Notice that at momenta larger than 250 MeV/c the pions were no more distinguishable from the muons and they were considered as a unique sample for the particle identification. This is not a big problem for the purposes of the study of the deposited energy resolution presented here, because, as it is shown in figure 4.15, at these momenta the two particles ionize almost in the same way.

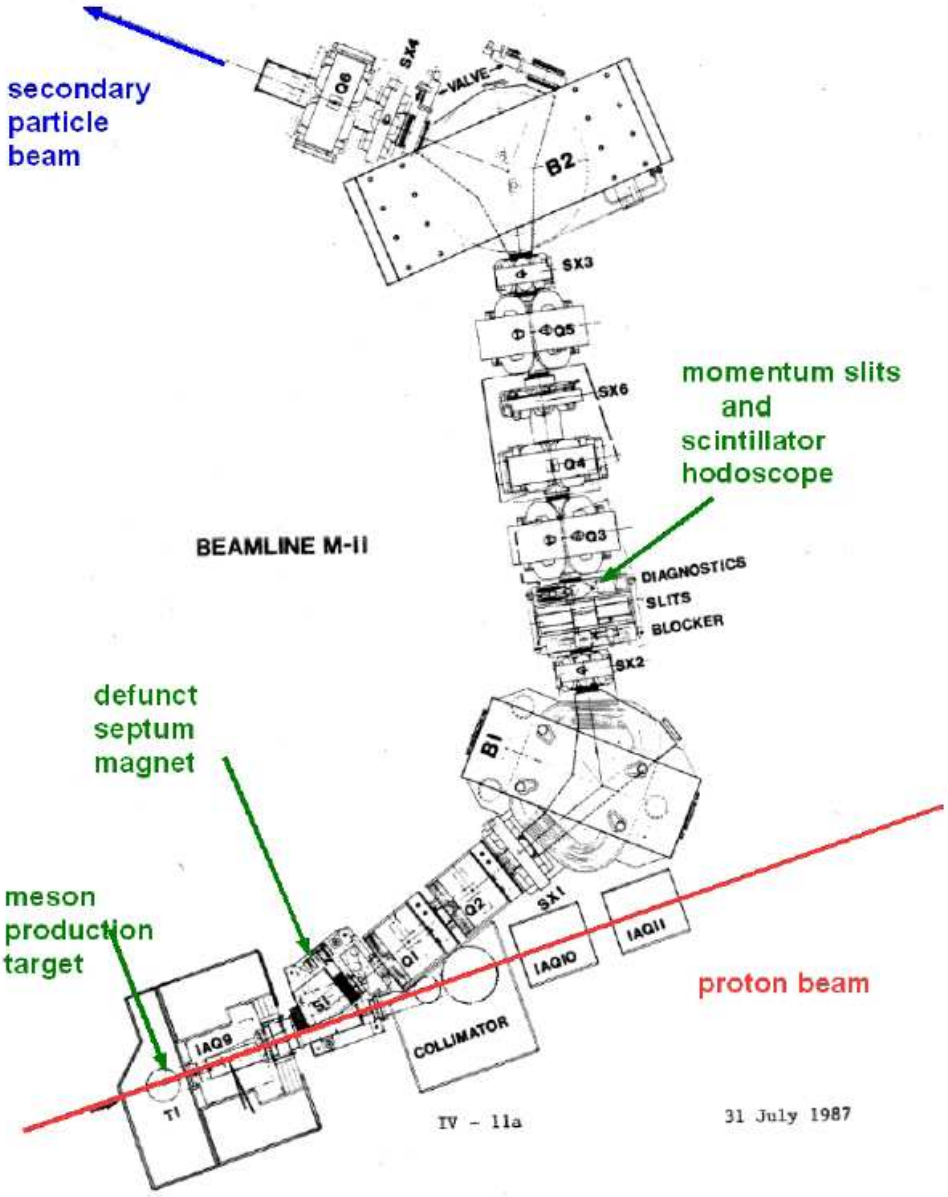

Figure 5.14: Schematic view of the M11 beamline: the hodoscope scintillator is indicated there, while the front and back scintillator and the TPC were installed at the end of the beamline, where the blue arrow is drawn.

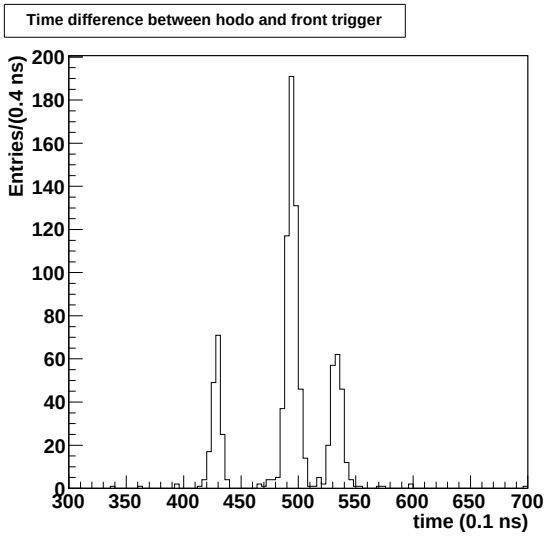

Figure 5.15: Difference between hodoscope and front scintillators time for particles with a momentum of 150 MeV/c. The peak on the left is produced by electrons, the central one by muons and the right one by pions.

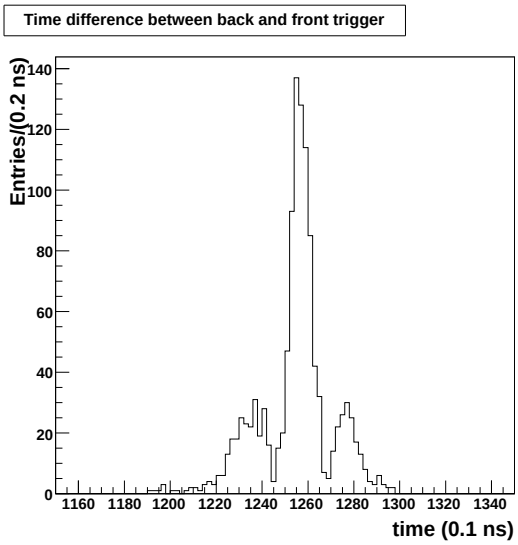

Figure 5.16: Difference between back and front scintillators time for particles with a momentum of 250 MeV/c. The peak on the left is produced by pions, the central one by muons and the right one by electrons.

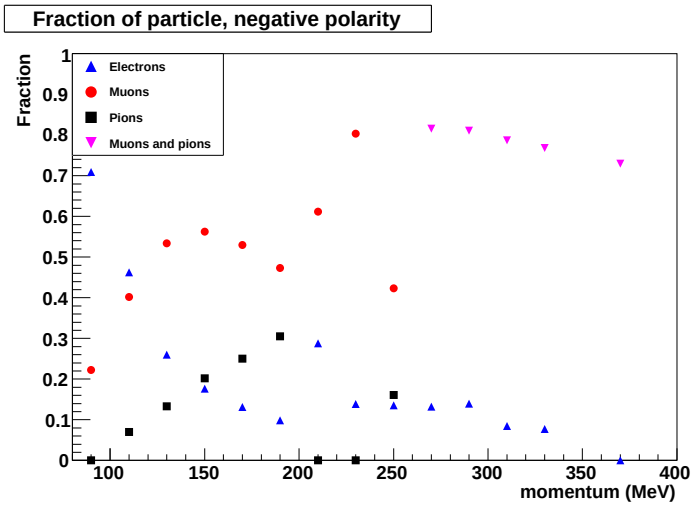

Figure 5.17: Beam composition as a function of the momentum obtained using the Time Of Flight informations. Below 200 MeV/c the trigger was given by front plus hodoscope scintillators, above 200 MeV/c front plus back scintillators were used.

5.2.2 The data taking: typical plots

During the tests the TPCs were filled with a mixture of $Ar/iC_4H_{10}/CF_4$ (95/2/3), that is the same gas mixture used during T2K TPCs operations and they were exposed to the beam with many different run conditions. Electronic settings, beam momentum, TPC position and angle were changed during the data taking. The beam was horizontal and mainly illuminated two MicroMegas modules. In figure 5.18 event displays of tracks observed in M11 are shown.

The cathode high voltage was set at a value of 25 kV, that corresponds to an electric field of 278 V/cm, while the MicroMegas high voltage was of 350 (or 360) V, that corresponds to 27 (or 28) kV/cm. The expected drift velocity in this configuration is 7.9 $cm/\mu s$. The electronics settings were changed during the tests: here we define as nominal parameters a shaping time of 200 ns and a sampling time of 30 ns.
The nominal TPC position was defined as the one in which the beam is in the horizontal plane, parallel to the MicroMegas. In this configuration the beam hits the center of the drift region, at a distance from the MicroMegas modules of approximately 45 cm. The reference system was defined as the one in which Z is the beam direction, Y is the vertical direction and X is the drift direction.
The M11 data were written to disk. After the data taking we reprocessed the raw data to transform them into the root format ready to be analyzed with the ND280 software, already described in 3.8.2 for the reconstruction part and in chapter 4 for the particle identification. We performed the analysis described here using this data format.
The track ionizes the gas and the charge drift to the MicroMegas surface. In the large majority of the events one track entered the TPC for each trigger, and it was reconstructed with 72 clusters (as it was described in 3.8.2); the majority of the clusters were composed by 2 pads. These distributions are shown in figure 5.19.

The typical charge distribution in each cluster is shown in figure 5.20. For each column we fitted the distribution with a Landau function and the Most Probable Value (MPV) of the distribution as a function of the column number is shown in figure 5.21. Even though, as we explained in chapter 4 the Landau model is not the best approximation of the ionization mechanism, a Landau fit of the charge per column distribution reproduces the data well enough and is a reliable way to monitor the correct functioning of the different MicroMegas pads.
As we can see the distribution of the MPV of the charge per column is stable along all the TPC. We can also see that in the first columns the MPV are slightly larger. This is probably due to some low momenta particles generated by interactions between the primary particles and the TPC internal walls.

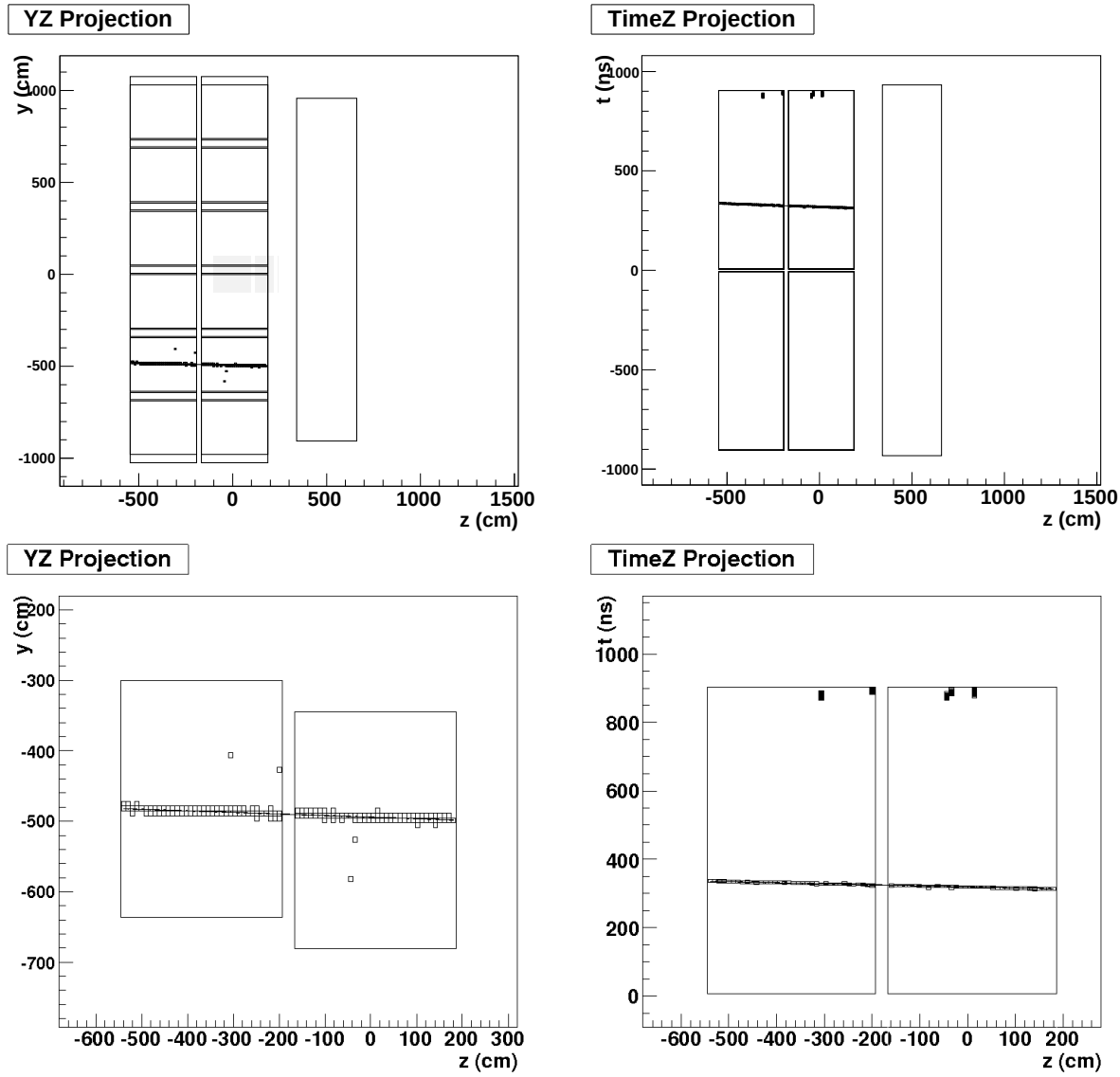

Figure 5.18: Event display of a typical track observed in M11 beam tests. On the upper plots the YZ (left) and the XZ (right) projections on the whole TPC Endplate, on the bottom plots the same projections with a zoom on the 2 MicroMegas (left) and on the endplate (right) hit by the particle.

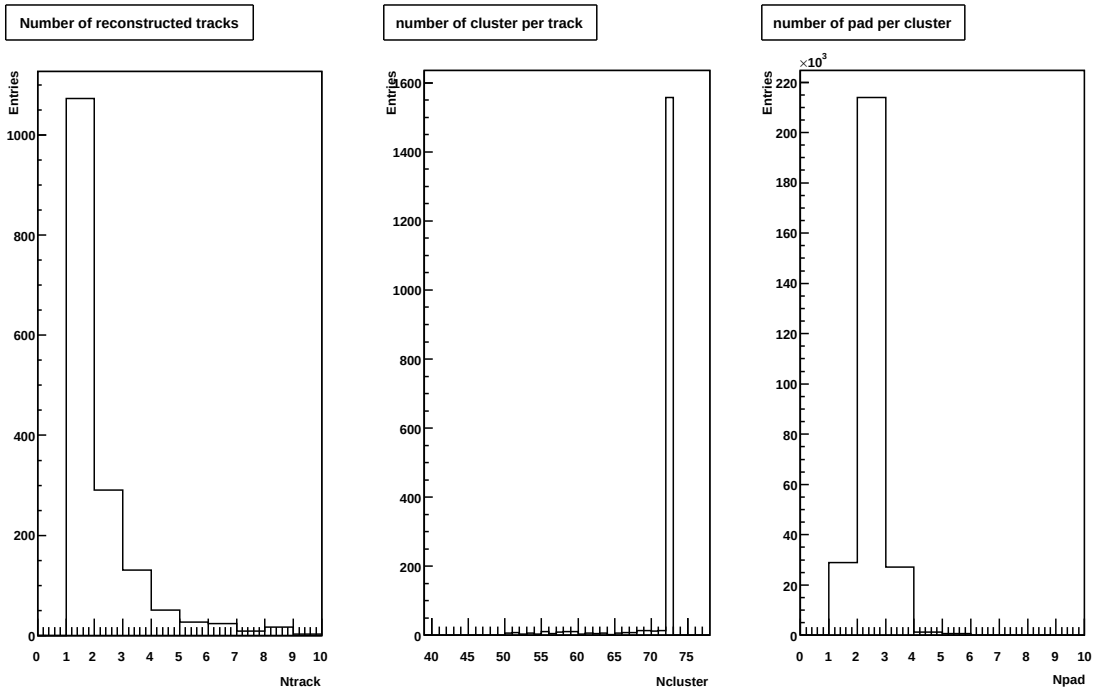

Figure 5.19: Number of reconstructed tracks (left), number of cluster in each track (center) and number of pads in each cluster (right) for data with the TPC in the nominal position and momentum of 150 MeV/c.

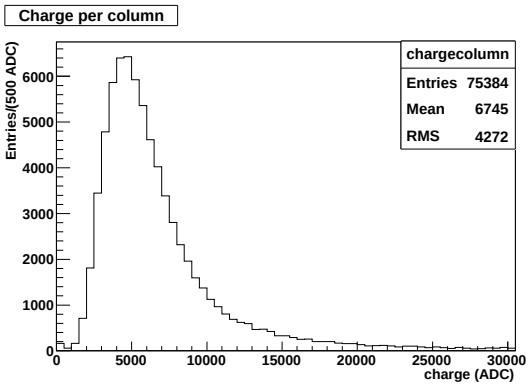

Figure 5.20: Charge per cluster distribution for data with the TPC in the nominal position and momentum of 150 MeV/c.

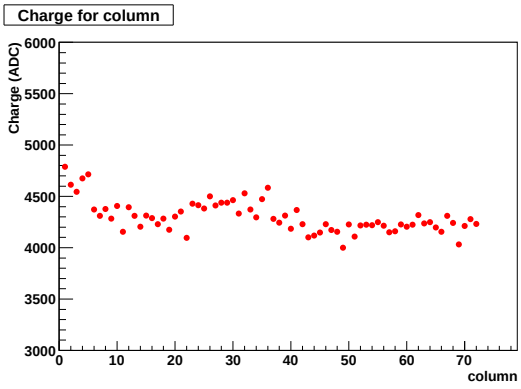

Figure 5.21: Most probable value of the Landau fit as a function of the MicroMegas column for data with the TPC in the nominal position and momentum of 150 MeV/c.

5.3 Energy resolution studies

With the M11 data we performed a study of the MicroMegas performances in terms of deposited energy resolution. To do this we selected, using the TOF, different samples of particles and we studied the energy resolution separately in the two MicroMegas modules and in the overall TPC, computing the truncated mean.
The method used to obtain the truncated mean was the one described in chapter 4 with the truncated mean defined as

$$C_T = \frac{1}{\alpha N} \sum_{i}^{\alpha N} C_C(i) \tag{5.3}$$

where $C_C(i)$ is the energy in cluster i, ordered according to increasing energy, N is the number of cluster energy measurements in the TPC and α is the truncation fraction (70% in our case).

5.3.1 Deposited energy on the different MicroMegas modules

As a first test we studied the resolution for the two different MicroMegas modules separately to look for possible differences between them. In figure 5.22 the distribution of the truncated mean C_T for a sample of muons of 150 MeV/c is shown separately for the two modules. In this case the truncated mean was performed using only 36 clusters for each measurement, that corresponds to the number of columns in one MicroMegas. The resulting deposited energy resolution is $(9.6 \pm 0.3)\%$ for the first module and $(10.6 \pm 0.4)\%$ for the second. The 5% gain differences between the two modules has been corrected in the following studies. In figure 5.23 the truncated mean distribution, for the same sample of particles, using all the 72 clusters is shown. In this case the resolution on the deposited energy is $(7.1 \pm 0.2)\%$. This value fully meets the requirement of measuring the deposited energy with a resolution better than 10%.

We also studied the dependence of the resolution on the truncation fraction α. With the Monte Carlo simulation we found that the truncation fraction that optimized the resolution was 70%. In the data, the dependence of the resolution from the cluster fraction, for the same sample of events of figure 5.23, is shown in figure 5.24: also in the M11 data the value that optimizes the resolution is 70%.

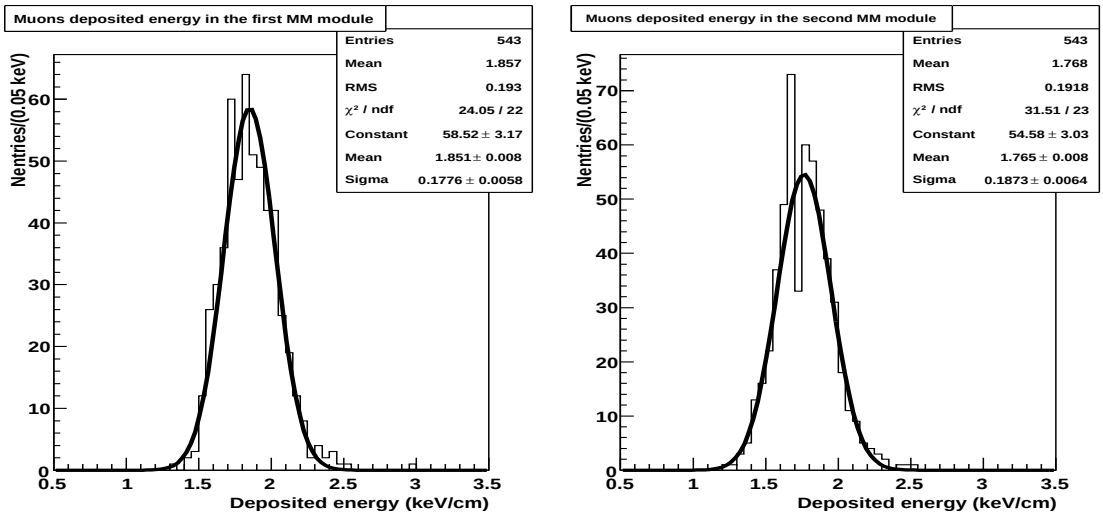

Figure 5.22: Deposited energy by muons of 150 MeV/c (run 3992) in the two MicroMegas modules.

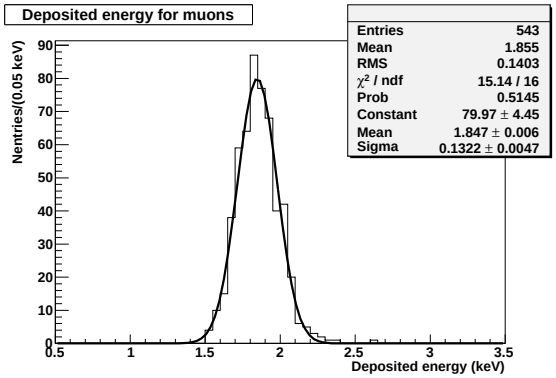

Figure 5.23: Deposited energy by muons of 150 MeV/c in the TPC.

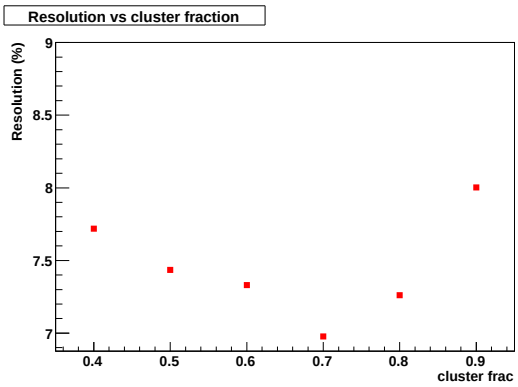

Figure 5.24: Dependence of the deposited energy resolution on the truncation fraction.

5.3.2 Deposited energy resolution for different particle samples

With the Time Of Flight it was possible to separate events in different samples according to the particle type. The beam composition, as it was obtained with the time of flight is shown in figure 5.17, here, in figure 5.25 we show the resolution on the truncated mean for electrons, muons and pions at 150 MeV/c. As we expected, thanks to the truncated method, the distribution for all the particles is well represented by a gaussian with a deposited energy resolution of $(7.1 \pm 0.2)\%$ for the muons, $(7.0 \pm 0.6)\%$ for the pions and $(5.8 \pm 0.4)\%$ for the electrons.

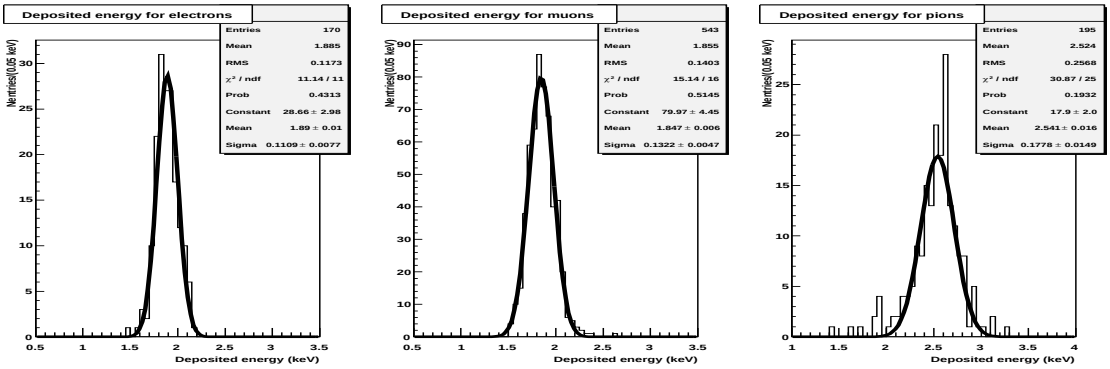

Figure 5.25: Deposited energy by electrons (left), muons (center) and pions (right) of 150 MeV/c crossing all the TPC.

5.4 Stability of the deposited energy measurement

Thanks to the precision of the measurement of the deposited energy we could also study the stability of the data taking analyzing runs with the same conditions taken at different times. It was also possible to study effects due to the absorption into the gas looking at data taken with different drift distances.
Before performing these studies we need to consider that the gain of the MicroMegas depends on the external pressure and it is necessary to correct for it. This correction can be computed by measuring the deposited energy for data taken with the same running conditions but different external pressure.

5.4.1 The correction for the gas pressure

A change in the gas pressure brings two main effects to the observed deposited charge: the first is a change in the number of electrons-ions pairs produced by the particle crossing the TPC gas. This number depends on the density of the gas and so depends on the pressure, increasing if the pressure increases.
But there is another effect that is important when a variation of the pressure occurs: an increase of the pressure decreases the mean free path of the electrons in the gas. In particular, in the MicroMegas amplification region, the total charge of the avalanche is directly related to the mean free path. A larger path will increase also the gain of the MicroMegas and so the measured truncated mean.
This latter effect, as it has already been observed in wire chambers experiments, is the dominant effect and the overall result is that the measured truncated mean decreases when the external pressure increases [49].
To study and parameterize this effect we need data taken at the same conditions and at different external pressures. For this purpose were particularly useful the data taken during the nights when the beam conditions and the electronic settings were not changed.
An example is shown in figure 5.26: here we can see the dependence of the measured truncated mean C_M on the external pressure, that varied between 1002 and 1007 mbar. According to this data we found that for a 1% variation of the external pressure, the MicroMegas gain varied by $(3.3 \pm 0.6)\%$.
Another measurement of the pressure dependence has been done using data taken during the tests performed with a MicroMegas prototype into the ex-HARP field cage (see section 5.1.2). During these tests a ^{55}Fe source was installed. This source continuously emitted 5.9 keV photons, that were reconstructed by the MicroMegas module on the opposite side of the field cage. In figure 5.27 we show the dependence of the gain from the external pressure for the ^{55}Fe source events. We observe a variation in the gain of $(3.1 \pm 0.3)\%$ for a 1% pressure variation. Notice that the two measurements do not represent the same effect as the number of electron-ion pairs produced by the photons emitted by the iron source do not depend on the pressure.

5.4.2 Stability of the data taking

Another interesting check that can be done using the measurements of the truncated mean is the stability of the gain. To do this check using the truncated mean measurements it is necessary to have data taken with the same conditions at different times. To test the stability with the same run conditions, we analyzed the deposited energy in the runs with the TPC in the nominal position at the begin and at the end of the data taking. In figure 5.28 we show, as an example, the mean value of the truncated mean distribution C_M for muons and electrons at a momentum of 250 MeV/c taken using the front plus back trigger.

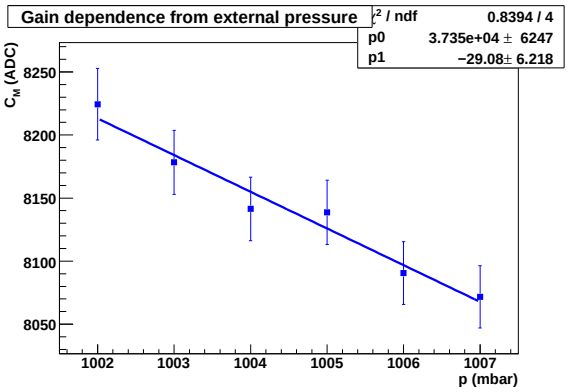

Figure 5.26: Dependence of the truncated mean C_T from the external pressure during the M11 tests.

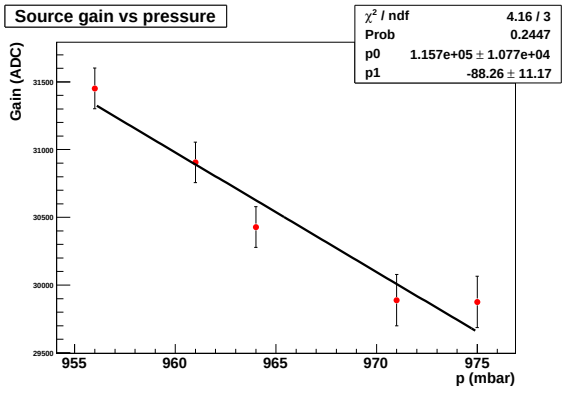

Figure 5.27: Dependence of the gain of the 5.9 keV γ emitted by the ^{55}Fe source during the MicroMegas tests in the HARP field cage.

After correcting for the external pressure the data are stable at the level of 1%, for both electrons and muons. The time interval between the first and the last set of points is one week.

5.4.3 Truncated mean dependence on the drift distance

The dependence of the truncated mean on the drift distance was also studied to check for possible absorption into the gas due to the presence of a too high quantity of oxygen. The oxygen absorbs the primaries electrons produced by the interaction of the charged particles with the gas and if in the gas there is too much oxygen its presence can be seen with the decrease of the signal when the drift distance is large. The presence of the oxygen in the TPC was monitored during the TPC beam test and a contamination of the order of 10 parts per million (ppm) was observed. This value is well within the accepted tolerances for the TPC.
To study this dependence we took data with the TPC in five different positions with drift distances of 15, 30, 45, 60 and 75 cm. The results for 2 different momenta, after the correction for the pressure, are shown in figure 5.29

As we can see from the figure no main effects were found in these data: further studies of this effect observed using cosmics will be shown in section 6.3.1.

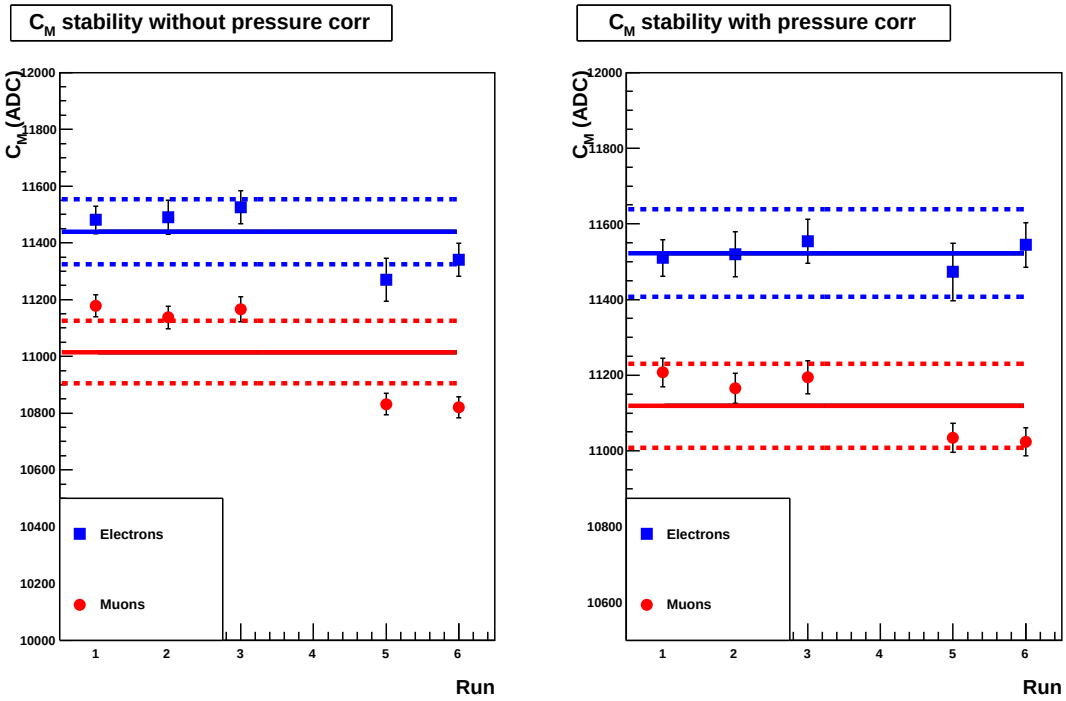

Figure 5.28: Stability of the mean value of the truncated mean measured for electrons and muons. The first three points are taken consecutively and the last two points are taken one week later. The continued lines correspond to the mean value of the truncated mean measurements while the dotted lines correspond to the mean value $\pm$ 1%. On the left plot the data are not corrected for the pressure while on the right plot the pressure correction is applied.

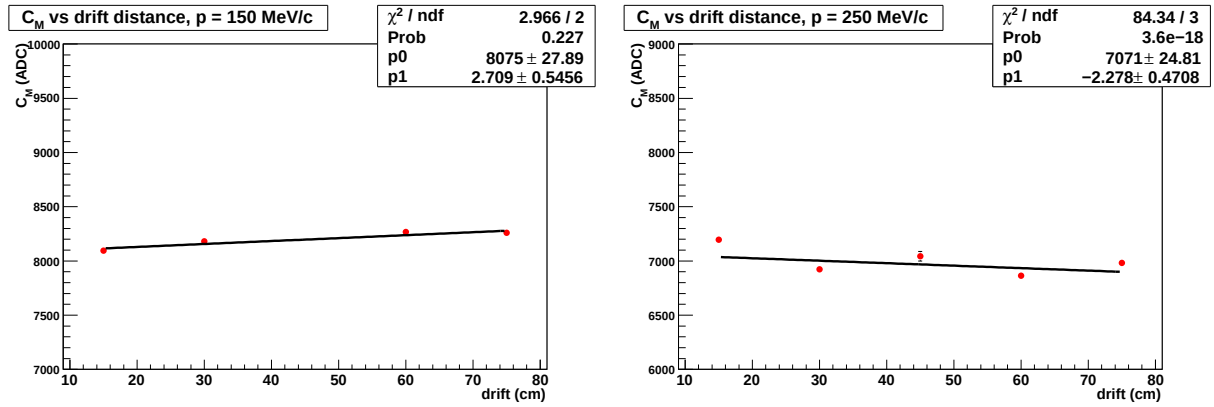

Figure 5.29: Dependence of the mean value of the truncated mean from the drift distance for particles of 150 MeV/c (left) and 250 MeV/c (right). On the X axis it is shown the drift distance, on the Y axis the observed truncated mean in ADC counts.

5.5 Calibration of the truncated mean

As we showed in the chapter 4, the mean value of the truncated mean C_M and the gaussian width σ_T depend on the number of samples over which the truncated mean is computed and on the sample length d, defined as the width of gas crossed by the particle passing from a MicroMegas column to the following one. Both these dependencies have been parameterized with the Monte Carlo simulation (see sections 4.5.2 and 4.5.3) and, as we will show in this section, have been checked with the M11 data.

5.5.1 Number of samples calibration

The dependence on the number of samples is important in the case of tracks produced by neutrino interactions that can cross only a part of the TPC before exiting from one side. This dependence can be simulated in the M11 data, using events with the TPC in the nominal position and computing the truncated mean using only a fraction of the 72 clusters. To take into account the differences due to the different gain of the pads we fitted with a constant the most probable values of the charge in the MicroMegas column (their distribution is shown in figure 5.21) and then, for each event and for each sample, we calibrated the charge measured according to formula:

$$\overline{C_C^i} = C_C(i) \cdot \frac{MPV(i)}{\overline{MPV}} \tag{5.4}$$

where C_C(i) and MPV(i) are the measured charge and the most probable value of the Landau fit in the i-th column and $\overline{MPV}$ is the mean of the most probable values of the 72 Landau fits.
This calibration should be applied pad per pad and not column per column but as the M11 beam always hits a well defined region of the MicroMegas modules, we can, in first approximation, apply the calibration in this way.
We changed the number of clusters used to compute C_T from 72 to 24 and in figure 5.30 the variation of the mean value of the truncated mean, of the gaussian width and of the deposited energy resolution as a function of the number of clusters used in the computation of the truncated mean is shown. The superimposed lines show the expected dependence according to the Monte Carlo simulation (see section 4.5.2).

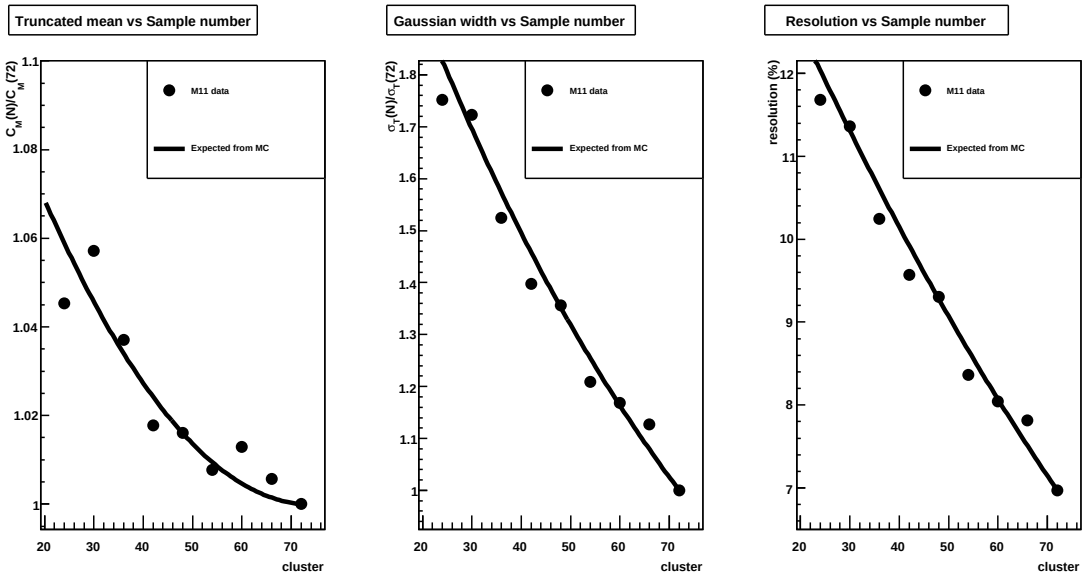

Figure 5.30: Dependence of the truncated mean (left), of the gaussian width (center) and of the resolution (right) on the number of samples. The superimposed line on the left and center plots is the expected dependence according to the Monte Carlo simulation.

The agreement between data and Monte Carlo is good and the resolution in the deposited energy measurement varies from 7.0% with all the 72 clusters, to 11.7% with 24 clusters.

5.5.2 Sample length calibration

As we showed in the section 4.5.3, the dependence of the truncated mean on the sample length is due to the fact that the peak of the distribution of the deposited energy does not scale linearly with the width of gas crossed by the particle (see figure 4.11). For this reason it is necessary to correct for the track angle and an additional parameter depending on the sample length, according to the formula 4.47 (see figure 4.12). With the M11 data we checked this parametrization measuring the truncated mean C_M after the correction of the charge deposited in each cluster for the track's angle:

$$a(d_i) = \frac{1}{\sqrt{1 + (\tan\theta^i_{xz})^2 + (\tan\theta^i_{yz})^2}} \tag{5.5}$$

Data has been taken with the TPC tilted by four different angles (0, 15, 30 and 40 degrees) with respect to the beam. These angles respectively correspond to a sample length d into each MicroMegas column of 0.97, 1.02, 1.14 and 1.27 cm.
In figure 5.31 the dependence of the deposited energy from the sample length in the data for two different momenta is shown, with superimposed the parameterized dependence in the Monte Carlo. We can clearly see the dependence from the sample length in the different particle sample. This dependence is in quite good agreement between data and Monte Carlo, with an underestimation of the dependence in the Monte Carlo of the order of 2%.

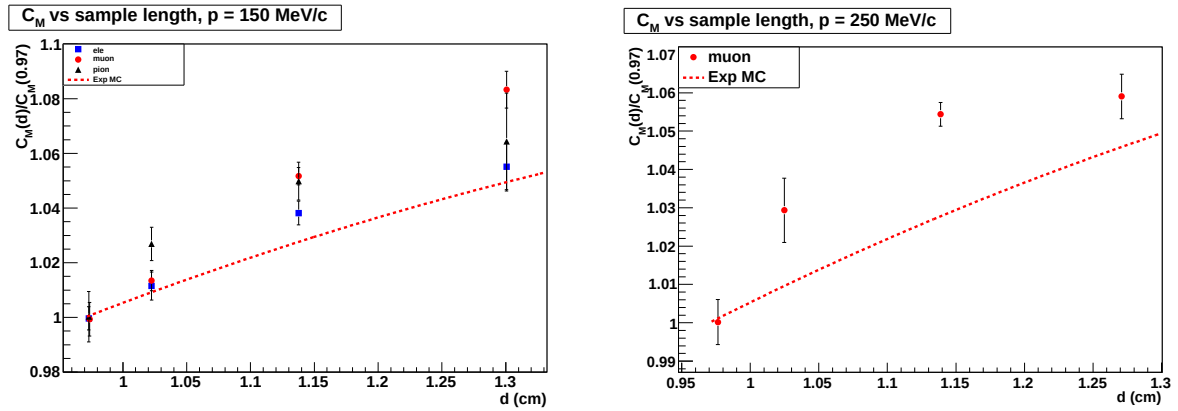

Figure 5.31: Dependence of the mean value of the truncated mean C_M from the sample length d for 150 MeV/c (left plot) and 250 MeV/c (right) and different particles. The superimposed lines represent the expected dependence according to the Monte Carlo simulation.

During the M11 beam test it was not possible to increase more the sample length because

only one endplate of the TPC was read and it was not possible to analyze more tilted tracks. An alternative way to change the sample length that does not imply changing the angle of the TPC, is to consider together the charge contained in n MicroMegas columns. In this way the sample length is

$$d_n = \frac{n \cdot d(0)}{a(d)} \tag{5.6}$$

and the charge contained in each measurement is

$$C_g^k = \sum_{i=k\cdot n+1}^{k\cdot n+n} C_C(i) \tag{5.7}$$

where C_g^k is the charge contained in each sample over which the truncated mean is computed and, if the track contains 72 clusters, the total number of energy measurements for the track is $72/n$.
We performed this measurement using $n = 1,\ 2,\ 3$ on the M11 data and on simulated events at 4 different angles. According to the total number of energy measurements we applied the calibration for the number of samples described in section 5.5.1. The results for the muon samples, are shown in figure 5.32 and we can see that also at larger sample lengths the agreement between data and Monte Carlo is good.

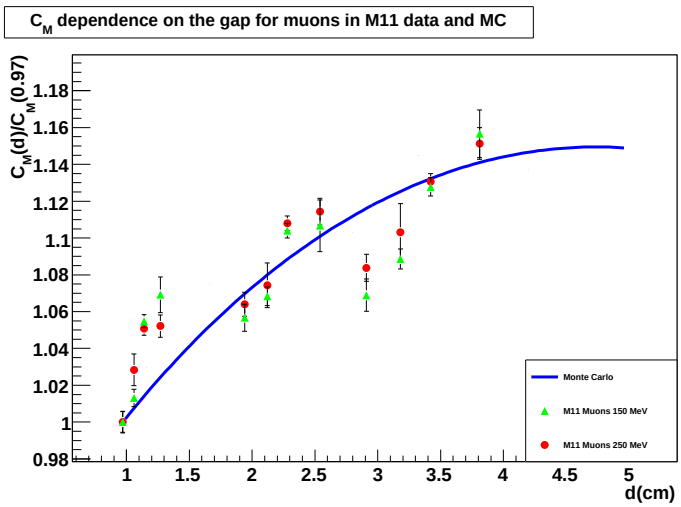

Figure 5.32: Dependence of the mean value of the truncated mean C_M on the sample length d for different angles and different numbers of columns in M11 data and Monte Carlo.

5.6 Dependence of the deposited energy on the particle momentum

In the previous chapter we showed how the energy loss in the gas depends on the particle momentum and mass and how we parameterized the curve using Monte Carlo data. Using the M11 data it was possible to analyse this dependence, taking data at different momenta with the TPC in the nominal position. The momentum step between two sets of data was 20 MeV/c.
Before comparing Monte Carlo and data some precautions have to be taken: in fact, looking at the time of flight distribution we observed that, in the M11 data, there was a shift of 15 MeV/c between the nominal momentum and the real momentum that the particles had when they entered the front scintillator. This shift was due to the failure of one of the magnet into the M11 beamline and the value of the shift has been measured using the Time Of Flight[82]. Moreover, before entering the TPC active region, the particles lose momentum crossing the front scintillator ($\sim 1.5\ cm$ of carbon) and the external materials of the TPC, composed by 0.32 cm of Aluminium and 2.48 cm of Rohacell. In these materials, a minimum ionizing particle loses $4.8 \pm 0.4\ MeV/c$ of its kinetic energy while a generic particle i loses

$$\Delta E_i = 4.8(MeV/c) \cdot \frac{C_M^i}{C_M^{MIP}} \tag{5.8}$$

In the following studies these shifts have been taken into account and the momentum of each data sample is not the nominal one but it is the one that the particles have when entering the TPC.

5.6.1 Resolution at different momenta

One of the requirements of the T2K TPCs is to measure the energy deposited by a track with a resolution better than 10% at the typical T2K beam energy. We have already shown in sections 5.3.1 and 5.3.2 that the resolution on the deposited energy for the different samples of particles was better than 10%.
Using the data taken during the momentum scan we measured the deposited energy resolution for the muons samples at different momenta. The measured resolution, shown in figure 5.33, is better than 8% for all the analyzed momenta except for two points, at 250 MeV/c and 270 MeV/c where the resolution is slightly worse but below the 9%. The worst resolution for that two momenta, is explained by the fact that, at momenta larger than 250 MeV/c it was impossible, using the Time Of Flight, to distinguish muons from pions and so these particles were considered together in the computation of the truncated mean. This can slightly

degrade the resolution, in particular at momenta of 250 MeV/c, where the expected energy loss for muons is different from the one of pions, while at higher momentum the two curves are almost coincident and the resolution of the measurement is not degraded by considering them together (see figure 5.34).

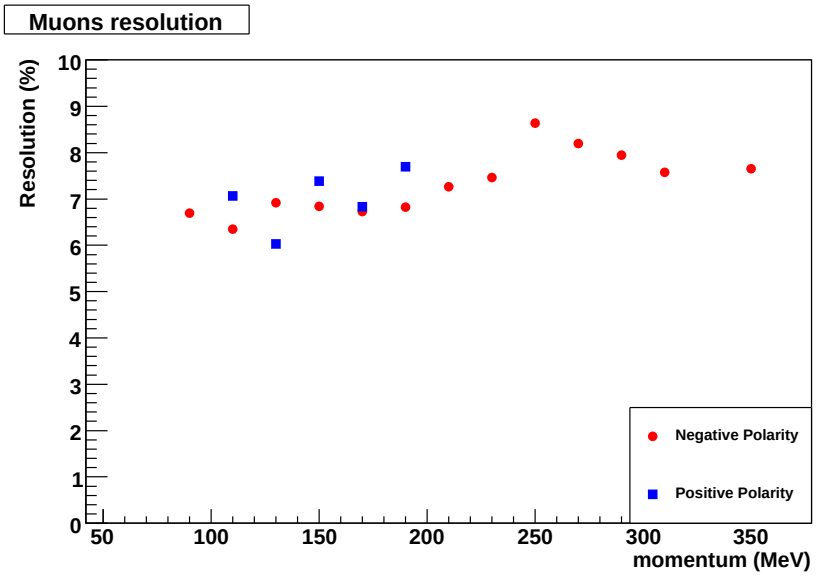

Figure 5.33: Deposited energy resolution for horizontal muons as a function of the momentum.

5.6.2 Truncated mean versus momentum

Using M11 data we then compared the energy loss curve predicted by the Monte Carlo simulation with the observed one in the data for muons, pions and electrons. In figure 5.34 the deposited energies for electrons, muons and pions are shown as a function of the momentum with superimposed the expected curves. The agreement between the expected and the measured energy loss is good especially for muons and pions. The energy loss by the electrons, instead, seems to be slightly overestimated in the Monte Carlo.

5.6.3 Separation between electrons and muons

The requirement to measure the deposited energy with a resolution better than 10% is needed to separate electrons from muons in the TPC and to provide a measurement of

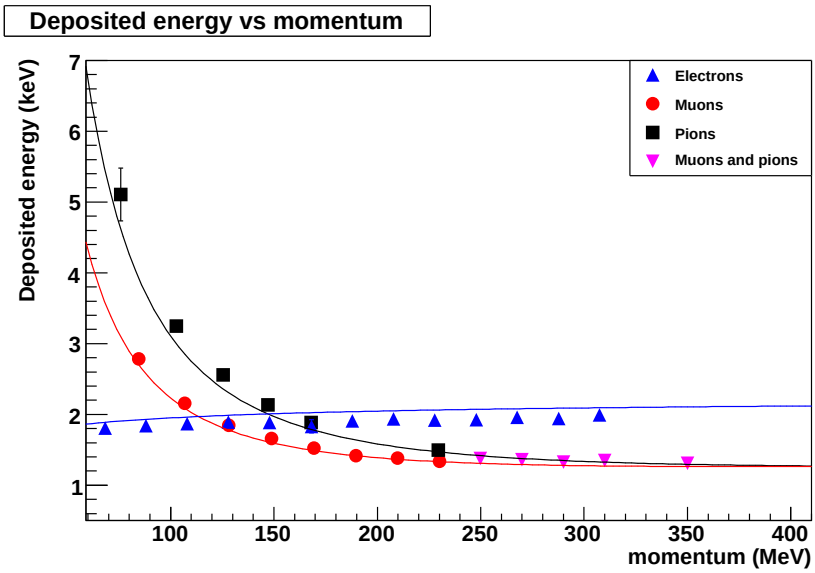

Figure 5.34: Deposited energy as a function of the momentum for samples of electrons, muons and pions. The curves show the expected deposited energy according to the Monte Carlo simulation described in [83].

the ν_e component in the T2K ν_μ beam (see chapter 7). This measurement is particularly important because the ν_e in the beam are one of the main background to the ν_e appearance signal in Super Kamiokande.
The test beam data provided the opportunity to have pure samples of electrons and muons studying with them the separation between the particles.

In figure 5.35 we show the separation (number of sigma) between muons and electrons. This separation is defined, for each momentum, as

$$N_\sigma = |\frac{C_M^\mu - C_M^e}{\sigma_T^\mu}| \tag{5.9}$$

and is found to be better than 4 for momenta larger than 200 MeV/c. A more detailed analysis of the TPC e/μ separation capability is shown in the next section.

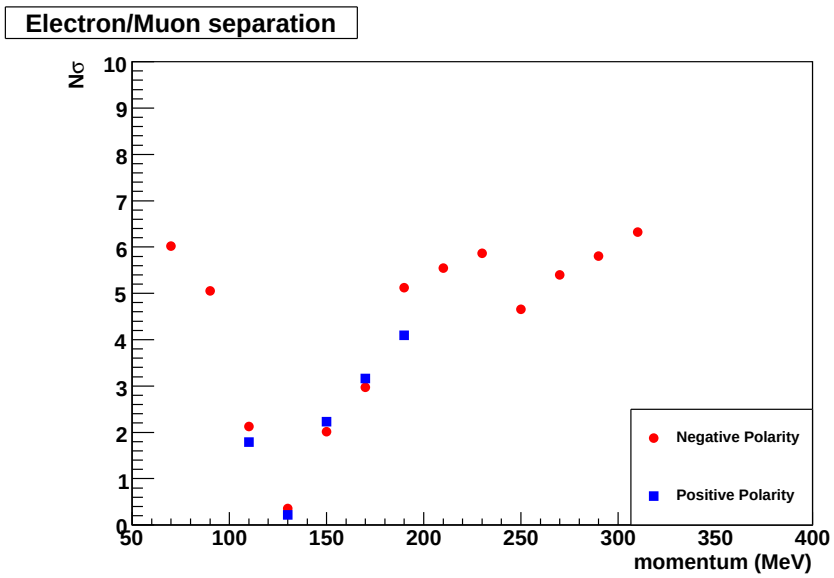

Figure 5.35: Number of sigma separation between muons and electrons as a function of the momentum.

5.6.4 Studies of electrons efficiencies and muons contaminations

For the T2K ν_e component analysis it is important to identify a small sample of neutrino interactions produced by electron neutrinos in a large sample of interactions produced by muon neutrinos. In the T2K beam the ν_μ flux will be approximately 200 times higher than the ν_e flux and to measure the electron neutrino component a very efficient muon rejection is needed. Muons background rejection needs to be of the order of 10^3 or more to have a signal to noise ratio better than 5:1.
Using the M11 data taken with momenta between 250 and 350 MeV/c we tested the particle identification methods in the TPC in terms of efficiency and purity in selecting electrons samples.
In this momentum region muons and pions are almost indistinguishable and the energy lost curves of muons/pions and of electrons are in a good approximation flat (see figure 5.34). This means that particles at different momenta can be considered together, providing a sample large enough of muons/pions and electrons.

In figure 5.36 the time difference between the front and the back scintillators for these data is shown. The fit is done with two gaussian distributions and the two peaks correspond to the muons/pions and to the electrons. The two distributions are partially overlapping

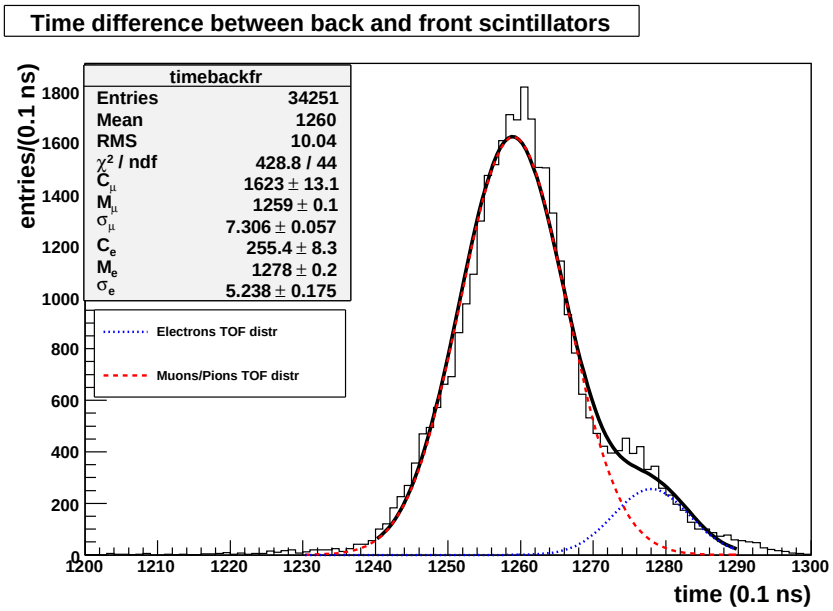

Figure 5.36: Time Of Flight distribution between front and back scintillators for the events analyzed. The distribution is fitted with two gaussians to estimate the Time Of Flight for the muons/pions (red curve) and for the electrons (blue curve).

and to select samples with the best possible purity for the muon/pion sample we required

$$124 < \Delta T\ (ns) < 126.5 \tag{5.10}$$

and for the electron sample

$$127.5 < \Delta T\ (ns) < 130 \tag{5.11}$$

the distributions obtained are shown in figure 5.37 and 5.38 respectively for muons/pions and for electrons.

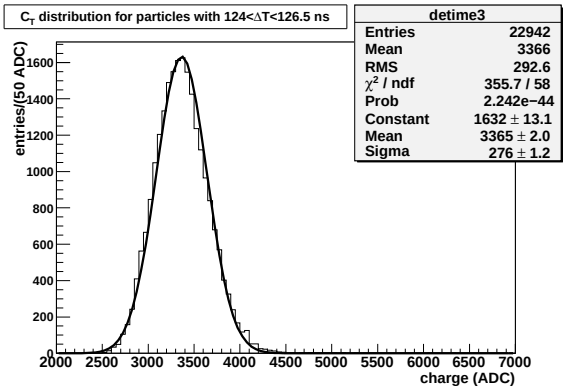

Figure 5.37: Measured truncated mean for the muon/pion sample selected with the TOF according to selection 5.10.

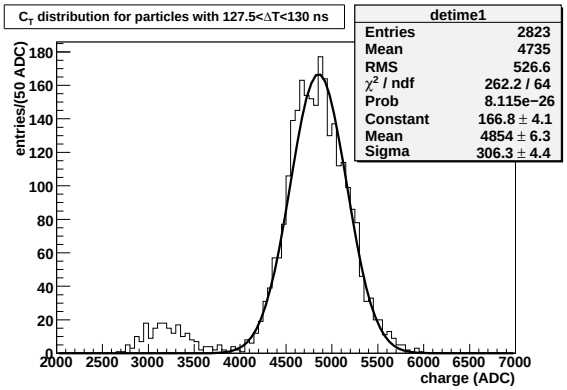

Figure 5.38: Measured truncated mean for the electron sample selected with the TOF according to selection 5.11.

To measure the electron efficiency we counted how many times the measured C_T for particles selected as electrons according to 5.11 was larger than the mean value of the distribution C_M^e minus 0, 1, and 2 σ_e respectively. To measure the muon/pion contamination we wanted to know how many times the measured C_T for particles selected as muons/pions according to the selection 5.10 was larger than C_M^e minus 0, 1, 2 and 3 σ_e. In the muon/pion sample of reconstructed tracks there were also few tracks with $C_T >> C_M^e$. All the events with $C_T > (C_M^e + 3\sigma_e)$ have been excluded from the computation of the purity because according to the PID methods they are not identified as a muon/pion nor as an electron.
As it is clear from the second peak of figure 5.38 the selection 5.11 does not provide a completely pure electron sample as some of the muons pass the cut 5.11. To study the electron efficiency we decided to take the number of tracks in the electron sample with $C_T > (C_M^e - 3\sigma_e)$ as the normalizing factor and to compute efficiencies with respect to this number.

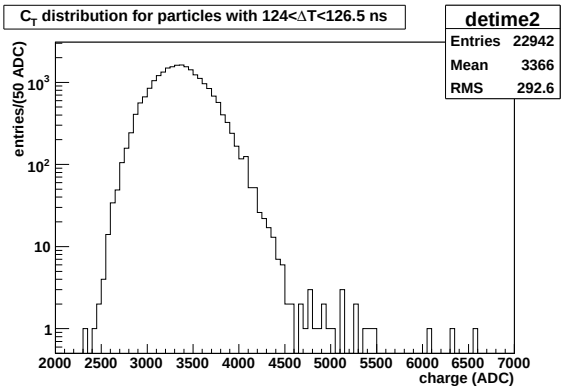

Figure 5.39: Measured truncated mean in logarithmic scale for the muon/pion sample selected with the TOF according to selection 5.10.

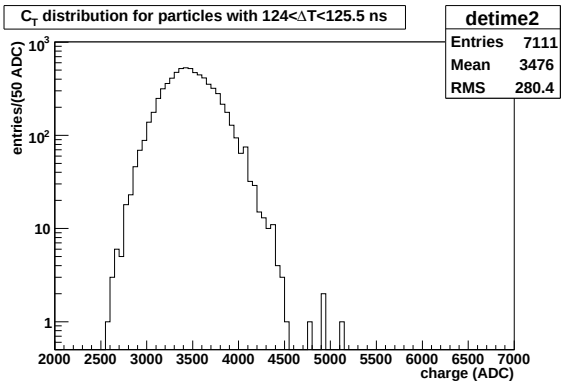

Figure 5.40: Measured truncated mean in logarithmic scale for the muon/pion sample selected with the TOF according to selection 5.12.

Also when we compute the fraction of muons identified as electrons it is possible that part of these tracks are electrons that pass the selection cut given by 5.10. This is visible on figure 5.39 where the same sample of figure 5.37 is plotted in a logarithmic scale. Here there might be a second peak with a measured truncated mean compatible with the one of the electrons. The estimation of the number of electrons in the muon and pion sample is difficult and we decided not to take them into account and to give a limit of the misidentification probability in the pessimistic hypothesis that the number of electrons in the sample is 0.
We also tried to change the selection on the TOF using, to select the muon/pion sample

$$124 < \Delta T\ (ns) < 125.5 \tag{5.12}$$

The truncated mean in logarithmic scale for this cut is shown in figure 5.40. Also in this case, even if the second peak on the distribution disappears, there are few tracks that have C_T compatible with C_M^e. These particles are likely to be electron but we cannot exclude the possibility that they are muons misidentified by the PID methods. Also in this case, we decided to consider them as misidentified muons and this cut, due to the minor number of events selected with 5.12, does not provide better limits on the contamination.
The results for electron efficiencies and muon contamination for the TOF selections of 5.10 are summarized in table 5.1.

From the table 5.1 we can see that with the T2K TPC, using the particle identification methods, we can identify electrons with an efficiency of the 85% and with a muon background rejection factor of 10^3. This rejection factor is a conservative estimate that does not

	e^-	Eff (%)	μ^-/π^-	Prob ($\mu \to e$) (%)
$C_T > C_M^e$	1293	49.4	13	(0.055 ± 0.015)
$C_T > (C_M^e - 1\sigma_M^e)$	2231	85.2	23	(0.10 ± 0.02)
$C_T > (C_M^e - 2\sigma_M^e)$	2576	98.4	98	(0.43 ± 0.04)
$C_T > (C_M^e - 3\sigma_M^e)$	2617	100	842	(3.6 ± 0.1)

Table 5.1: Summary of the efficiency and contamination studies. The number of entries in the muon/pion sample over which the contamination is computed is 22935.

take into account the possible presence of some electrons in the muon/pion sample. Even with this limit it will be possible to measure the ν_e component in the T2K beam with a signal to noise ratio of the order of 5:1.

5.7 Straggling functions

In the section 4.5.3 we showed that, according to the Monte Carlo simulation, the calibration for the sample length was different between electrons and other particles. This can be explained if the ionization mechanisms of the primary particle are different according to the particle nature. If this is true some differences should be seen also in the straggling functions [71], that represent the energy lost by a particle crossing a given width of gas.
Obviously the energy loss depends also on the beta gamma of the particle. For this reason, to compare the straggling functions of muons and electrons it is necessary to find a momentum at which they ionize in a similar way. At low energy this happens when the muon curve of the deposited energy versus the momentum, is proportional to $1/\beta^2$ while the electrons curve is in the flat region (see figure 5.34). Due to the differences between data and Monte Carlo, the intersection point of the electrons curve with the muons one is not the same. In the data muons and electrons have the same ionization at a momentum of 130 MeV/c while in the Monte Carlo this happens at 114 MeV/c.

Measuring the straggling function is equivalent to measuring the charge released in a MicroMegas column by particles with the same angles with respect to the TPC. In particular, the measurement of the charge per column for particles that horizontally cross the TPC will provide the measurement of the straggling functions for particles that cross 0.97 cm of Argon. In figure 5.41 the charge per cluster distribution for muons and electrons in the Monte Carlo is shown, while in figure 5.42 we show the same distributions in the data. In the Monte

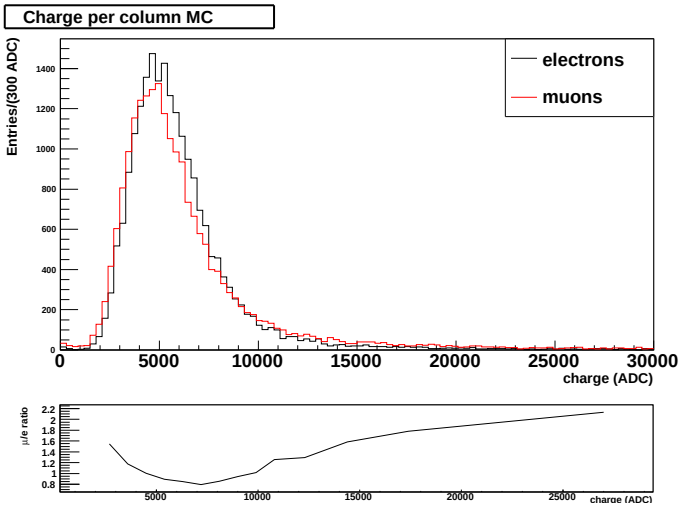

Figure 5.41: Top plot: charge per column distribution obtained from the Monte Carlo simulation for horizontal muons and electrons. Bottom plot: Ratio between the number of muons and the number of electrons in the different charge bins of the upper plot.

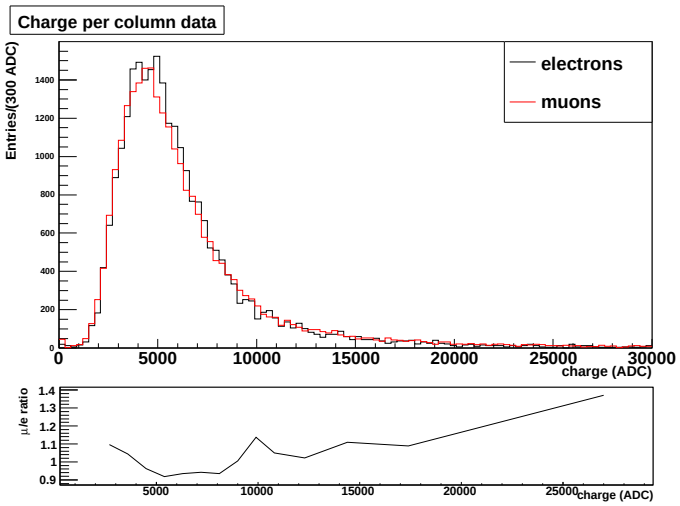

Figure 5.42: Top plot: charge per column distribution obtained from the M11 data for horizontal muons and electrons with a nominal momentum of 150 MeV/c (run 3992). The muons distribution is scaled by a factor of 2.1% to take into account the different ionization between the two samples. Bottom plot: Ratio between the number of muons and the number of electrons in the different charge bins of the upper plot.

Carlo simulation the distributions for muons and electrons are slightly different, while in the data the distributions are more similar. We also took into account the fact that in the data at 130 MeV/c there is still a difference of 2.1% in the measurement of the deposited energy for the two particles.
A Kolmogorov-Smirnov test, performed over the electrons and muons distributions of the charge per column in the Monte Carlo and in the data with and without the scaling factor gives the probabilities shown in table 5.2.

	MC	Data not scaled	Data scaled
Probability	$1.9 \cdot 10^{-16}$	$1.7 \cdot 10^{-9}$	$1.8 \cdot 10^{-4}$

Table 5.2: Results of the Kolmogorov-Smirnov test obtained comparing the charge per column distribution in data (run 3992) and in the Monte Carlo simulation

From the table and from the distributions of figure 5.41 and 5.42 we can see that the agreement between the distributions in the data is better than the one that we observe in the Monte Carlo but the probability of compatibility is still very low. We also observe a similar pattern of the ratios between muons and electrons in data and Monte Carlo. In both, in fact, the muons have a longer high energy tail with respect to the electrons.

5.8 Conclusions

The tests described in this chapter show the TPC performances in particular in terms of deposited energy resolution. These analyse s allowed us to validate our TPCs before their installation in JPARC and to develop better software tools.
In particular we checked our Monte Carlo parameterization of the deposited energy curve on the data and we showed that we can reach a deposited energy resolution of 8% or better at different momenta.
We showed that, with the measurement of the truncated mean, we can also monitor the stability of the TPCs and measure the dependence of the gain on the external conditions.
Finally we could also check, using monoenergetic particles with a known angle with respect to the TPC, the dependencies of the energy loss on the track angle and on the number of samples, that we had parameterized using the Monte Carlo simulation.

Chapter 6

Installation and commissioning of the TPCs in the ND280 facility

The TPCs, together with the others ND280 off-axis detectors have been installed in the ND280 facility in the Fall of 2009. During this period I spent four months at JPARC working on the installation and the commissioning of the TPCs in ND280 (three months between September and December 2009 and one month in February 2010). At the end of the commissioning of all the ND280 detectors, the magnet was closed and in January 2010 the ND280 detectors were ready to take the first T2K physics data: for this first period of data taking all the ND280 detectors were installed with the exception of the Barrel ECAL that will be installed in the magnet at the end of the first physics run; in 2010 only the downstream module of ECAL was taking data.
The work that I have done in this period can be divided into three main parts:

- Installation of the TPCs into the pit and commissioning of the front-end electronic
- Online monitoring of the TPCs
- Commissioning of the system with cosmic and neutrino data

The TPCs installation was done in the following way: the first two TPCs arrived at JPARC in the Summer and were installed in the pit at the beginning of October 2009, while the third TPC arrived at JPARC in November and was installed in ND280 in December 2009.
In this chapter we will describe the work done in this period for these three different parts.

6.1 Installation of the TPCs in the ND280 pit

After being tested in the M11 beam test, all the electronics has been dismounted from the TPC and the TPCs were shipped by plane to Japan. Once the TPCs arrived in Japan we re-installed the electronics on the MicroMegas modules in a clean room and we tested that everything was correctly working taking, module by module, some pedestal runs with a stand alone acquisition system. The expected mean value of the pedestals is ~ 250 *ADC* counts while their RMS is expected to be below 4.5 *ADC* counts.
An example of a map of all the pads of one MicroMegas module with the mean values and the RMS of the pedestals is shown in figure 6.1.

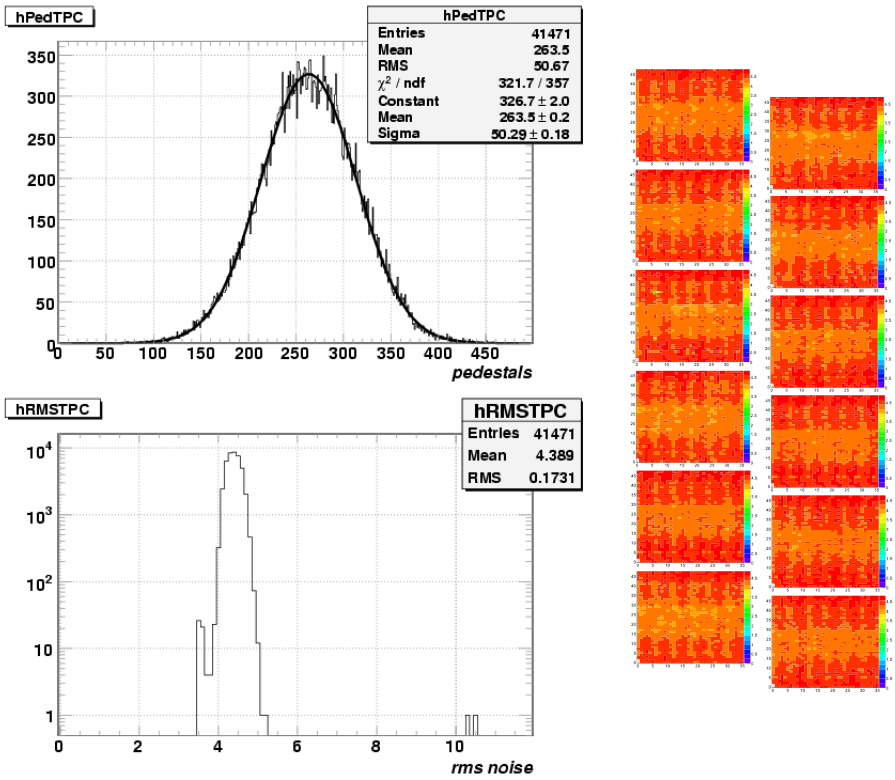

Figure 6.1: Mean values and RMS of the pedestals measured in the Clean Room for one TPC Endplate.

The first 2 TPCs were then installed in the ND280 pit the 10th of October 2009. The TPC Module 0 was put in the position 2 (between the 2 FGDs) while the TPC Module 1 has been installed in the position 3 (between the second FGD and the Downstream ECAL). The last TPC has been mounted in the position 1 in December 2009.

Before and after the installation of the TPCs I participated in all the phases of the installation and in several quality checks of the MicroMegas modules and of the electronics. These activities consisted in:

- Test of the MicroMegas in the clean room: to be sure that the modules were correctly working they were turned on one by one in dry air up to the voltage at which they produced the first spark (at about 800 V).
- Test of the Front-End electronics in the clean room
- Development and test of the High Voltage Slow Control and implementation of the monitoring histograms and of the spark rate measurements
- Installation and commissioning of the Low Voltage Slow Control
- Installation and commissioning of the Back-End electronics

In particular, after the installation in the pit I helped in the development of the TPC data acquisition. The specification for the ND280 detectors was to reach an acquisition rate of 20 Hz to be able to take, together with beam triggers, also pedestals, laser and cosmics trigger. Two different types of cosmic triggers were available: one (FGD cosmic trigger) provided by the coincidence between 2 FGDs and one (TripT cosmic trigger) provided by different combinations of the TripT detectors (SMRD, ECAL and P0D).
Reaching the requested rate for the TPCs was challenging due to the large number of channels that had to be read for each trigger and also to the necessity of taking pedestals and laser triggers without zero suppression.
After several months of tests, this rate was attained in February with the following settings:

- Beam and Cosmic trigger: reading all the channels, all the 511 time bins, with zero suppression and a 4.5 sigma threshold we had a latency of 25 ms.
- Laser trigger: reading only the 4 MicroMegas illuminated by the laser at each trigger, the first 50 time samples, without zero suppression we reached a latency of 52 ms.
- Pedestal trigger: reading 8 MicroMegas per trigger, the first 30 time samples, without zero suppression we reached a latency of 47 ms.

This was satisfactory as it allowed us to obtain all the information from all the channels for beam and cosmics. Concerning the laser triggers, it is a known signal that can be issued at a well defined position and time, having in this way all the charge arriving on the MicroMegas surface in the first 50 time samples and on a known DCC.
Finally for the pedestals we were not interested in getting all the information for each trigger

as, to know the pedestal for a given channel it was enough to put together the information coming from different pedestal triggers.
For the first T2K physics run the electronics settings have been set in the following way:

- ASIC shaping time: 200 ns
- ASIC sampling time 40 ns : given the drift velocity in our gas, this provides, with 511 time bins, a 20 μs time window that was enough to manage, with some safety, the 12 μs of drift time and the 3 μs of beam time
- ASIC SCA gain 120 fC: compromise between the necessity of having a gain small enough to not have ADC saturation but large enough to not affect the energy resolution.

6.2 Online Monitoring

During the period spent in Japan I also took care of the developing of the online monitoring plots for the TPCs.
This has been done within the framework of the ND280 online monitoring with the aim to provide online histograms to ensure that the different detectors were correctly working during the data taking.
The TPCs online monitoring provides realtime basic information on the correct working of all the TPCs components (in particular the front-end electronics, the MicroMegas high voltage and the laser system), helping shifters in detecting problems during the data taking. Some plots have been developed to monitor the trigger types and to check that we were not missing beam spills during the data taking (see figure 6.2) and some other plots have been done to monitor the TPCs.

Here we will show some examples of these plots to provide an idea of how the TPCs were working during the first T2K physics run:

- in figure 6.3 some summary plots are shown: these plots show the distribution of the charge on each hit, the number of time samples of the hits, the arrival time of the charge during cosmic and beam trigger and the ratio between the charge and the number of time samples on the hits;
- in figure 6.4 the occupancy on all the MicroMegas pads of the three TPCs is shown for cosmic triggers and laser data: notice one MicroMegas on the TPC3 that has a lower gain. This problem appeared at the begin of the physics run in March and has not been solved until the end of the run as the magnet was closed and the TPCs were not accessible;

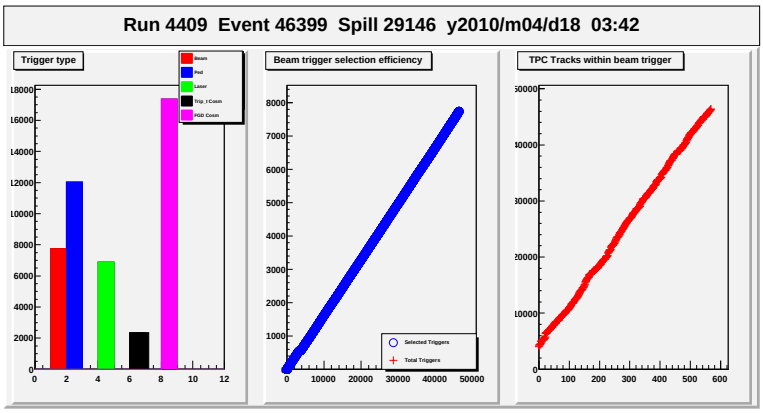

Figure 6.2: Left plot: summary of the different trigger types acquired during the data taking (beam, pedestals, laser and cosmics); central plot: number of beam spills issued by the accelerator and acquired by the ND280 DAQ: on the x-axis the total number of events is shown while the y-axis show the number of beam trigger; right plot: number of TPC tracks (on the x-axis) observed during beam spills and corresponding event number (on the y-axis)

- in figure 6.5 the mean and the RMS of the charge detected on each ASICs of the TPCs are shown; also here we can see the problem with the MicroMegas module on the TPC3.

6.3 TPC calibration chain

The Particle Identification method, based on the measurement of the truncated mean, is sensitive to the total amount of charge detected on each cluster of the track.
The detected charge is a function, not only of the energy deposited by the track during the ionization process but it depends also on the characteristics of the MicroMegas modules (pad dimensions and module gain), of the electronics and of the external conditions (temperature and pressure).
All these effects have to be taken into account before reconstructing the tracks. The TPC calibration chain is done in four steps:

1. Relative calibration of the MicroMegas gain on a module by module basis
2. Relative calibration of the gain of all the pads of each MicroMegas module

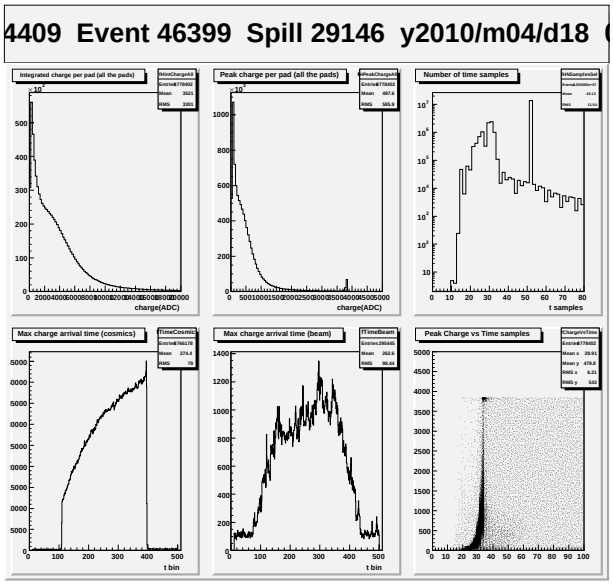

Figure 6.3: TPC Summary plots obtained with the online monitoring: on the upper plots the integrated charge per hit (left), the peak of the charge per hit (center) and the number of time samples per hit (right) are shown. On the bottom plots the arrival time of the charge on the MicroMegas for cosmics (left) and beam (center) and the ratio between the charge and the number of time samples are shown.

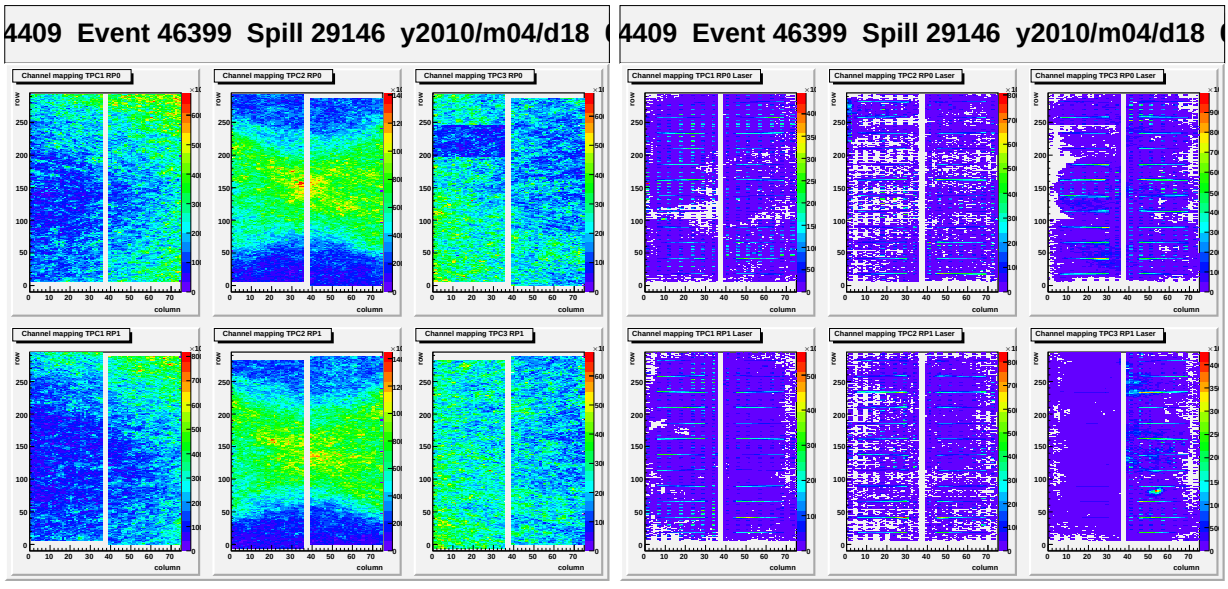

Figure 6.4: Occupancy on the three TPCs for cosmics (left) and laser (right) triggers.

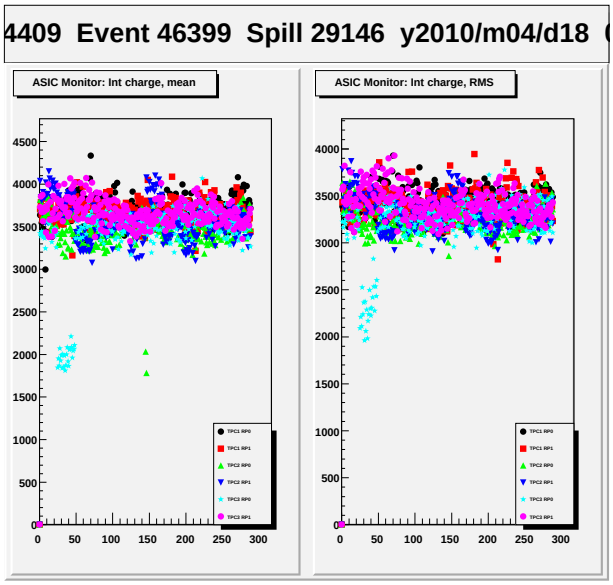

Figure 6.5: Mean value and RMS of the charge detected on each TPC ASIC during cosmic triggers.

3. Electronics calibration, to take into account the differences in the electronics

4. Calibration for the external conditions

The latter effect is calibrated using the realtime information coming from the monitor chambers (see section 3.7.2). For the second effect we used the data coming from the test bench where the gain of each pad with respect to the others of the same module has been measured (see section 5.1.1) while to take into account the third effect a specific calibration of all the electronics cards used on the three TPCs has been done.
The first effect is the most important to consider and, even if we had the value of the average gain of each module measured at the test bench, we decided to develop different methods to calibrate the MicroMegas modules in situ, during the data taking. Here we will show two methods that have been studied, both of them using the deposited energy in the clusters: the first one uses the deposited energy by cosmics crossing the TPCs and the second uses the one deposited by through going muons coming with the beam. This latter method has been then used as the default method for the module by module calibration.

6.3.1 MicroMegas calibration with cosmics

To perform a calibration of the MicroMegas modules using tracks we need to reconstruct the tracks crossing the TPCs and select tracks that release in the TPC gas similar amounts of energy through the ionization processes. The occupancy of the cosmics on the three TPCs is shown in figure 6.4.
For the calibration we selected a sample of minimum ionizing particles, requiring reconstructed momenta between 300 and 600 MeV/c. For each of these tracks we corrected the charge per column for the track angle and we filled one histogram per each MicroMegas module with the distribution of the charge per column. Examples of these distributions for some of the modules are shown in figure 6.6. Each distribution is fitted with a Landau function to estimate the Most Probable Value.

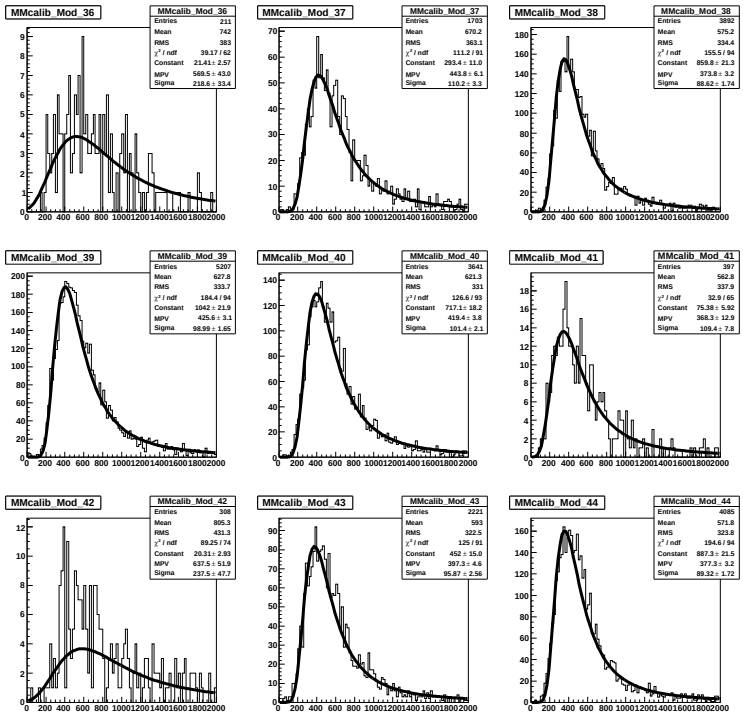

Figure 6.6: Distribution of the charge per column observed for cosmic MIP tracks on nine MicroMegas modules.

We also tested the possibility of fitting the distributions with a convolution of a Landau and a Gauss function that would better reproduce the shape of the charge per column distributions due to the ionization processes in the gas. We noticed that the obtained results in terms of MPV were compatible between the two fits and for simplicity in the fitting

procedure we decided to use the fit with a Landau function.
In figure 6.7 the distribution of the 72 Most Probable Values (normalized to the one of the first MicroMegas module) and their dispersion, that is of 4.9%, is shown.

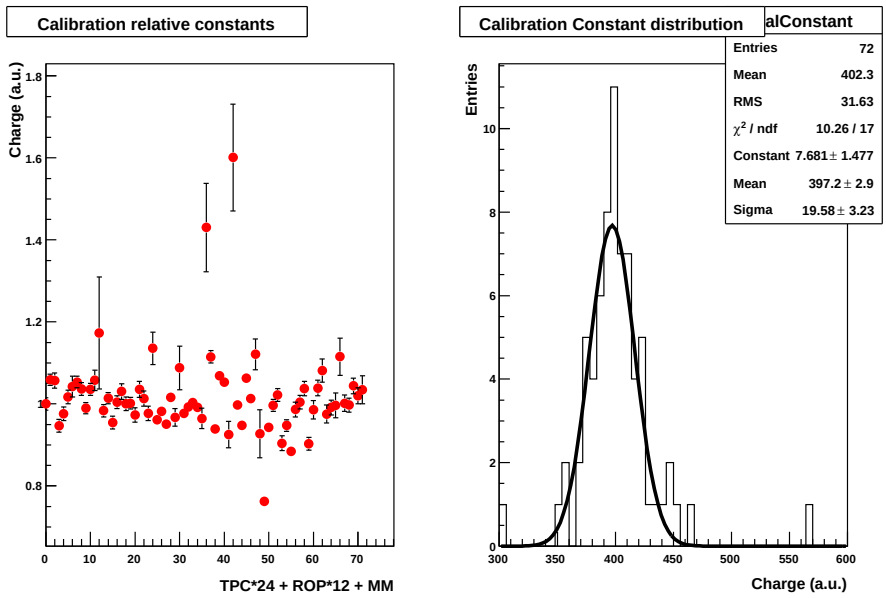

Figure 6.7: Distribution of the Most Probable Values of the charge per column observed for cosmic MIP tracks on the 72 MicroMegas modules and their dispersion.

As we can see from the figures 6.6 and 6.7, due to the trigger cosmic effects, the occupancy among the MicroMegas modules is different and for some of the modules we need a lot of cosmic triggers to have a proper fit. Moreover some of the tracks crossing these modules come from cosmic showers that have deposited energy different from the ones of a MIP.
These are the two main weak points of the calibration with cosmic rays and this effect encouraged us in looking into another possible source of calibration: the through going muons coming with the beam.

6.3.2 MicroMegas calibration with through going muons

The through going muons are muons originated by beam neutrinos interactions with the materials surrounding the ND280 detectors, like the concrete of the pit walls. Some of these muons (the ones produced with larger energies) enter the ND280 detectors and cross the three TPCs where their tracks are observed.

While the statistics is much lower than in the case of the cosmics, the advantage of the through going muons is that they cross in a uniform way the three TPCs (see figure 6.8), providing enough statistics to obtain proper calibration constants for all the modules. Moreover the contamination of particles that are not muons is negligible.

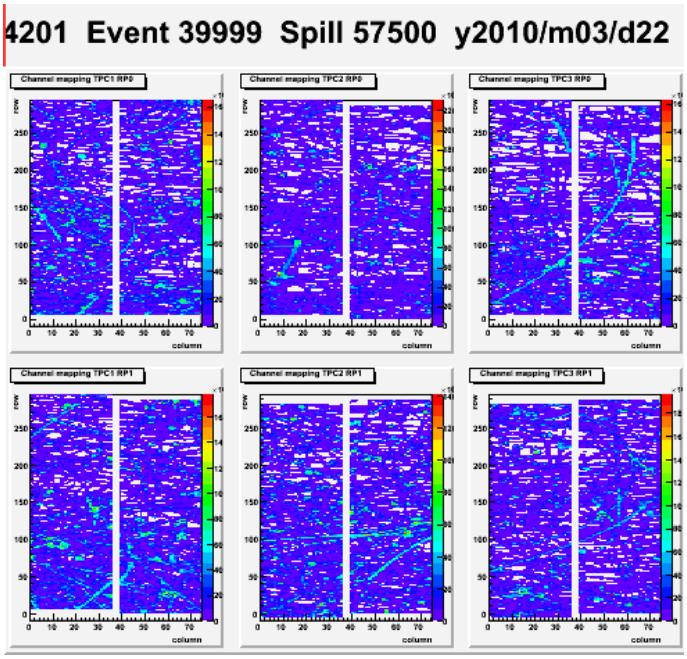

Figure 6.8: Occupancy of the tracks arriving during beam triggers on the two readout planes of the three TPCs.

To select through going muons we required particles coming during beam triggers, with reconstructed momenta between 700 MeV/c and 2 GeV/c. Examples of the distribution of the charge per column, corrected for the reconstructed angle, for some of the MicroMegas are shown in figure 6.9. Each distribution is fitted with a Landau function.

In figure 6.10 we show the distribution of the 72 Most Probable Values (normalized to the one of the first MicroMegas module) and their dispersion, that is 4.6%.

The distributions show the good uniformity of the gain of the MicroMegas modules. We also check the calibration constants obtained with this method over different runs. In figure 6.11 a comparison between the constants obtained using the neutrino runs of March and April 2010 are shown. As we can see the variations between the two runs are small and this indicates the good stability of this method to obtain the relative gains of the modules.

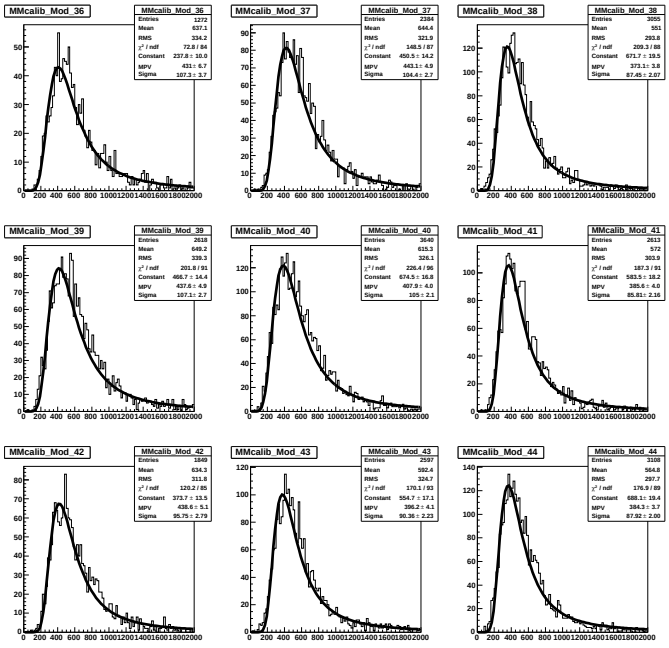

Figure 6.9: Distribution of the charge per column observed for through going muons tracks on nine MicroMegas modules.

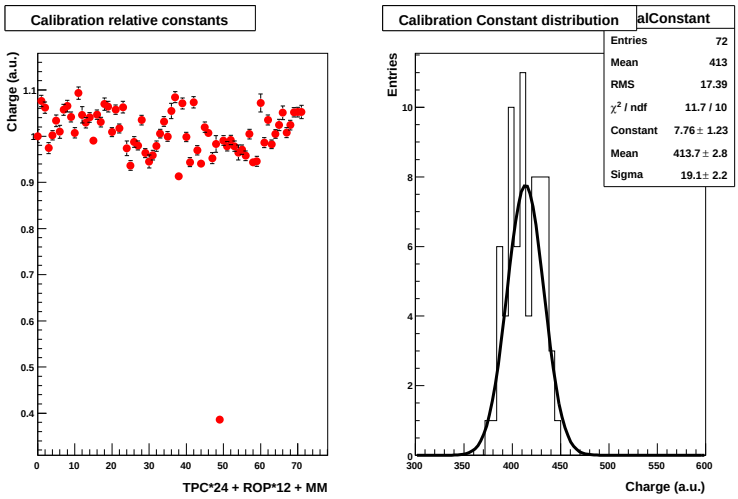

Figure 6.10: Distribution of the Most Probable Values of the charge per column observed for through going muons tracks on the 72 MicroMegas modules and their dispersion.

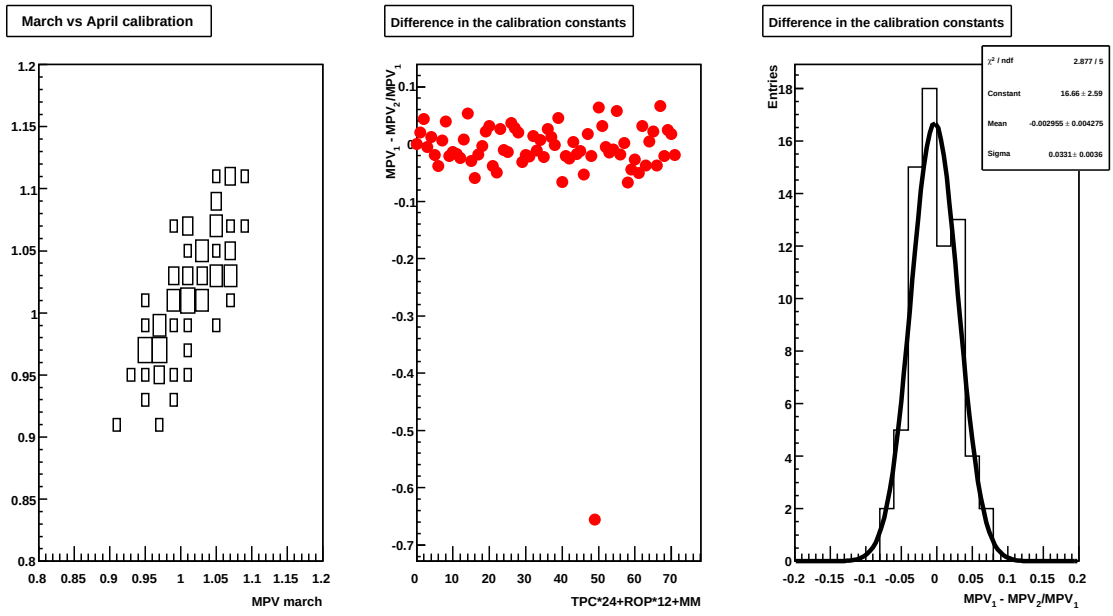

Figure 6.11: Stability of the calibration constants using through going muons for two different neutrino runs: March and April 2010. In the left plot is shown the correlation of the calibration constants for the two runs, while in the central plot and in the right plots the relative differences are shown: on the central plot we can clearly see the problem already shown in figure 6.5 with the gain of one of the MicroMegas that dropped during April run.

For the first physics run of the T2K experiment we decided to compute a table of the calibration constants, using through going muons, for each month and apply them to the data.

6.4 Deposited energy measurements

We used the first data collected with the TPCs to test the particle identification methods that I have developed during this thesis. In this section we will show the results of these tests, using cosmics and through going muons.

6.4.1 Energy deposited by cosmic tracks

In December 2009, after the installation of the TPCs in the ND280 pit, we started their commissioning using cosmic rays. These cosmics have been taken with different trigger configurations and with the magnet on and off.
For the purposes of this thesis, in which we are interested in measuring the deposited energy resolution of the TPCs, we will show results of the analysis of the cosmics taken with the magnetic field on and FGD cosmics trigger. In figure 6.4 the occupancy of the cosmics on the 3 TPCs were shown and in figure 6.12 we find some event displays of reconstructed cosmics tracks.

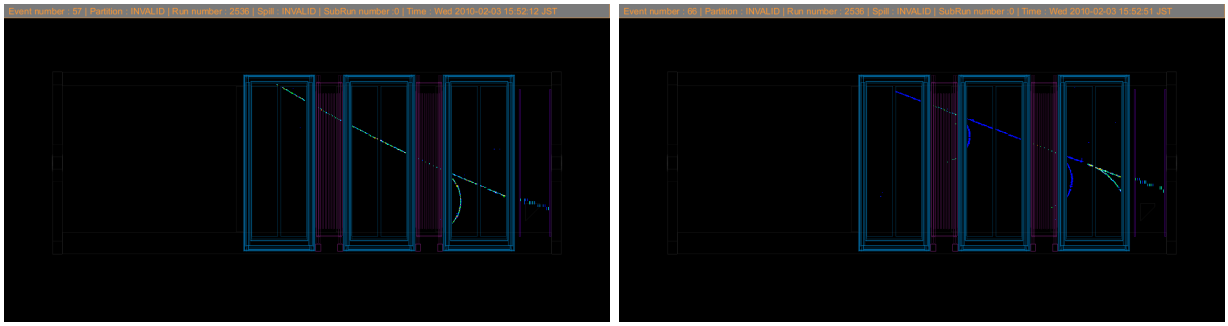

Figure 6.12: Examples of event display of cosmics crossing the TPCs.

As we can see from these figures, the FGD cosmics trigger provides mainly crossing the upper and the bottom parts of TPC1 and TPC3 and the central part of TPC2.
The tracks were reconstructed with the ND280 software. For each track we reconstructed the momentum and we measured the truncated mean of the charge using the methods described

in chapter 4.

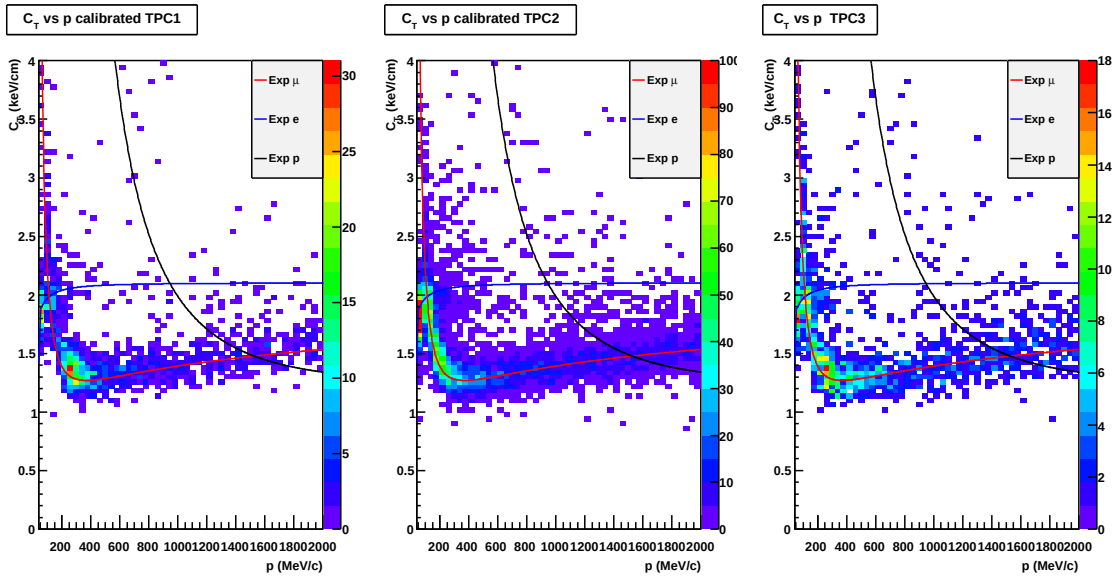

Figure 6.13: Distribution of the truncated mean C_T versus the reconstructed momentum in the three TPCs. The superimposed lines are the Monte Carlo expectations for muons (red), electrons (blue) and protons (black)

In figure 6.13 the distribution of the truncated mean C_T as a function of the reconstructed momentum is shown. The superimposed curves are the expected curves for electrons, muons and protons, according to the parameterization of equation 4.50. As expected the majority of the cosmic tracks are muons and they follow well the expected Monte Carlo curve.

Even if the majority of the tracks are muons, in the sample there are also some electrons, in particular at low momenta, coming from cosmic showers entering the TPC. This can be seen if we divide our sample in momenta slices and we look at the truncated mean distribution (see figure 6.14): at momenta between 200 and 400 MeV/c we observe, as we showed in chapter 4 a second peak in the C_T distribution, at larger values of C_T; this peak is due to electrons in our sample of particles.
We also fitted with a gaussian the distributions of figure 6.14 to measure the deposited energy resolution using the cosmics: in figure 6.15 we show the resolution as a function of the momentum with and without the use of the calibration constants described in the previous section.

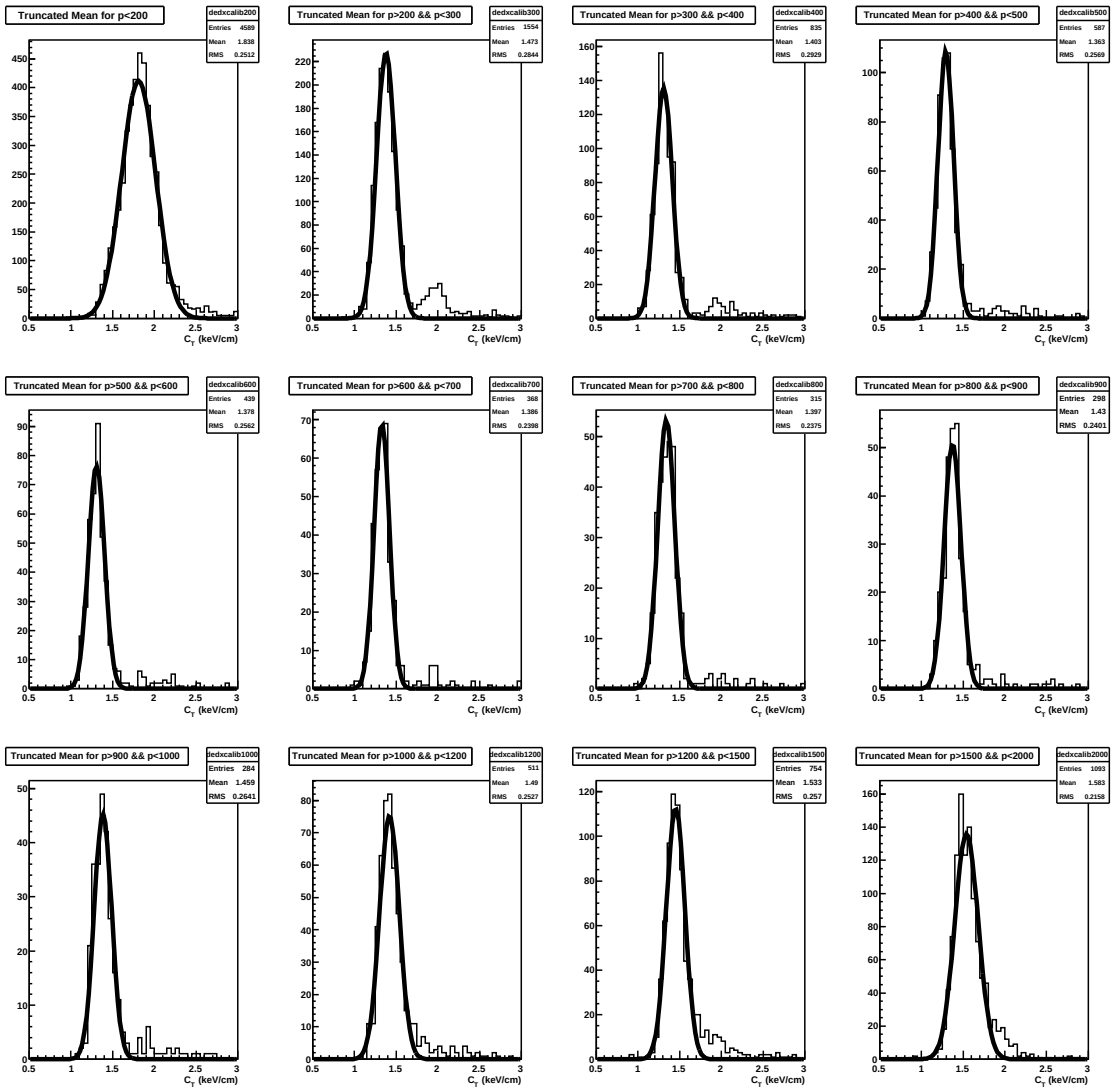

Figure 6.14: Distribution of the truncated mean C_T for different momenta intervals (from 0 to 2 GeV/c). The distributions are fitted with a gaussian to get the resolution. The second peak at low momenta is due to electrons entering in the TPCs.

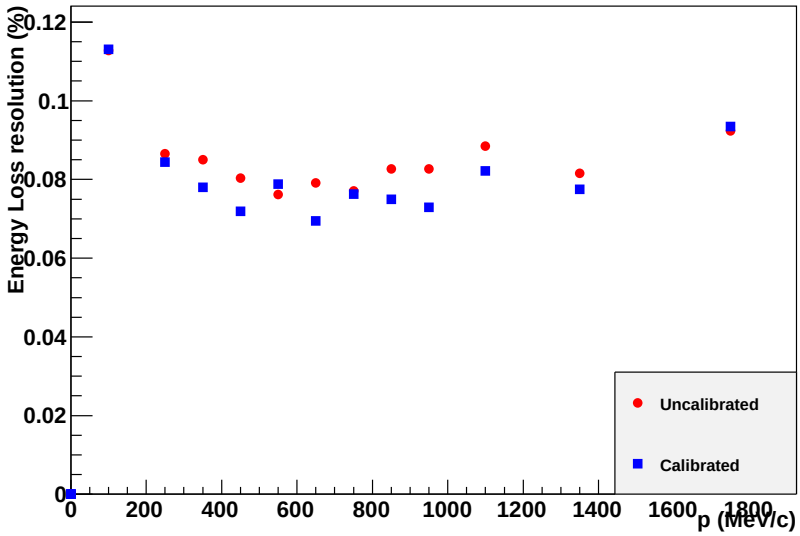

Figure 6.15: Resolution on the deposited energy measurement as a function of the momentum: the red points are the resolution obtained without using the calibration constants while the blue points are obtained using the calibration constants.

As we can see the resolution improves if we use the calibration constants and we obtain a resolution on the deposited energy that is 8% or better for momenta larger than 200 MeV/c, while the point at lower momentum has a worst resolution as it contain both, muons and electrons that at this momentum are not distinguishable.

6.4.2 Systematic effects on the measurement of the deposited charge

In the sections 4.5.2 and 4.5.3 we showed how the measurement of the truncated mean depends on the number of samples used in its measurement and on the width of gas crossed by the track in the sample (the sample length).

These dependencies have been parameterized and the data are corrected to take them into account: in figure 6.16 we show the truncated mean measured as a function of the sample length and of the number of samples after the correction for these parameters; as we can see the distributions are flat and this indicate that the calibration factor computed

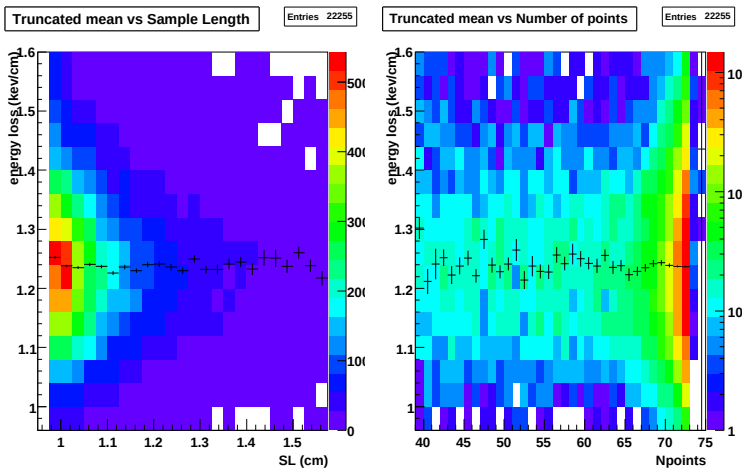

Figure 6.16: Dependency of the truncated mean on the sample length (left) and on the number of samples (right).

with the Monte Carlo properly works and the PID performances are not degraded by these dependencies.
Another possible dependency that had been studied with the M11 data was the dependency on the drift distance (see section 5.4.3): given the gas mixture in our TPC we do not expect any absorption of the electrons along the drift direction but using the cosmic data another effect has been observed: as we can see from the left plot of figure 6.17 the truncated mean measured for tracks with a larger drift time (near the cathode) is larger than the one of the tracks near the MicroMegas. The effect is small (of the order of 2%) and once observed in the data has been observed also in the Monte Carlo. During M11 tests we had observed some indication of this effect but they were not conclusive (see section 5.4.3).

The explanation for this effect is that the tracks crossing the TPC near the cathode are subject to a larger transverse diffusion and clusters with a larger ionization will affect not only the charge measured on the pads on the corresponding column (that is rejected by the truncated mean method) but also the charge measured on the neighboring columns, bringing to an overall increase of the truncated mean.
The dependency has been parameterized and a correction has been added to the PID methods for both, data and Monte Carlo.

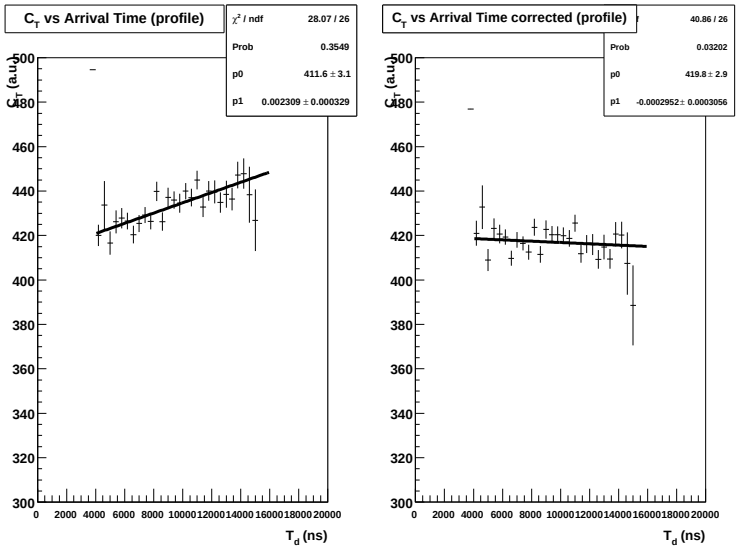

Figure 6.17: Dependency of the truncated mean on the drift distance before (left) and after (right) the correction for this effect.

6.4.3 Muons and electrons samples: comparison of the data with the Monte Carlo

The cosmics data mainly provide muon tracks and cosmic showers. To test the Particle Identification performances we would like to identify clean sample of the different particles and compare their deposited energy with the one observed in the Monte Carlo and in the M11 data. To select sample of the different particles we applied the following criteria:

- Muons: easy to do as the majority of the particles are muons. To select a muon sample we required at maximum one track per TPC. In this way we reject the cosmic shower as we can see from the distribution of the truncated mean in the different momenta slice (see figure 6.18) in which the second peak due to the electrons disappears. In figure 6.19 we show the scatter plot of C_T as a function of the momentum in the three TPCs: also in this case we see that the majority of the points that did not follow the muon curve in figure 6.13 disappeared.

- Electrons: selecting them is more difficult in the cosmics data. In this case we want to select the cosmic showers; to do this we required at least one TPC with more than one reconstructed track. This enhances the number of electrons in our sample as we

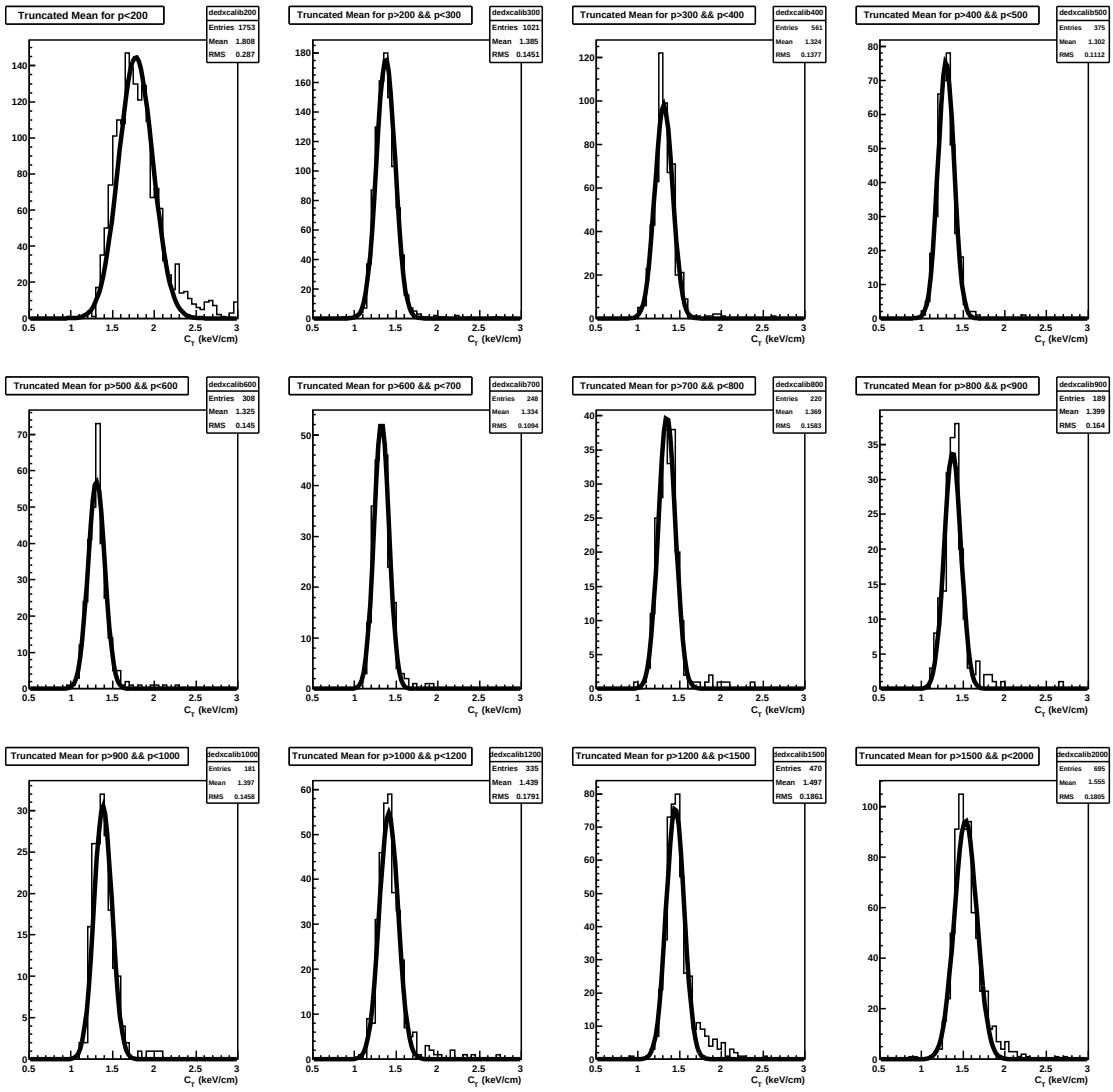

Figure 6.18: Distribution of the truncated mean C_T for different momenta slice (from 0 to 2 GeV/c), requiring at maximum one track per TPC: notice that the second peak observed in figure 6.14 disappear in this case.

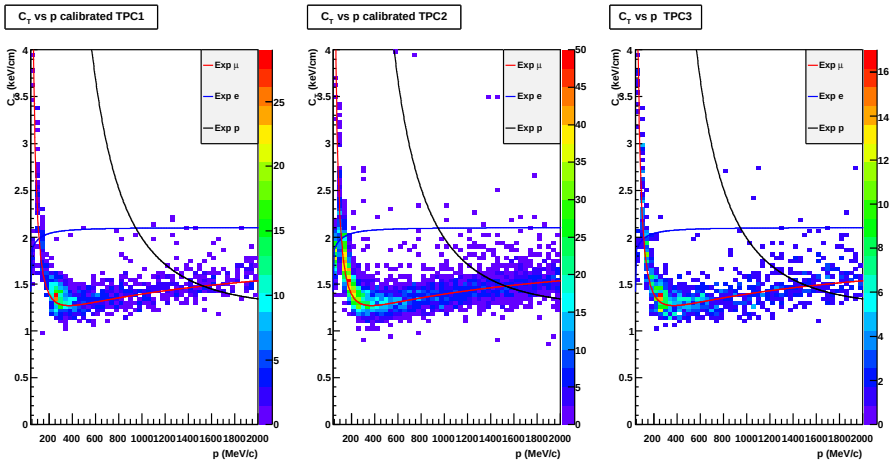

Figure 6.19: Distribution of the truncated mean C_T versus the reconstructed momentum in the three TPCs, when we require at maximum one track per TPC. The superimposed lines are the Monte Carlo expectations for muons (red), electrons (blue) and protons (black)

can see from figure 6.20 but only at low momenta (below 400 MeV/c) it is possible to identify them.

- Protons: this is impossible to do with the cosmics. We will show samples of protons observed in the neutrino data in the next section.

Once we selected the samples of electrons and muons we compared them to the parameterized deposited energy curve (given by equation 4.50). This is shown in figure 6.21 and it can be directly compared to the corresponding figure obtained during the analysis of the M11 data shown in figure 5.34: the Monte Carlo simulation used in the two curves is the same and we can see that the agreement between data and Monte Carlo is good in both cases for the muons while for the electrons the deposited energy seems to be overestimated in the Monte Carlo: to take into account this effect we changed our parameterization of the deposited energy curve in the electron hypothesis, parameterizing it accordingly to the point observed during the M11 tests.

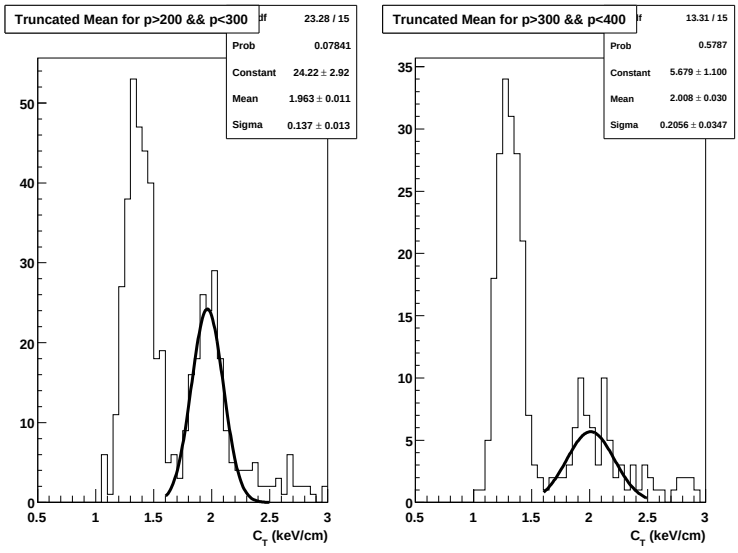

Figure 6.20: Distribution of the truncated mean C_T at low momenta (between 200 and 400 MeV/c), requiring at least one TPC with more then one reconstructed track: the second peak, that corresponds to the electrons is enhanced and it has been fitted with a gaussian function to get the mean value of C_T for electrons.

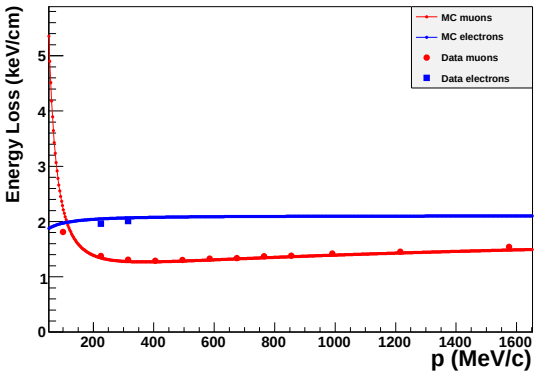

Figure 6.21: Comparison between data and Monte Carlo for electrons and muons: the muons points are obtained from the fit of the distributions in figure 6.18 while the electrons are obtained from the fit of the distributions in figure 6.20; the Monte Carlo for muons and electrons is obtained from the parameterization 4.50

6.4.4 Energy deposited by beam related events

We repeated the same studies using the first tracks collected during beam triggers. For these studies we analyzed all the physics data collected in March and April 2010. Some examples of neutrino interactions in the ND280 detectors are shown in figure 6.22.

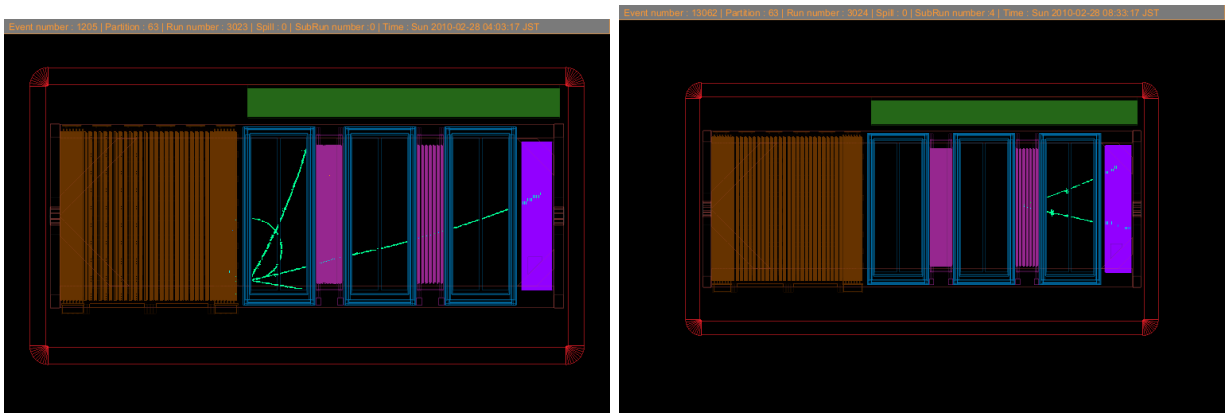

Figure 6.22: Examples of event display of neutrino interactions in the P0D and in the second FGD with track crossing the TPCs.

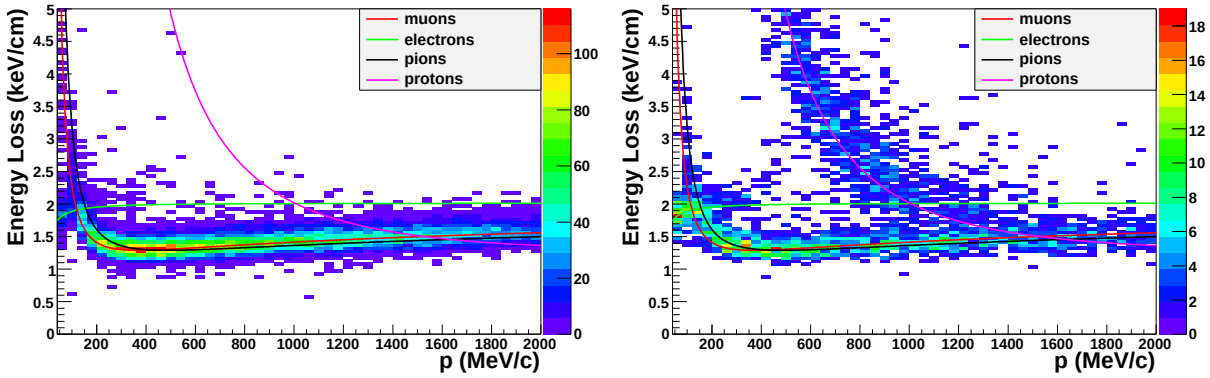

Figure 6.23: Truncated mean versus the reconstructed momentum for negative beam related tracks(left plot) and positive beam related tracks (right plot).

Using the reconstruction of the charge of each track we divided the reconstructed tracks between positive and negative according to the reconstructed curvature in the TPC and we measured for each of them the deposited energy. In figure 6.23 is shown the deposited energy

as a function of the momentum for the two samples of tracks: as we can see the negative tracks are mainly muons (both, through going muons and muons produced in neutrino interactions in the FGDs or in the P0D), with few low energy electrons, while in the positive tracks we can easily recognize three samples of particles:

- High ionizing particles that are different from the MIPs at momenta lower than 1 GeV/c and that are compatible with the expected proton curve;
- MIPs compatible with the expected muons curve: given their positive charge are mostly pions produced in neutrino interactions;
- Low momenta positrons (up to 300 MeV/c) that follow the expected electron curve.

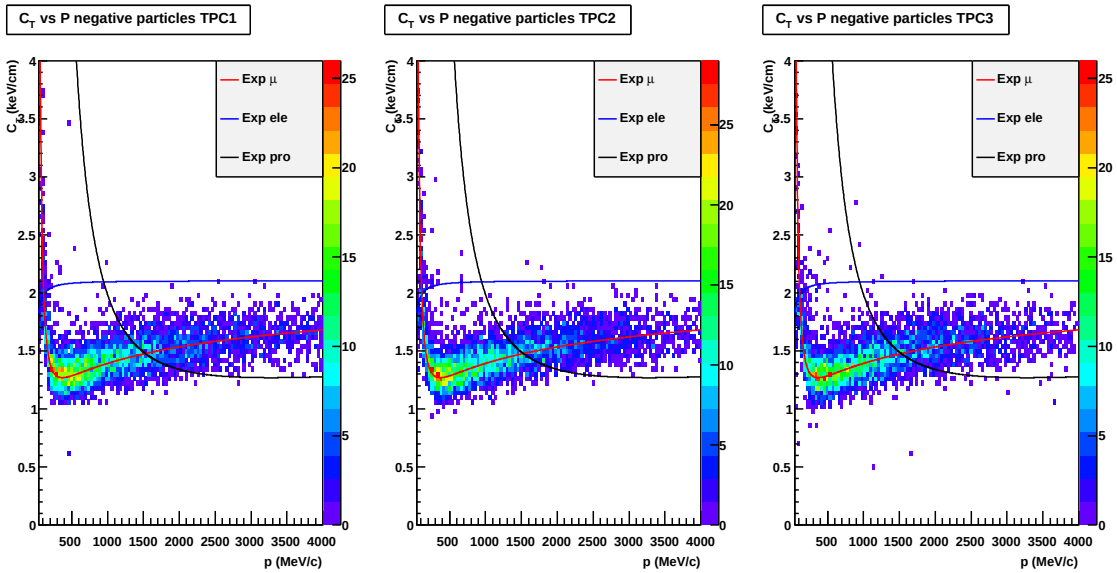

Figure 6.24: Truncated mean as a function of the reconstructed momentum for negative tracks in the three TPCs.

In figures 6.24 and 6.25 the same plots are shown for different samples in the three TPCs. An interesting result is the fact that, as it was mentioned in section 6.2 one of the MicroMegas module in the TPC3 had a lower gain during the first physics run (starting from the month of April). This would have a strong effect on the measurement of the truncated mean for tracks crossing this module, as it is shown on the left plot of figure 6.26 where we can clearly see a second set of points that have the same slope of the expected muon curve but at lower values of deposited energy. After the calibration of the MicroMegas modules (right plot of figure 6.26) this second set of points disappears and the particle identification

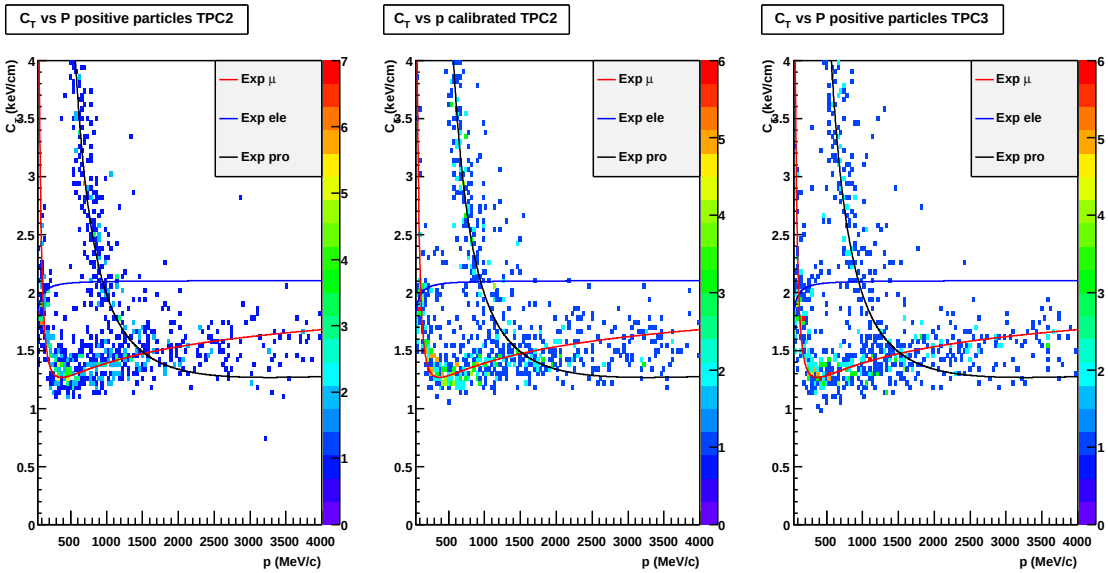

Figure 6.25: Truncated mean as a function of the reconstructed momentum for positive tracks in the three TPCs.

performances are not degraded by this problem.

We also divided the events in momentum bins to check the deposited energy resolution: the results for tracks with momenta lower than 1 GeV/c is shown in figure 6.27: the distributions are gaussian and the deposited energy resolution is of 8% for all the momenta; the values are slightly larger than in the case of the cosmics as we put together data taken during different days and no corrections for temperature and pressure are applied.

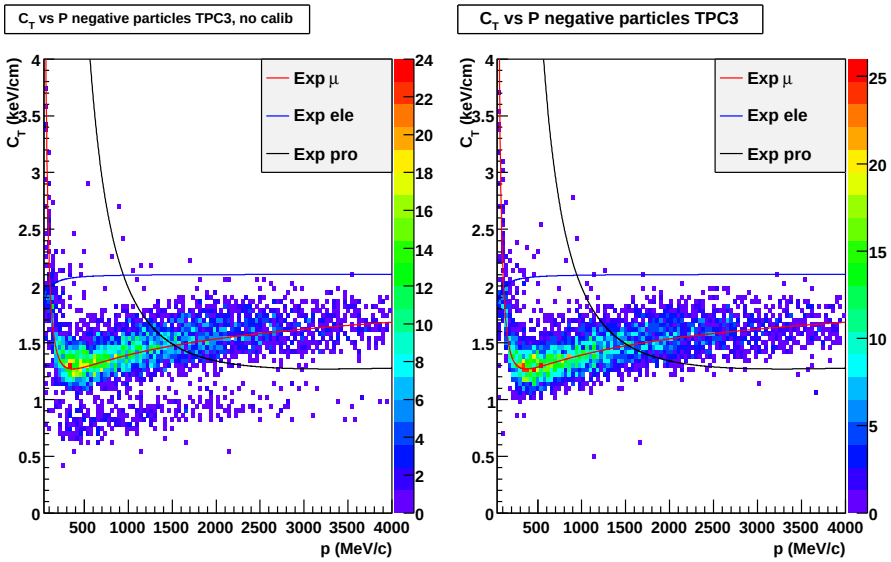

Figure 6.26: Truncated mean as a function of the reconstructed momentum for negative tracks in the TPC3 before and after the MicroMegas calibration.

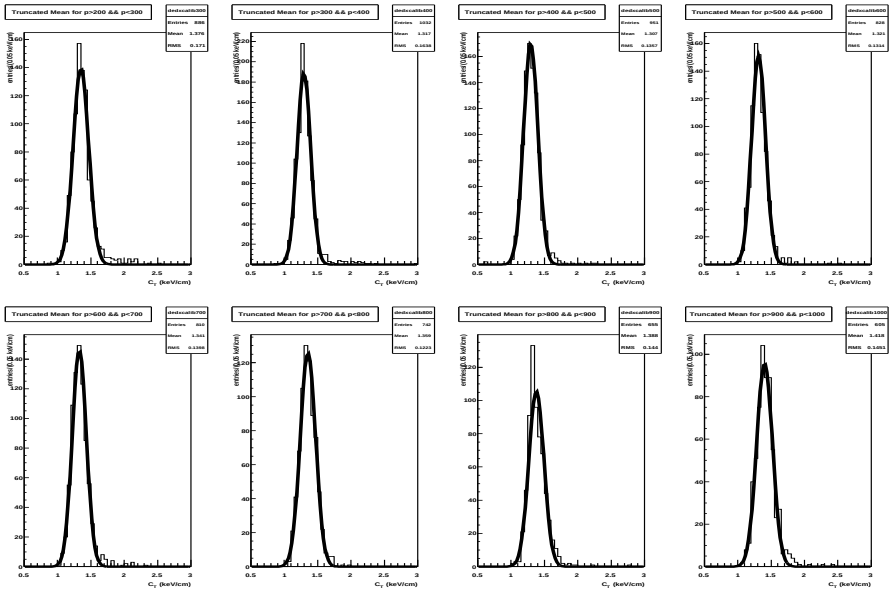

Figure 6.27: Distribution of the truncated mean for negative tracks divided in momenta intervals of 100 MeV/c from 200 MeV/c to 1 GeV/c.

6.4.5 PID performances: pulls

For the Particle Identification in the TPCs we defined the pull variable, for different particle hypothesis, given by equation 4.51. In figure 6.28 we show the distribution of the pulls δ_E obtained for the beam related tracks in the two hypothesis, muons and protons. As expected, the negative tracks are compatible with the pulls in the muon hypothesis, while for the positive tracks we have two different samples of particles: one compatible with the muons and the other compatible with the protons.

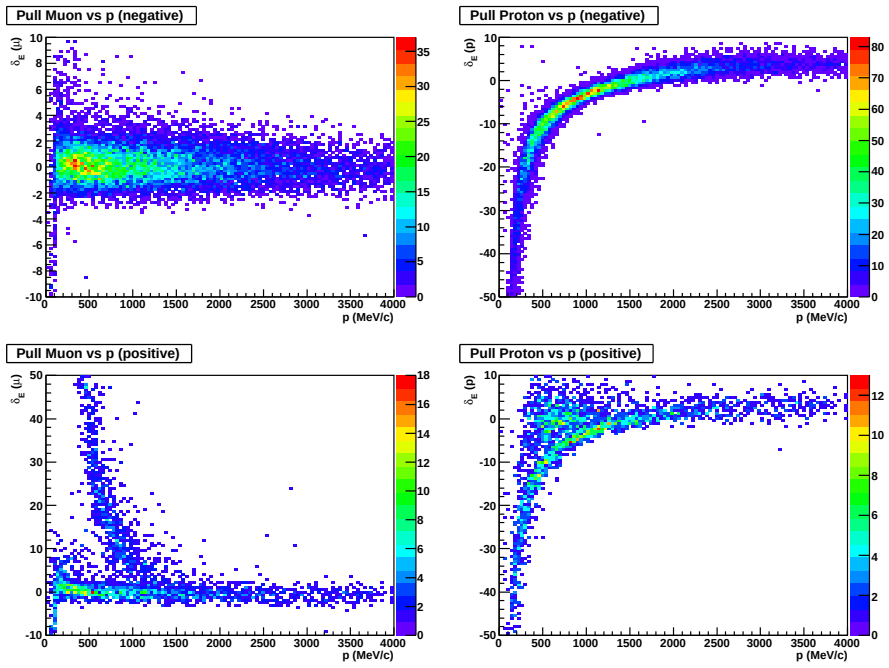

Figure 6.28: Pull distribution in the muon and proton hypothesis for negative tracks (upper plots) and positive tracks (bottom plots).

In figure 6.29 the distribution of the pull for negative tracks, with momenta between 200 and 2000 MeV/c, in the muon hypothesis and in the events with only one track per TPC is shown. The request of one track per TPC is done to select only through going muons and have in this way a clean sample of muons. The width of the distribution is slightly larger than 1. This is due to the fact that the $\sigma_o(i)$ in equation 4.51 is computed according to the expected Monte Carlo deposited energy resolution that is slightly better than the data.

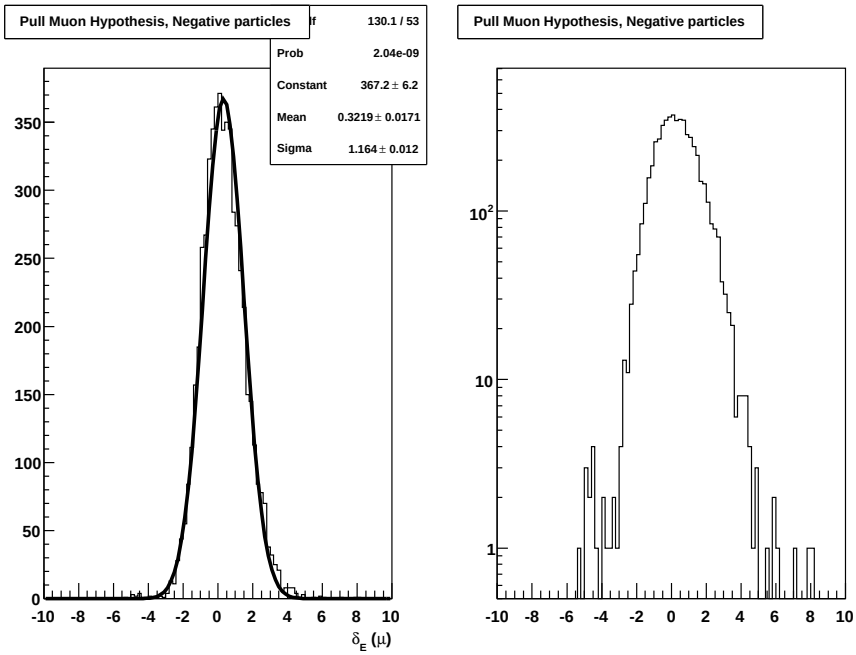

Figure 6.29: Pull in the muon hypothesis for negative tracks: on the right plot the same distribution is shown in logarithmic scale to stress the presence of electrons in the sample.

Chapter 7

Analysis of the T2K beam electron component using the ND280 tracker

In this chapter we will describe the analysis that I developed to measure the electron neutrino intrinsic component in the beam using the ND280 tracking detectors.
The analysis uses the TPC particle identification capability to select a clean sample of electrons while additional cuts have been studied to reject the remaining background, mainly coming from neutrino interactions with the production of one π^0.
This analysis is of primary importance for the T2K experiment as the intrinsic electron neutrino beam component is the main background to the electron neutrino appearance signal that will allow to measure the parameter θ_{13} of the neutrino mixing matrix.
Moreover this analysis naturally enters in this thesis work as, to recognize the small electron neutrino component in the beam, we need to fully use the particle identification methods described in chapter 4.
After an introduction on the origin of the ν_e component in the T2K beam, we will describe the analysis based on the official T2K Monte Carlo simulation.

7.1 Introduction

The main goal of the T2K experiment is the search for the electron neutrino appearance in SuperKamiokande that will lead to the measurement of the angle θ_{13} in the neutrino mixing matrix. The SuperKamiokande ν_e appearance analysis has been described in section 2.1.1.
For this measurement there are two main backgrounds: the first one coming from neutral current neutrino interactions in SuperKamiokande with the production of one π^0 decaying in

2 γs that can be misidentified as electron like ring; the second one coming from the intrinsic ν_e contamination in the beam.
The first is a reducible background that can be reduced improving the algorithms used in SuperKamiokande to recognize one ring e-like events (coming from a ν_e interaction) from two ring e-like events (coming from π^0) while the latter is an irreducible background in SuperKamiokande as the ν_e coming from $\nu_\mu \rightarrow \nu_e$ oscillation are obviously identical to ν_e already present in the beam when the neutrinos are produced. In table 2.1 we showed the expected background to the SuperKamiokande ν_e appearance analysis. As we can see from the table, the two backgrounds are of the same order of magnitude and each represent $\sim$ 10% of the signal if $\sin^2 2\theta_{13} = 0.1$.
Both backgrounds will be studied in ND280: to estimate the background coming from π^0 measurements of the cross-sections of the neutrinos interactions with π^0 in the final state will be done, mainly from the P0D and the ECAL, while for the electron neutrino component, the spectrum at ND280 will be measured by the tracker system, studying charged current neutrino interactions with the production of one electron in the final state and then it will be extrapolated to SuperKamiokande.
The expected level of the ν_e component is of the order of 1.5% (0.5% in the region between 400 and 800 MeV, that corresponds to the oscillation peak). In this chapter we will show how we can measure this component in the ND280 Tracker by studying neutrino interactions in the FGD with tracks that cross the TPCs. Also the informations coming from the ECAL particle identification will be used.
The aim of the analysis is to select a sample of charged current interactions originated from an electron neutrino. As we will see the main background to this analysis comes from electrons, indirectly produced by the decay of a π^0, that enter the TPC.
Once this measurement is done, to establish the intrinsic ν_e contamination in the ν_e appearance measurement, the measured fluxes and spectra have to be extrapolated to the far detector (SuperKamiokande). This will be done using the far-to-near ratio; this ratio has already been introduced for the ν_μ in section 2.2. For the ν_e the same quantity can be defined and as we will show it is sensibly different from the ratio in the ν_μ case.
The analysis described in this chapter is a Monte Carlo analysis, based on the simulation of the T2K beam Monte Carlo simulation, done using $JNUBEAM$. In the next sections, before starting the description of our analysis, we will introduce the origin of the ν_e component in the T2K beam and we will show how the measurements done at the Near Detector will be extrapolated to the Far Detector. These studies have been performed by T2K collaborators using $JNUBEAM$ and the data collected in NA61 experiment (see section 2.3.3): the values quoted in the next sections have been taken from the T2K-NA61 internal note [85].

7.1.1 The ν_e sources in the T2K beam

A common aspect of all the conventional neutrino beams used for long baseline experiments is that they mainly produce muon neutrinos or antineutrinos but they also have an intrinsic electron neutrino component. Measuring this component is fundamental especially in experiments, like T2K, that search for the ν_e appearance.
The unavoidable presence of electron neutrinos is one of the reasons for which non conventional neutrino beams are being studied (see section 1.5): in fact they can produce beam with a known composition of neutrino families, 100% ν_e in the case of the beta beams and 50% ν_μ and 50% ν_e for the neutrino factories.
In conventional beam, instead, a small quantity of ν_e is produced together with the ν_μ and the number and spectrum of the electron neutrinos present in the beam before the oscillation have to be measured.
The ν_e component in the neutrino beams mainly comes from two sources: the first one is the decay of kaons (charged and neutral) produced by the interactions of the primary protons with the T2K target and the second one is the decay of the muons, produced by the pion decays, in the decay tunnel.
In figure 7.1 the expected ν_e flux and the individual contributions coming from kaons and muons are shown.

ν_e sources: kaon decays In all the neutrino beams, neutrinos are produced from the interaction of a primary proton beam with a target, that in the case of the T2K experiment is made of graphite. In these interactions several mesons are produced. The great majority of them are charged pions that, being the lightest are the easiest to produce, but in the proton-graphite interaction also a fraction of kaons is produced. The charged kaons mainly decay in hadronic modes or in the 2 body leptonic mode ($K^+ \rightarrow \mu^+ + \nu_\mu$) but a non negligible part of them decay according the so called K^+_{e3} decay. This decay has a branching ratio of 5% (see [47]) and produces electron neutrinos in the final state according to the decay

$$K^+ \rightarrow \pi^0 + e^+ + \nu_e. \tag{7.1}$$

The K^+_{e3} decay occurs in the decay tunnel and the electron neutrino produced propagates together with the others neutrino towards ND280 and SuperKamiokande.
According to the Monte Carlo simulation, the expected contribution of the K^+ to the ν_e flux at the near detector is of 32%. A final remark is that the charged kaons are produced with a higher energy with respect to the one of the pions (see figure 7.1). Therefore also the neutrinos coming from K^+_{e3} decay populate the high energy part of the T2K spectrum.
Another source of ν_e comes from the K^L_0 decays:

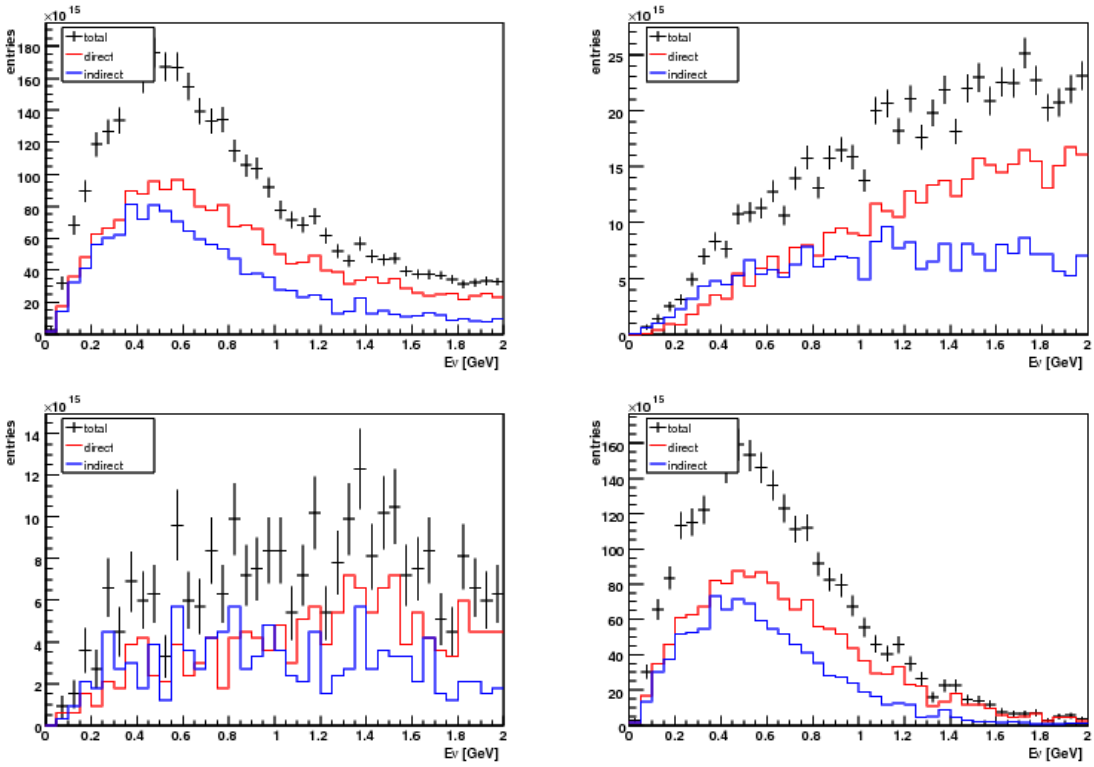

Figure 7.1: Expected ν_e flux from all the contributions (top left) from K^+ (top right), from K^0_L (bottom left) and from μ^+ (bottom right). In all the plots a direct contribution is a neutrino coming from the primary proton interaction, while an indirect contribution is a neutrino coming from reinteractions in the target or in the beamline.

$$K_0^L \rightarrow \pi^{\pm} + e^{\pm} + \overset{(-)}{\nu_e} \tag{7.2}$$

These decays contribute for 10% to the total ν_e flux at the near detector and give the main contribution (83.2%) to the $\overline{\nu}_e$ flux.

ν_e sources: muon decays The second source of ν_e comes from muons produced by pion decays together with the ν_μ. The muons have a lifetime of 2.2×10^{-6} s and therefore a small fraction of them can decay in the decay tunnel, before reaching the beam dump, according to

$$\mu^+ \rightarrow e^+ + \bar{\nu_\mu} + \nu_e \tag{7.3}$$

producing in this way electron neutrinos.
For this reason the decay tunnel can not be too long and its length has to be chosen according to a compromise between the number of pions decaying in the tunnel and the number of muon decays.
In the T2K beam the expected contribution of the μ^+ decay to the ν_e flux at the near detector is of 58%.

7.1.2 ν_e fluxes at ND280 and SuperKamiokande

In the T2K beam the expected ν_e component is 1.5% when considering all the energy range and it becomes 0.5% if we consider only the $\nu_\mu \rightarrow \nu_e$ oscillation region that is in the energy range between 400 and 800 MeV/c. This difference is due to the fact that all the ν_e sources are three body decays and in contrast with what happens for the ν_μ they are not enhanced at 700 MeV by the off-axis configuration of the T2K beam. Moreover ν_e coming from the kaons are produced at higher energy.
Given these numbers, to perform a clean analysis of the ν_e component, we need a ν_μ rejection factor of the order of 10^3.
Another important fact is that, for the reasons already mentioned in section 2.2, the neutrino spectra at the near and at the far detector are different. These differences can be seen in the figures 7.2 and 7.3 in which the expected neutrino spectra for the four neutrino types (ν_μ, $\overline{\nu}_\mu$, ν_e, $\overline{\nu}_e$) at ND280 and at SuperKamiokande are shown.

The goal of our analysis is to provide a measurement of the ν_e spectrum at the near detector. Once it will be known, with the beam Monte Carlo information, it will be possible

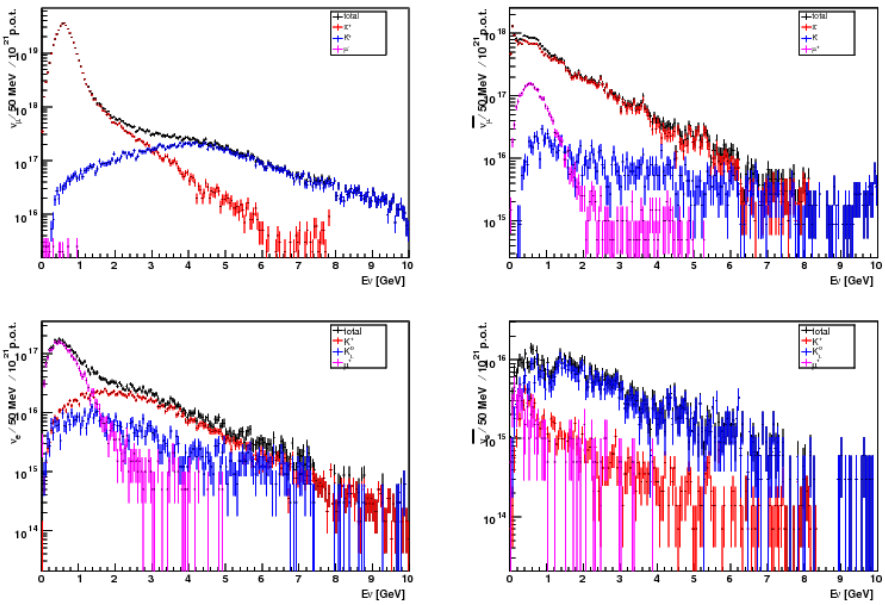

Figure 7.2: Expected composition of the ν_μ (top left), $\overline{\nu}_\mu$ (top right), ν_e (bottom left) and $\overline{\nu}_e$ energy spectra at the near detector.

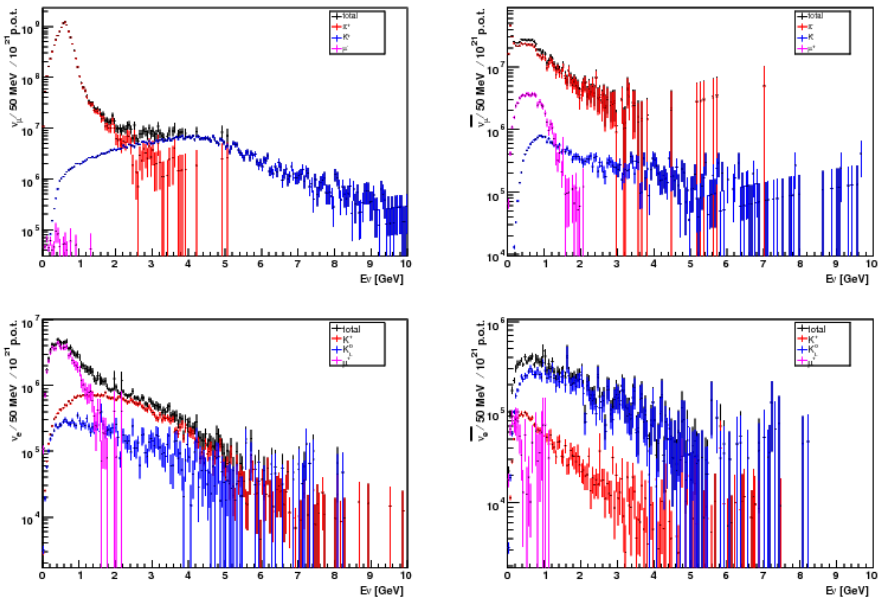

Figure 7.3: Expected composition of the ν_μ (top left), $\overline{\nu}_\mu$ (top right), ν_e (bottom left) and $\overline{\nu}_e$ energy spectra at SuperKamiokande.

to extrapolate the ν_e spectrum at the far detector, using the far-to-near ratio. This spectrum will be then compared to the observed spectrum at SuperKamiokande, to determine the neutrino oscillation parameters. This procedure is used also for the ν_μ spectra and in figure 7.4 the expected far-to-near ratios for the four neutrino types are shown.

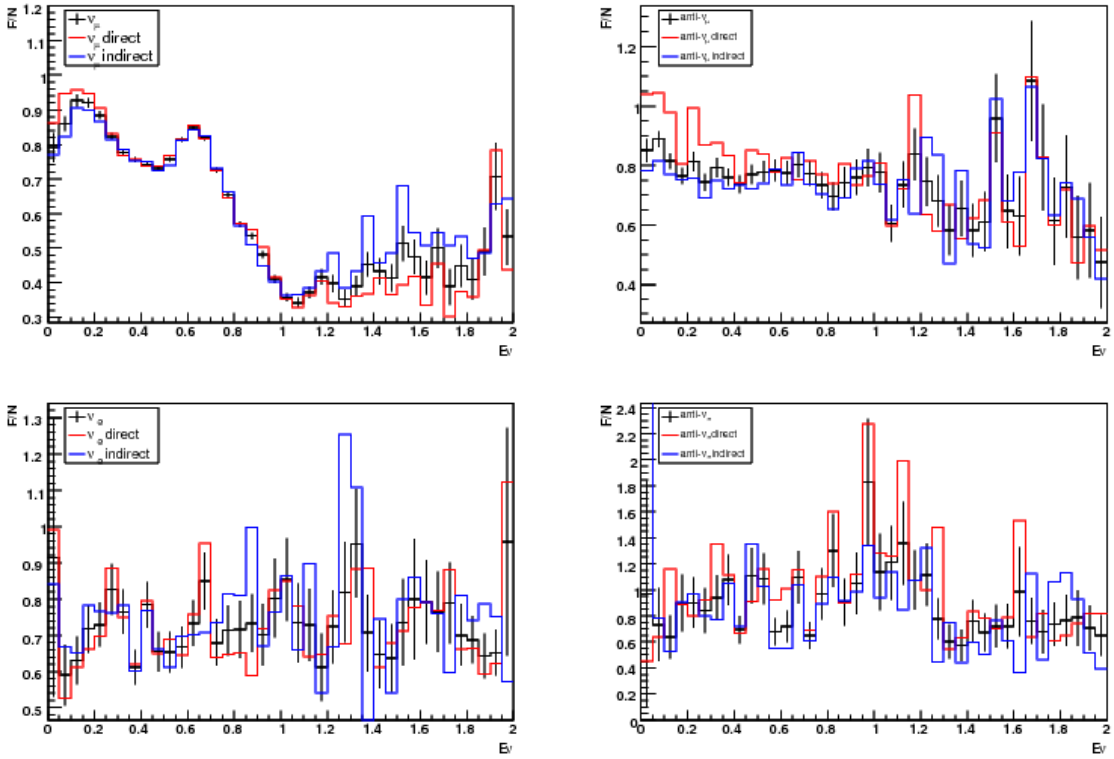

Figure 7.4: Far-to-near ratio prediction for ν_μ (top left), $\overline{\nu}_\mu$ (top right), ν_e (bottom left) and $\overline{\nu}_e$ fluxes.

As we can see from these figures, while the far-to-near ratio for the ν_μ is strongly dependent on the neutrino energy, the far-to-near ratio for the ν_e is flatter. This is due to the different solid angle at which the Near and the Far Detector see the neutrino source. In the case of the ν_μ, that comes from a two body decay, the T2K off-axis configuration enhances the solid angle effects and the far-to-near ratio is strongly different in the two detectors. In the case of the ν_e instead they come from a three body decay and the solid angle effects are not enhanced by the T2K off-axis configuration, giving a flatter far-to-near ratio.

7.2 Measurement of the ν_e component: Monte Carlo analysis

In view of the first T2K data taking we developed a Monte Carlo based analysis to measure the ν_e component in the beam using the tracker. The purpose of this analysis was to show the capability of such measurement using the TPC particle identification and also to understand which was the number of expected ν_e events in the first physics run.

7.2.1 Monte Carlo sample

We performed this analysis using samples of neutrino interactions coming from the official T2K Monte Carlo production.
The analysis has been performed in two steps: at the beginning we used a sample of 100000 interactions in the two FGDs, using the single spill mode. This means that only the particles coming from neutrino interactions were simulated and not all the particles produced by neutrino interactions in other ND280 detectors were simulated. These number of interactions correspond to 4.2×10^{20} POT (Proton On Target). This is not the case as, during the experiment data taking, neutrinos arrive to the ND280 detectors in spills. The amount of neutrinos in each of these spills depends on the power of the beam and when many neutrinos are grouped together it is possible to have neutrinos interactions in other part of the ND280 detectors producing particles (in particular photons) that can interact in the FGDs producing an additional background to our analysis. This effect has been considered using a Monte Carlo simulation in which the full spill configuration was simulated. The assumed beam power was 100 kW and considerations on this additional background are shown in section 7.3.
The neutrino interaction generator GENIE was used while the events were then simulated by the GEANT4 based package of the ND280 software.
At the T2K neutrino energy range the main interaction channel is the Charged Current Quasi Elastic (CCQE) but also non quasi elastic channels and neutral currents have important rates as it is shown in figure 7.5.

In Table 7.1 the interaction rates for the different neutrino types in the CC and CCQE channels are shown. An interesting point to notice is that the CCQE channel is more important for the muon neutrinos than for the ν_e. This is the expected behavior because the electron neutrinos component is larger at higher neutrino energy where the CCQE is not the main channel for the interactions.

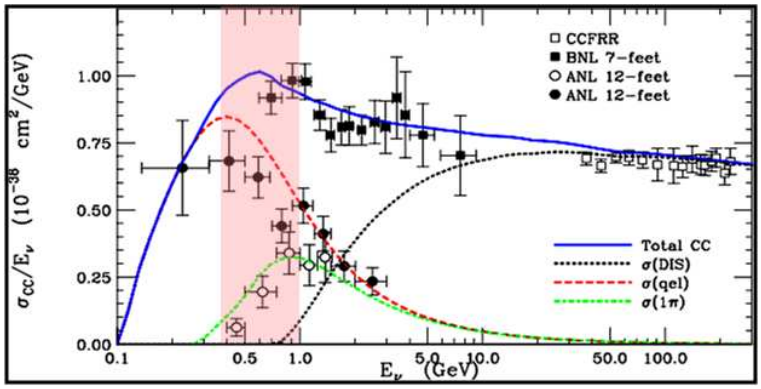

Figure 7.5: Neutrino cross-sections in the GeV region. The pink region corresponds to the energy of the T2K beam.

Neutrino type	Total interactions	%	CC	%	CCQE	%
ν_μ	94780	95.0	68624	72.4	36357	38.3
$\overline{\nu}_\mu$	3353	3.4	2262	67.4	840	25.1
ν_e	1488	1.5	1096	75.3	373	25.0
$\overline{\nu}_e$	115	0.1	78	67.8	20	17.4

Table 7.1: Neutrino interaction samples and rates in the MDC0 files used for the analysis.

7.2.2 Particle Identification methods

The ν_e analysis is mainly based on the TPC capability to distinguish muons from electrons. The methods developed to distinguish the two leptons are fully explained in chapter 4 and the TPC particle identification performances has been described in chapter 5. As a reminder the particle identification in the TPCs is based on the measurement of the truncated mean $\overline{C}_T$ of the energy released by the charged particles that cross the TPC gas. This quantity has been defined in 4.43.
$\overline{C}_T$ is a function of only $\beta\gamma$ and once the momentum is measured it allows to distinguish the different charged particles crossing the TPC. To quantify the particle identification we defined, in the formula 4.51, the pull variable $\delta_E(i)$.
In the analysis we also use the ECAL Particle Identification to reject a fraction of the muon background. This method distinguishes tracks from showers in the electromagnetic calorimeter and is explained in [84].

7.2.3 Lepton track selection

The strategy for this analysis is to select the lepton track produced in the neutrino interactions and then to use the Particle Identification method to select the electron sample. The typical interaction in the FGD is the CCQE interaction shown in figure 7.6:

$$\nu_l + n \rightarrow l^- + p \tag{7.4}$$

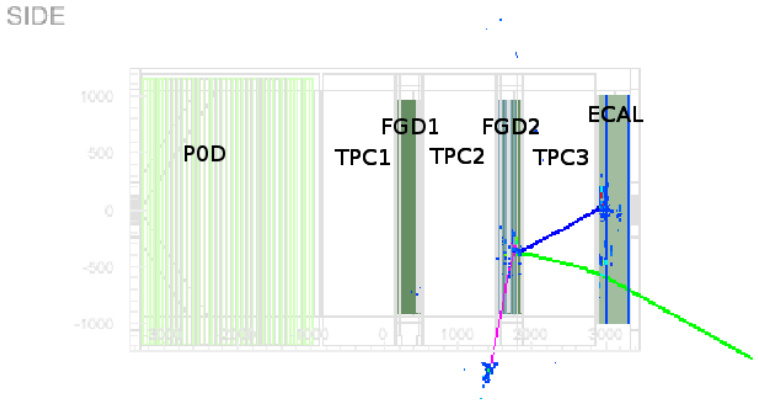

Figure 7.6: Event display of a simulated neutrino interaction in the second FGD. The green track is a muon, the blue is a proton and the pink is a neutron.

where l is the lepton (e or μ). The lepton track in this event will be unambiguously identified by the fact that the track has a negative charge. Other interactions, with the production of several negative tracks are possible and in this case we will select as the lepton candidate the track with the larger reconstructed momentum.
The lepton track selection used in this analysis is the following:

1. We select the negative track with the largest momentum in the TPC2. If no tracks are found in the TPC2, we select the negative track with the largest momentum in the TPC3

2. We require that the starting point of the track is in the corresponding FGD fiducial volume (FGD1 for tracks in TPC2 and FGD2 for tracks in TPC3)

3. We require additional criteria on the curvature to select a track as negative (see equation 7.5)

Here the TPC are labeled following the ND280 convention (see figure 7.6): the TPC1 is downstream of the P0D, the TPC2 is downstream of the first FGD, and the TPC3 is downstream of the second FGD.
A vertex in the FGD fiducial volume is defined as a vertex in the FGD inner volume, excluding the outer 10 cm in X and in Y and the first and last 1 cm in Z.
To select a negative track we based the definition on the curvature measurement. The curvature is well defined for low momentum tracks while for tracks with momenta larger than 1 GeV/c the curvature is smaller and it is more difficult to unambiguously define the charge of the track. For this reason to improve the efficiencies of our analysis we implemented a charge selection dependent on the reconstructed momentum. For low momentum particles ($p < 1\ GeV/c$) we defined a track as negative if it is negative at 2 σ that means that, defining the curvature C and its error $\sigma(C)$ to select the track as negative we require

$$C + 2\sigma(C) < 0 \tag{7.5}$$

If instead the reconstructed momentum is large ($p > 1\ GeV/c$) we only required $C < 0$.
In Table 7.2 a summary of the effects of the cuts on the number of selected events of signal and background is shown. We consider as a signal (N_S) events in which the selected track has been produced by a ν_e interaction in the FGD while the events originated by a ν_μ interactions are considered as background (N_b). The efficiency is then computed as:

$$E_{sel}(k) = \frac{N_S(k)}{N_{\nu_e}^{CC}} \tag{7.6}$$

where k is the cut index and $N_{\nu_e}^{CC}$ is the total number of charged current ν_e interaction in the sample (1096 interactions). In the table also the Figure Of Merit (FOM) is shown. The FOM is defined as:

$$FOM(\alpha) = \frac{N_S}{\sqrt{(N_S + N_B + (\alpha N_B)^2}} \tag{7.7}$$

The reason for including the FOM is that our knowledge of the background, due to the uncertainties in the neutrino cross-sections, is limited and the use of the FOM is a way to keep into account these systematic effects. We used three different values of α, 0, 0.1, 0.2. $\alpha = 0$ corresponds to an analysis without systematic uncertainties on the background, $\alpha = 0.1$ and $\alpha = 0.2$ correspond to a systematic uncertainty of 10% and 20% respectively. Given the small numbers of ν_e that we expect for the first period of the T2K data taking, the analysis proposed here has been optimized to get the best possible efficiency with reasonable level of purity.
In terms of FOM better results can be obtained, changing the lepton selection, by selecting the most energetic track of the event, without any request on the particle charge and then, once the track is selected, requiring that the charge is negative.

Cut type	N Sel signal (ν_e)	N Sel back (ν_μ)	Efficiency (%)	FOM ($\alpha = 0$)	FOM ($\alpha = 0.1$)	FOM ($\alpha = 0.2$)
TPC Track	722	42646	65.8	3.5	0.17	0.085
FGD FV	488	29290	44.4	2.8	0.17	0.083
Negative curvature	443	26143	40.3	2.7	0.17	0.085
TPC PID	354	2322	32.2	6.8	1.5	0.76
$P > 200\ MeV/c$	249	421	22.7	9.6	5	2.8
1 elike track	184	174	16.8	9.7	7.2	4.6
ECAL PID	180	134	16.4	10	8.1	5.6

Table 7.2: Summary of the ν_e analysis cuts: selected events, efficiencies and Figure Of Merit.

Cut	Total Signal	e^- (ν_e)	μ^- (ν_e)	e^+ (ν_e)	p (ν_e)	π (ν_e)	Total Back	e^- (ν_μ)	μ^- (ν_μ)	e^+ (ν_μ)	p (ν_μ)	π (ν_μ)
Elike tracks	184	184	0	0	0	0	174	101	44	3	14	12
ECAL PID	180	180	0	0	0	0	134	98	9	3	13	11

Table 7.3: Particle ID of the tracks selected in the last analysis steps.

7.2.4 Electrons selection

Once the lepton is selected we separate electrons from muons. This can be done using the equation 4.51. The pull distribution $\delta_E(i)$ in the electron hypothesis is shown in figure 7.7: as expected this distribution is not centered at zero because, given the ratios between ν_μ and ν_e in the T2K beam, at this stage of the analysis we mainly selected muons.
To select the electron sample we cut on the value of $\delta_E(i)$, requiring $-2.5 < \delta_E(i) < 3$. In figure 7.8 we show the distribution of $\delta_E(i)$ for events in which the interaction was originated by a ν_e.

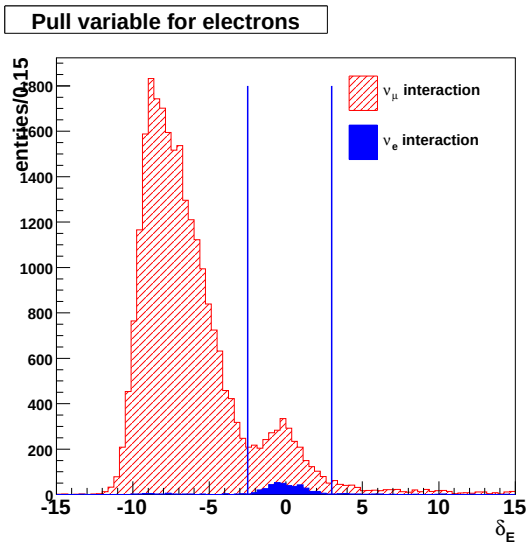

Figure 7.7: Pull distribution in the electron hypothesis. As the majority of the tracks at this point of the selection are muons the pull distribution is not centered at zero.

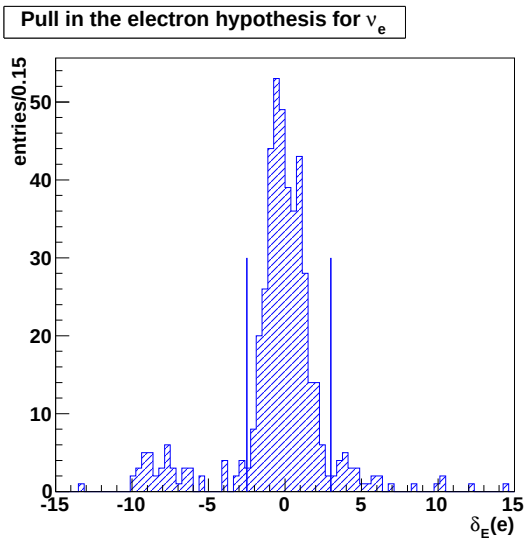

Figure 7.8: Pull distribution in the electron hypothesis for ν_e interactions. The red lines correspond to the cut used in the analysis.

At this point we add a cut on the reconstructed momentum, by requiring that the particles have a reconstructed momentum in the TPC larger than 200 MeV/c. The reasons for having this cut are the following:

- As it can be seen in figure 4.19 the curve of the energy deposited by a muon is flat until 200 MeV but at lower momenta it starts to increase as β^{-2} and it crosses the electron curve approximately at 150 MeV/c: in this region it will not be possible to distinguish electrons from muons using only the TPC PID;
- As we will show later, the main background to this analysis comes from neutrino events

with the production of π^0 in the interaction. The distribution of the electrons produced is typically softer with respect to the electrons produced by the ν_e interactions.

For these reasons including tracks with energy lower than 200 MeV/c will increase both the muon and the π^0 background. In figure 7.9 we show the momentum of the events selected before the cut on the reconstructed momentum. As we can see in the first two momentum bins that corresponds to particles with momenta smaller than 200 MeV/c the events coming from ν_μ interactions are much more than the events coming from ν_e interactions.

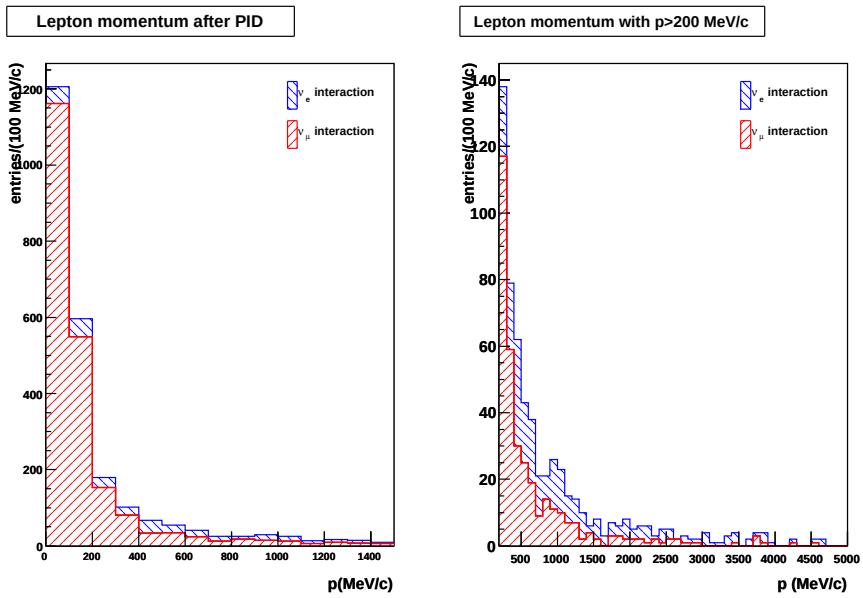

Figure 7.9: Momentum distribution for signal (blue) and background (red) after the PID selection: on the left plot all the momenta are shown, on the right plot only the events with momenta larger than 200 MeV/c.

With this selection we select a sample of particles mainly composed of electrons (see Table 7.3) with a contamination of misidentified muons and few misidentified pions. Nevertheless a large fraction of electrons do not come from a ν_e interactions but from a ν_μ interaction in which the selected electron comes from the conversion of one of the two γs produced in a π^0 decay. This can happen in two cases. The first case is a neutral current interaction in which no muons are produced and one of the electrons is selected as the most energetic particle. The second case is a charged current interaction in which one of the electrons produced in the π^0 decay is reconstructed with a momentum larger than the one of the muon or the muon, because of the geometrical acceptance, is not reconstructed.
As we can see from the Table 7.2 at this stage of the analysis the sample is composed of 37% of ν_e interactions. In figure 7.9 the momentum distribution for the signal and the background

is shown. As expected the background is mainly concentrated at low momenta given the softer spectrum of the π^0.

7.2.5 Background rejection in the electron sample

As we show in Table 7.2 with the cut on the pull in the electron hypothesis we select a sample composed mainly of ν_e events but with a large component of electrons and other particles coming from ν_μ events.
We studied two additional cuts to reject the background:

- Number of $e-like$ reconstructed track in the TPC
- Particle Identification in ECAL

In the next paragraphs we will explain these two cuts.

Number of $e-like$ tracks As we already discussed the main background in the ν_e analysis comes from events in which an electron coming from a π^0 is selected. These background tracks come from the conversion of one of the two γs produced by the π^0 decay while the signal comes directly from a ν_e interaction.
In both cases the particle selected is an electron so it is not possible to distinguish between the signal and the background using the Particle Identification methods developed for the ND280 detectors.

One possibility studied here to distinguish the events is the multiplicity of e-like tracks. An e-like track is defined as a reconstructed track with a value of the pull in the electron hypothesis $|\delta_E(e)| < 3$. In figure 7.10 is shown the number of reconstructed tracks (without including the selected one) that are e-like.
As we can see in the case of ν_μ events in almost 50% of the cases there are one or more e-like reconstructed tracks, while in the case of ν_e events only in 20% of the cases there are other e-like reconstructed tracks. We introduce a cut rejecting from the analysis all the events in which there is more than one reconstructed e-like track.
In the case of the signal the tracks mainly come from a shower produced by the electron in the FGD and looking at the topology of the event in the FGD it will be probably possible to distinguish between the signal and the background.
In Table 7.2 are shown the number of events, the efficiencies and the FOM after this cut.

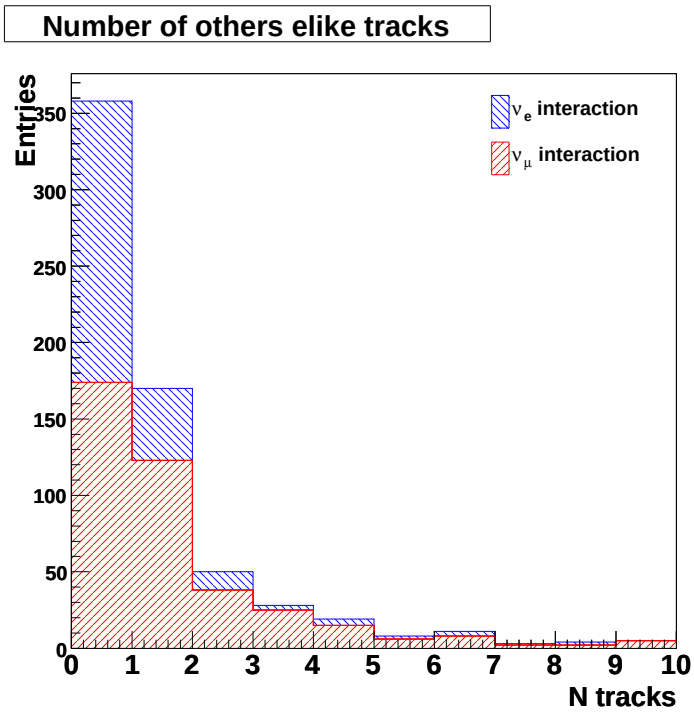

Figure 7.10: Number of e-like reconstructed tracks in the TPC for the ν_e signal (blue) and the ν_μ background (red) events

Particle Identification in ECAL As it is shown in the Table 7.3 another part of the background comes from particles that are misidentified by the TPC Particle Identification methods. In these events the truncated mean or the reconstructed momentum is not correct and the pulls do not provide the correct identification of the particle.
As we can see from the Table 7.3 this background, even if is not dominant is not negligible and the analysis can be improved considering the information provided by ECAL.
To use this information we perform a matching between the end point of the reconstructed TPC track and the starting point of the reconstructed ECAL shower or track. We considered that the TPC track and the ECAL cluster match if $|X_{TPC} - X_{ECAL}| < 30\ cm$, $|Y_{TPC} - Y_{ECAL}| < 30\ cm$ and $|Z_{TPC} - Z_{ECAL}| < 30\ cm$.

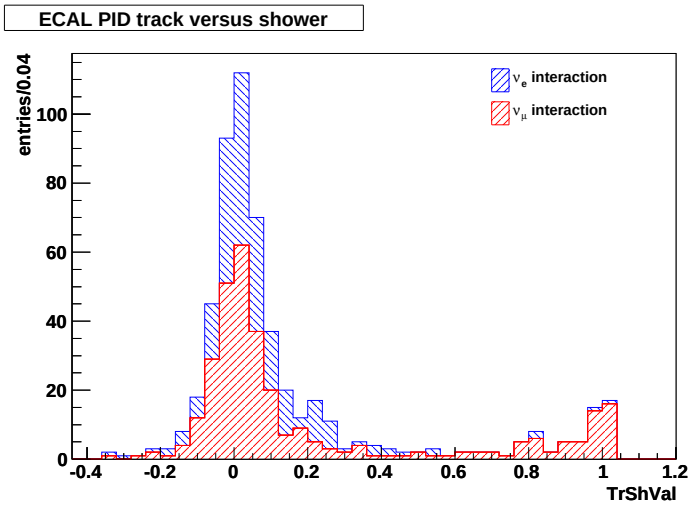

Figure 7.11: Value of the ECAL TrShVal variable that distinguishes between tracks and shower. In blue ν_e events are shown while in red there are ν_μ events.

When the match is found we look at the ECAL variable $TrShVal$ that distinguishes between tracks (that in the calorimeter corresponds to muons) and shower (electrons or hadrons). In figure 7.11 the value of this variable for ν_e and ν_μ events is shown. As we can see in the case of the ν_e there are no muons in the events and the PID variable is peaked at zero. In the case of the ν_μ interaction instead, there is a majority of the events with values around zero: these events are mainly electrons coming from π^0 selected as signal. But there is also a second class of background events in which the PID variable is of the order of 1. These events are muons and can be rejected by requiring that $TrShVAL < 0.75$.

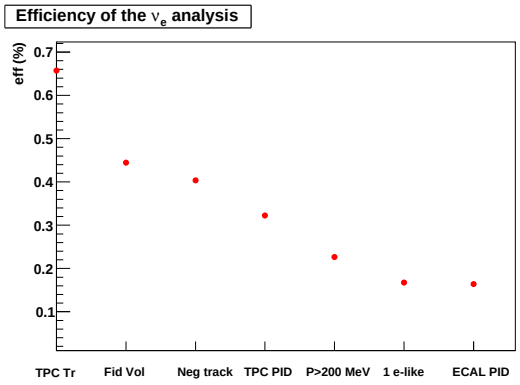

Figure 7.12: Efficiency of the analysis for the different cuts. The efficiency is given with respect to the total number of ν_e charged current interactions in the analyzed sample.

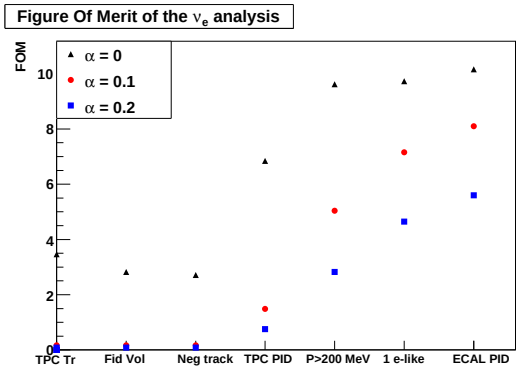

Figure 7.13: Figure Of Merit of the analysis as a function of the different cuts and for different values of the systematic errors on the background.

7.2.6 Properties of the selected sample

In figure 7.12 we show the efficiency as a function of the cuts. At the end of the analysis selection the efficiency, defined as the number of selected events divided by the total number of CC ν_e events is 16.4%. In figure 7.13 the Figure Of Merit for different values of the systematic error on the background, α, is shown. We can see that for $\alpha = 10\%$ and $\alpha = 20\%$ the quality of the analysis improves using the cuts explained in this note.

In figure 7.14 and 7.15 the momentum and angular distributions of the selected particles are shown. As we can see the background is mainly concentrated at low momenta, because the electrons originated by the π^0 have a softer spectra. Also the angular distribution is more peaked at $\cos(\theta) \sim 1$ for the ν_e events. Knowing the angle and the momentum we can also compute the energy of the neutrinos in the hypothesis of Charged Current Quasi Elastic interactions. In this hypothesis the neutrino energy, neglecting the electron mass and the Fermi nucleon motion, is given by

$$E_\nu = \frac{m_N p_e}{m_N - p_e(1 - cos\theta_e)} \tag{7.8}$$

where m_N is the nucleon mass and p_e and θ_e are the electron reconstructed momentum and angle. The neutrino energy in the CCQE hypothesis for the signal and the background is shown in figure 7.16.

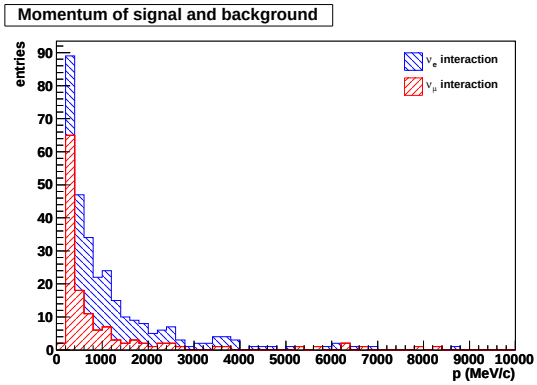

Figure 7.14: Reconstructed momentum distribution for the particles selected with the electron neutrino analysis.

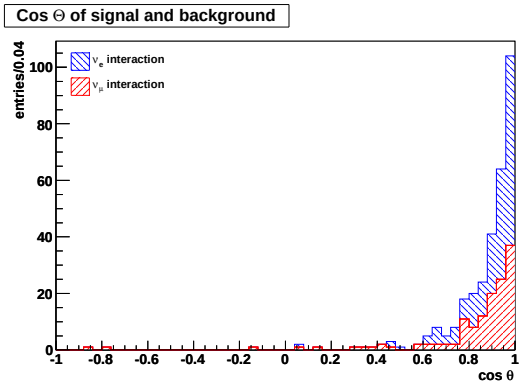

Figure 7.15: Reconstructed distribution of the cosine of the angle for the particles selected with the electron neutrino analysis.

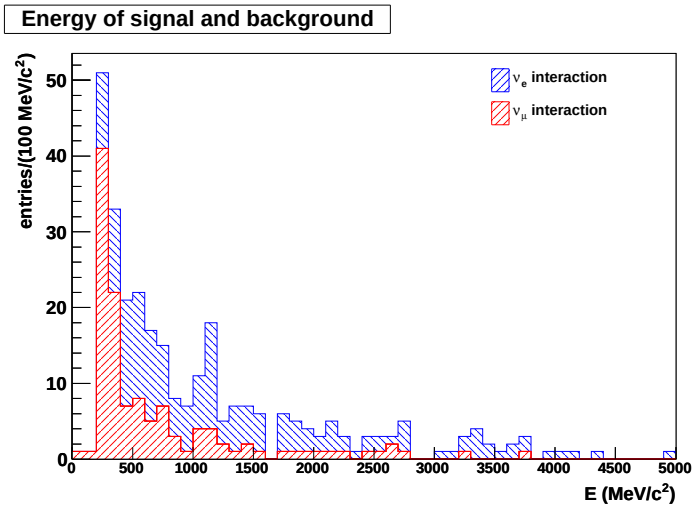

Figure 7.16: Neutrino reconstructed energy in the CCQE hypothesis for signal (blue) and background (red).

7.3 Additional background coming from full spill simulation

An additional source of background that is not considered if we only simulate one neutrino interactions in the FGD is the fact that electron tracks can come also from photons, produced by interactions in other ND280 parts (the P0D or the magnet), that convert in the FGD.
The number of neutrino interactions per spill depends on the intensity of the T2K beam, increasing if the power increases. This means that this background is not directly dependent on the power of the beam but the rejection criteria of this background that we will show in the following of this section depends on the beam intensity, giving a better rejection power if the intensity of the beam is low. We performed a study of this background in the hypothesis of a beam power of 100 kW and without considering the presence of the Barrel ECAL, that, when it will be installed, will be able to stop the majority of the photons coming from interactions in the magnet. These conditions correspond, to a good approximation, to the T2K configuration for the first physics run.
We analyzed a number of events corresponding to 1×10^{20} POT and applying the same selection explained in section 7.2 we found the results shown in table 7.4. As we can see from this table the results in terms of selection efficiency and of background coming from interactions in the FGDs are compatible with the ones observed with the table 7.2, but we have large source of background coming from interactions in other detectors that produce tracks in the tracker.

Cut type	N Sel signal (ν_e)	N Sel back (ν_μ)	N Back (ν_μ FGD)	Eff (%)	FOM ($\alpha = 0$)	FOM ($\alpha = 0.1$)	FOM ($\alpha = 0.2$)
FGD FV	114	12917	5860	46.5	1	0.088	0.044
Negative Track	107	11827	5242	43.6	0.98	0.09	0.045
TPC PID	78	1974	404	31.8	1.7	0.39	0.2
$p > 200\ MeV/c$	57	223	72	23.2	3.4	2	1.2
1 elike tr	46	115	36	18.7	3.6	2.7	1.8
ECAL PID	43	103	34	17.5	3.6	2.7	1.8

Table 7.4: Summary of the ν_e analysis results using full spill simulation: selected events, efficiencies and Figure Of Merit. The background in the second column is the total background, the one in the third column is the background coming from neutrino interactions in the FGDs.

Part of this background can be rejected using the timing information from FGDs, P0D and SMRD (in the future also the Barrel ECAL will be important for this rejection): in fact for tracks coming from interactions in other detectors we might find hits in the corresponding

detectors at the same time as the selected track hits in the FGD.
To study this background we considered as a signal all the interactions in the FGDs and as a background all the interactions in which the vertex was in another detector and we look at the difference between the mean of the time in the FGDs and the time of the hits in the P0D. As we can see from figure 7.17 in the case of the signal, as the hits in the P0D and in the FGD are not correlated, the time difference are distributed over the different bunches of the spill. In the case of the background instead the hits are correlated and the time difference is zero.

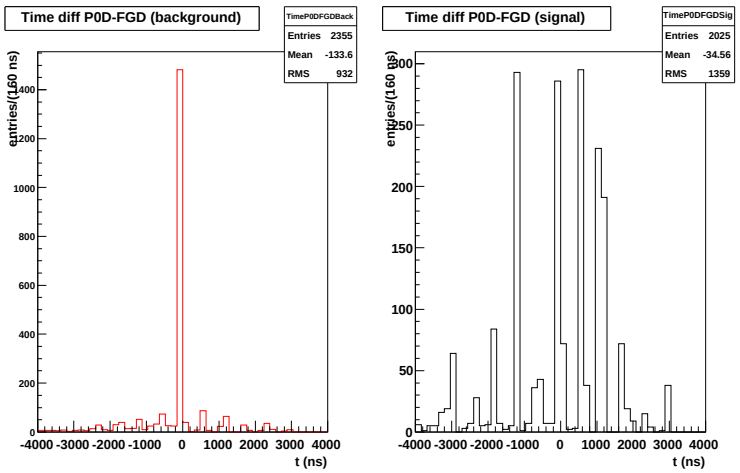

Figure 7.17: Time difference between the mean time of the FGD hits and the P0D hits in the same spill in case of interactions in the P0D (left) and in the FGD (right)

In figure 7.18 we show the time differences between the FGD and the SMRD hits. In this case, as for each spill at 100 kW we expect seven interactions in the magnet, the probability of having an interaction in the FGD and another interaction in the magnet occurring at the same bunch is high. For this reason we decided to consider only the two inner iron plates of the magnet as photons coming from interactions in the outer part of the magnet will have a low probability of arriving to the FGDs.

To reduce the background we decided to reject all the events with hits with time difference smaller than 200 ns in the P0D or in the SMRD. Adding this selection to the analysis we select 39 ν_e interactions in the FGDs with 48 events of background (32 coming from interactions in the FGDs and 16 from interactions in other part of the ND280 detectors. In figure 7.19 the momentum of the signal and the background is shown.

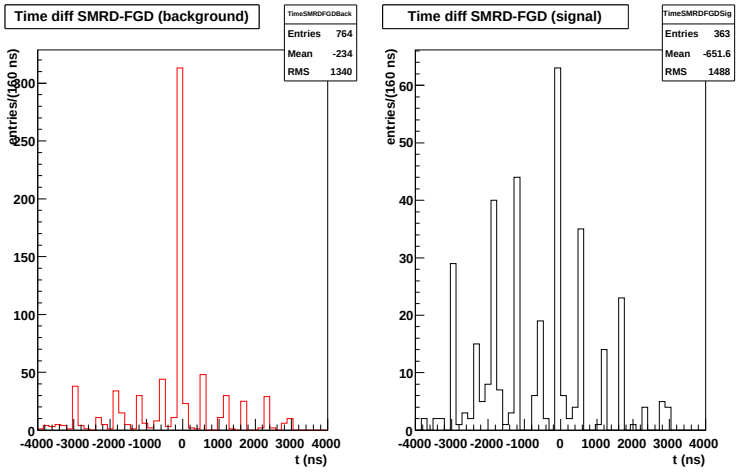

Figure 7.18: Time difference between the mean time of the FGD hits and the P0D hits in the same spill in case of interactions in the SMRD inner part (left) and in the FGD (right).

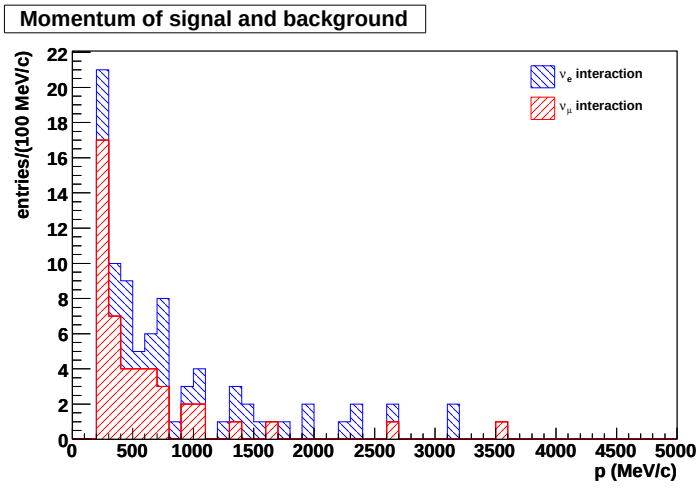

Figure 7.19: Reconstructed momentum of the electrons for signal (blue) and background (red).

The analysis shown in this section is only a first study of the background coming from interactions outside the tracker. It will be very important to carefully study this background in the future as it will be proportional to the beam power and when the beam will reach the nominal power of 750 kW this background will be much larger than in the case of 100 kW. It will be important to check the effect of the barrel ECAL that will probably stop the majority of the photons coming from the magnet but will also be the target of other neutrino interactions that could produce a background to the ν_e analysis.
Another possibility to perform a better analysis will be to try to measure this background as we will show in the next section.

7.4 Measurement of the electromagnetic background

As we have shown in the previous sections of this chapter we will be able to identify a ν_e interaction in the tracker with a purity of the order of 50 %. The background to this measurement mainly come from electrons not coming from ν_e and, in smaller part, from misidentified muons (see table 7.3).
To have a better confidence in our measurement it would be nice not to have completely relied on the Monte Carlo to know the background but to measure it.
For what concerns the background coming from muons this can be estimated from the results of the M11 beam tests presented in section 5.6.4. The limitation of this method is that the momentum range was lower than the one of the T2K neutrino interactions: more useful limits on this contamination will be shown in the next chapter using through going muons in the ND280 pit.
The electromagnetic background is instead more difficult to estimate as we do not have sources of this kind of events. One interesting possibility to measure it is to repeat the same analysis to select a ν_e sample but selecting the lepton not as a negative track but as a positive track. In this case the signal should be zero as electrons coming from ν_e interactions have negative charge while the electromagnetic background will be the same as a photon conversion produce an electron and a positron with the same characteristics and the probability of selecting one or the other is the same if we invert the requirement on the charge.
Doing this on the Monte Carlo sample used in section 7.3 (without the selection time selection to increase the electromagnetic background) we obtain the momentum distribution shown in figure 7.20: as expected the signal almost disappears but we have a large background coming from protons that at large momenta deposit in the gas the same energy of electrons.

This indicates that it will be very difficult to use this method to measure the electromagnetic background for all the momenta region but we can try to measure it at low momenta

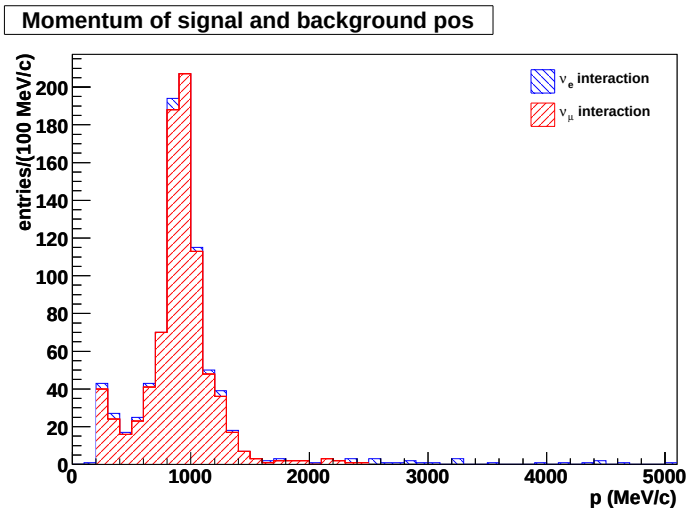

Figure 7.20: Reconstructed momentum of the electrons for signal (blue) and background (red) selecting positive tracks.

(between 200 and 500 MeV/c) where the larger part of this background is concentrated.
In figure 7.21 we show, for momenta between 250 and 500 MeV/c, the number of background events doing the positive and the negative selection. As we can see the distributions are in good agreement and we are confident that it will be possible to use this method to measure the electromagnetic background also in the data: more detailed studies will be presented in the next chapter.

7.5 Conclusions

In this chapter we have shown the results of the Monte Carlo analysis of the ν_e component in the T2K beam. We showed that, doing a charged current analysis and using the Particle Identification in the TPC and in ECAL we are able to select a clean sample of electrons with small contamination of others particles.
The majority of these electrons come from ν_e interactions in the FGD but a not negligible part of them comes from ν_μ interactions with the production of a π^0. Methods to reject this background have been studied and presented here.
At the end of the analysis we are able to select ν_e CC events with an efficiency of 16.4%. The total number of ν_e interactions found is 180 while the total background is 134 events.

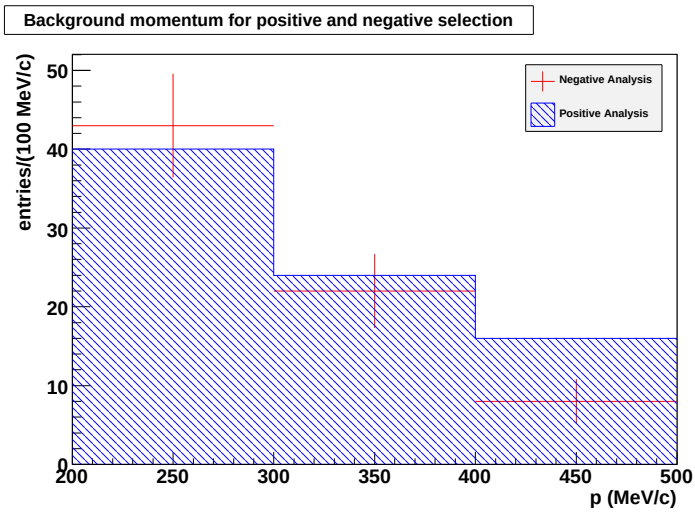

Figure 7.21: Reconstructed momentum for background with positive (blue area) and negative (red cross) selection.

We also developed methods to reject the background coming from neutrino interactions in other ND280 detectors and methods to measure the electromagnetic background. These ideas need to be better investigated in the future when all the ND280 detectors will be installed and a larger number of data and Monte Carlo events will be available.
The number of simulated neutrino interactions roughly corresponds to the expected number of neutrino interactions in the FGD in two years of data taking at the power of 100 $kW \times 10^7$ sec.

Chapter 8

Selection of neutrinos interactions in the Tracker with the first T2K physics run

T2K started its first physics run in January 2010. This physics run ended at the end of June 2010 for a summer shutdown.
In this chapter we will describe the selection that we developed to identify charged current interactions in the FGDs looking at the lepton track entering the TPCs: the purpose of our analysis is to measure the ratio between the ν_e and the ν_μ component in the beam: to do this we need to select both, ν_μ and ν_e, measuring their interaction rate and their spectra: as we will show this can be done using the TPC PID.
The goal of our analysis is to select an inclusive sample of charged current ν_μ interaction and an inclusive sample of charged current ν_e interactions. The latter will be used to measure the ν_e component in the beam while first will be used as normalization factor.
In particular for the analysis of the ν_e we have also developed methods to measure on the data the two possible backgrounds to the ν_e, already introduced in chapter 7: the muonic and the electromagnetic backgrounds.
Due to the lack of statistics and time constrains not all the selection criteria shown in chapter 7 has been used on the data for the ν_e selection. In particular the use of the other detectors as a veto and the use of the PID in ECAL were not applied to the data: this decrease the purity of our ν_e sample. In the future better results could be obtained by using these selection criteria.

8.1 The first T2K physics run

This analysis has been performed on all the data registered by ND280 during the first T2K physics run in the accelerator Runs 31, 32, 33 and 34 between March and June 2010. The official data quality selection has been applied on these data. In figure 8.1 the accumulated number of POT over this period is shown. In Table 8.1 the number of POT during the different accelerator runs and used for this analysis is shown.

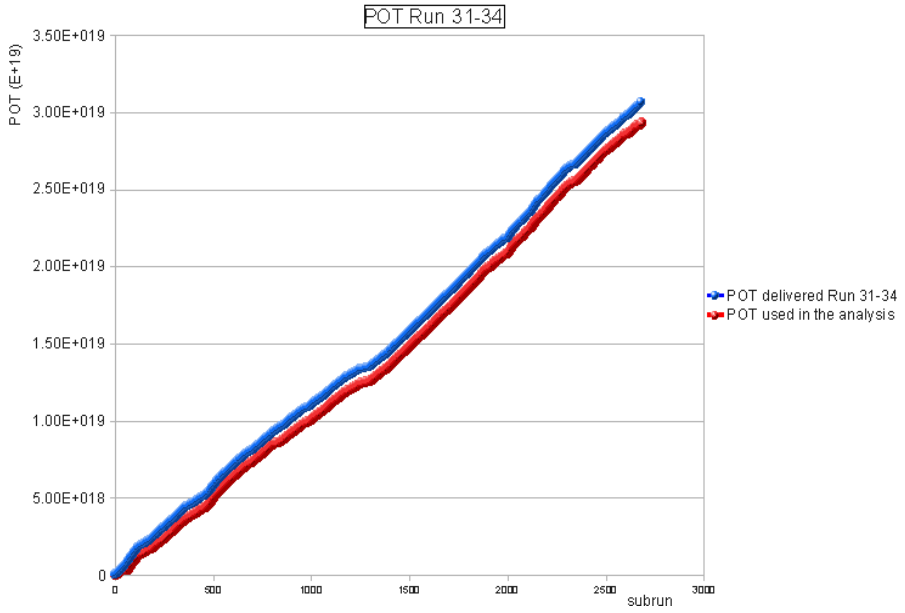

Figure 8.1: Integrated number of Proton On Target delivered to ND280 detectors during the first T2K physics run and integrated number of Proton On Target used in the analysis presented in this note as a function of the ND280 acquisition subrun.

For the Monte Carlo simulation we used the official MCP1 production that reproduces the configuration of the first T2K physics run. Simulations using two different generators for the neutrino interactions, GENIE[87] and NEUT[86], are available. We performed the analysis using both the generators but in this chapter we will show only results compared to GENIE. The statistics used in the Monte Carlo is 4.94×10^{20} POT and we also used a special sample containing only ν_e interactions corresponding to 3×10^{21} POT.

8.1.1 The selection criteria

The ND280 software provides a global reconstruction through all the detectors of all the reconstructed tracks. This global reconstruction is sensible to possible problems in the

Run	POT 10^{19}
31	0.15
32	0.74
33	1.17
34	0.88
Total	2.94

Table 8.1: POT used in the analysis for the different accelerator Runs of the first T2K physics run.

alignment between the detectors and in the individual detectors reconstruction. The goal of our analysis is to select interactions without using the global reconstruction but using only the reconstruction in the TPC and a list of hits in the FGD that were then associated to the extrapolated TPC track to define a vertex.
FGD hits are associated to the TPC tracks with a simple algorithm. TPC2 (TPC3) tracks are extrapolated back to FGD1 (FGD2), using a linear extrapolation in the x-z plane, a circle in the y-z plane. For each hit the distance from the track is computed and the hit is considered to be associated to the track if the distance between the extrapolate track and the hit in the FGD, Δx (in case of vertical bars) or Δy (in case of horizontal bars) is less that 3 cm in absolute value (see figure 8.2). In this way, we define for each track a starting point in the FGD, that is the associated FGD hit with the lowest z. To define a time of the event, we consider the minimum time of all the FGD hits associated to the track.

Once the association is done we need to define the selection criteria to select the events. The definition these criteria has been guided by these considerations:

- the copious (ten times more abundant than neutrino interactions in the tracker) background from through-going muons, produced by neutrino interactions in the sand or the concrete wall of the ND280 pit;
- the background from neutrino interactions in the magnet, producing both tracks that enter the basket from the sides and also producing neutral particles that may interact in the FGD;
- the goal to retain a high efficiency;
- the goal to use simple selection criteria.

Taking into account all these points we defined the following selection criteria:

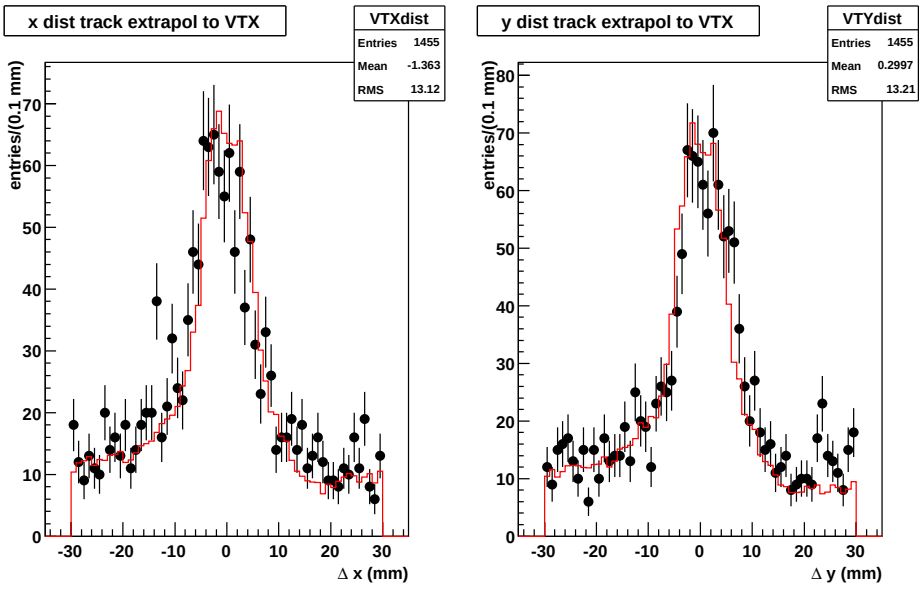

Figure 8.2: Distance between the position of the hits associated as the vertex and the track extrapolation

1. Use only events associated to beam trigger;
2. No track in TPC1;
3. At least one track in TPC2 with FGD point in the fiducial volume in FGD1;
4. We select the track with the highest momentum and then we require this track to be negative: we call it the lepton;
5. If there is no track in TPC2, redo 3. and 4. for TPC3 and FGD2.

Here we require that the TPC tracks contain at least 36 clusters. The fiducial volume (FV) is defined as following: the FGD point x and y should be smaller than 80 cm in absolute value, and it should not be in the first (lowest z) layer of FGD, that is z>140 mm (FGD1) and z>1530 mm (FGD2). The total volume is 1.6x1.6x0.33 = 0.85 m^3 for one FGD.

These first cuts are common to both the ν_e and the ν_μ selection, with the exception of cut *i*4.: in the case of ν_μ analysis instead of selecting the track with highest momentum and then require it to be negative, we select the most energetic track among the negative tracks.

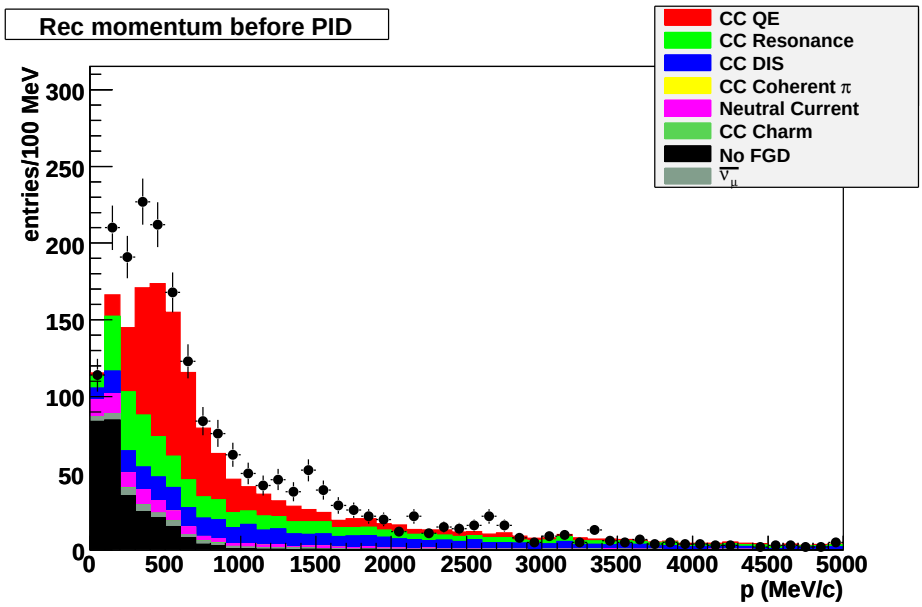

Figure 8.3: Momentum distribution of the lepton momentum for the selected events.

The momentum of the selected lepton track in data and MC is shown in figure 8.3 and the time distribution, where we can clearly see the six bunches of which is composed each spill, is shown in figure 8.4.

After the selection of the lepton track we can use the TPC PID to select electron or muons. The distribution of the truncated mean C_T as a function of the reconstructed momentum for the lepton track in data and MC is shown in figure 8.5. As we can see from this figure the majority of the tracks are compatible with the muon hypothesis but we can also see some electrons and some protons. Using the pull δ_E defined in 4.51, we can select alternatively muons or electrons. To select muons we require that the absolute value of the pull in the muon hypothesis is smaller than 2 while to select electrons we require the pull in the electron hypothesis to be $-1 < \delta_E(e) < 2$ and we also require $\delta_E(\mu) > 2.5$. The reason of the different cuts will be explained in section 8.3.1.

8.1.2 Analysis efficiencies

Before describing the results of the analysis we start describing the efficiencies for ν_μ and ν_e analysis: we studied the efficiency of the ν_μ selection a function of the neutrino energy and the position of the vertex in the FGD.

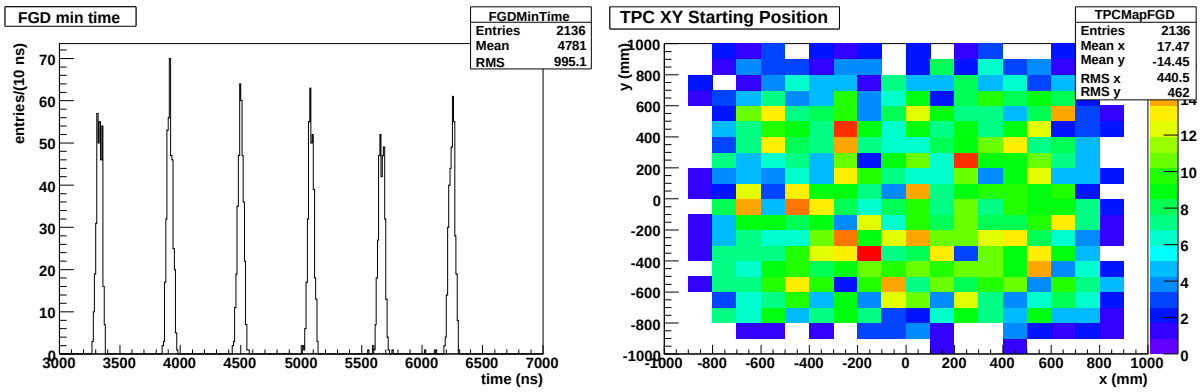

Figure 8.4: On the left plot: time of the selected event in the FGD where six bunches are clearly visible; on the right plot starting position of the selected track in the TPC: no accumulation on the edges is visible and this indicates that the selected tracks are not entering from the side.

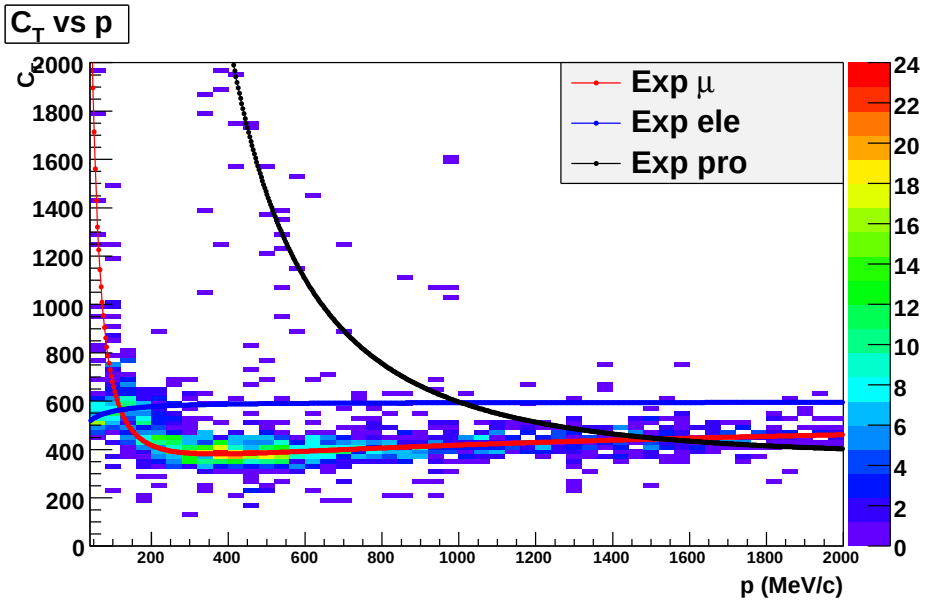

Figure 8.5: Distribution of the reconstructed truncated mean as a function of the momentum for the lepton track, with superimposed the expected distributions for muons, electrons and protons.

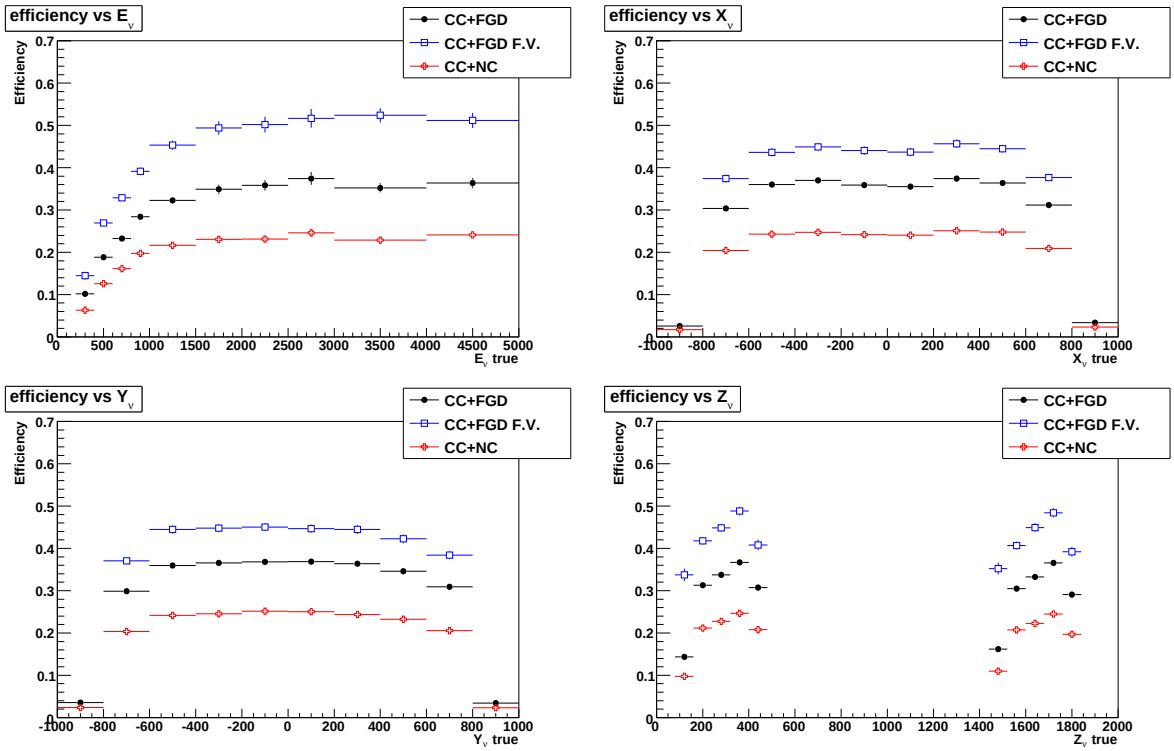

Figure 8.6: Efficiency vs E_ν (upper left), X_ν (upper right), Y_ν (bottom left), Z_ν (bottom right).

The study was done separately for these three samples, namely:

1. all interactions in the FGD both CC and Neutral Current (NC);
2. CC only interactions;
3. CC interactions in the FGD fiducial volume.

These contributions are shown separately in figures 8.6. The overall efficiency of our analysis is 18% with respect to the total number of interactions in the FGD and $38.3 \pm 0.2\%$ with respect to the charged current interactions in the FGD Fiducial Volume.

In figure 8.7 we show the efficiency of the ν_e analysis as a function of the neutrino energy. The overall efficiency of the analysis is $29.9 \pm 0.7\%$ with respect to charged current interactions in the FGD Fiducial Volume ($22.4 \pm 0.6\%$ for electron momentum below 2 GeV).

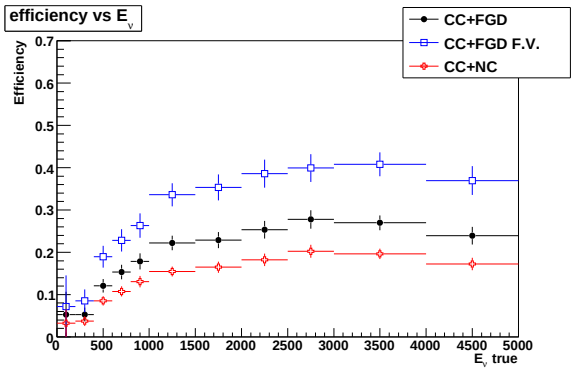

Figure 8.7: Efficiency of the ν_e analysis as a function of the neutrino energy (GENIE).

The smaller efficiency with respect to the ν_μ analysis is due to the different cut $i4.$ and to the tighter PID criterion described previously.

8.2 Muon neutrino sample in the tracker

The selection of muon neutrino interactions is important for our purposes because they will provide the normalization factor for the measurement of the $N(\nu_e)/N(\nu_\mu)$ ratio. ν_μ interactions are selected using the PID cut described above. After applying the PID muon selection we obtain a sample of 1455 events (1360 expected according to the Monte Carlo). In figure 8.8 we show the number of interactions candidates selected by our analysis as a function of the integrated number of POT. As expected this number growth linearly with the POT. In figure 8.9 we show the number of points for the reconstructed tracks: the majority of them cross all the TPCs and then the number of points is 72.

Various distributions relative to this sample are shown in figure 8.10 while in Table 8.2 the fractions of the different interactions classes and backgrounds as estimated by the MC simulation types are reported.

The level of background with interactions outside the FGD has been confirmed by a visual scanning of the selected events. The fraction of Neutral Currents has been estimated using the MC simulation. Subtracting these two contributions we estimate that our sample contains $N_{sel}(\nu_\mu) = 1324$ events due to ν_μ CC interactions in the FGD.
From this study we can conclude that we can select with high efficiency a rather pure sample of ν_μ interactions. The Monte Carlo simulation reproduces generally very well the various

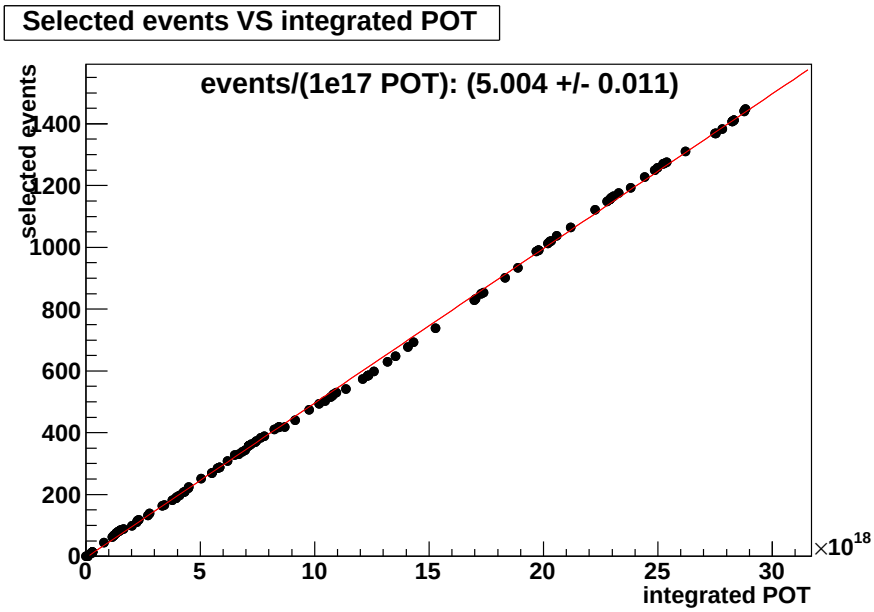

Figure 8.8: Number of selected events vs integrated POT.

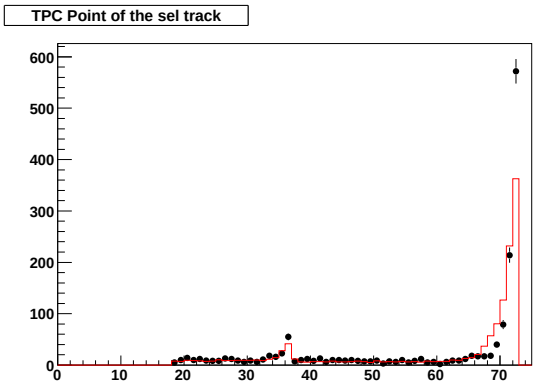

Figure 8.9: Number of reconstructed points for selected tracks: the black points are for the data, the red histogram for the Monte Carlo simulation.

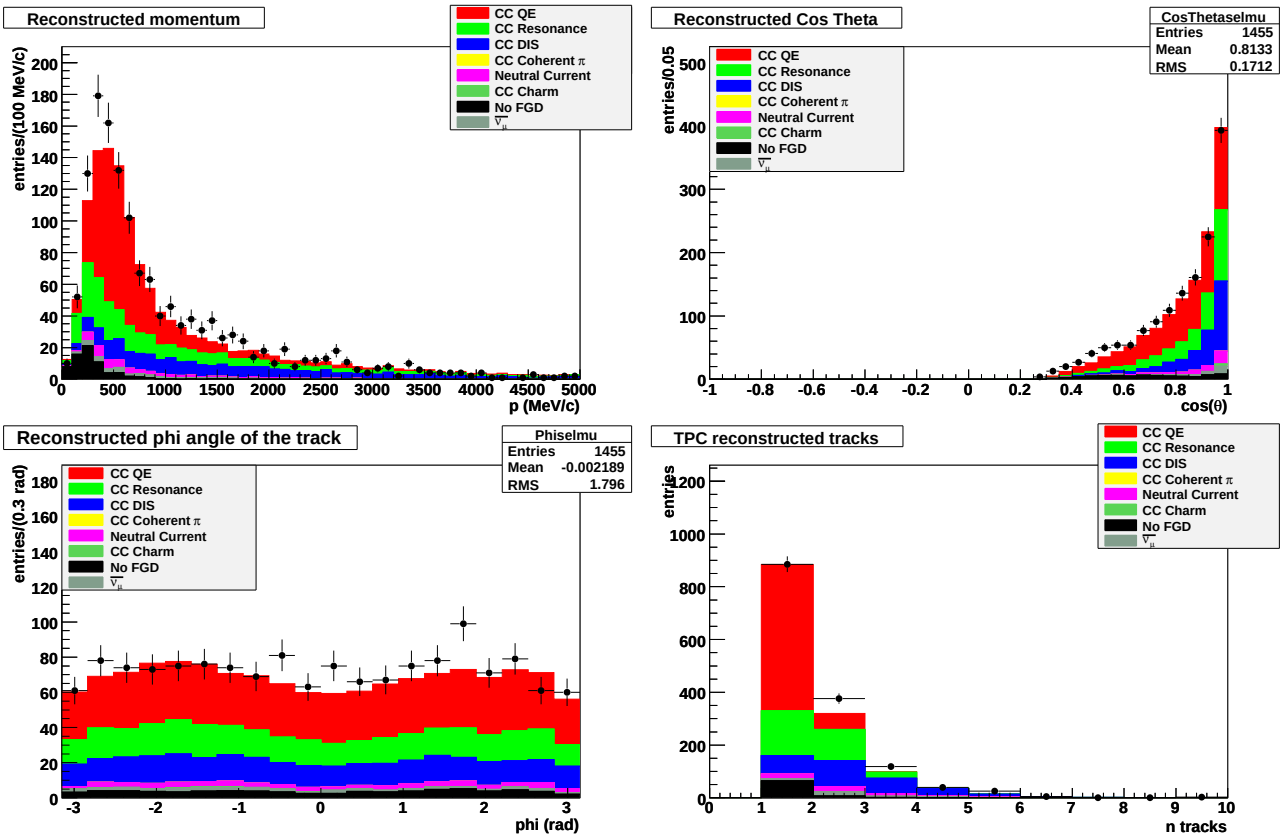

Figure 8.10: Distribution of : a) the muon momentum, b) cos(θ), c) muon azimuthal angle, d) track multiplicity in the TPC for the ν_μ selected events.

Component	Fraction (%), before PID	Fraction (%), after PID
CCQE	36.1 ± 0.5	44.9 ± 0.7
CC Resonance	21.0 ± 0.4	23.7 ± 0.5
CC DIS	19.2 ± 0.4	19.9 ± 0.5
CC Charm	0.4 ± 0.1	0.4 ± 0.1
Neutral Current	5.2 ± 0.2	3.9 ± 0.2
No FGD	15.9 ± 0.4	5.2 ± 0.2
$anti-\nu$	2.2 ± 0.1	2.1 ± 0.2

Table 8.2: Fraction of the different interaction types present in the selected sample before and after the PID selection.

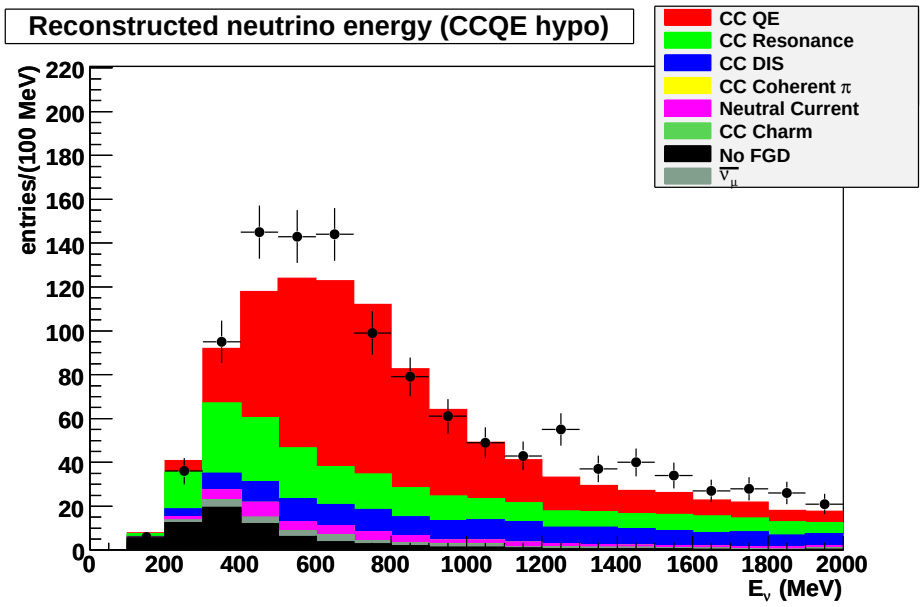

Figure 8.11: Distribution of reconstructed neutrino energy in the CCQE hypothesis for the selected muons.

distributions: discrepancies are not larger than 10%. We can therefore be confident that the bulk of neutrino interactions are correctly reproduced by our Monte Carlo simulation: this is important to correctly predict the background level in the ν_e sample. Moreover we can normalize our ν_e sample to the ν_μ sample and thereby reduce the systematical uncertainty.

8.3 Electron neutrino selection in the tracker

The selection of electron neutrino interactions in the tracker is more difficult than the selection of muon neutrinos as the expected ratio $N(\nu_e)/N(\nu_\mu)$ in the T2K beam is of the order of 1%.
We also expect the purity of this selection to be lower than in the case of the ν_μ: the main backgrounds are due to the misidentification of muons and to ν_μ producing π^0 in the final state: both these backgrounds has been already introduced in chapter 7: as we will show in this section our aim is to measure them using the data.
The first background, coming from misidentified muons, can be estimated selecting a clean sample of through going muons and measuring the misidentification probability. We will describe it in the next section. The second background can be controlled at low momenta

by selecting, instead of negative tracks, positive tracks (this method was already introduced in 7.4): in this way we will select mainly positrons coming from photon conversions.

8.3.1 Muon misidentification probability

It is very important for our analysis to estimate the muon misidentification probability using the data as the energy loss distributions measured in the data and in the Monte Carlo for electrons have some differences: in particular, as we showed in section 5.6, the Monte Carlo slightly overestimates the energy deposited by the electrons and also the deposited energy resolution is slightly better in the Monte Carlo with respect to the data. The combination of these two effects makes the misidentification probability using the Monte Carlo lower.

To measure the muon misidentification probability we need to select a clean sample of muons: the idea was already introduced during the analysis of the M11 data (see section 5.6.4), but given the differences in the momenta distributions between the M11 data and the neutrino data we need to check again the misidentification probability. The best way that we found to select a clean sample of muons was to select the through going muons: these muons are originated in the material surrounding the ND280 pit and enter the basket, crossing the three TPC.
We analyzed the same data set described above and we selected events in which there was one and only one reconstructed track in each of the three TPC. We also required the three tracks to be negative and to further constraint our sample we require the track in the last TPC to be compatible with a muon.
Then we measured the ionization loss of these tracks and we counted how many times the muon passed our ν_e PID selection. The plot of the pull distribution in the electron hypothesis versus the momentum for these tracks is shown in figure 8.12.

The misidentification probability is not constant with respect to the momentum: to measure this probability we divided our sample in different momentum bins from 200 MeV/c to 5 GeV/c. Momenta below 200 MeV/c have not been considered as there the muon energy loss curve crosses the electron curve.

In Table 8.3 the number of misidentified events and the associated misidentification probability in several momentum regions are shown. From the misidentification probability we can then infer the number of muons tracks that enter in our electron sample by considering the muon spectrum shown in figure 8.10.

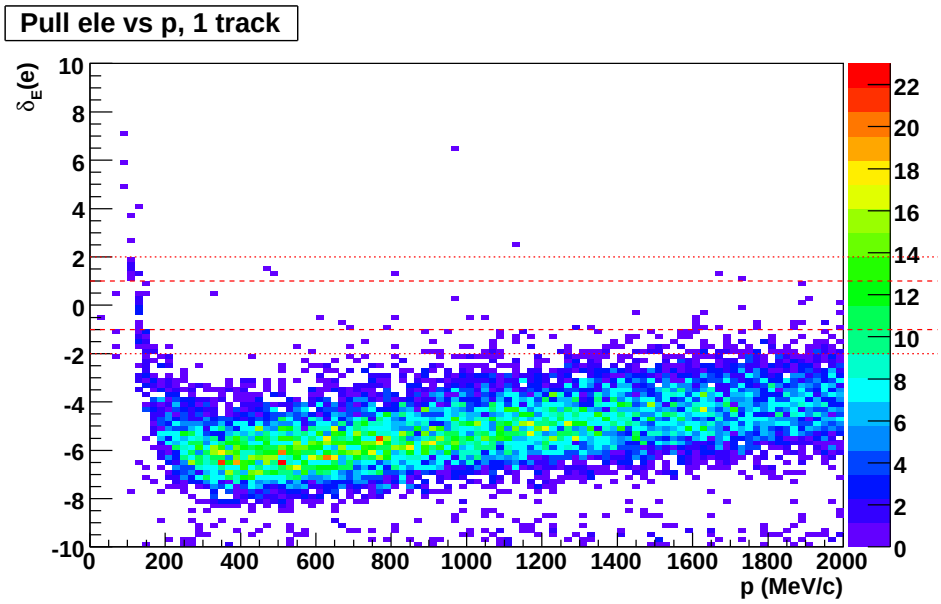

Figure 8.12: Distribution of the TPC PID pull in the electron hypothesis as a function of the reconstructed momentum for through going muons.

Momenta (MeV/c)	N ev $-1 < \delta_E(e) < 2$	N ev $\lvert\delta_E(e)\rvert < 2$	N tot	Mis prob (%) $-1 < \delta_E(e) < 2$	Mis prob (%) $\lvert\delta_E(e)\rvert < 2$
$200 < p < 500$	3	7	1966	0.15 ± 0.09	0.36 ± 0.13
$500 < p < 1000$	9	25	3767	0.24 ± 0.08	0.66 ± 0.13
$1000 < p < 1500$	11	64	3238	0.34 ± 0.10	1.98 ± 0.25
$1500 < p < 2000$	27	128	2413	1.12 ± 0.22	5.30 ± 0.47
$2000 < p < 3500$	99	423	3352	2.95 ± 0.30	12.62 ± 0.61
$3500 < p < 5000$	68	220	955	7.12 ± 0.86	23.04 ± 1.55

Table 8.3: Muon misidentification probability estimated using through going muons in different momenta region.

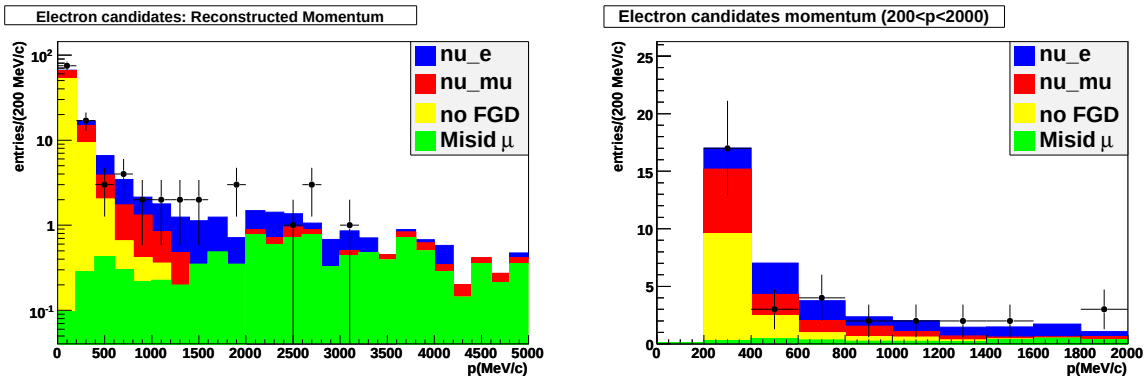

Figure 8.13: Distribution of the reconstructed momentum of the electron candidates (GENIE). On the left plot the distribution is shown for all the momenta while on the right plot only momenta between 200 MeV/c and 2 GeV/c are selected.

Momenta	Observed	Expected	Exp ν_e	Exp ν_μ FGD	Exp no FGD	Mis Muons
All momenta	116	123.8 ± 2.6	13.3 ± 0.9	27.0 ± 1.3	69.9 ± 2.0	13.5 ± 0.6
$200 < P < 2000$	35	37.3 ± 1.5	9.5 ± 0.8	11.4 ± 0.8	11.9 ± 0.8	4.5 ± 0.5

Table 8.4: Selected events in the ν_e analysis in data and Monte Carlo. The Monte Carlo contribution is split in 3 categories: ν_e interactions (signal), ν_μ interactions in the FGD and ν_μ interactions outside the FGD. We also added to the background the component coming from misidentified muons.

8.3.2 Selection of electron neutrino candidates

To select electron neutrino candidates in the tracker we perform the same analysis as in the case of the ν_μ except for the PID electron selection described previously. With this selection we obtain a sample of 116 events (35 with electron momentum between 200 MeV/c and 2 GeV/c).
As we can see from figure 8.13 the agreement between data and Monte Carlo is very good: in Table 8.4 we show the selected number of events in data and Monte Carlo.

In figures 8.14 and 8.15 we show different distributions for the selected electron neutrino candidates: number of reconstructed tracks in the event, the number of e-like tracks, the distributions of $cos(\theta)$ and ϕ angle and the reconstructed neutrino energy: all these distributions show a good agreement between data and Monte Carlo.

The selected sample is composed of four different categories of events: the signal, the

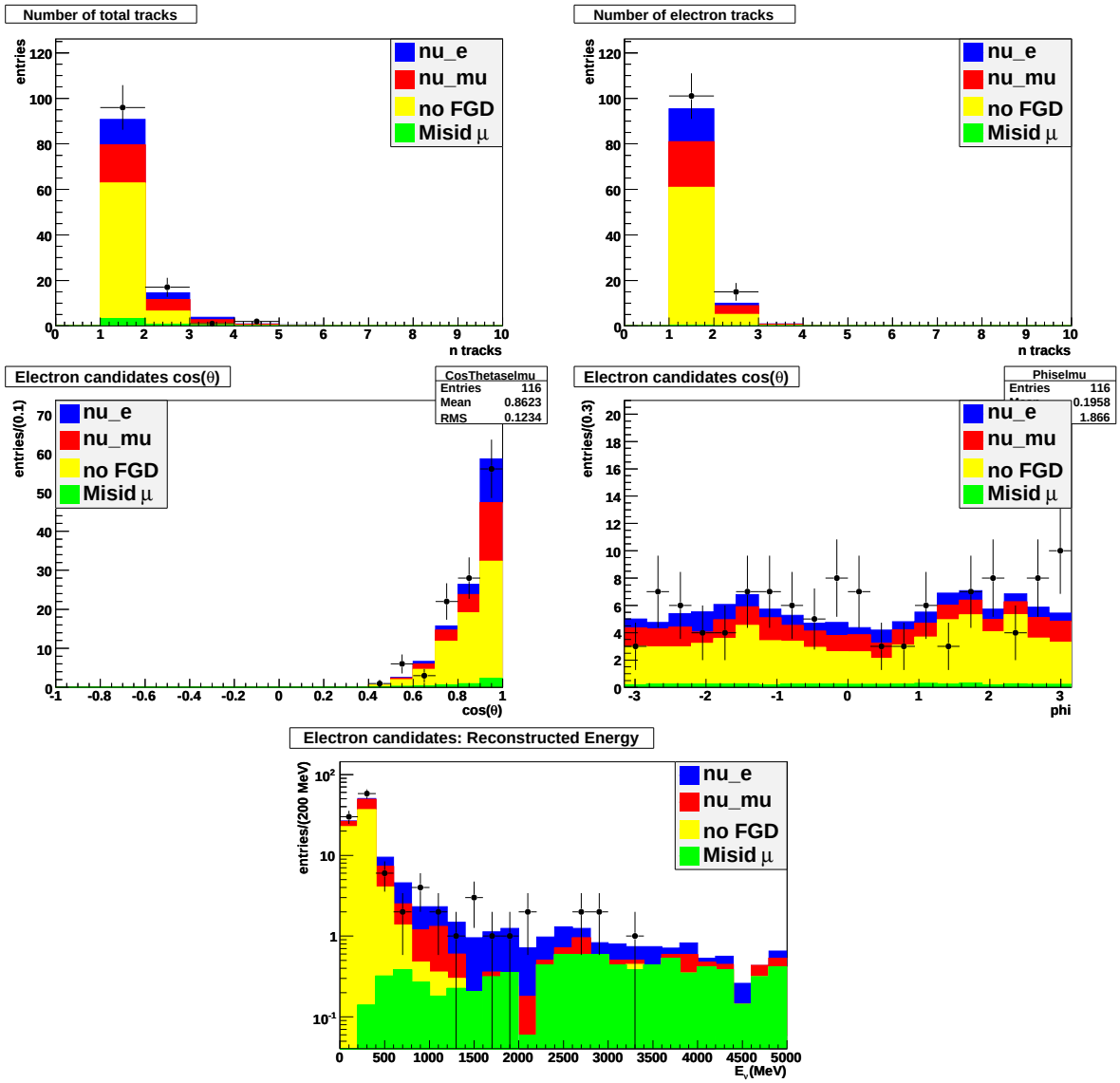

Figure 8.14: Distribution of the number of reconstructed tracks (upper left), of the number of electron like tracks (upper right), of the reconstructed electron $cos(\theta)$ (center left), of the reconstructed electron ϕ angle (center right) and reconstructed neutrino energy (bottom) for all the momenta.

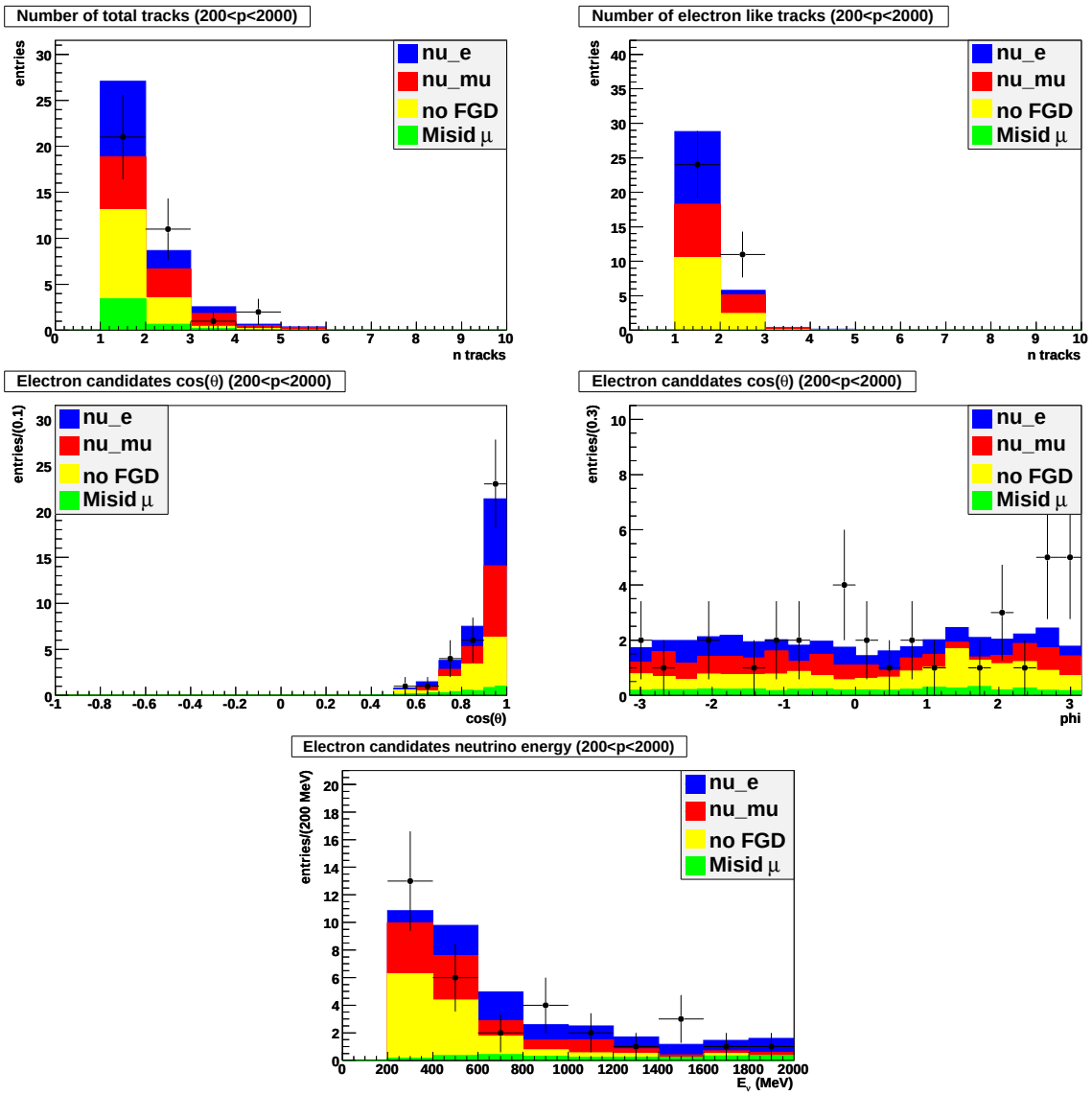

Figure 8.15: Distribution of the number of reconstructed tracks (upper left), of the number of electron like tracks (upper right), of the reconstructed electron $cos(\theta)$ (center left), of the reconstructed electron ϕ angle (center right) and reconstructed neutrino energy (bottom) for the electron momenta between 200 and 2000 MeV/c (GENIE).

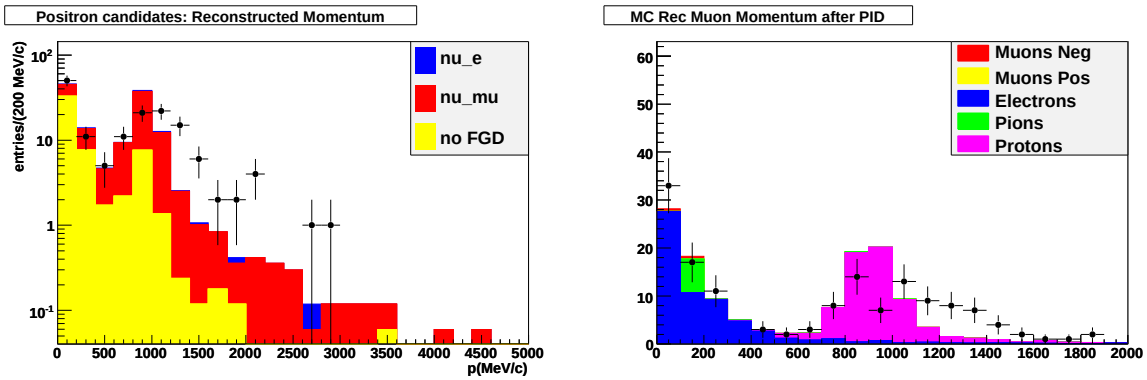

Figure 8.16: Distribution of the reconstructed momentum for the positron sample: on the left plot we show the Monte Carlo expectations divided in different neutrino events type, on the right plot it is divided in different particle id in the TPC: notice that the bump between 500 and 1000 MeV/c is due to protons.

background coming from interactions in the FGD, the background coming from interactions outside the FGD and the background coming from misidentified muons. The last source of background has been measured using the data while the first two have been estimated using the Monte Carlo simulation.

8.3.3 Cross-check of the ν_e selection: the positive analysis

The analysis of events with positrons allows to select a control sample: the idea is to perform exactly the same selection but requiring, instead of negative tracks, positive tracks for the lepton. The aim is to select positrons in the TPCs coming from the conversion of photons in the FGD and measure in this way the electromagnetic component of the background to our analysis. In figure 8.16 we show the reconstructed momenta of the selected tracks. As we can see from this figure at momenta between 500 MeV/c and 1 GeV/c we select also a large amount of protons that at these momenta have similar ionization loss as the electrons. Therefore, useful comparison between the backgrounds in the positron and the electron analysis can be drawn only for tracks below a momentum of 500 MeV/c. In Tables 8.5 we show the number of selected events using the positive analysis in data and Monte Carlo.

The MC confirms that below 500 MeV/c the background in the positive analysis is indeed at the same level as the background in the negative analysis (except for the momenta

Momenta	Observed	Expected	Exp ν_e	Exp ν_μ FGD	Exp no FGD
All momenta	151	129.0 ± 3.6	3.7 ± 0.6	74.1 ± 2.7	51.1 ± 2.3
$200 < P < 2000$	95	78.3 ± 2.8	2.6 ± 0.5	58.1 ± 2.4	17.6 ± 1.3

Table 8.5: Selected events in the positive analysis in data and Monte Carlo. The Monte Carlo contribution is split in 3 categories: ν_e interactions (signal), ν_μ interactions in the FGD (comprising a large proton component) and ν_μ interactions outside the FGD.

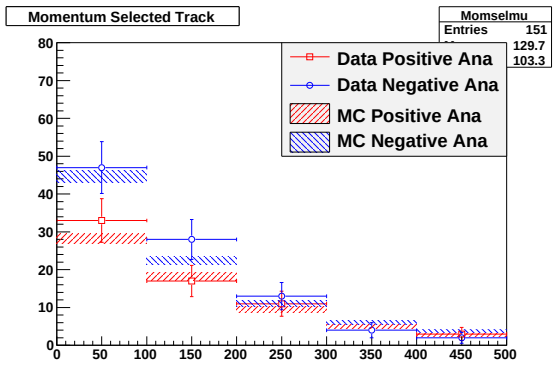

Figure 8.17: Distribution of the reconstructed momentum of the electron candidates using the negative and the positive analysis in data and Monte Carlo.

below 100 MeV/c, to be investigated further).
Moreover the data and MC distributions are in very good agreement as it is shown in figure 8.17. For the purposes of this analysis, given the low statistics, we will not use the positive analysis to measure the electromagnetic background but we use it as an important validation of our background estimation.

8.4 Measurement of the ν_e component

Having selected a sample enriched in ν_e, we now turn to the measurement of the the ν_e component. To do so, we restrict our sample requiring that the electron momentum lies in the (0, 2) GeV/c range. This sample, as explained before, is composed of four event categories:

1. interactions occurring outside the FGD ("NO FGD"), and mainly producing a low energy photon that converts in the FGD;

2. ν_μ interactions in the FGD ("NUMU"), where the muon escapes detection (short track in the TPC, escaping from the side of the FGD) or proceeding through NC. In both cases a π^0 is also produced and one of its photons converts producing at least an electron track in the FGD that is selected;

3. ν_μ interactions in the FGD ("MISID"), where the muon is misidentified as an electron.

4. ν_e CC interactions ("Signal") in the FGD, that is our signal, where the electron is reconstructed and identified in the TPC.

The measurement is performed with a binned (bin width 100 MeV) likelihood fit on the electron momentum measured in the TPC. The total PDF F for the fit is written as:

$$F(p) = N_{TOT}[f_{nf}g_{nf}(p) + f_{nm}g_{nm}(p) + f_{mis}g_{mis}(p) + (1 - f_{nf} - f_{nm} - f_{mis})g_{sig}(p)] \quad (8.1)$$

where p is the electron momentum, N_{TOT} is the number of ν_e selected events between 0 and 2 GeV/c (110), f_{nf} is the fraction of "NO FGD", f_{nm} is the fraction of "NUMU", and f_{mis} is the fraction of "MISID". Each PDF $g(p)$ is normalized to unity.
The PDFs g_{nf}, g_{nm} and g_{sig} are computed using the Monte Carlo simulation, while g_{mis} has been estimated from the data as explained previously. The fraction f are either floated or varied as described in the following.

In the reference fit (Table 8.6) we float the "NO FGD" fraction f_{nf} as this component could more easily be affected by imperfections of the MC simulation, either in the description of the materials or the description of the inclusive π^0 neutrino production cross-section.
We also attempt a fit (second line of the Table), where both "NO FGD" and "NUMU" fractions are floated but the correlation of these two fraction is 97 %, greatly inflating the resulting errors. A third fit (third line of the Table) floats only the total fraction of "NO FGD" and "NUMU" components.
We then vary the "NUMU" fraction f_{nm} by 20 % with respect to the MC prediction and the "MISID" fraction f_{mis} by 30 %. Finally we also made the reference fit using the NEUT generator.

In Table 8.7 we give an estimate of the systematic uncertainties on $N_{sel}(\nu_e)$, obtained from the result of Table 8.6. We have conservatively varied the fraction f_{nm} and f_{mis} by 20 and 30 % respectively.

We finally obtain

$$N_{sel}(\nu_e) = 10.6 \pm 5.2(stat) \pm 1.9(syst) \quad (8.2)$$

and using the results of the ν_μ selection and correcting for the efficiencies (see table 8.8)

f_{nf}	f_{nm}	f_{mis}	f_{sig}	N signal	Comment
0.657 ± 0.047	0.207	0.040	0.096	10.6	reference
0.753 ± 0.184	0.082 ± 0.210	0.040	0.125	13.8	float f_{nf} and f_{nm}
0.867 ± 0.050	0	0.040	0.094	10.3	float sum of f_{nf} and f_{nm}
0.625 ± 0.047	0.248	0.040	0.086	9.5	f_{nm}* 1.2
0.689 ± 0.048	0.166	0.040	0.106	11.6	f_{nm}* 0.8
0.655 ± 0.047	0.207	0.028	0.110	12.1	f_{mis}* 0.7
0.659 ± 0.047	0.207	0.052	0.082	9.1	f_{mis}* 1.3
0.643 ± 0.048	0.223	0.040	0.094	10.4	NEUT

Table 8.6: Results of the likelihood fit for the fraction of ν_e events. The first line reports the reference fit, and we have defined $f_{sig} = (1 - f_{nf} - f_{nm} - f_{mis})$.

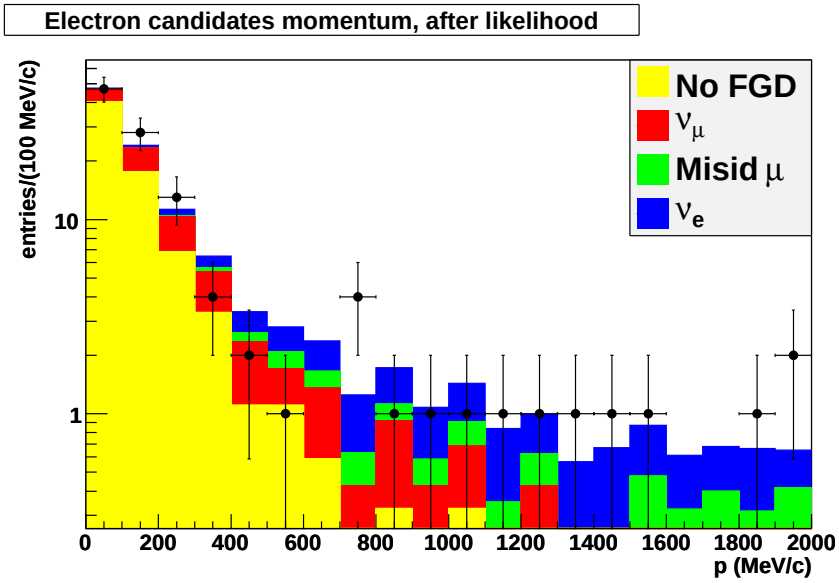

Figure 8.18: Result of the likelihood fit. The data points are shown together with the background components: "NOFGD" (yellow), "NUMU" (red), "MISID" (green) and signal (blue).

Source	Uncertainty
NuMu fraction	1.1
Misid	1.5
NEUT	0.2
Tot Syst	1.9

Table 8.7: Systematical uncertainties relative to the fitted number of ν_e events.

N (ν_e)	$10.6 \pm 5.2(stat) \pm 1.9(syst)$
ϵ (ν_e)	$(22.2 \pm 0.6)\%$
N $(\nu_\mu)^{CC}$	$1324 \pm 36(stat)$
ϵ (ν_μ)	$(38.3 \pm 0.2)\%$

Table 8.8: Summary table of the analyses with the numbers used to compute the ν_e/ν_μ ratio.

$$\frac{N(\nu_e)}{N(\nu_\mu)} = \frac{N_{sel}(\nu_e)\epsilon(\nu_\mu)}{N_{sel}(\nu_\mu)\epsilon(\nu_e)} = (1.37 \pm 0.67(stat) \pm 0.25(syst))\%. \tag{8.3}$$

8.5 Conclusion

In this chapter we have described the first analysis of the data performed at the T2K Near Detector: we presented a measurement of the ν_e component of the T2K beam with the first physics run. This measurement is based on the ND280 tracker and mainly the TPC PID capabilities. We have reported a selection of ν_μ interactions with good agreement between data and MC. A ν_e selection is also presented leading to a sample enriched in our signal. We have performed a fit of the ν_e component of this sample and obtain the following result:

$$\frac{N(\nu_e)}{N(\nu_\mu)} = (1.37 \pm 0.67(stat) \pm 0.25(syst))\%, \tag{8.4}$$

where the first uncertainty is statistical and the second is systematical.
The measurement is in good agreement with the expected ν_e component in the beam and it is still statistically dominated: in the next years more data and the use of informations from other ND280 detectors will improve the precision of this measurement.

Chapter 9

Conclusions

This thesis is devoted to the measurement of the $\nu_\mu \rightarrow \nu_e$ appearance with the T2K experiment. To do this I have developed various tools and methods and worked on different topics, from detector tests and installation to TPC reconstruction and physics analysis. All these tasks are strongly linked together and contribute to different aspects of a global effort towards the main goal of the T2K experiment.
In particular, the aim of this thesis is the measurement of the intrinsic ν_e component of the beam with the Near Detector. The main detector used in this measurement is the ND280 TPC. For what concern the detector hardware I have contributed to the beam test at TRIUMF. Between 2009 and 2010 I have participated to the installation and the commissioning of the TPCs at the ND280 building: during this period I helped in the commissioning of the DAQ system and I developed the online monitoring of the TPCs.

The main part of my thesis work has been done to develop the particle identification methods in the TPCs: the requirements for the T2K TPCs was to have a deposited energy resolution better than 10% to distinguish electrons from muons, measuring in this way the electron neutrino component in the T2K beam, that is one of the main background to the ν_e appearance at the far detector.

I started developing the PID method using a Monte Carlo simulation: we found that the best method to identify particles was to measure the truncated mean of the charge deposited by the particles crossing the TPC gas: we found that a deposited energy resolution of 7% could be obtained by retaining the 70% of the clusters with less energy deposited.

The method has been tested analyzing the beam test data: these data have been taken at TRIUMF where we had a beam composed by electrons, muons and pions with momenta

up to 400 MeV/c: the analysis of these data confirmed that the resolution on the deposited energy in the TPCs was of the order of 7% and we also observed that the separation between electrons and muons was larger than 5σ for momenta larger than 200 MeV/c.

We also confirmed the PID methods using cosmics and beam data taken at JPARC during the commissioning of the TPCs: these data were particularly important because it was the first time that we could measure at the same time the momentum and the energy deposited by the particles. Moreover we had particles with larger momenta with respect to the ones that we had during the beam test, allowing us to study the PID methods in an energy range more interesting for the T2K experiment.

Once the PID methods were established, the most natural way to use it was to do an analysis to measure the ν_e component in the beam: this is one of the most important measurement to be done at the T2K Near Detector and as we showed in the thesis it makes extensive use of the PID methods.

This analysis is difficult because the ratio between the ν_e and the ν_μ is of the order of 1%: the first step to perform the analysis is to have a reliable way to reject the muons and this can be obtained using the TPC PID: we started showing the feasibility of this analysis at ND280 performing a Monte Carlo based analysis that allowed us to study the different problematics and the backgrounds present in the analysis.

Finally when the first data of the T2K experiment were available we started to look at them with the aim of measuring the ν_e component: the first step was to select a sample of neutrino interactions in the tracker: this sample was mainly composed by ν_μ interactions and we studied them to confirm our Monte Carlo simulation and also to have the normalizing factor for the ν_e measurement. The agreement in the ν_μ analysis between data and Monte Carlo was very good and this encouraged as to move forward and try to measure the ν_e.

Also in the ν_e case the agreement between data and Monte Carlo was remarkable and we developed a likelihood fit to extract the ν_e signal, finding 10.6 events. We then used the ν_e and ν_μ samples together to perform a first measurement of the ν_e/ν_μ ratio in the T2K beam that resulted to be:

$$\frac{N(\nu_e)}{N(\nu_\mu)} = (1.37 \pm 0.67(stat) \pm 0.25(syst))\%, \tag{9.1}$$

in good agreement with the expectations from the beam simulation.

This analysis is only the first step towards a precise measurement of the ν_e flux at the Near Detector: it is still statistically dominated and in the near future more data, together with a more refined analysis that uses also the other ND280 detectors, will help us in doing a more precise measurement of the ν_e component to constrain their flux a SuperKamiokande, contributing in this way to the main goal of T2K, that is the study of ν_e appearance in the Far Detector.

Bibliography

[1] J. Chadwick, *Proc. R. Soc. London (A)* 136, 692 (1932)

[2] E. Fermi, Z. Phys. 88, 161 (1934)

[3] C. L. Cowan, F. Reines, F. B. Harrison, H. W. Kruse and A. D. McGuire, Science 124, 103 (1956)

[4] G. Danby, J. M. Gaillard, K. Goulianos, L. M. Lederman, N. Mistry, M. Schwartz and J. Steinberger, Phys. Rev. Lett. 9, 36 (1962)

[5] K. Kodama *et al.* [DONUT Collaboration], Phys. Lett. B 504, 218, 2001

[6] S. L. Glashow, Nucl. Phys. 22, 579 (1961); S. Weinberg, Phys. Rev. Lett. 19, 1264 (1967); A. Salam, "Weak and Electromagnetic Interactions", in *Elementary Particle Theory, Proc. 8th Nobel Symp.*, 367 (1968)

[7] C. Weinheimer, *[ArXiv:hep-ex/02100050]*

[8] W. M. Yao et al. [Particle Data Group], J. Phys. G 33, 1 (2006).

[9] R.N. Mohapatra, G. Senjanovic, Phys. Rev. Lett. 44 (1980) 912

[10] C. Arnaboldi et al. (CUORICINO), Phys. Rev. C78 (2008) 035502

[11] I. Abt et al., arXiv:hep-ex/0404039, 2004.

[12] Danilov, M. et al., Phys. Lett. B480 (2000) 12-18

[13] R. Arnold et al. (NEMO), Nucl. Phys. A765 (2006)

[14] B. Pontecorvo, J.E.T.P. 33 429 (1957)

[15] Z. Maki, M. Nagakawa and S. Sakata, Prog. Theor. Phys. 28, 870 (1962)

[16] R. J. Davis, D. S. Hamer and K. C. Hoffman, Phys. Rev. Lett. 20, 1205 (1968)

[17] L. Wolfenstein, Phys. Rev. D 17, 2369 (1978).

[18] S.P. Mikheev and A. Yu. Smirnov, Sov. J. Nucl. Phys. 42, 913 (1985).

[19] J. Bahcall home page, http://www.sns.ias.edu/ jnb/

[20] Hampel, W. et al. (GALLEX), Phys. Lett. B420 (1998) 114-126.

[21] Abdurashitov, J. N. et al., Astropart. Phys. 25 (2006) 349-354

[22] M. Altmann et al. (GNO), Phys. Lett. B616 (2005) 174

[23] K. S. Hirata *et al.* [KAMIOKANDE-II Collaboration], Phys. Rev. Lett. 63, 16 (1989)

[24] S. Fukuda *et al.* [SuperKamiokande Collaboration], Phys. Rev. Lett. 86, 5651 (2001)

[25] Q. R. Ahmad *et al.* [SNO Collaboration], Phys. Rev. Lett. 87, 071301 (2001)

[26] K. Eguchi *et al.* [KamLAND Collaboration], Phys. Rev. Lett. 90, 021802 (2003)

[27] M. Apollonio *et al.* [CHOOZ Collaboration] Phys.Lett. B466 (1999) 415-430

[28] E. Aliu *et al.* [K2K Collaboration] Phys. Rev. Lett. 94, 081802 (2005)

[29] P. Adamson *et al.* [Minos Collaboration] Phys.Rev.Lett. 97, 191801 (2006)

[30] Guler, M. et al. (OPERA), CERN-SPSC-2000-028, 2000

[31] Geer, S., Phys. Rev. D57 (1998) 6989-6997

[32] Zucchelli, P., Phys. Lett. B532 (2002) 166-172.

[33] S. Davidson, E. Nardi and Y. Nir, Phys. Rept. 466, 105 (2008)

[34] R. H. Cyburt, B. D. Fields, K. A. Olive and E. Skillman, Astropart. Phys. 23, 313 (2005)

[35] W. Hu and S. Dodelson, Ann. Rev. Astron. Astrophys. 40, 171 (2002)

[36] A. D. Sakharov, Pisma Zh. Eksp. Teor. Fiz. 5, 32 (1967) [JETP Lett. 5, 24 (1967 SOPUA,34,392-393.1991 UFNAA,161,61-64.1991)].

[37] T2K letter of Intent (http://jnusrv01.kek.jp/public/t2k/loi/loi.v2.030528.pdf)

[38] D. Beavis et al., Proposal of BNL AGS E-889, (1995).

[39] K. T. McDonald, An Off-Axis neutrino beam, hep:ex/0111033v1

[40] Y. Hayato et al., J-PARC Neutrino Facility Technical Design and Development (Interim) Report, KEK-Internal Report (2003), http ://neutrino.kek.jp/jhfnu/

[41] A. Suzuki et al., Nucl. Instrum. Meth. A329, 299 (1993).

[42] S. Fukuda et al, The SuperKamiokande detector Nucl. Instrum. Meth. A501 2003, (418-462)

[43] H. Maesaka The K2K SciBar detector (2005) Nuclear Physics B - Proceedings Supplements, 139 (1-3 SPEC. ISS.), pp. 289-294.

[44] GEANT: Detector Description and Simulation Toolkit, CERN Programming Library Long Writeup W5013, GEANT version 3.21

[45] http://www.staff.uni-mainz.de/zeitnitz/Gcalor/gcalor.html

[46] M. Gazdzicki et al, Study of Hadron Production in Hadron-Nucleus and Nucleus-Nucleus Collisions at the CERN SPS, CERN-SPSC-2006-034

[47] *Review of Particle Physics*, Phys. Lett. B 667 (2008) 1.

[48] C. Ramsauer, Ann. Phys. 66 (1921) 546.

[49] W. Blum and L. Rolandi, Particle detection with drift chambers, Springer-Verlag Berlin Heidelberg (1993).

[50] E.B.Wagner, F.J. Davies and G.S. Hurst J. Chem. Phys. 47 (1967) 3138.

[51] P. Langevin, C. R. Acad. Sci. (Paris) 146 (1908) 530.

[52] R.L. Gluckstern, Nucl. Instr. and Meth. 24 (1963) 381.

[53] A. Oed, Nucl. Instr. and Meth. A 263 (1988) 351.

[54] F. Sauli, Nucl. Instr. and Meth. A 386 (1997) 531.

[55] G. Charpak, I. Giomataris, Ph. Rebougeard and J.P. Robert, Nucl. Instrum. Methods A376, 29 (1996)

[56] B. Peyaud, Nucl. Instr. and Meth. A 535 (2004) 247.

[57] E. Ferrer Ribas et al., Nucl. Instr. and Meth. A 581 (2007) 217.

[58] F. Kunne et al., Nucl. Instr. and Meth. A 536 (2005) 61.

[59] T2K ND280 TPC Technical Design Report, T2K internal document

[60] S. Biagi, Nucl. Instr. and Meth. A421 (1999) 234.

[61] I. Giomataris et al., Micromegas in a Bulk, Nucl. Instr. Meth. A 560 405, 2006

[62] A. Delbart, R. De Oliveira and J-L. Ritou, Production process of a bulk micromegas for the T2K-TPC, CEA-Saclay/DAPNIA/T2K-TPC internal note EDMS6234, 12/16/2005

[63] P. Baron et al., AFTER an ASIC for the Readout of the large T2K Time Projection Chambers, IEEE NSS07 conference record N29-7 1865, 2007.

[64] D. Calvet et al., The Back-end Electronics of the Time Projection Chambers in the T2K Experiment, IEEE 17th Real Time Conference

[65] Xilinx ML405 Evaluation Platform User Guide, UG210 (v1.2) March 21, 2007. [Online]. Available: http://www.xilinx.com

[66] A.Cervera-Villanueva, J.J.Gomez-Cadenas, J.A.Hernando, RecPack, a general reconstruction toolkit, Nuclear Science Symposium Conference Record, 2003 IEEE Publication Date: 19-25 Oct. 2003, Volume: 3.

[67] D. Karlen, P. Poffenberger and G. Rosenbaum, TPC performance in magnetic fields with GEM and pad readout, accepted by Nucl. Instr. Meth. A, arXiv:physics/0509051.

[68] W.P. Jesse and J. Sadaukis, Phys. Rev. 100 (1955) 1755.

[69] G.G. Meisels, J. Chem. Phys. 41 (1964) 51.

[70] E.J. Kobetich and R. Katz, Phys. Rev. 170 (1968) 391.

[71] H. Bichsel, A method to improve tracking and particle identification in TPCs and silicon detectors, Nuclear Instruments and Methods in Physics Research A 562 (2006) 154.

[72] W.W.M. Allison, J.H. Cobb, Ann. Rev. Nucl. Part. Sci. 30 (1980) 253.

[73] L. Landau, J. Phys. VIII (1944) 201.

[74] H. Bichsel, Rev. Mod. Phys. 60 (1988) 663.

[75] H. Bethe, Ann. Phys. 5, 325 (1930).

[76] U. Fano, Ann. Rev. Nucl. Sci. 13, 1 (1963).

[77] J. W. Gallagher, C. E. Brion, J. A. R. Samson, and P. W. Langhoff, J. Phys. Chem. Ref. Data 17, 9-153 (1988).

[78] E. D. Palik, Handbook of optical constants of solids, Academic Press, 1985.

[79] K. Lassila-Perrini, L. Urban, Nuclear Instruments and Methods in Physics Research A 362 (1995) 416-422

[80] S. Anvar *et al.*, Large Bulk Micromegas detectors for TPC applications, Nuclear Instruments and Methods in Physics Research A602(2009) 415 420.

[81] M.G. Catanesi et al., Nucl. Instrum. and Meth. A571 (2007) 527.

[82] C. Nantais, S. Yen, M11 Beam Momentum, FGD internal presentation

[83] C. Giganti M. Zito, The Particle Identification in the T2K TPC, T2K-TN-001

[84] A. Carver, The Particle Identification in the T2K ECAL, T2K-TN-002

[85] N. Abgrall B. Popov, Prediction of neutrino fluxes for T2K: NA61 data taking and analysis strategy, T2K/NA61 internal note 2009-01

[86] *NEUT*. Y. Hayato, Acta Phys. Pol. B 40, 2477 (2009).

[87] *The GENIE Neutrino Monte Carlo Generator*. Nucl.Instrum.Meth.A614:87-104,2010. arXiv:0905.2517v2 [hep-ph].

Acknowledgements

There are many many people that contributed to make these three years of Thesis exciting and productive.
I want to start thanking my supervisor Marco Zito: during these years I have always found his door open and he gave me a lot of help in discussing and (usually) solving the problems; this thesis would not have been possible without him.
I also want to thanks all the components of the SPP T2K group: Edy, Georges, Sandrine, Olivier, Flor, Michael they all helped me when I needed.
Particularly I wish to thanks Jerome and Andrea: I cannot avoid having some coffee breaks but thanks to them these pauses were also very productive and allowed me to understand something more of MicroMegas or neutrino physics.
Finally I wish to spend some words for Francois Pierre: working with him has been an honour for me: I will always remember his enthusiasm when we started to look at the first neutrino data and I'll miss him a lot.
Besides the SPP group I also want to thanks Alain and Denis for all the hardware help that they provided to me, especially during my Japanese period!
Also all the people in the T2K collaboration help me a lot during these years. I am grateful to all of them but in particular I wish to thanks Federico for his help with the TPC software and DAQ (I think we exchanged more than 1000 email in three years!), Morgan and Nakaya San for all their help during my experience with T2K and previously with SciBooNE, Roberto for all his help with MIDAS while I was in Japan (and for being the best possible run coordinator for the T2K coffee machine!) and Magali for all the biru that we took together (et bien sur pour l'organization du POT de these!!).
Finally I want to thanks the K2K/SciBooNE/T2K group in Rome: it's thanks to the experience that I had there during my master thesis that I decided to do the PhD and they had to support me when my maximum achievement in particle physics was to write hello world using ROOT... Quindi grazie Camillo, Lucio, Pier Ferruccio e Ubaldo!
Then I have to thank my Italian friends and my French friend (including the Germans..). I met a lot of nice people during these three years and all contributed to make this period so beautiful. Here I wish to mention some of them that I met shortly after arriving in Paris and that have been with me for all the period: grazie Francesca, Martin, Michela, Pietro and Stefania!

Desidero infine ringraziare la mia famiglia per essermi stati sempre vicini durante tutti i miei anni di studi, per avermi fatto sempre sentire il loro supporto e per aver sopportato tutti i miei viaggi in Giappone e in Canada!